INSTITUTE OF SCIENCES AND ENGINEERING

DEPARTMENT OF ELECTRICAL AND ELECTRONICS ENGINEERING

SENSORLESS PERMANENT MAGNET SYNCHRONOUS MACHINE CONTROL BASED ON STATOR FEEDFORWARD VOLTAGE ESTIMATION

A Dissertation

submitted by

OMER CIHAN KIVANC

in partial fulfillment of the requirements for the degree of

DOCTOR OF PHILOSOPHY

August 2016

Program: Mechatronics Engineering

SENSORLESS PERMANENT MAGNET SYNCHRONOUS MACHINE CONTROL BASED ON STATOR FEEDFORWARD VOLTAGE ESTIMATION

A Dissertation

by

OMER CIHAN KIVANC

submitted to the Institute of Sciences and Engineering of

OKAN UNIVERSITY

in partial fulfillment of the requirements for the degree of

DOCTOR OF PHILOSOPHY

Approved by:

Asst. Prof. S. Baris Ozturk
Supervisor

Prof. R. Nejat Tuncay
Member

Assoc. Prof. Ozgur Ustun
Member

Assoc. Prof. Burak Kelleci
Member

Asst. Prof. Murat Yilmaz
Member

August 2016

Program: Mechatronics Engineering

ABSTRACT

SENSORLESS PERMANENT MAGNET SYNCHRONOUS MACHINE CONTROL BASED ON STATOR FEEDFORWARD VOLTAGE ESTIMATION

A low-cost, high-performance position sensorless control method for permanent magnet synchronous machine is proposed. In the proposed method, the dynamically enhanced stator feedforward dq–axes voltages derived from a steady-state PM synchronous machine model are modified for the speed sensorless PM synchronous machine drive. The dynamic resemblance of dq–axes PI current regulator outputs are composed of components of the feedforward voltage models. While the proposed method uses feedforward stator voltage estimation method in the estimation of variables showing rapid change, the stator resistance and rotor flux linkage values that change slowly are estimated with the model reference adaptive system (MRAS). Since the proposed method is based on back-EMF estimation, distortion effects caused from parameter changes are reduced with online parameter updates using multi-parameter estimation with MRAS. Compared to other sensorless control methods used in the literature and industry, an efficient method which is simple, applicable in wide speed range is achieved.

With the aim of enabling integration of the developed method into low-cost permanent magnet synchronous machine (PMSM and PMSG) drive systems, the space vector pulse width modulation method is proposed for a four switch three-phase inverter structure without requiring the rotor position angle. Thus, an effective control method in wide speed range for low power PMSM and PMSGs are obtained.

This study is organized as follows. Introduction and modeling, simulation of a speed sensored field-oriented control (FOC) of a permanent magnet synchronous motor (PMSM) drive are expressed in Chapter I. In Chapter II, a simple and efficient position sensorless speed control method based on feedforward voltage estimation for PMSM improved with multi-parameter estimation using MRAS method for SSTP is proposed and described in detail. In Chapter III, a simple, effective and low-cost position sensored speed control scheme for PMSM drive using four-switch three-phase inverter (FSTP) is developed and discussed. In Chapter IV, a position sensorless speed control method based on stator feedforward dq–axes voltage estimation (FFVE) has been designed and described in detail for low-cost four-switched three-phase (FSTP) PMSM drive. In Chapter V, a simple and efficient position sensorless control method based on feedforward voltage estimation for permanent magnet synchronous generator (PMSG) improved with multi-parameter estimation using MRAS method is designed and developed. In Chapter VI, the control of direct-drive PMSG along with load side inverter control are performed and discussed using a bi-directional, two-level, back-to-back voltage source rectifier/inverter with total of eight switches for the variable speed wind turbine. Finally, concluding remarks, are expressed in Chapter VII.

Keywords: Permanent magnet synchronous motor (PMSM), space-vector PWM (SVPWM), four-switch three-phase (FSTP) inverter, reduced switch inverter, sensorless control, stator feedforward voltage estimation (FFVE), direct drive, sustainable energy, model reference adaptive system (MRAS), parameter estimation, permanent magnet synchronous generator (PMSG).

KISA ÖZET

SÜREKLİ MIKNATISLI SENKRON MAKİNELER İÇİN İLERİ BESLEMELİ STATOR GERİLİM TAHMİNİ METODUNA DAYALI SENSÖRSÜZ KONTROL YÖNTEMİ GELİŞTİRME

Yapılan çalışmada sürekli mıknatıslı senkron makineler (SMSM) için düşük maliyetli, yüksek performanslı bir pozisyon sensörsüz kontrol metodu önerilmektedir. Önerilen metotta ileri beslemeli dq–ekseni stator gerilimleri, SMSM sürekli hal denklemleri kullanılarak sensörsüz kontrol algoritması elde dilmiştir. PI akım kontrolörlerinin çıkış değerlerinden faydalanılarak ileri beslemeli stator gerilim modelleri oluşturulmuştur. Önerilen yöntem hızlı değişim gösteren parametrelerin tahmininde ileri beslemeli stator gerilimi tahmin yöntemini kullanırken, yavaş değişim gösteren stator direnci ve rotor halkalanma akısı parametrelerini model referans adaptif sistem (MRAS) ile tahmin etmektedir. Önerilen metodun zıt-EMK tahminine dayalı bir yöntem olması sebebiyle parametre değişiminden kaynaklanan bozucu etkiler MRAS ile çoklu parametre tahmini yapılarak, online parametre güncellemesi ile giderilmektedir. Literatürde ve endüstride kullanılan diğer sensörsüz kontrol metotları ile karşılaştırıldığında basit, uygulanabilir ve geniş hız aralığında verimli çalışan bir metot elde edilmiştir.

Geliştirilen metodun düşük maliyetli SMSM tahrik sistemlerine entegrasyonunu sağlamak amacıyla rotor pozisyon açısına ihtiyaç duymayan bir dört anahtarlı üç fazlı evirici yapısı için uzay vektör darbe genişlik modülasyonu (UVDGM) yöntemi

önerilmektedir. Böylelikle küçük güçlü SMSM'de düşük hızlarda etkin bir kontrol yöntemi sağlanmış olacaktır.

Yapılan çalışmanın akış organizasyonu sırasıyla ifade edilmektedir. Bölüm 1'de Giriş ve MATLAB/Simulink programında yer alan MATLAB fonksiyonları kullanılarak pozisyon sensörüne sahip bir SMSM'nin alan-yönlendirmeli kontrolünün modelleme, simülasyonu yapılmıştır. Bölüm 2'de MRAS metodu ile çoklu parametre tahmini yapılarak SMSM için basit ve verimli bir ileri beslemeli stator gerilim tahminine dayalı pozisyon sensörsüz kontrol metodu geliştirilmiş ve detaylı bir şekilde ifade edilmiştir. Bölüm 3'de pozisyon sensörlü SMSM'nin hız kontrolü için dört anahtarlı evirici topolojisi ve düşük maliyetli, verimli bir kontrol algoritması geliştirilmiştir. Bölüm 4'de SMSM hız kontrolü için ileri beslemeli stator gerilim tahminine dayalı bir sensörsüz kontrol algoritması geliştirilmiş ve Bölüm 3'de önerilen eksiltilmiş anahtarlı evirici topoloji kullanılarak düşük maliyetli bir tahrik sistemi elde edilmiştir. Bölüm 5'de ileri beslemeli stator gerilim tahminine dayalı sensörsüz kontrol algoritması çoklu parametre tahmini ile bir arada uygulanmış ve doğrudan tahrikli, küçük güçlü sürekli mıknatıslı senkron generatörlerin (SMSG) geniş bir hız aralığında çalışmasına imkan tanıyan bir sensörsüz kontrol metodu geliştirimiştir. Bölüm 6'da ise Bölüm 5'de önerilen sensörsüz kontrol algoritması düşük maliyetli ve eksiltilmiş anahtarlı, sırt-sırta bağlı, iki seviyeli çevirici kontrollü SMSG'ler için geliştirilmiş ve detaylı olarak anlatılmıştır. Geliştirilen metotlar simülasyon ve deneysel çalışmalar ile desteklenmiş ve Bölüm 7'de elde edilen bulgular ve sonuçlar ifade edilmiştir.

Anahtar Kelimeler: Sürekli mıknatıslı senkron makineler (SMSM), uzay vektör darbe genişlik modülasyonu (UVDGM), dört anahtarlı üç fazlı evirici (DAÜF),

eksiltilmiş anahtarlı evirici, sensörsüz kontrol, ileri beslemeli stator gerilim tahmini, doğrudan tahrik, sürdürülebilir enerji, model referans adaptif sistem (MRAS), parametre tahmini, sürekli mıknatıslı senkron generatör (SMSG).

To All Endless Nausea and Utopias

ACKNOWLEDGMENT

I would like to thank my thesis advisor Asst. Prof. S. Baris Ozturk who has provided full support from the date we met and started to work together, a depth of gratitude. His contribution to success of several projects and scientific studies we accomplished together and his effort for keeping pace with my complex studying order are unforgettable. I believe that I should write a separate title for Prof. R. Nejat Tuncay. I thank him for his contributions to my being as a modern, innovative, enterprising researcher and academician during our collaboration. Our road adventures, football conversations, searches for bypass (road), and sharing his bread with me every day with the same excitement are most important motivation factors for creating this dissertation. I thank Assoc. Prof. Ozgur Ustun whom we carried out many projects and academic studies together in Mekatro R&D Company, for all his supports in our collaboration. I express my gratitude towards the great Soviet Scientist Prof. Parviz Ali-Zade whom we got my first patent and article together, for all his supports and helps. I thank Assoc. Prof. Burak Kelleci, Asst. Prof. Bahar Tanyas, Asst. Prof. Basar Ozkan, Asst. Prof. Didem Kivanc Tureli, Prof. Mithat Idemen, Asst. Prof. Gunseli Gorur, Asst. Prof. Suleyman Biyikli, Alper Celikel, Gizem Erden, Gurkan Bozkurt, Berkin Atila and T. Eren Mungan that we worked together in Okan University and provided full support to me, for their helps and supports.

I express my gratitude to Ali Riza Yikilmaz, Yuksel Dogan and Ali Baz that we lived and proceeded together during my education life, to Gurkan Tosun who gave all kinds of technical and moral support during our collaboration and to other colleagues

at Mekatro R&D Company and to TUBITAK who provided support to the project from which this dissertation is created.

I thank my “Dulcinea” Deniz Turk who witnessed to all processes of the dissertation and never refrained to support.

I thank my sister Ipek Kivanc, my mother and my father who are so valuable for me and irreplaceable, for their beliefs and supports to me at my all difficult times.

Lastly, I thank my endless friends Ahmet Hamdi Tanpinar, Yusuf Atilgan, Oguz Atay, Cervantes, Jean-Paul Sartre, Albert Camus, Isaac Newton, Ernest Hemingway, Franz Kafka, Aldous Huxley, Yasar Kemal, Orhan Kemal and Fikret Kizilok that their supports to me at my all difficult times.

TABLE OF CONTENTS

LIST OF TABLES

LIST OF FIGURES

SYMBOLS

v_d Stator d–axis Voltage

v_q Stator q–axis Voltage

i_d d–axis Current in the Rotor Reference Frame

i_q q–axis Current in the Rotor Reference Frame

R_s Stator Winding Resistance

L_d d–axis Inductance

L_q q–axis Inductance

L_s Average Inductance

λ_{dr} Flux Linkage Due to the Permanent Magnet Rotor Flux

ω Rotor Angular Electrical Velocity

$\overrightarrow{v_s}$ Complex Space Vectors of the Stator Voltages

$\overrightarrow{i_s}$ Complex Space Vectors of the Stator Currents

$\overrightarrow{\lambda_s}$ Complex Space Vectors of the Rotor Flux Linkages

$v_{sa}(t)$, $v_{sb}(t)$, $v_{sc}(t)$ Instantaneous Values of Stator Phase Voltages

$i_{sa}(t)$, $i_{sb}(t)$, $i_{sc}(t)$ Instantaneous Phase Currents

$\lambda_{sa}(t)$, $\lambda_{sb}(t)$, $\lambda_{sc}(t)$ Instantaneous Stator Flux Linkages

S_a, S_b, S_c Status of the Three Switches

V_{dc} DC Bus Voltage

T_a, T_b, T_c Three-Phase Duty Cycles

λ_f Rotor Flux Linkage

ω_e Rotor Angular Electrical Velocity

G MRAS Gain Matrix

$\widehat{R}_s$ Estimated Stator Resistance

$\hat{\lambda}_f$ Estimated Rotor Flux Linkage

$\hat{\imath}_q$ Estimated q–axis Current

$\hat{\imath}_d$ Estimated d–axis Current

$k_{p_{res}}$ Estimated Resistance Proportional Regulator Coefficient

$k_{i_{res}}$ Estimated Resistance Integrator Regulator Coefficient

$k_{p_{flux}}$ Estimated Rotor Flux Linkage Proportional Regulator Coefficient

$k_{i_{flux}}$ Rotor Flux Linkage Integrator Regulator Coefficient

$\widehat{R}_0$ Estimated Last Stator Resistance

$\hat{\lambda}_{f0}$ Estimated Last Rotor Flux Linkage

v_d^* Stator d–axis Voltage Reference

v_q^* Stator q–axis Voltage Reference

i_d^* d–axis Reference Current

i_q^* q–axis Reference Current

Δv d–axis Current Regulator Output

K Scheduled Gain of Feedforward Voltage Control

Z Center Point of the Split Capacitors Indice

$\mathcal{V}_\alpha$ Component of Reference Stator Voltage Vector on Direct Axis Stationary Reference Frame

$\mathcal{V}_\beta$ Component of Reference Stator Voltage Vector on Quadrature Axis Stationary Reference Frame

$\mathcal{V}_{AN}$ Phase–a Voltage

$\mathcal{V}_{BN}$ Phase–b Voltage

$\mathcal{V}_{CN}$ Phase–c Voltage

$\mathcal{V}_{AZ}$ Phase–a Voltage Calculated Using the Pole Voltages

$\mathcal{V}_{BZ}$ Phase–b Voltage Calculated Using the Pole Voltages

$\mathcal{V}_{CZ}$ Phase–c Voltage Calculated Using the Pole Voltages

$\mathcal{V}_{NZ}$ Phase Voltage–Neutral Calculated Using the Pole Voltages

$\mathcal{V}_{ref}$ Stator Reference Voltage

X, Y Variables for Sector Determination

$\mathcal{V}_1$, $\mathcal{V}_2$, $\mathcal{V}_3$, $\mathcal{V}_4$ Four Voltages Space Vectors

T Total Time Duration

T_0 Time Duration of Null Vector

t Experimental/Simulation Time

ρ Air Density

r Radius of Wind Turbine Rotor Plane

v_w Wind Speed

C_p Turbine Power Coefficient

λ Tip-Speed Ratio

β Pitch Angle

c_i Coefficicents of Wind Turbine Model

λ_{opt} Optimal Tip-Speed Ratio

P_{wind} Wind Power

P_{tur} Output Mechanical Power of Wind Turbine

p Pole Number

T_e Electromechanical Torque

$T_{e_{opt}}$ Optimal Electromechanical Torque Reference

$\hat{\omega}_r$ Estimated Rotor Speed

$\dot{e_d}$ Derivative of d–axis Current Estimation Error

$\dot{e_q}$ Derivative of q–axis Current Estimation Error

R_0 Initial Resistance

T_0 Initial Temperature

$\propto$ Winding Temperature Constant (Copper)

m Modulation Index

$V_{LL(rms)}$ Line to Line RMS Voltage

U_{DC} Rectifier/Inverter Common DC Bus

R_{Load} Load Resistance

L_{Load} Load Inductance

L_2 Inductance in the Side of Grid/Load

L_1 Inductance in the Inverter Side Input

C_f Filter Capacitance

R_{dp} Parallel Damping Resistance

ABBREVIATIONS

FOC Field-Oriented Control

PMSM Permanent Magnet Synchronous Machine

MCU Microcontroller Unit

AC Alternative Current

IPMSM Interior Permanent Magnet Synchronous Machine

SVPWM Space Vector Pulse Width Modulation

MMF Magneto-Motive Force

VSI Voltage Source Inverter

PWM Pulse Width Modulation

DC Direct Current

PI Proportional-Integral

DMC Digital Motor Control

TI Texas Instruments

CCS Code Composer Studio

PM Permanent Magnet

DSP Digital Signal Processing

IGBT Insulated-Gate Bipolar Transistor

EMF Electro-Motive force

FFVE Feedforward Voltage Estimation

MRAS Model Reference Adaptive System

BLDC Brushless DC

EKF Extended Kalman Filter

RLSE Recursive Least Squares Estimation

ANN Artificial Neural Network

FL Fuzzy Logic

SMO Sliding Mode Observer

SMPMSM Surface Mounted Permanent Magnet Synchronous Machine

LPF Low Pass Filter

FSTP Four-Switch Three-Phase

SSTP Six-Switch Three-Phase

DTC Direct Torque Control

PFC Power Factor Correction

CCW Counter Clock Wise

FFT Fast Fourier Transform

THD Total Harmonic Distortion

IM Induction Motor

IFOC Indirect Field-Oriented Control

FV Flux Vector

PMSG Permanent Magnet Synchronous Generator

DFIG Doubly Fed Induction Generator

SG Synchronous Generator

IG Induction Generator

MPPT Maximum Power Point Tracking

SMPMSG Surface Mounted Permanent Magnet Synchronous Generator

FFVC Feedforward Voltage Control

EEMF Extended Electro-Motive Force

IEEE Instute of Electrical and Electronics Engineers

IEC International Electrotechnical Commission

IPM Interior Permanent Magnet

HF High Frequency

TUBITAK The Scientific And Technological Research Council Of Turkey

IE International Efficiency

I. INTRODUCTION

Back-EMF estimation plays an important role in todays' industrial applications as a method that can ensure the stability in wide speed range compared to other methods. In this study, a simple and effective position sensorless speed control method for both surface mount and interior permanent magnet synchronous motors are proposed. The dynamically enhanced modified feedforward stator dq–axes voltages that are derived from a steady-state PM synchronous machine model are applied to the PM motor. The dynamic resemblance of the actual PM machine is accomplished by the help of d^*– and q^*–axes PI regulator outputs which are composed as the components of the feedforward voltage models. q–axis PI current regulator output with a simple filtering formulates the speed estimation algorithm and the output of the d–axis PI regulator acts as the part of the derivative representation in the feedforward voltage equations.

In Chapter I, modeling and simulation of a speed sensored FOC of a PMSM drive is developed by using MATLAB Function blocks in MATLAB/Simulink. This method allows easier algorithm and software development stages for experimental studies compared to the classical block diagram approach. The superiority of the method over commonly used “Code Generation” tools is also emphasized. First, a MATLAB/Simulink model of the FOC of PMSM drive is developed by using MATLAB programming in MATLAB Functions similar to C coding techniques. The results of the simulation are presented. Then, the MATLAB programming based codes developed in simulation are implemented in a TMS320F28335 floating-point MCU by using C programming language and the experimental results are obtained. Finally, the results of the simulation and experiments are compared.

A simple and efficient position sensorless speed control method based on feedforward voltage estimation for PMSM improved with multi-parameter estimation using MRAS method is proposed in Chapter II. The dynamically enhanced stator feedforward dq–axes voltages that are derived from steady-state PMSM model are modified for the speed sensorless drive. The dynamic resemblance of the actual PM machine is accomplished by the help of d– and q–axes PI current regulator outputs which are composed as the components of the feedforward voltage models. In order to improve performance of the proposed sensorless PMSM control method, stator resistance and rotor flux linkage in feedforward voltage estimation model is continually updated in PMSM steady-state model by estimating them. Thus, a sensorless control methods which is dynamic, industrial and not affected by parameter changes. The proposed control method with MRAS parameter estimation for PMSM has been simulated by using MATLAB/Simulink. Simulation results demonstrate the feasibility and effectiveness of the proposed method. The whole control system is implemented with 1 kW PMSM drive controlled by a TMS320F28335. Experimental results demonstrate the feasibility and effectiveness of the proposed method for PMSM under various load and speed conditions.

In many applications where especially low power is demanding such as in consumer products and light electric vehicles, the development of a reduced cost three-phase inverter is essential to decrease the overall drive cost along with removing the position sensor. The overall price of the three-phase inverter is mainly determined by the number of semiconductor switches. The main contribution of Chapter III is achieve a simple, effective and low-cost position sensored speed control scheme for PMSM drive using FSTP. Moreover, it is also shown in this chapter that by proper connection

of the PM motor terminals to the FSTP inverter legs, SVPWM for FSTP inverter is successfully achieved by using a novel and simple sector determination method without requiring any position or voltage sensors. The proposed FSTP VSI based sensored speed control method is applicable to both surface-mounted as well as interior type PM motors. The proposed method has been simulated by using MATLAB/Simulink and implemented with a 1 kW PMSM drive controlled by a TMS320F28335 floating-point DSP. Simulation and experimental results shows the feasibility and effectiveness of the proposed SVPWM algorithm under full-load condition using FSTP inverter.

In Chapter IV, a simple and low-cost position sensorless speed control method based on stator FFVE for both SPMSM and IPMSM is proposed using space vector PWM based FSTP inverter with a simple sector determination. The dynamically enhanced stator feedforward dq–axes voltages that are derived from a steady-state PM synchronous machine model are modified for the speed sensorless PMSM drive. The dynamic resemblance of the actual PM machine is accomplished by the help of d– and q–axes PI current regulator outputs which are composed as the components of the feedforward voltage models in which the q–axis PI current regulator output with a first order low-pass filter formulates the speed estimation algorithm in a closed-loop fashion similar to PLL and the output of the d–axis PI current regulator acts as the derivative representation. The proposed method is quite insensitive to multiple simultaneous resistance, inductance and rotor flux linkage variations due to the dynamic effects of the PI current regulator outputs that are used in the stator feedforward voltages with a proper high possible K gain selected between 4 to 7 in the q–axis voltage estimation algorithm. The proposed speed sensorless control scheme has been simulated by using MATLAB/Simulink and implemented with a 1 kW PMSM drive controlled by a

TMS320F28335 floating-point DSP. Simulation and experimental results demonstrate the feasibility and effectiveness of the proposed stator FFVE based position sensorless speed control scheme for PMSM under full-load condition using FSTP inverter.

A simple and efficient position sensorless control method based on feedforward voltage estimation for PMSG improved with multi-parameter estimation using MRAS method is proposed in Chapter V. The dynamically enhanced stator feedforward dq–axes voltages that are derived from steady-state PMSG model are modified for the sensorless drive. In direct-drive wind turbine systems, because of low back-EMF amplitude in the generator output at very low speed generator operation, the rotor flux linkage cannot be predicted correctly. Fixed-speed IG, DFIG, SG, and PMSG are widely used in wind turbines as generators. Also, the rotor flux linkage that changes due to aging, vibration, humidity and temperature reduces the drive control performance. In order to obtain the maximum power in PMSG vector control and to achieve accurate current control, the rotor speed should be known. Vector control is often used in PMSG control, because it has a simple structure and is suitable for various industrial systems. In the power equation, maximum power is obtained as a function of torque and speed. In the proposed method, a variable-speed wind turbine system with back to back converter structure is connected to common DC-link. The converter at the generator side is used to obtain the maximum power from different wind speeds; the grid side converter on the other hand is used to transmit the power produced from the generator to static grid (off-grid). In Chapter V, electrical simulation model in MATLAB/Simulink is designed and developed. The simulation results are given and analyzed in detail. The proposed sensorless control scheme has been implemented with 1 kW PMSG drive controlled by a TMS320F28335.

The main goal of Chapter VI is to provide electric power generation using a renewable and portable method in rural and geographically problematic areas where energy transmission is not possible. Electric power generation from wind with low-cost, efficient and portable small-scale wind turbine during natural disasters (earthquake, fire, flood, etc.) leading to catastrophic consequences (long electrical black-outs) and for individual low power applications is targeted. The control of gearless PMSG along with load side inverter control in this chapter are performed using a bi-directional, two-level, back-to-back voltage source rectifier/inverter with total of eight switches for the variable speed wind turbine. The speed of the turbine at the generator side, therefore the speed of generator used in the maximum power point tracking algorithm is obtained by the novel and simple position sensorless feedforward stator voltage control method using SVPWM. This method is proposed in the literature for the first time for synchronous generators along with the MRAS rotor flux and stator resistance estimation method for minimizing the total cost. Due to increase of temperature, magnets in the PMSG lose their magnetization (de-magnetization). Therefore, one of the major advantages and novelty of using MRAS rotor flux linkage estimator in this system is to correct the changes in the flux values in the control system. Due to its simplicity and effectiveness, the load side control is achieved by using four-switch grid side inverter. To observe the total system performance, a three-phase passive load is used at the inverter output. The low-pass LCL-filter is designed and used in the load side to reduce current and voltage harmonics and increase stability and efficiency of the power network. The overall system is designed, modeled and analyzed in Matlab/SIMULINK and the results are compared, verified and validated with the real-time DSP system.

1.1. Introduction to Matlab Function Based Approach to FOC of PMSM Drive

Recently, AC motor control and driving strategies are attracting more and more interest. Development of embedded systems, observers and control systems are enabling new algorithms in motor control. The complex nature of these algorithms causes difficulties in programming. MATLAB/Simulink® is commonly used for modeling and simulation of electromechanical systems and their control applications before the realization step. It is usually expected that experiments yield results similar to those obtained in the MATLAB/Simulink simulation environment.

Usually, a MATLAB/Simulink simulation model of an AC motor drive is developed in the literature by using classical Simulink® blocks that are available in the standard Simulink Library [1]–[12]. Although, initial developments of the algorithms designed by connecting the library blocks in Simulink Library makes the development stage easy, the future addition or modifications of the system become quite difficult. Moreover, the development of AC motor drive simulation models can also be achieved by using the motor control blocks in MATLAB/Simulink Embedded Coder® [13]–[15]. The MathWorks®, Inc. developed the Embedded Coder toolbox for certain microprocessor families such as the Texas Instruments® (TI) C2000 microprocessor family which is widely used in motion control applications. The C2000 family offers superior performance in motor control applications. If the experimental motor control system consists of a C2000 microcontroller family, it is an option to build the simulation model of an AC motor drive system by using the blocks provided in Embedded Coder. However, this toolbox is an additional cost to the standard MATLAB/Simulink package and does not allow modifications of its blocks.

The simpler, easily modifiable and more economical choice of MATLAB/Simulink modeling and simulation of an AC motor drive is to use MATLAB Functions. The handicaps given above are overcome by using MATLAB Function blocks in MATLAB/Simulink. Most of the motor control applications nowadays require the C programming language. Therefore using C programming like MATLAB Programming in MATLAB Functions in MATLAB/Simulink produces a similar approach as opposed to the classical block diagram based modeling of an actual system. Using the classical block diagram approach also creates difficulties in understanding and improving the system during future modifications.

In this study, a proposed MATLAB/Simulink model of a speed sensored field-oriented control (FOC) of a PMSM drive is developed by using MATLAB programming in MATLAB Functions similar to the C programming language [130]. Therefore, the goal of a simple, easily modifiable and economical MATLAB/Simulink modeling method that helps the smooth transition to the experimental stage is achieved. This is especially true for systems that are programmed in the C language. During the application stage, MATLAB function based drive modules are manually converted to the C language and implemented in a TI's TMS320F28335 Delfino floating-point MCU. Finally, the results of the simulation and experiments are compared.

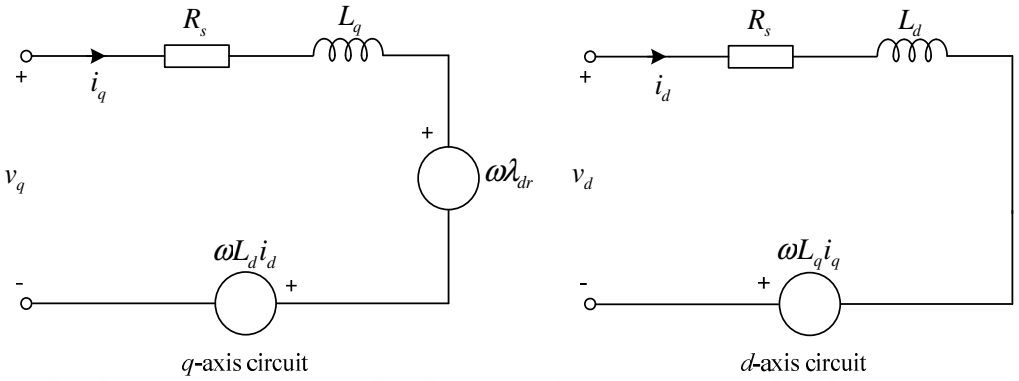

Figure I.1. Equivalent electrical circuit diagrams of quadrate q– and d–axes synchronous reference frame that apply to both surface-mount and interior permanent magnet synchronous machines (IPMSM) [16], [17].

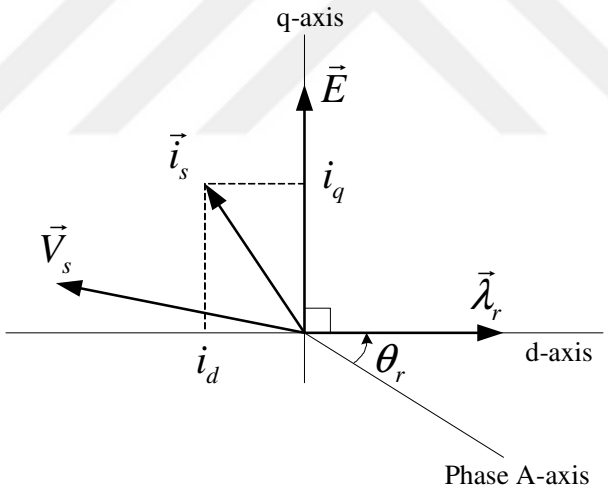

Figure I.2. Basic phasor diagram for PMSM [16].

1.2. FOC of PMSM Drive

1.2.1. Dynamic mathematical model of interior PMSM

The dq model in the rotating synchronous reference frame shown in Figure (I.1) is used to analyze the IPMSM for the field-oriented control (FOC). The stator voltage

equations of the IPMSM in the rotating dq reference frame are given by (I.1) and (I.2), omitting the influences of magnetic field saturation and magnetic hysteresis as

$$v_q = R_s + L_q \frac{di_q}{dt} + (\omega i_q L_d + \omega \lambda_{dr}) \tag{I.1}$$

$$v_d = i_d R_s + L_d \frac{di_d}{dt} - \omega i_q L_d \tag{I.2}$$

where v_d, v_q, i_d, i_q are the stator d– and q–axes voltages and currents in the rotor reference frame, respectively; R_s is the stator winding resistance; L_d and L_q denote the d– and q–axes inductance, respectively; ω is the rotor angular electrical velocity; and λ_{dr} is the flux linkages due to the permanent magnet rotor flux [16]–[18].

1.2.2. Vector control of PMSM

For superior driving performance of PMSM, vector control, or field-oriented control (FOC), is widely used. As shown in Figure I.2, for simplicity and to remove the time-varying quantities, the two-axis theory is used for FOC of sinewave drives. To produce the maximum torque in FOC, q–axis current and the rotor flux linkage aligned with the d–axis are kept in quadrature form, as depicted in Figure I.2. The d– and q–axes current phasor components, i_d and i_q, are generally fixed to the rotor reference frame. To obtain i_d and i_q from the instantaneous phase currents, a reference frame transformation, such as Park transformation is employed [16].

For switching of the inverter, the space vector pulse with modulation (SVPWM) is used in PMSM drives. The space vector form of the stator voltage equation in the stationary reference frame is shown in (I.3)

$$\overrightarrow{v_s} = R_s \overrightarrow{i_s} + \frac{d\overrightarrow{\lambda_s}}{dt} \tag{I.3}$$

where R_s, $\overrightarrow{v_s}$, $\overrightarrow{i_s}$, and $\overrightarrow{\lambda_s}$ are the resistance of the stator winding, complex space vectors of the three phase stator voltages, currents, and flux linkages, respectively. These vectors are stated in the stationary reference frame fixed to the stator. The resultant stator reference frame voltage, current, and flux linkage space vectors are shown in (I.4), (I.5) and (I.6), respectively.

$$\overrightarrow{v_s} = \frac{2}{3}[v_{sa}(t) + a v_{sb}(t) + a^2 v_{sc}(t)] \tag{I.4}$$

$$\overrightarrow{i_s} = \frac{2}{3}[i_{sa}(t) + a i_{sb}(t) + a^2 i_{sc}(t)] \tag{I.5}$$

$$\overrightarrow{\lambda_s} = \frac{2}{3}[\lambda_{sa}(t) + a \lambda_{sb}(t) + a^2 \lambda_{sc}(t)] \tag{I.6}$$

where $a = e^{j2\pi/3}$and $a^2 = e^{j4\pi/3}$ are spatial operators for orientation of the stator windings; $v_{sa}(t)$, $v_{sb}(t)$, and $v_{sc}(t)$ are the instantaneous values of stator phase voltages; $i_{sa}(t)$, $i_{sb}(t)$, and $i_{sc}(t)$ are the instantaneous phase currents; $\lambda_{sa}(t)$, $\lambda_{sb}(t)$, and $\lambda_{sc}(t)$ are the stator flux linkages. They are calculated by multiplying instantaneous phase values by the stator winding orientations.

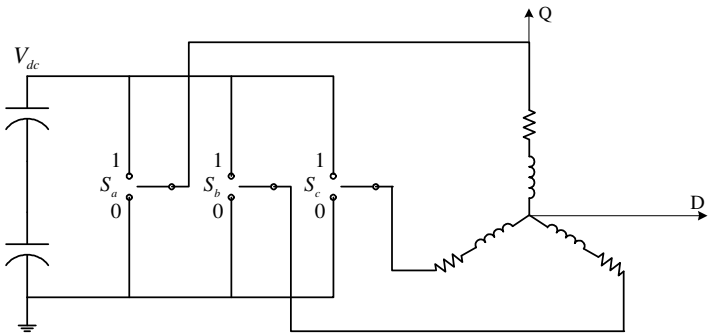

Figure I.3. Voltage source inverter (VSI) connected to the $R-L$ load [21].

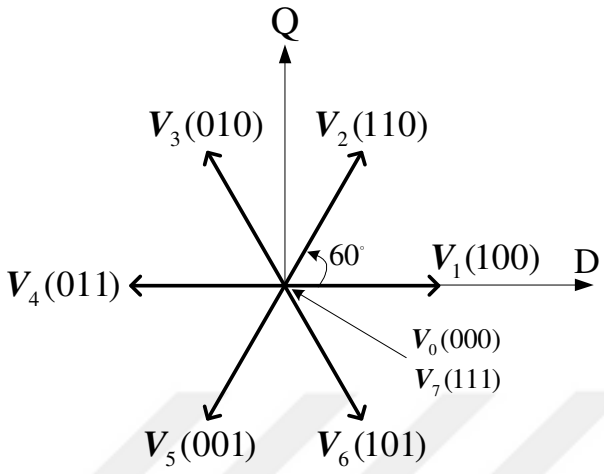

Figure I.4. Eight possible voltage space vectors obtained from VSI [22].

The phase–a is chosen as the stator reference axis in the direction of maximum MMF. The b– and c–axes stator reference frames are selected 120° and 240° (electrical degree) ahead of the a–axis, respectively.

When the three-phase windings are fed by an inverter, as shown in Figure I.3, the primary voltages $v_{sa}(t)$, $v_{sb}(t)$, and $v_{sc}(t)$ are determined by the status of the three switches, S_a, S_b, and S_c. If the switch is at state 0 that means the phase is connected to the negative and if it is at 1 it means that the phase is connected to the positive leg. The eight basic voltage space vectors defined by the combination of inverter switches are illustrated in Figure I.3 [19].

For example, phase–a is connected to V_{dc} if S_a is one, otherwise phase–a is connected to zero. This is similar for b–axis and c–axis. There are six nonzero voltage vectors: $V_1(100)$, $V_2(110)$, …, $V_6(101)$ and two zero voltage vectors: $V_7(000)$ and $V_0(111)$. The six nonzero voltage vectors are 60° apart from each other as in Figure I.4 [19].

The stator voltage space vector (expressed in the stationary reference frame) representing the eight voltage vectors can be shown as

$$v_s(S_a, S_b, S_c) = \frac{2}{3} V_{dc}[S_a + aS_b + a^2 S_c] \tag{I.7}$$

where V_{dc} is the DC-link voltage, S_a, S_b, and S_c are the switching states, and the coefficient of 2/3 is the coefficient comes from the Park transformation [19].

1.2.3. Components of FOC of PMSM drive

The major components of the FOC of PMSM drive are shown in Figure I.5. The system consists of speed, d– and q–axes current PI regulators, Park and Clarke transformations, inverse Park transformation, space vector generation, speed calculation, current and encoder signal conditionings and PWM generator modules. In Figure I.5, an incoming speed command profile goes into a speed PI regulator which outputs q–axis reference current. The d–axis current reference is set to zero for surface-mount PMSM. These current references and their corresponding feedbacks are DC quantities for the PI regulators to track easily. The outputs of the current PI regulators generate stator dq–axes voltage references which are also in DC quantities. To apply sinewave currents to the motor, these DC voltage quantities are then transformed into the instantaneous sinusoidal voltage commands for the individual stator phases using the rotor angle feedback and the inverse reference frame transformation matrix (inverse Park transformation).

The space vector PWM generator converts the stationary reference frame voltage references into abc frame based duty cycle equivalences. These three-phase duty cycles (T_a, T_b, and T_c) are then brought into a PWM generator for the inverter to generate the appropriate three-phase pulsed-voltages that are applied to the motor. To obtain the dq–

axes current feedbacks in DC quantities, first a– and b–axes AC currents are transformed into stationary values using Clarke transformation and then the stationary current values acquired from Clarke transformation are set up as inputs to the Park transformation along with the rotor position feedback signal to generate the equivalent DC feedback quantities in dq reference frame.

In PMSM, the rotor windings are already along the d– and q–axes, only the stator windings quantities need transformation from three-phase quantities to the two-phase dq rotor rotating reference frame quantities. Therefore, Park transformation is used to transform the stator quantities of a PMSM onto a dq reference frame that is fixed to the rotor, with the positive d–axis aligned with the magnetic axis of the rotor which has a permanent magnet in PMSM. The dq transformation matrix (Park transformation) used for currents and the inverse Park transformation used for voltages are given respectively by

$$\begin{bmatrix} i_d \\ i_q \end{bmatrix} = \begin{bmatrix} cos\,\theta & sin\,\theta \\ -\,sin\,\theta & cos\,\theta \end{bmatrix} \begin{bmatrix} i_\alpha \\ i_\beta \end{bmatrix} \tag{I.8}$$

$$\begin{bmatrix} v_\alpha \\ v_\beta \end{bmatrix} = \begin{bmatrix} cos\,\theta & sin\,\theta \\ -\,sin\,\theta & cos\,\theta \end{bmatrix} \begin{bmatrix} v_d \\ v_q \end{bmatrix}. \tag{I.9}$$

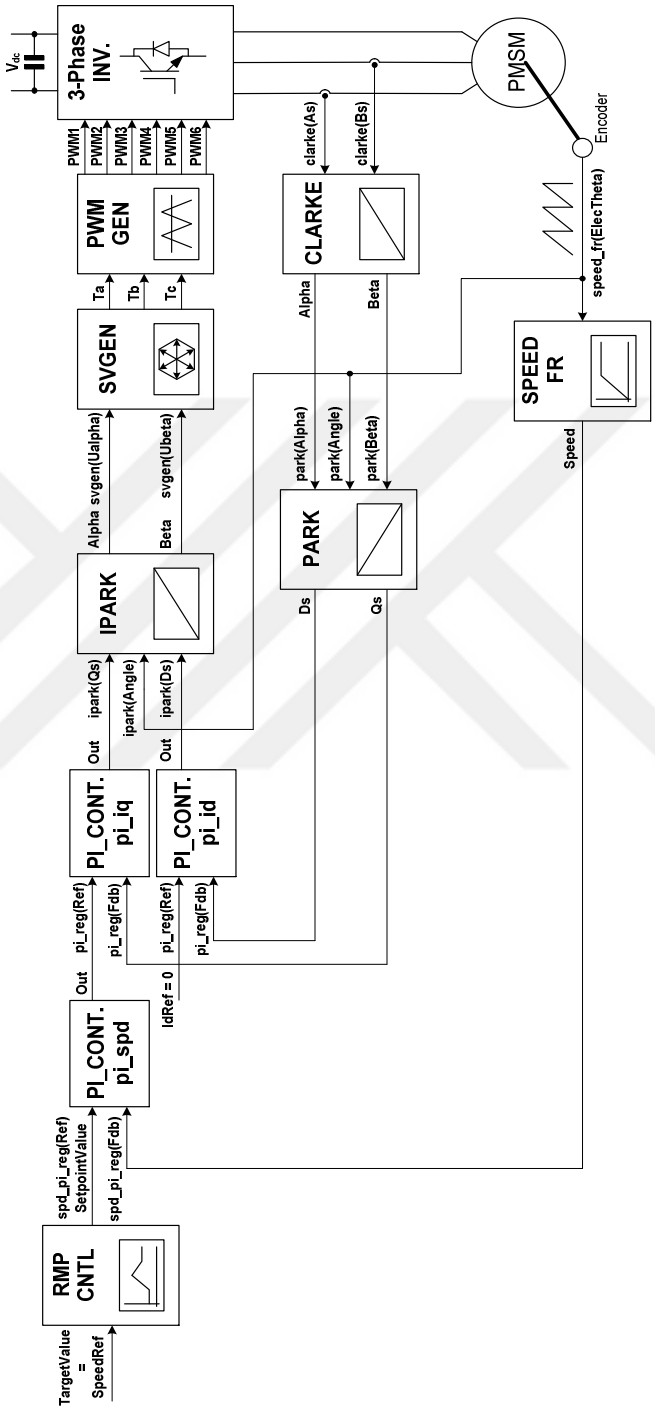

Figure I.5. Overall block diagram of the speed sensored FOC of PMSM drive [20].

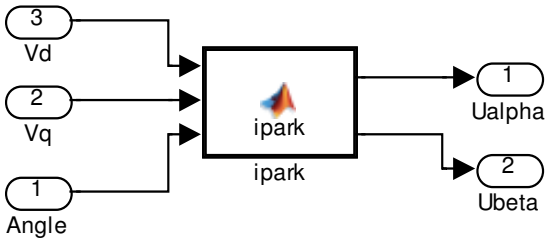

Figure I.6. MATLAB Function based inverse Park transformation.

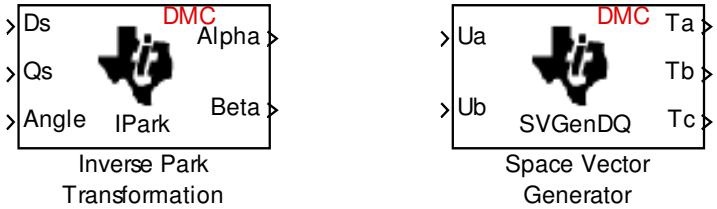

Figure I.7. "Code Generation" toolbox blocks (Embedded Coder DMC modules).

It is possible to separate the motor complex space vectors into stationary real and imaginary parts with the Clarke transformation. By using the Clarke transformation in FOC of AC motor drive, stator currents are transformed from three-phase to two-phase quadrature equivalent values as inputs to the Park transformation. The Clarke transformation matrix for a balanced three-phase system is defined as

$$\begin{bmatrix} i_\alpha \\ i_\beta \end{bmatrix} = \begin{bmatrix} 1 & 0 \\ \frac{1}{\sqrt{3}} & \frac{2}{\sqrt{3}} \end{bmatrix} \begin{bmatrix} i_a \\ i_b \end{bmatrix}. \tag{I.10}$$

1.3. Proposed FOC of PMSM Drive Model Based on Matlab Functions in Matlab/Simulink

C programming like codes written in MATLAB Programming language are developed for the simulation of the FOC of PMSM drive in MATLAB/Simulink using MATLAB Function blocks without using expensive additional toolboxes such as Embedded Coder.

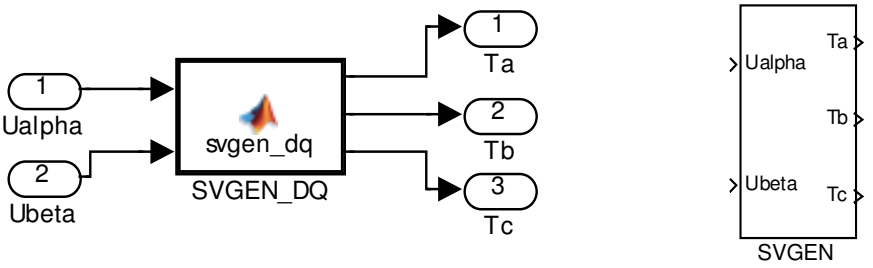

Figure I.8. "Code Generation" toolbox blocks (Embedded Coder DMC modules).

Motor control codes developed in C language by Texas Instruments are created in a modular basis [20]. Developers that create algorithms using the same basis can model the system by using MATLAB Function blocks.

As algorithms are being developed in MATLAB Function blocks, other electrical components such as electrical machines and inverters can also be modeled by using MATLAB/Simulink SimPowerSystems™ library components in the same system model. Although, this causes an additional cost to the system, more realistic simulation models are obtained. The cost effective solution is to represent the electrical machine and inverter models mathematically by using classical Simulink and MATLAB Function blocks. MATLAB Function blocks can also be used in Embedded Coder for real-time implementation of FOC of PMSM drive if desired.

The MATLAB Function based inverse Park transformation model given in (I.10) is shown in Figure I.6. The mathematical representation written in the MATLAB Programming language is provided in the bottom side of the Figure I.6. In a similar fashion, Clarke and Park transformations, PI Controllers, Space Vector PWM Generator, Ramp Control, and Speed Calculation modules are also created by MATLAB Functions. The developed MATLAB Functions work in the same manner as

the blocks in Embedded Coder. However, there are limitations in the Embedded Coder since TI's Digital Motor Controller (DMC) blocks in Embedded Coder do not allow modifications. In Figure I.7, inverse Park transformation and Space Vector Generator DMC blocks (modules) are illustrated. MATLAB Function blocks require C like MATLAB programming language. By this method, it is easy to develop and test the algorithms which are suitable for TI C2000 microcontrollers.

Development of the simulation model before the actual implementation is important. It is quite hard to switch from the simulation platform of FOC of PMSM drive to the experimental stage. Moreover, programming microcontrollers is a quite tedious task. The FOC algorithm tested in the MATLAB/Simulink simulation platform by using MATLAB Functions instead of classical Simulink blocks makes switching to the experimental stage a lot easier due to the above mentioned reasons and generates much more realistic results in simulation.

One of the other advantages of using the MATLAB Function based blocks instead of DMC blocks is to enable development of new algorithms instead of the known ones that are provided in the Embedded Coder toolbox. The six-switch version of Space Vector Generator (SVGEN_DQ) block from DMC module is shown in Figure I.7. In this block, modifications are not allowed. However, Figure I.8 shows the MATLAB Function based SVGEN_DQ block which is easily modifiable.

The inside of the SVGEN_DQ MATLAB Function module is provided in Appendix B. Appendix C represents the C code version of the SVGEN_DQ module available in the TI motor development application library. Appendix D includes flowchart of the SVGEN_DQ module.

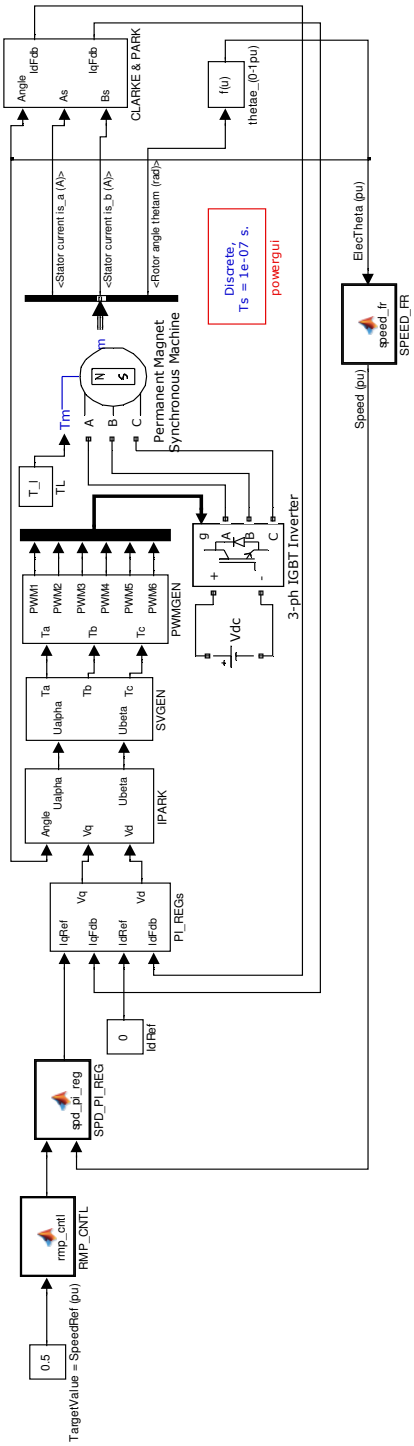

Figure I.9. Overall MATLAB/Simulink block diagram of the proposed speed sensored FOC of PMSM drive using MATLAB Function.

The similarities are clearly seen between MATLAB Function version and C programming version of the SVGEN_DQ module. The FOC of PMSM drive that is proposed by Texas Instruments® is illustrated in Figure I.9. In this figure, the closed loop speed control is performed with a ramp speed reference profile. The speed control is achieved by applying a speed PI regulator. Position information is obtained by an optical encoder. The encoder signals are converted to speed information by SPEED_FR block. The rest of the FOC components are also seen in Figure I.9. In Figure I.9, FOC of PMSM drive model developed in MATLAB/Simulink with MATLAB Functions along with electrical components is shown. Inverter and electrical machine parameters are selected to be the same as the experimental setup. The MATLAB Function blocks are then manually converted to the C language based version to be used in the Code Composer Studio™ (CCS) IDE. It is observed that any modifications made either in simulation or in experiment produce the same results in each platform.

1.4. Simulation and Experimental Results

1.4.1. Simulation results

The proposed drive system shown in Figure I.9 has been simulated in MATLAB/Simulink using an electrical IGBT inverter and electrical PM motor model from the SimPowerSystems toolbox in order to demonstrate the validity of the speed sensored FOC of a PM synchronous motor drive.

To set the gating signals of the power switches from the output of the SVPWM module easily and represent the real conditions in simulation as close as possible, the proposed drive scheme including the electrical model of the actual PM motor and the inverter with power semiconductor switches considering the snubber circuit and the

parameters of the switches are designed in MATLAB/Simulink using the SimPowerSystems blocksets. The dead-time of the inverter and non ideal effects of the PM synchronous machine are neglected in the simulation models. The DC-link voltage V_{dc} is set to 400 V [21], [22].

The switching frequency is chosen as 10 kHz. The sampling interval of the electrical components from SimPowerSystems is selected to be thousand times slower than the sampling time. In the simulations, electrical components and mathematical functions run together. When the switching frequency is 10 kHz, the mathematical functions that run parallel should be sampled faster than 10 kHz. In this case, this is set a thousand times faster than 100 μs sampling rate. If the sampling step is low, the simulation slows down. Similarly, in experiment, the switching update is accomplished in 10 kHz rate as in simulation. However, the microcontroller runs the algorithms in 150 MHz clock frequency and the PWM update is performed in 10 kHz independent of the algorithm sampling as oppose to the simulation. These results in high frequency ripples in the actual current waveforms in experiment compared to the ones in simulation.

In Figure I.10, the speed results under full load start-up condition (2 N·m) is given with a ramp speed reference from zero speed to 0.5 p.u. (450 r/min) in 2 s. As it can be seen in Figure I.10 that the proposed MATLAB Function based speed sensored field-oriented control is able to drive the PM motor without any instability under full load start-up condition. Figure I.11 demonstrates the steady-state phase–a current waveform under rated full load at start-up. At 7.5 s (steady-state), step-down full load rejection (full load to zero load) is applied and the speed response is provided in Figure I.10. No instability is observed even under full load rejection at steady-state.

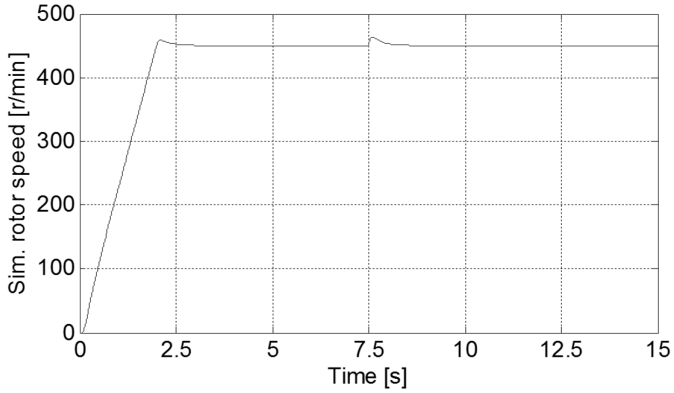

Figure I.10. Simulated rotor speed feedback under full load start-up (2 N·m).

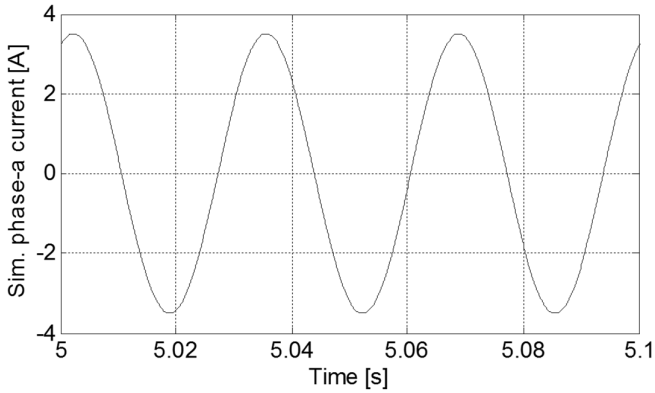

Figure I.11. Simulated phase–a current waveform at steady-state (0.5 p.u. = 450 r/min) under full load condition.

1.4.2. Experimental setup

The experimental set-up shown in Figure I.12(a) and Figure I.12(b) consists of a Magtrol AHB-6 model hysteresis dynamometer set, a SEMIKRON Semiteach inverter, a PM synchronous motor, an eZdsp™ board with TI's TMS320F28335 MCU chip, an interface board and a signal conditioning card.

The Magtrol dynamometer set contains a 6 N·m hysteresis brake, a DSP6001 model programmable DSP torque controller, and a Magtrol TMS306 model torque transducer to monitor the load torque and shaft speed which is installed between the hysteresis brake and the motor.

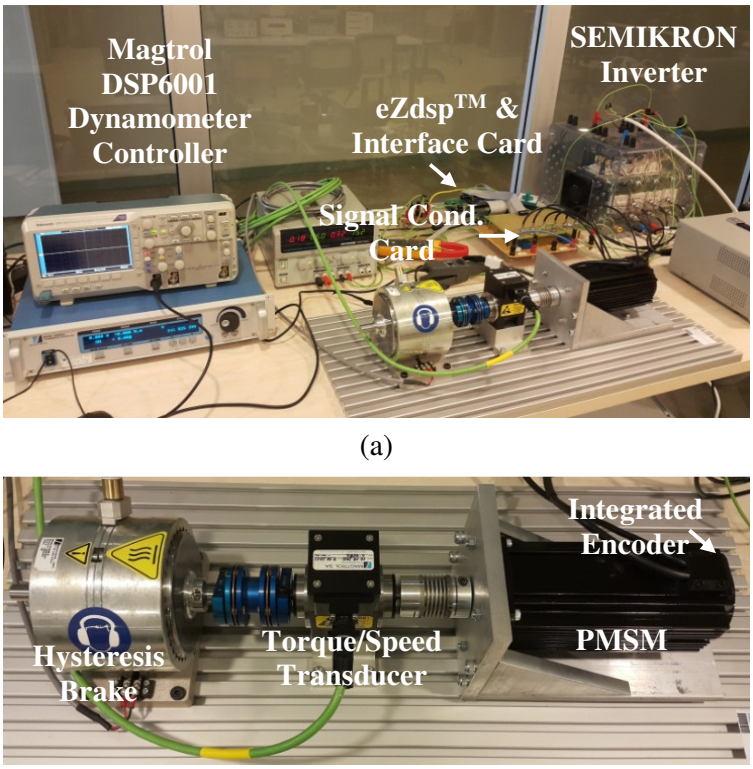

Figure I.12. Experimental test-bed. (a) Dynamometer controller, inverter, DSP control unit, and interface and signal-conditioning cards. (b) PM synchronous motor with integrated incremental position encoder (2500 pulse/rev.) coupled to hysteresis brake through torque/speed transducer.

The signal conditioning card which comprises of two LEM™ LA25NP model current sensors measure two motor phase currents and converts the real-world analog current values into equivalent low-voltage values. The interface board that is connected to the signal conditioning card scales the voltage values into proper positive representations for the MCU to sensitize. The SEMIKRON® Semiteach™ PWM VSI consists of SKM 50 GB 123D model IGBT modules, SKHI 22 model gate drivers with 4.3 μs dead-time, and two 2200 μF caps. The inverter has a maximum DC-link voltage of 750 V and RMS current of 30 A.

In addition, an optical incremental encoder integrated to the PM servo motor with 2500 ppr resolution is used to detect the actual position. The speed sensored control scheme is verified using an off-the-shelf 2 N·m surface-mounted PMSM drive which is coupled to the overall system, as shown in Figure I.12(b) .

1.4.3. Experimental results

The feasibility and practical features of the sensored speed control scheme of a PMSM drive with sinusoidal back-EMF have been evaluated using an experimental test-bed, shown in Figure I.12(a) and Figure I.12(b) . The same conditions are applied as in simulation. The control algorithm is digitally implemented using the eZdsp™ board from Spectrum Digital®, Inc. based on a TI's floating-point Delfino MCU (TMS320F28335), as shown in Figure I.12(a) .

The experimental results are shown in Figure I.13 and Figure I.14. Figure I.13 shows experimental waveform of the speed response when zero to 0.5 p.u. ramp speed reference is applied starting at the tenth seconds under rated load condition as in simulations. It is seen in Figure I.13 that the feedback speed reaches the reference top speed in 2 s as in simulation. The full load rejection is applied at 17.5 s. The drive system under full load rejection is still stable and the speed feedback tracks the reference speed closely. Figure I.14 shows the steady-state current waveform under full load condition.

To investigate the current waveform in the experiment, noise filter of 14 kHz is employed in the Tektronix™ oscilloscope to remove the high frequency ripples in the current waveform. It is seen that the results obtained from experiments are similar to those that are obtained in the simulations.

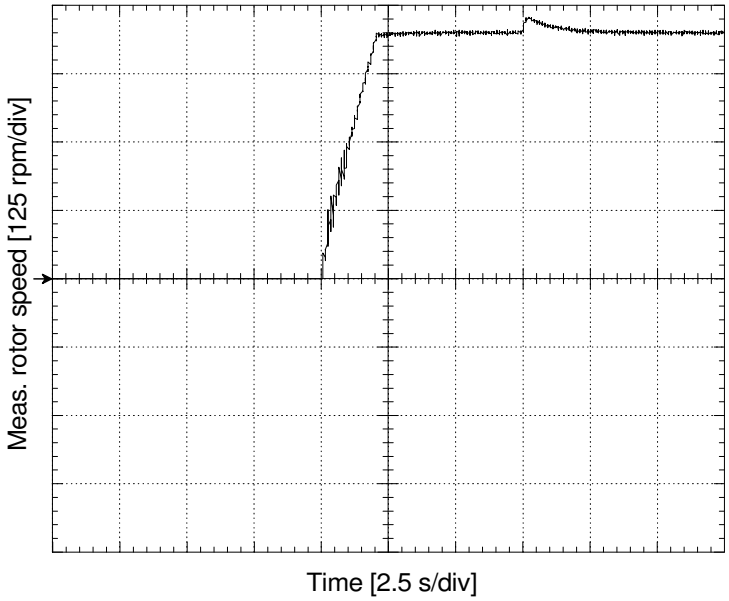

Figure I.13. Experimental rotor speed waveform under full load start-up (2 N·m).

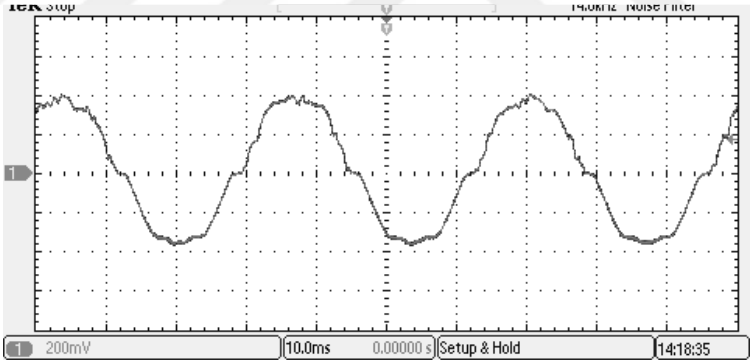

Figure I.14. Experimental phase–a current waveform at steady-state (0.5 p.u. = 450 r/min) under full load condition (1A/100mV).

The differences observed in the transient responses between simulation and experiment are because of the dissimilarities in data sampling rate, additional delay due to dynamometer torque controller, nonlinear characteristics of the machine and hysteresis brake, mismatch of moment of inertia, damping and friction of the overall system compared to the one used in simulations.

Due to slight misalignment and mechanical possible slippage in the motor coupling, phase current shows some harmonic signatures on the positive cycle and the

rotor speed has oscillatory behavior at start-up as seen in Figure I.13 and Figure I.14, respectively. Moreover, because the dead-time effect is not compensated, the phase current waveform exhibits some additional distortion especially at zero crossings and at around positive and negative peaks. The rotor speed data are obtained by using M-TEST 5.0 Motor Testing Software of Magtrol dynamometer at 0.01 s sample rate.

1.5. Conclusion

In this chapter, a simple, easily modifiable and more economical choice of modeling and simulation of a speed sensored FOC of a PMSM drive is developed by using MATLAB Function blocks in MATLAB/Simulink. This method allows easier algorithm and software development stages for experimental studies compared to the classical block diagram approach. The superiority of the method over commonly used "Code Generation" tools such as MATLAB/Simulink™ Embedded Coder is also emphasized. The proposed MATLAB/Simulink model of a speed sensored FOC of a PMSM drive scheme is built by using MATLAB programming in MATLAB Functions similar to C programming language. Then, the MATLAB programming based codes developed in simulation are implemented in a TI's TMS320F28335 Delfino floating-point MCU by using C programming. Simulation and experimental results are compared and the results show the effectiveness of the proposed modeling of the FOC of PMSM drive.

II. IMPROVED STATOR FEEDFORWARD VOLTAGE ESTIMATION (FFVE) BASED SENSORLESS PMSM DRIVE USING MULTI-PARAMETER ESTIMATION BASED ON MODEL REFERENCE ADAPTIVE SYSTEM (MRAS)

Permanent magnet synchronous motor (PMSM) with sinusoidal shape back-EMF and brushless DC (BLDC) motor with trapezoidal shape back-EMF drives have been extensively used in many applications, ranging from servo to traction drives due to several distinct advantages such as high power density, robustness, high efficiency, large torque to inertia ratio and better controllability [23]. Since 1980s, with developments in microcontroller/DSP, power electronics and microelectronics, the sensorless control methods to achieve comparable performance in sensored vector control have been investigated. Although BLDC motor drives require a simple control with expensive position hall-effect sensors, these sensors are susceptible to heat and mounting them on to the machine is a difficult task. On the other hand, PMSM with sinusoidal shape back-EMF requires much more precise position sensors such as an optical encoder and resolver for FOC [24], [25].

However, attaching these position sensors to the motor is associated with cost, space, mechanical burden, noise interference and reliability. Therefore, there is a motivation to eliminate position sensor from the drive and operate it as “sensorless” or “encoderless” [26]. Although only position sensor is eliminated for sensorless control, the motor position must be obtained using only electrical quantities (such as motor currents, inverter DC-link voltage, voltage at the motor terminals, etc.) [24]. Therefore,

current and/or voltage sensors are required to achieve a position sensorless drive scheme. There are different techniques for sensorless operation of permanent magnet synchronous motors and they are divided in two main groups: 1) back-EMF estimation and 2) high/low frequency signal injection utilizing the magnetic saliency. While sensorless control methods based on back-EMF estimation show very good performance at medium and high speeds, they do not give good results at low and very low speeds due to back-EMF estimation to be made at a sufficient level [25], [27]–[29]. Although the second method high-frequency signal injection provides effective results at low speed levels and the estimation of initial rotor position, it is not widely used in industry because of oscillations that occur in medium and high speeds due to the born of injecting extra current or voltage signal, estimated bandwidth width and the difficulty of integration into industrial drives. Because PMSM steady-state model is taken as a reference in sensorless control methods based on back-EMF estimation, necessary stability cannot be achieved at low and zero speed and mismatches of parameters and variation of loading conditions, low speed operation and field weakening area [30]–[32]. The main reason for these problems is that the methods based on back-EMF estimation are affected by the parameter variation [33]. Variations in stator resistance and rotor flux linkage complicate the position estimation, since the back-EMF based methods are based on PMSM mathematical model [24]. Especially in low-speed operation, field position estimation errors occur due to the variations of motor parameters. Stator resistance changes due to temperature change and magnetic saturation [23], [34], [35]. In order to minimize the effects of these changes and to tune the control parameters correctly [36], [37]. In the literature Extended Kalman Filter (EKF), Model Reference Adaptive System (MRAS), Recursive Least Squares

Estimation (RLSE), Artificial Neural Network (ANN), Fuzzy Logic (FL) and deterministic observers are used in online parameter estimation [24]–[34]. Because ANN and FL methods contain too much mathematic calculations, their applications for industrial drives are difficult task [25], [26]. While the EKF method gives suitable results in parameter estimation, it has the disadvantages of complex algorithm structure and the challenge of parameter adaptation [48]–[50]. While the RLSE method is used in the estimation of electrical and mechanical parameters due to the mass of differential expression it reduces the performance of the microprocessor and cause the system to respond slowly [51], [52]. Although the Sliding Mode Observers (SMO) provides rapid stability, it is insufficient in low speed region and because the parameters need to be tuned, it is not a suitable on-line estimation method [53]. Therefore, it is not suggested in industrial and low cost applications. In the basic approach of parameter estimation, parameters change slowly and rapid changes are estimated using various methods and with hybrid methods [54], [55]. While speed, inertia and position are parameters that change rapidly, stator resistance and the rotor flux linkage change slowly [54]. Stator inductance is the dominant parameter in transient state and in field weakening region [53]. Thus, simplicity and rapid response capability of the proposed MRAS for PMSM drives is the most outstanding parameter estimation method compared to other techniques [56], [57]. Predictability of stator resistance and rotor flux linkage independently is important for PMSM drive systems which require estimation of motor variables individually with minimum error [51].

In this chapter, the sensorless control method used for IM is proposed for PMSM. Back-EMF estimation plays an important role in todays' industrial applications as a method that can ensure the stability in wide speed range compared to other methods

[58]. In this study, a simple and effective position sensorless speed control method for both surface mount and interior permanent magnet synchronous motors are proposed. The dynamically enhanced modified feedforward stator dq–axes voltages that are derived from a steady-state PM synchronous machine model are applied to the PM motor. The dynamic resemblance of the actual PM machine is accomplished by the help of d^*– and q^*–axes PI regulator outputs which are composed as the components of the feedforward voltage models [59]. q–axis PI current regulator output with a simple filtering formulates the speed estimation algorithm and the output of the d–axis PI regulator acts as the part of the derivative representation in the feedforward voltage equations.

Because the proposed method depends on back-EMF estimation, it is affected by the parameter variation [23]. Elimination of the position errors stemmed from parameter change is estimated with online rotor flux linkage and stator resistance using MRAS and the updates are provided in the feedforward voltage estimation model. With the MRAS parameter estimation, performance and stability of the sensorless drive scheme in steady state and in low speed are improved. In similar hybrid algorithms, in addition to a position estimation method, an observer algorithm and on-line parameter estimation method are required as superiors [24], [60], [61]. Especially in low speed operation in order to improve the position estimation, EKF and MRAS are used together and a hybrid position control algorithm is suggested [26], [45]. In the method while rotor flux variation is estimated by EKF, position estimation is accomplished by MRAS [45]. In the other studies, while MRAS is used in the estimation of slowly changing parameters the SMO is used for the position estimation [56], [42], [62]. In controlling of the sensorless PMSM drive that is developed by using V/Hz and FOC, Luenberger

observer is developed for rotor flux estimation and the effects caused from rotor flux linkage change are minimized [53], [63], [64]. The most important reason of using these hybrid approaches is that parameters affect each other and one prediction algorithm does not give the desired result. However, when compared to other methods, because MRAS's being simple and applicable it provides fast stability in parameter estimation. Therefore, it is presented as an important advantage in the study for the proposed sensorless control method [47].

This chapter is organized as follows. The principle of the stator feedforward voltage estimation based position sensorless speed control technique improved by multiple parameter estimation is presented in Section 2.1. In Section 2.1.1, the dynamic and steady-state models of surface mounted permanent magnet synchronous motors (SMPMSM) are explained in detail. In Section 2.1.2, multiple parameter estimation method based on MRAS is explained. In Section 2.2, the proposed stator feedforward voltage control is presented using MRAS parameter estimation sensorless speed control strategy. Moreover, the proposed control methods are designed and described in detail. In Section 2.3, electrical simulation model in MATLAB/Simulink is designed and developed. The simulation results are given and analyzed in detail. In Section 2.4, the proposed speed sensorless control scheme has been implemented with 1 kW PMSM drive controlled by a TMS320F28335. The hardware implementation and experimental results of the proposed sensorless PM synchronous motor drive including steady-state load disturbance are presented and discussed. Simulation and experimental results demonstrate the feasibility and effectiveness of the proposed position sensorless stator feedforward voltage estimation control (FFVE) scheme improved by MRAS multiple

parameter estimation for permanent magnet synchronous motors under full-load condition.

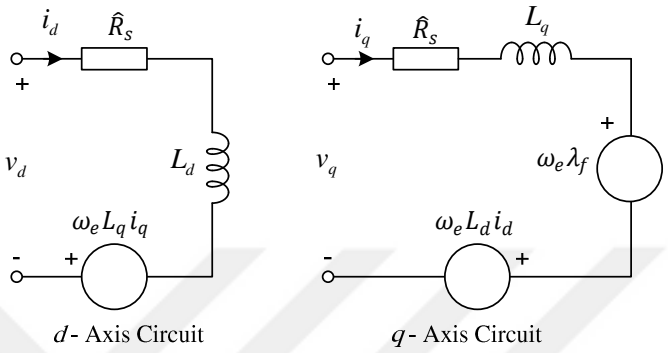

Figure II.1. Equivalent electrical circuit diagrams of IPMSM in q– and d–axes synchronous reference frame.

2.1. Proposed Sensorless PMSM Control Based on Stator FFVE with Multi-parameter Estimation

2.1.1. Dynamic and steady-state mathematical model of IPMSM

The dynamic dq model in rotating synchronous reference frame shown in Figure II.1 is used to analyze the IPMSM for the FOC. The stator voltage equations of the IPMSM in the rotating (rotor/synchronous) dq reference frame are given by (II.1) and (II.2), omitting the influences of magnetic field saturation and magnetic hysteresis as

$$v_q = i_q R_s + L_q \frac{di_q}{dt} + \omega_e L_d i_d + \omega_e \lambda_f \tag{II.1}$$

$$v_d = i_d R_s + L_d \frac{di_d}{dt} - \omega_e L_q i_q \tag{II.2}$$

where v_d, v_q, i_d, i_q are the stator d– and q–axes voltages and currents in the rotor reference frame, respectively; R_s is the stator winding resistance; L_d and L_q denote the d– and q–axes inductance, respectively; ω_e is the rotor angular electrical velocity; and

λ_f is the flux linkage due to the permanent magnet rotor flux [16], [17]. The steady-state form of dq–axes stator voltage equations can be derived from (II.3) and (II.4) by making derivative terms equal to zero in each equation as

$$v_q = i_q R_s + (\omega_e L_d i_d + \omega_e \lambda_f) \tag{II.3}$$

$$v_d = i_d R_s - \omega_e L_q i_q. \tag{II.4}$$

2.1.2. Rotor flux linkage and stator resistance estimator based on model reference adaptive system (MRAS)

PMSM motor parameters vary depending on temperature, frequency, load conditions and work zone [65], [45]. In order to eliminate the effects of parameter changes, an MRAS observer structure is suggested for the proposed sensorless control scheme. While the rotor position errors occur from stator resistance change at low speeds, this problem is eliminated with multi-parameter estimation; the effects of the rotor flux linkage change caused from permanent magnets are also eliminated [24], [25], [54].

A high performance PI regulator is used for PMSM sensorless speed control; for low speeds and transients an adaptive MRAS observer, shown in Figure II.2, is used. In addition to rotor flux linkage and stator resistance change, feedforward voltage estimation method is used together with MRAS in order to eliminate disturbance effects in position estimation. Principally, MRAS depends on the principle that reference and estimation models are compared and the obtained error is regulated by an adaptive model until stability is achieved [56].

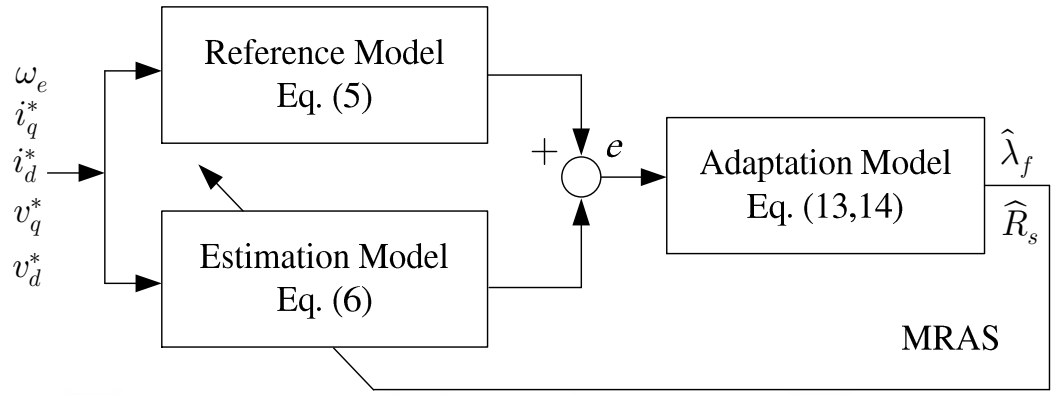

Figure II.2. MRAS principle block diagram.

MRAS adaptation mechanism estimates slowly varying parameters based on the hyperstability theory [37]. In the proposed method, MRAS is superior to feedforward voltage estimation. It provides prevention of disruptive effects caused from parameter variation. MRAS basic equation consists of feedforward linear model and non–linear feedback components. In (II.10), while the $(A+G)i_{\left[\begin{smallmatrix}q\\d\end{smallmatrix}\right]}$ matrix is solved for feedforward linear model; $\Delta A\hat{i}_{\left[\begin{smallmatrix}q\\d\end{smallmatrix}\right]} + \Delta \mathrm{d}$ symbolizes the nonlinear variable. G_1 and G_2 coefficient in G matrix ensures feedforward linear model to be a positive and real number [66]. Non-linear block is solved according to POPOV integral equation. Equations for reference model shown in Figure II.2 are expressed in (II.5).

$$\begin{bmatrix}\frac{di_q}{dt}\\ \frac{di_d}{dt}\end{bmatrix} = \underbrace{\begin{bmatrix}\frac{-R_s}{L_q} & \frac{-L_d}{L_q}\omega_e\\ \frac{L_q}{L_d}\omega_e & \frac{-R_s}{L_d}\end{bmatrix}}_{A}\begin{bmatrix}i_q\\ i_d\end{bmatrix} + \underbrace{\begin{bmatrix}\frac{1}{L_q} & 0\\ 0 & \frac{1}{L_d}\end{bmatrix}}_{B}\begin{bmatrix}v_q\\ v_d\end{bmatrix} + \underbrace{\begin{bmatrix}\frac{-\lambda_f}{L_q}\omega_e\\ 0\end{bmatrix}}_{d} \tag{II.5}$$

where $\widehat{R}_s$ and $\hat{\lambda}_f$ are the estimated stator resistance and rotor flux linkage, respectively which are the outputs of the adaptation model. $\widehat{R}_s$ and $\hat{\lambda}_f$ are updated in the estimation block in the closed loop system, as a result $\hat{i}_q$ and $\hat{i}_d$ currents are predicted.

$$\begin{bmatrix} \frac{di_q}{dt} \\ \frac{di_d}{dt} \end{bmatrix} = \underbrace{\begin{bmatrix} \frac{-\widehat{R}_s}{L_q} & \frac{-L_d}{L_q}\omega_e \\ \frac{L_q}{L_d}\omega_e & \frac{-\widehat{R}_s}{L_d} \end{bmatrix}}_{\hat{A}} \begin{bmatrix} \hat{i}_q \\ \hat{i}_d \end{bmatrix} + \underbrace{\begin{bmatrix} \frac{1}{L_q} & 0 \\ 0 & \frac{1}{L_d} \end{bmatrix}}_{\widehat{B}} \begin{bmatrix} v_q \\ v_d \end{bmatrix} + \underbrace{\begin{bmatrix} \frac{-\hat{\lambda}_f}{L_q}\omega_e \\ 0 \end{bmatrix}}_{\hat{d}} + \begin{bmatrix} G_1 & 0 \\ 0 & G_2 \end{bmatrix} \begin{bmatrix} \hat{i}_q - i_q \\ \hat{i}_d - i_d \end{bmatrix} \tag{II.6}$$

Adaptation model on the other hand is obtained by solving the nonlinear and feedforward linear model together. ΔA and Δd are used to obtain the reference and estimated currents that are the outputs of the estimation and reference models.

$$\Delta A = \begin{bmatrix} \frac{-R_s}{L_q} & \frac{-L_d}{L_q}\omega_e \\ \frac{L_q}{L_d}\omega_e & \frac{-R_s}{L_d} \end{bmatrix} - \begin{bmatrix} \frac{-\widehat{R}_s}{L_q} & \frac{-L_d}{L_q}\omega_e \\ \frac{L_q}{L_d}\omega_e & \frac{-\widehat{R}_s}{L_d} \end{bmatrix} \tag{II.7}$$

$$\Delta d = \begin{bmatrix} \frac{-\lambda_f}{L_q}\omega_e \\ 0 \end{bmatrix} - \begin{bmatrix} \frac{-\hat{\lambda}_f}{L_q}\omega_e \\ 0 \end{bmatrix}. \tag{II.8}$$

In (II.11), the error of the MRAS current estimators. Selection of accurate values of G_1 and G_2 gains given in (II.6) eliminate the algebraic loop problem occurs in simulation and experimental studies [66]. The error correction is accomplished by an adaptation model. G matrix given in (II.6) is an observer gain matrix in which the parameters should be adjusted properly [56]. False selection of the G matrix parameters causes algebraic loops.

$$e = \begin{bmatrix} \hat{i}_q - i_q \\ \hat{i}_d - i_d \end{bmatrix} \tag{II.9}$$

$$\dot{e} = (A + G)i_{\begin{bmatrix} q \\ d \end{bmatrix}} + \Delta A\hat{i}_{\begin{bmatrix} q \\ d \end{bmatrix}} + \Delta \mathrm{d}. \tag{II.10}$$

According to the error given in (II.10) that (II.11) is obtained when (II.5) and (II.6) are solved collectively. The errors $\hat{i}_q - i_q$ and $\hat{i}_d - i_d$ given in (II.9) are adjusted with the help of PI regulator coefficients that are defined according to the POPOV inequality criteria in (II.12) [48].

$$\begin{bmatrix} \frac{d(\hat{i}_q - i_q)}{dt} \\ \frac{d(\hat{i}_d - i_d)}{dt} \end{bmatrix} = \left(\begin{bmatrix} \frac{-R_s}{L_q} & \frac{-L_d}{L_q}\omega_e \\ \frac{L_q}{L_d}\omega_e & \frac{-R_s}{L_d} \end{bmatrix} + \begin{bmatrix} G_1 & 0 \\ 0 & G_2 \end{bmatrix} \right) \begin{bmatrix} \hat{i}_q - i_q \\ \hat{i}_d - i_d \end{bmatrix} + \left(\begin{bmatrix} \frac{-R_s}{L_q} & \frac{-L_d}{L_q}\omega_e \\ \frac{L_q}{L_d}\omega_e & \frac{-R_s}{L_d} \end{bmatrix} - \begin{bmatrix} \frac{-\widehat{R}_s}{L_q} & \frac{-L_d}{L_q}\omega_e \\ \frac{L_q}{L_d}\omega_e & \frac{-\widehat{R}_s}{L_d} \end{bmatrix} \right) \begin{bmatrix} \hat{i}_q \\ \hat{i}_d \end{bmatrix} + \left(\begin{bmatrix} \frac{-\lambda_f}{L_q}\omega_e \\ 0 \end{bmatrix} - \begin{bmatrix} \frac{-\hat{\lambda}_f}{L_q}\omega_e \\ 0 \end{bmatrix} \right) \tag{II.11}$$

$$\int_0^{t_0} \left[(i_d - \hat{i}_d)\frac{-i_d}{L_d} + (i_q - \hat{i}_q)\frac{-i_q}{L_q} \right] \left(R_s - \widehat{R}_s \right) \mathrm{dt} \geq -{\gamma_0}^2. \tag{II.12}$$

Adaptation equations for $\widehat{R}_s$ and $\hat{\lambda}_f$ are given in (II.13) and (II.14), respectively. where $k_{p_{res}}$, $k_{i_{res}}$, $k_{p_{flux}}$, $k_{i_{flux}}$, $\widehat{R}_0$, $\hat{\lambda}_{f0}$ are the estimated resistance proportional regulator coefficient, estimated resistance integrator regulator coefficient, estimated rotor flux linkage proportional regulator coefficient, rotor flux linkage integrator regulator coefficient, and the estimated last stator resistance and rotor flux linkage, respectively.

$$\widehat{R}_s = -(k_{p_{res}} + \frac{k_{i_{res}}}{s})(L_d i_{d_{est}}(i_d - \hat{i}_d) + i_{q_{est}}(i_q - \hat{i}_q)) + \widehat{R}_0 \tag{II.13}$$

$$\hat{\lambda}_f = -\left(k_{p_{flux}} + \frac{k_{i_{flux}}}{s} \right) \omega_e (i_q - \hat{i}_q) L_q + \hat{\lambda}_{f0}. \tag{II.14}$$

Stator resistance and rotor flux linkage estimation values in (II.12) guarantees to give faster response than the closed loop cycle. Since large selected state errors are constantly growing and small selected estimation time gets longer, selection of proper regulator parameters are crucial for minimizing the steady-state error [50].

In the proposed MRAS method, a low-pass filter (LPF) is used to overcome the rise of the estimated rotor flux linkage value at low speed and at zero crossing and distortion effects caused from stator resistance estimation. In the situations where LPF is not used at low speed, the estimation values are small and cause the output of the feedforward voltage estimation values to be faulty [67].

2.2. Details of the Proposed Sensorless PMSM Drive Based on Stator FFVE Using Multi-parameter Estimation Based on MRAS

The dq–axes stator voltages in field oriented control are used in order to perform the current control located in the inner loop more dynamically [40]. In the literature, similar to the method proposed for induction motor sensorless speed control, stator voltage references v_d^* and v_q^* are added to the PMSM steady-state equation as feedforward estimator signals [58], [68], [69]. The control principle is adopted where the current in q–axis is controlled by speed of rotation or frequency of stator voltage applied to q–axis winding. The amplitude of q–axis voltage is obtained by neglecting the derivative term and assuming that real currents closely follow reference values $i_q = i_q^*$ and $i_d = i_d^*$ (reference values are marked with $*$ in the superscript and heat $\wedge$ above is the symbol indicates estimates). Below are the modified feedforward stator voltage equations for the proposed speed sensorless scheme given in dq reference frame.

$$v_q^* = i_q^* \widehat{R}_s + \left(\omega_e L_d i_d^* + \omega_e \hat{\lambda}_f\right) + K\Delta v \tag{II.15}$$

$$v_d^* = i_d^* \widehat{R}_s - \omega_e L_q i_q^* + \Delta v. \tag{II.16}$$

During steady-state operation, while d–axis current, i_d, minimizes the rotor flux linkage error, q–axis current, i_q, reference is obtained from the output of the speed regulator and controls the torque indirectly. The rotor flux linkage is defined as proportional to the rate of change of i_q and it is adjusted to force the d–axis current equal to zero at steady-state [70], [71]. As a result, the actual dq–axes voltages resulted to be proportional to the reference dq–axes voltages. In the method that is suggested in [72] by Okuyama et al. for induction motor, the relationships of the d–axis current regulator output Δv and rotor flux linkage $\hat{\lambda}_f$ are represented in (II.17), (II.18) and (II.19) as

$$\Delta v = \frac{L_m}{L_q}(-\omega_e \hat{\lambda}_f) \;\; for \;\; L_m \neq L_q \neq L_d \tag{II.17}$$

$$\Delta v = -\omega_e i_q L_q \;\; for \;\; L_m = L_q = L_d \tag{II.18}$$

$$\frac{\omega_e}{i_q} \approx \hat{\lambda}_f. \tag{II.19}$$

As it is seen in (II.20) that the rotor flux linkage $\hat{\lambda}_f$ is proportional to Δv.

$$\hat{\lambda}_f \approx -\Delta v \tag{II.20}$$

PMSM equations given in (II.15) and (II.16) show that dq–axes currents depend on dq–axes voltages and rotor angular velocity. In the proposed method, q–axis is the output of d–axis PI current controller located in the voltage equation; Δv is the output of q–axis PI current controller.

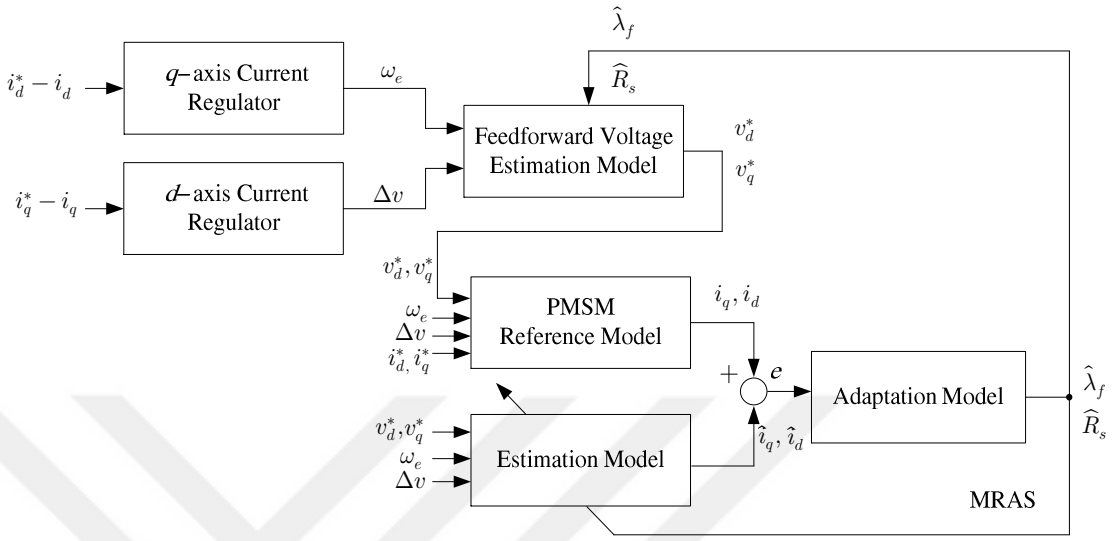

Figure II.3. Feedforward voltage estimation principle with MRAS multiple parameter estimation method.

It is the electrical angular estimated speed ω_e which is the output of the q–axis current regulator depending on the gain of K that enables the system to response dynamically and provides the system to protect its stability especially at low speeds [59]. The gain K is set manually and improves the response of the PMSM at low speeds expressed in (II.21) as

$$\frac{\lambda_q}{\hat{\lambda}_f} = \frac{\frac{1}{K\omega_e}p}{1+\frac{1}{K\omega_e}p}. \tag{II.21}$$

In the proposed method shown in Figure II.3, the rotor flux linkage value is updated in the feedforward voltage estimation model. In the stator voltage estimation, stator resistance is adjusted according to the error between reference d–axis current and feedback d–axis current component. In order to eliminate the errors caused from the stator resistance and rotor flux linkage variation in the PMSM, multi-parameter estimation using MRAS method is performed.

MRAS parameter estimation equations should be modified to be used in the proposed modified stator feedforward voltage estimation equations. PMSM reference frame and adjustable models that are given in (II.1), (II.2) and (II.6), respectively are modified accordingly. The novel MRAS mathematical models are derived to be used in accordance with the feedforward voltage estimation model. The variable $K\Delta v$ in the reference model is added to construct the proposed steady-state PMSM motor equation. These modified and simplified equations are given in (II.22) and (II.23) as

$$\dot{\hat{i}}_q = \frac{-L_d}{L_q}\omega_e \hat{i}_d - \frac{\widehat{R}_s}{L_q}\hat{i}_q + \frac{v_q}{L_q} - \frac{\hat{\lambda}_f}{L_q}\omega_e - \frac{K\Delta v}{L_q} \tag{II.22}$$

$$\dot{\hat{i}}_d = \frac{-\widehat{R}_s}{L_d}\hat{i}_d + \frac{L_q}{L_d}\omega_e \hat{i}_q + \frac{v_d}{L_d} - \frac{\Delta v}{L_d}. \tag{II.23}$$

A complete block diagram representation for a field-oriented control of the proposed speed sensorless PMSM scheme based on feedforward stator voltage estimation using a space vector PWM (SVPWM) voltage-source inverter (VSI) is illustrated in Figure II.5. For the system to work with PMSM, rotor flux linkage value and position are important for stable operation [73]. The resulting feedforward voltage estimation signals are represented in Figure II.3. The stator voltages applied to the motor are calculated by (II.15) and (II.16). Note that estimation of rotor angular speed, ω_e, is obtained by passing ω_e obtained from output of the PI current regulator in q–axis through a first order filter.

In Figure II.4, block diagram of the speed and position estimation method is illustrated. The time constant of the filter depends on the overall system mechanical characteristics and heavily affects the dynamics and stability of the sensorless control scheme.

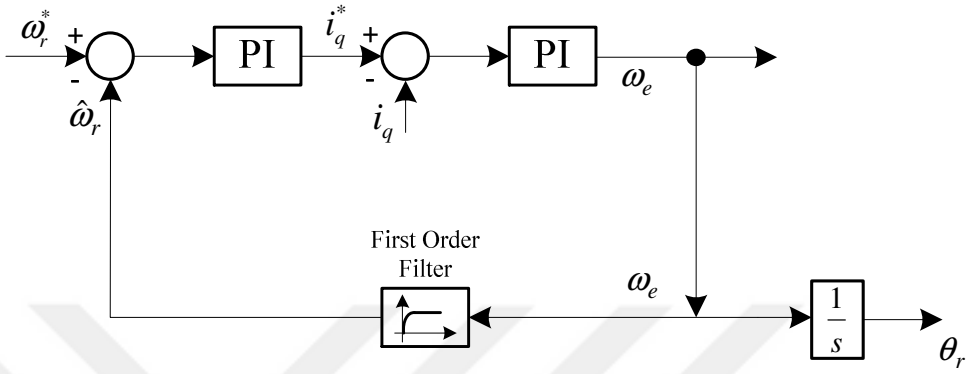

Figure II.4. Rotor speed and rotor angle estimation blocks.

2.3. Simulation Results

The proposed drive system shown in Figure II.5 has been simulated in MATLAB/Simulink® using an electrical IGBT inverter and electrical PM motor model from the SimPower Systems toolbox in order to demonstrate the validity of the proposed speed sensorless PM motor drive scheme.

To set the gating signals of the power switches from the output of the SVPWM module easily and represent the real conditions in simulation as close as possible, the proposed drive scheme including the electrical model of the actual PM motor and the inverter with power semiconductor switches considering the snubber circuit and the parameters of the switches are designed in MATLAB/Simulink® using the SimPower Systems block sets. The dead-time of the inverter and non-ideal effects of the PM synchronous machine are neglected in the simulation models. The DC-link voltage V_{dc} is set to 400 V. The switching frequency is chosen as 10 kHz.

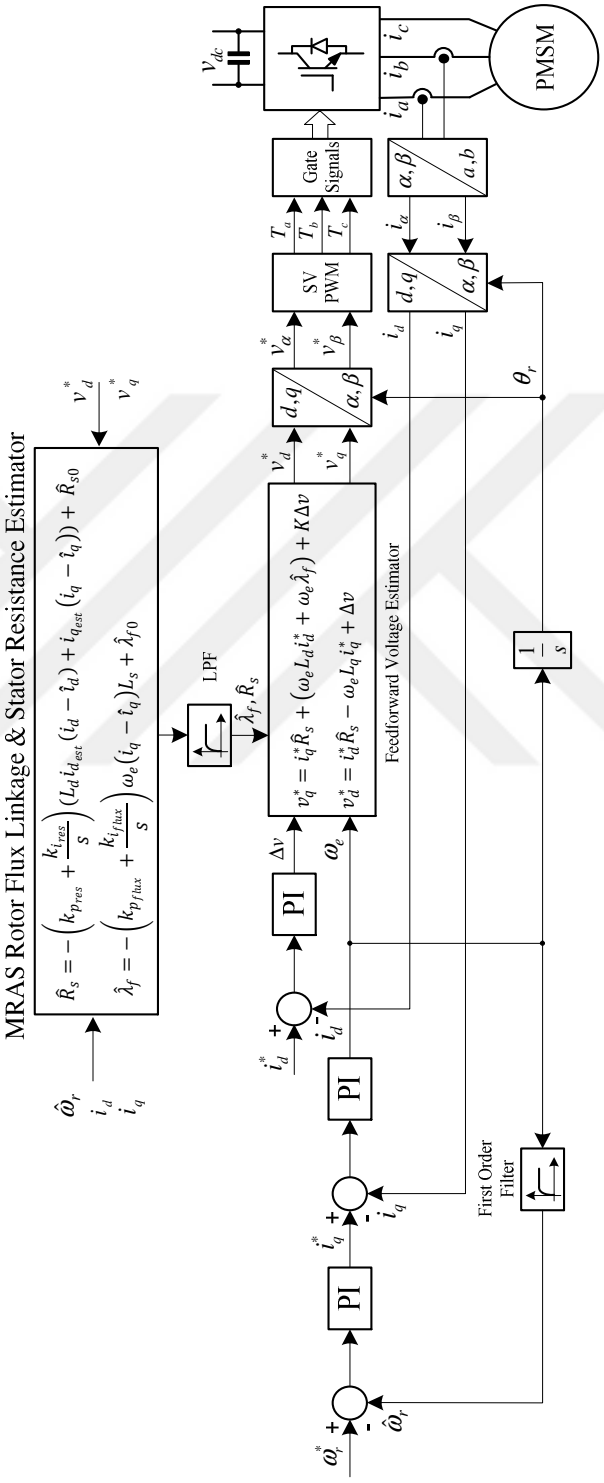

Figure II.5. Overall block diagram of proposed sensorless PMSM drive model based on MRAS parameter estimation.

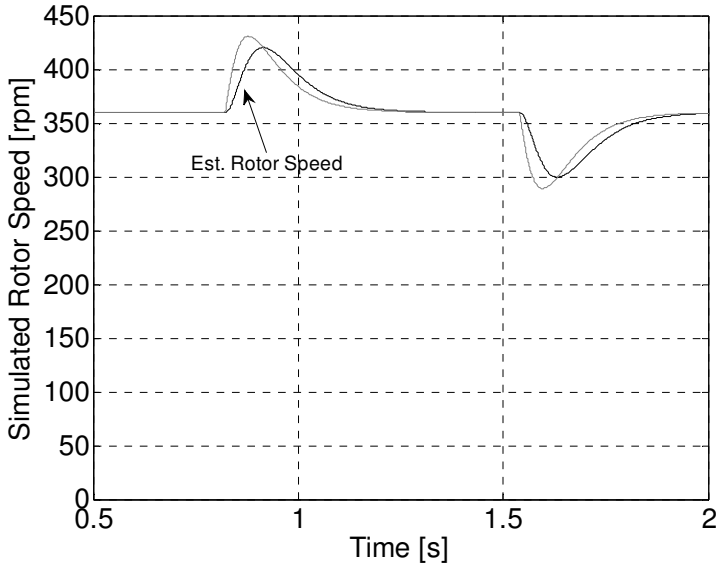

Figure II.6. Simulated steady-state speed response when full load (2 N·m) rejection is applied at t = 0.9 s and full load injection is applied at t = 1.55 s under 360 r/min speed reference without parameter estimation.

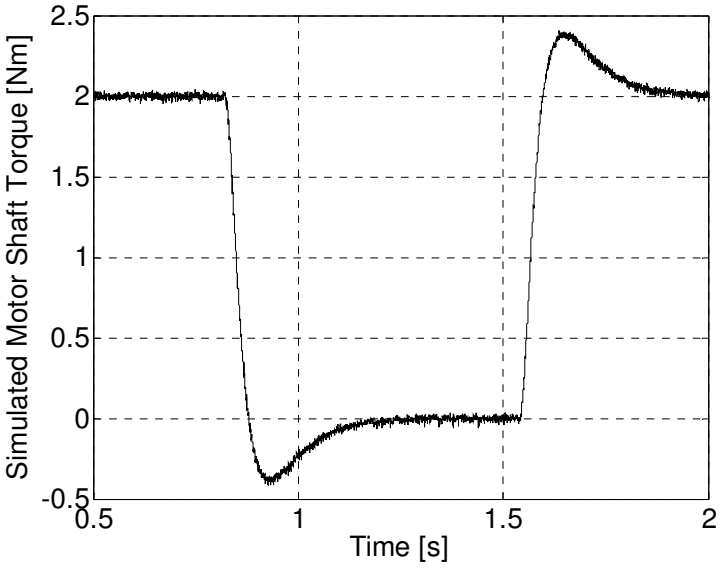

Figure II.7. Simulated steady-state torque response when full load (2 N·m) rejection is applied at t = 0.9 s and full load injection is applied at t = 1.55 s under 360 r/min speed reference without parameter estimation.

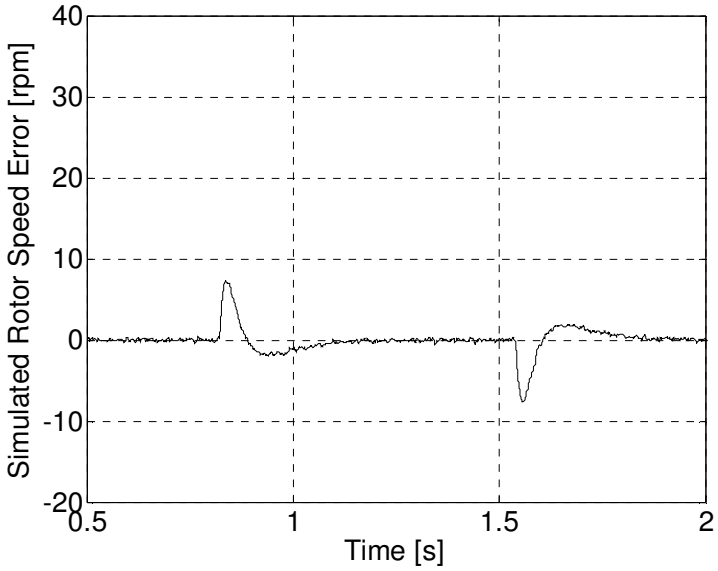

Figure II.8. Simulated steady-state speed response error (estimated and actual speed) when full load (2 N·m) rejection is applied at t = 0.9 s and full load injection is applied at t = 1.55 s under 360 r/min speed reference without parameter estimation.

In Figure II.6, the medium speed performance is simulated. In Figure II.7, motor shaft torque response is represented. The load rejection and load injection simulations are performed at 360 r/min steady-state speed for the proposed sensorless control scheme, as shown in Figure II.5. In this simulation, parameter estimation is not integrated to the proposed feedforward voltage estimation based sensorless control. The proposed method has dynamic structure and good response to sudden load changes. These are some of the main advantages of the proposed scheme compared to the other back-EMF based sensorless methods. In this case, the response time of the PMSM is under 0.2 s. The gain K given in (II.15) regularizes the performance of the overall system. Therefore, in medium speed ranges, the value of K is adjusted manually. In the performed simulations, it is observed that the selection of small K values results in non-stability in the system. Therefore, it is selected as 5.

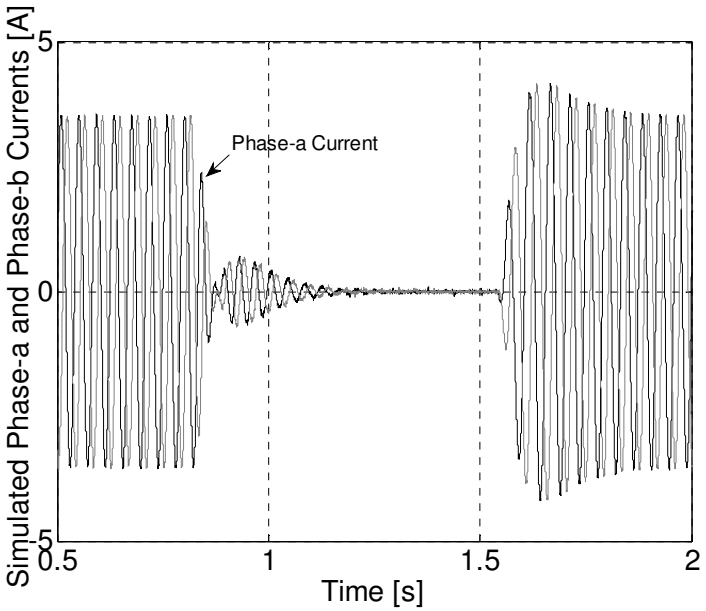

Figure II.9. Simulated steady-state (360 r/min) phase–a and –b current waveforms under full load (2 N·m), load rejection and load injection.

Speed error is shown in Figure II.8 under full load rejection and injection conditions. The error between actual and estimated speeds is very small and it is observed that the error converges to zero very quickly. In Figure II.9, the transient and steady-state phase–a and –b current waveforms are presented.

In simulation studies, multiple parameter estimator based on MRAS and PMSM model are run as an open-loop to verify the MRAS and sensorless algorithm. To be able to obtain an open-loop operation of PMSM, the steady-state operation is desired for the correct estimation of parameters. To achieve a steady-state operation, constant synchronous reference frame voltage values are given to the machine terminal and the initial speed is selected in the speed integrator of the PMSM model as 360 r/min.

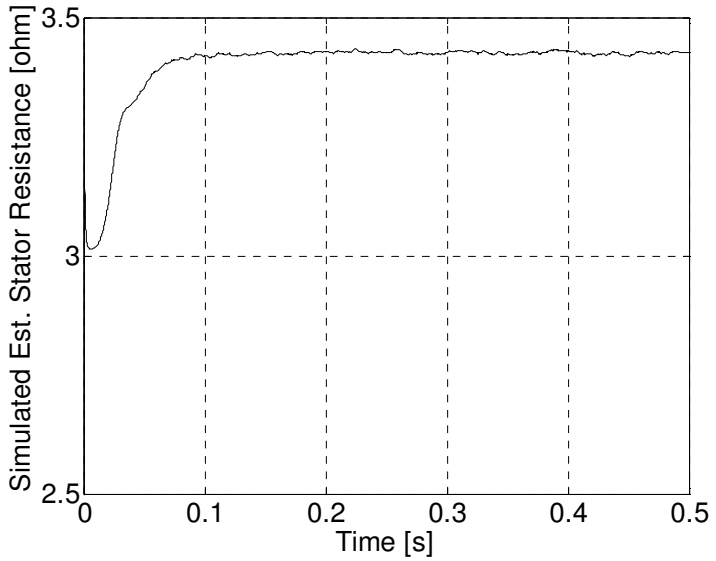

Figure II.10. Simulated stator resistance initial value estimation ($R_s = 3.4\ \Omega$).

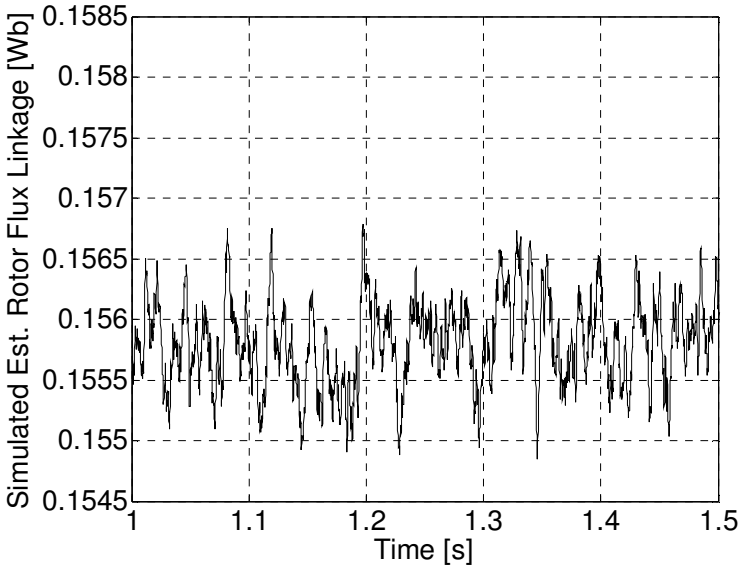

Figure II.11. Simulated rotor flux linkage initial value estimation ($\lambda_f = 0.15$ Wb).

In Figure II.10, the estimated stator resistance converges to actual value very well ($R_s = 3.4\ \Omega$). Figure II.11 shows the estimation of the rotor flux linkage. It is seen that the estimated rotor flux linkage converges to actual value quite well. The effect of stator resistance and rotor flux linkage variations on the overall performance of the proposed drive is investigated in simulations. The stator resistance and inductance estimates are chosen initially 50% greater than the actual values in the PM machine model. There is no parameter adaptation method is used in this simulation.

For the investigation of the behavior of the PMSM at under 270 r/min speed region, first the speed reference is set at 270 r/min and then the set point is changed to 240 r/min stepwise at t = 1 s, as shown in Figure II.12. Also, speed error is presented in Figure II.13.

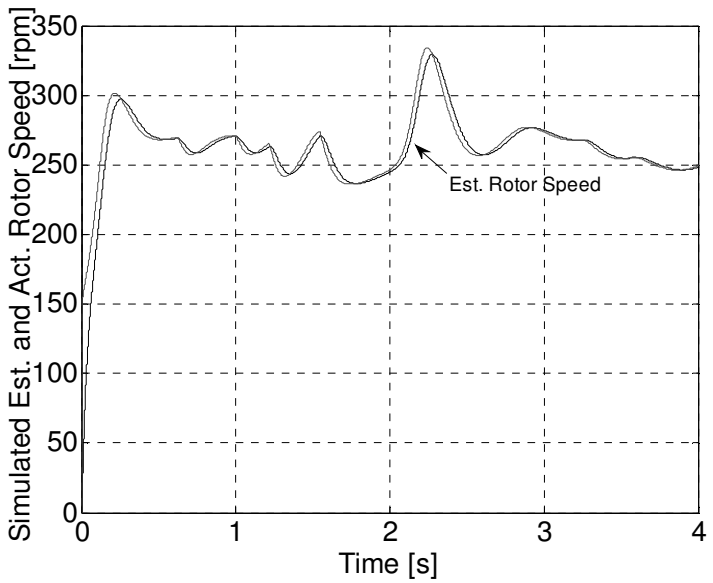

Figure II.12. Simulated steady-state speed response when full load (2 N·m) under 270 r/min speed reference with open-loop multiple parameter estimation.

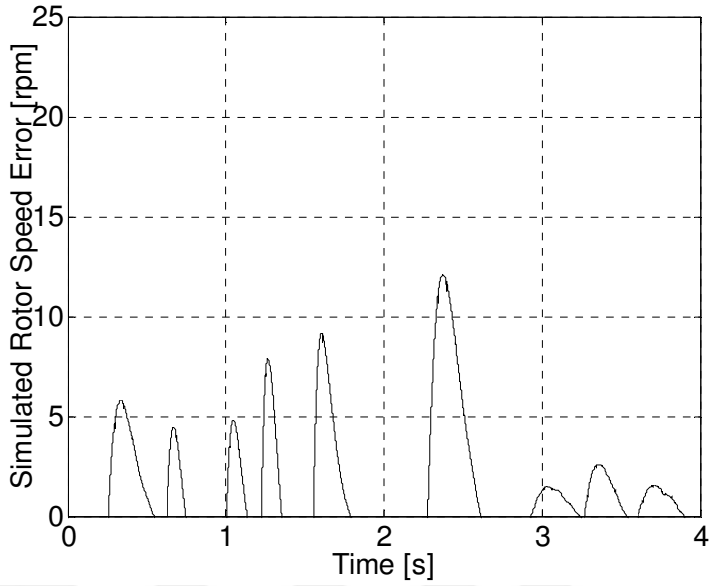

Figure II.13. Simulated steady-state rotor speed error when full load (2 N·m) under 270 r/min speed reference with open-loop parameter estimation when λ_f is decreased by 40% and R_s is increased by 50%.

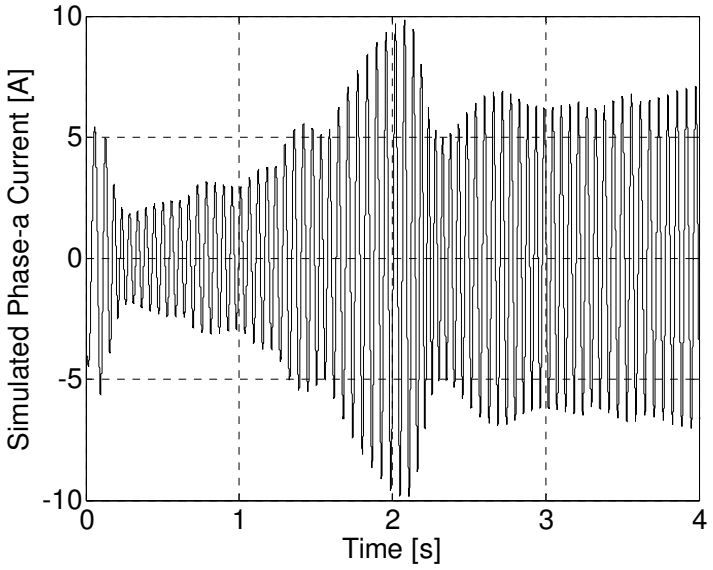

Figure II.14. Simulated transient (270 r/min) phase–a and –b current waveforms under full load (2 N·m) with open-loop parameter estimation when λ_f is decreased by 40% and R_s is increased by 50%.

Stator resistance and rotor flux linkage values vary depending on the operation condition. In order to improve the sensorless control performance, it is desired that motor parameters are estimated continuously and are updated in the feedforward voltage estimation equations. In practice, stator resistance and rotor flux linkage values cannot be changed anytime desired. However, in simulation studies, SimPower System PMSM model enables changing the rotor flux linkage value in steady-state. Figure II.14 shows the speed performance of the proposed sensorless method. Although, the starting of the machine has a distortion and the phase–a current shown in Figure II.15 that the PM machine draws a more current at transient. Simulation results for the Figure II.12 to Figure II.15 correspond to open-loop parameter estimation independent from sensorless control algorithm; on the other hand Figure II.16 to Figure II.20 shows the simulated combined parameter estimation and sensorless control algorithm.

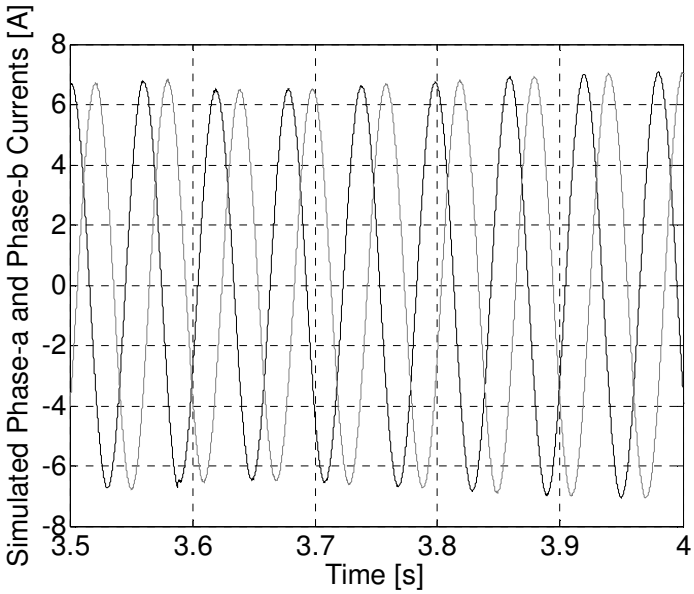

Figure II.15. Simulated steady-state (270 r/min) phase–a and –b current waveforms under full load (2 N·m) with open-loop parameter estimation when λ_f is decreased by 40% and R_s is increased by 50%.

As seen in Figure II.16, rotor flux linkage is increased 40% and stator resistance is increased 50%. As a result of these parameter changes, while a stability of 270 r/min could not be achieved in Figure II.12, a stability of 100 r/min in Figure II.18 is maintained.

For the investigation of the behavior of the MRAS parameter estimation algorithm, initial stator resistance value is increased linearly from the initial value starting from 45 seconds to 50% higher than the initial value in ten seconds, as shown in Figure II.13. The error between real and observed stator resistance is around ≤1% during the steady-state between 48 s and 50 s. Also, the observed error for rotor flux linkage variation in which the actual value started from 0.9 seconds to 40% lower than the original value in three seconds is given in Figure II.14. This error is considerably small which is around 0.5%. The reason for getting a high performance result is calculating MRAS PI gains and tuning it right.

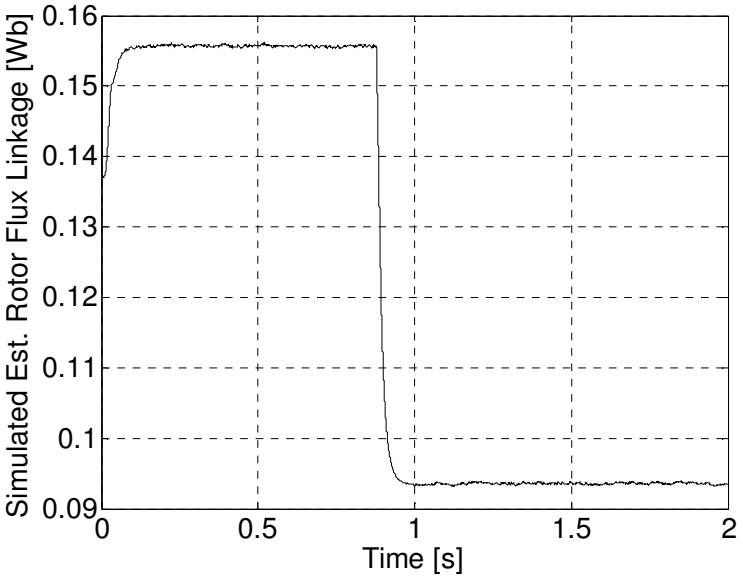

Figure II.16. Simulated rotor flux linkage estimation when λ_f is decreased by 40% and R_s is increased by 50%.

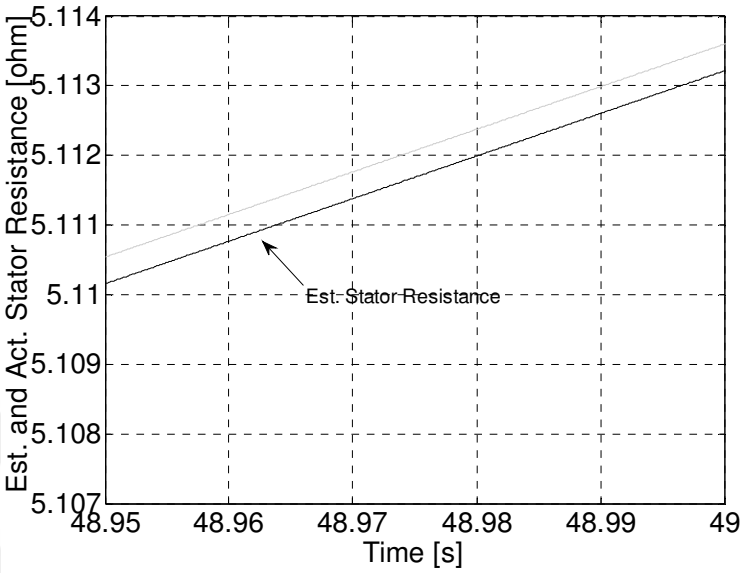

Figure II.17. Simulated stator resistance estimation when λ_f is decreased by 40% and R_s is increased by 50%.

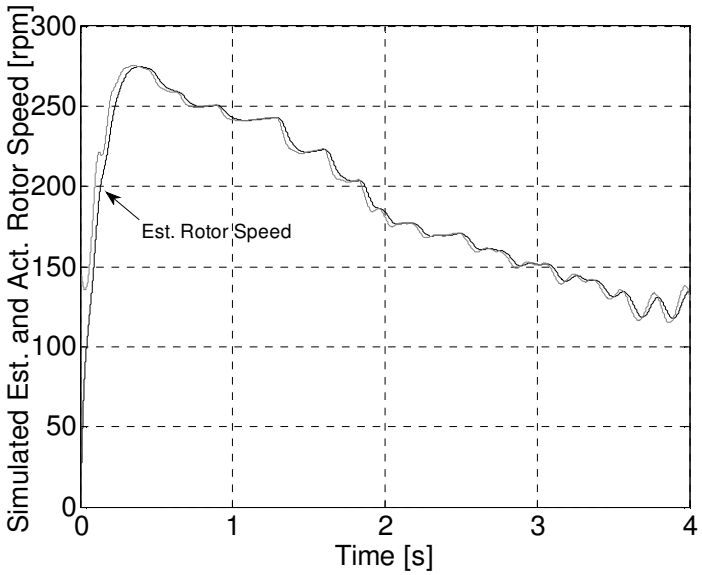

Figure II.18. Simulated steady-state (from 270 r/min to 135 r/min) phase–a and –b current waveforms under full load (2 N·m) with parameter estimation when λ_f is decreased by 40% and R_s is increased by 50%.

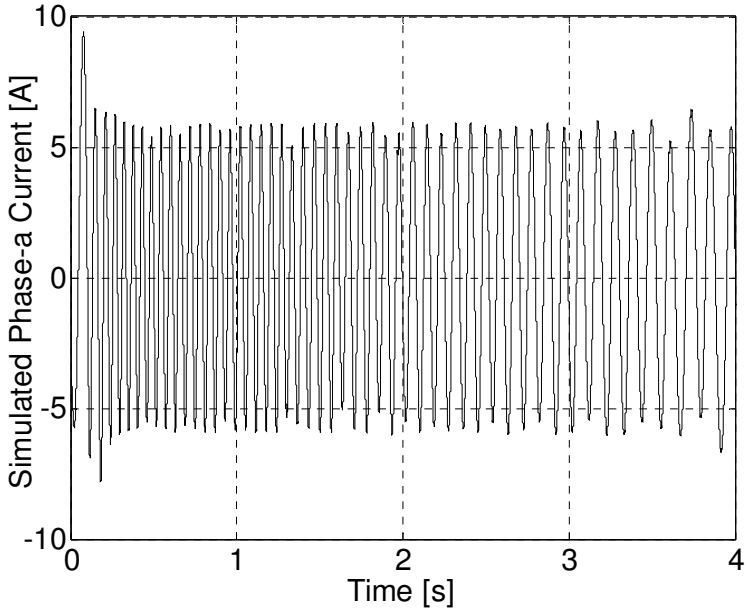

Figure II.19. Simulated steady-state phase–a current waveform under full load (2 N·m) with parameter estimation when λ_f is decreased by 40% and R_s is increased by 50%.

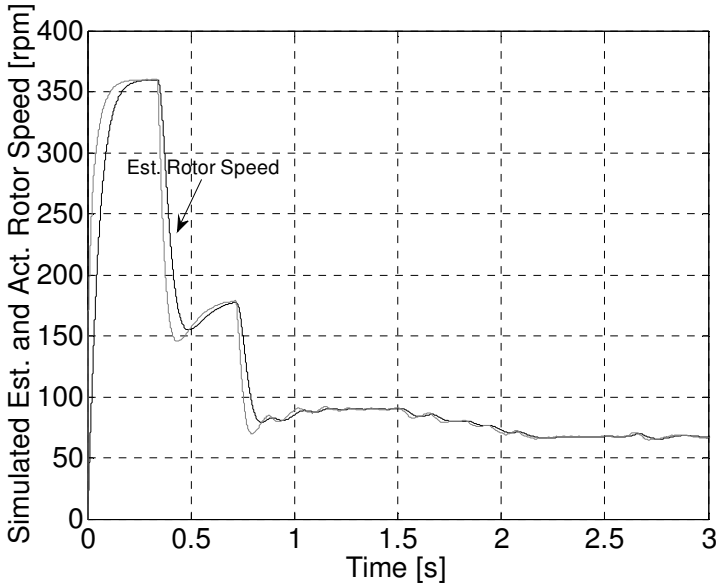

Figure II.20. Simulated steady-state (from 360 r/min to 63 r/min) speed response under full load (2 N·m) with parameter estimation when λ_f is decreased by 40% and R_s is increased by 30%.

In Figure II.18, it can be seen the results of the parameters estimated, obtained by updating the feedforward estimation block in each cycle as closed-loop. Despite the initial rotor flux linkage value is increased 40% and resistance value is increased 50%, sensorless control can still maintain the stability until 135 r/min. Under the same circumstances, phase–a current value is shown in Figure II.19. Although the current peak value is rising, there is not any non-stability in steady-state. In the measurements done with stator resistances changed in a 30% ratio, it is seen in Figure II.20 that sensorless control can be performed in simulation environment up to 63 r/min.

2.4. Experimental Results

The experimental set-up consists of a Magtrol AHB-6 model hysteresis dynamometer set, a SEMIKRON Semiteach inverter, a PM synhronous motor, a eZdsp™ board with TMS320F28335 DSP chip, and an interface and a signal conditioning cards. The Magtrol dynamometer set contains 6 N·m hysteresis brake, a DSP6001 model programmable DSP torque controller, and a Magtrol TMS306 model torque transducer to monitor the load torque and shaft speed which is installed between hysteresis brake and the motor. The signal conditioning card which comprises two LEM LA25NP model current sensors which read two motor phase currents and converts the real-world analog current values into equivalent low-voltage values. Interface card that is connected to the signal conditioning card scales the voltage values into proper positive representations for the DSP to sensitize.

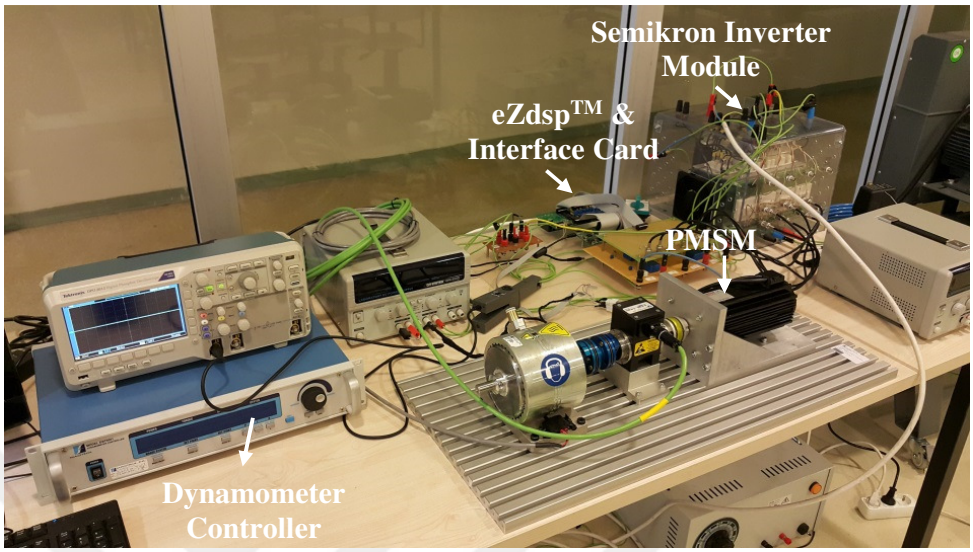

Figure II.21. Experimental test-bed.

The SEMIKRON Semiteach PWM voltage-source inverter (VSI) which comprises SKM 50 GB 123D model IGBT modules, SKHI 22 model gate drivers with 4.3 μs dead-time, and two 2200 mF caps. The inverter has a maximum DC-link voltage of 750 V and RMS current of 30 A.

In addition, an optical incremental encoder integrated to the PM servo motor with 2500 ppr resolution is used to detect the actual position/speed for evaluating the estimators. The proposed sensorless control scheme is verified using an off-the-shelf 2 N·m surface-mounted PMSM drive which is coupled to the overall system, as shown in Figure II.21. The parameters and specifications of the PMSM are provided in Appendix A.

In Figure II.22 shows start-up performance of proposed control method. There is unstable state is observed at experimental no-load start-up using the proposed sensorless scheme, as shown in Figure II.5.

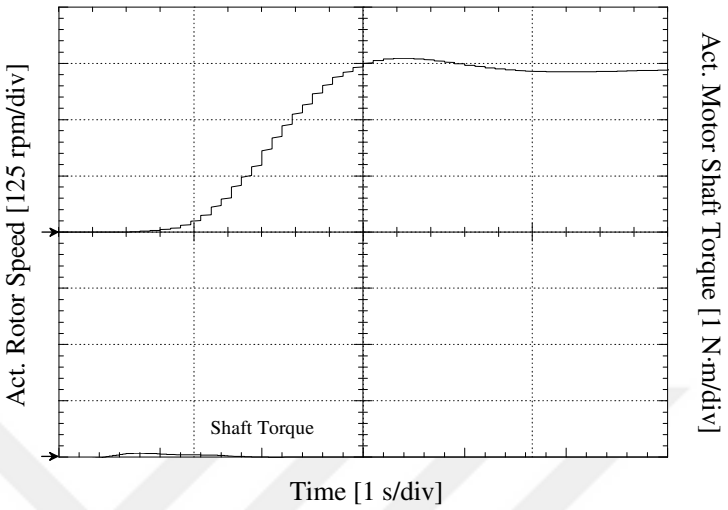

Figure II.22. Experimental rotor speed waveform under no load start-up (2 N·m) without parameter estimation.

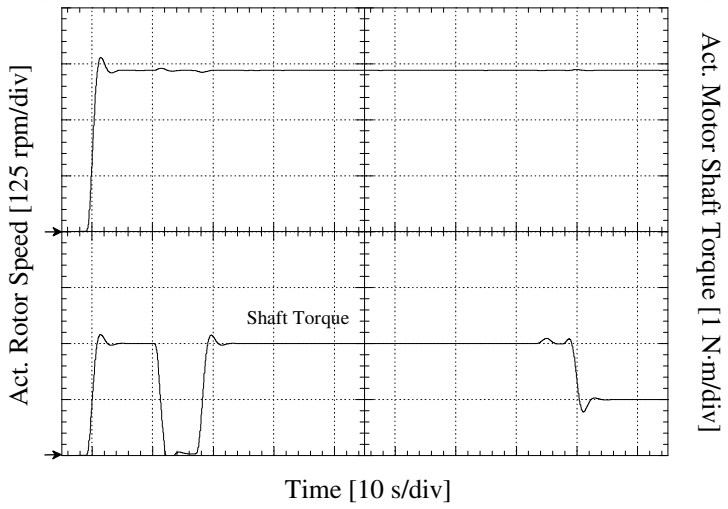

Figure II.23. Experimental speed response when full load rejection (2 N·m) is employed at t = 15 s and full load injection is employed at t = 82 s under 360 r/min steady-state speed without parameter estimation.

The experiment in Figure II.23 corresponds to the simulation in Figure II.6. In Figure II.23, without any estimation of parameters, results of load rejection and load injection of PMSM under 2 N·m load are shown. At the moment t = 0 s, PMSM is started with no load. At t = 3 s, reference torque is adjusted as 2 N·m. Also, feedforward voltage estimation has provided the stability of 360 r/min motor speed at desired response time by sensorless control. At t = 13 s, dynamometer load is adjusted to zero and the response of PMSM against sudden change of load is observed. At t = 19 s, the transient state performance is examined under transient conditions.

Figure II.24 shows the comparison of estimated speed values and the speed measured from encoder. The speed with reference value 0.4 p.u. has same values measured from encoder and estimated by feedforward voltage estimation control. This result shows the successful operation of sensorless control method at medium and high speeds to sudden speed and load changes.

Δv, is d–axis PI regulator output, variation is shown in Figure II.25 and also Δv is discussed in (II.15) – (II.19). ω_e, is q–axis PI regulator output, variation is shown in Figure II.26 and also ω_e, is discussed in (II.15) – (II.19). Actual data were obtained using Code Composer Studio real-time graph for Figure II.25 and Figure II.26. Figure II.27 shows the estimated position and measured position graph based on proposed sensorless control algorithm. Also, results illustrates that the estimated position tracks the actual position very well.

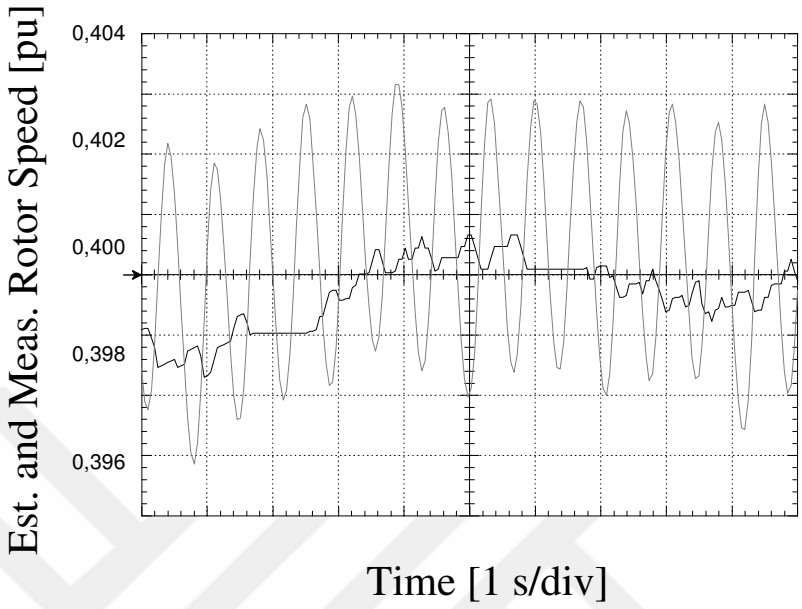

Figure II.24. Experimental estimated and measured rotor speed (360 r/min).

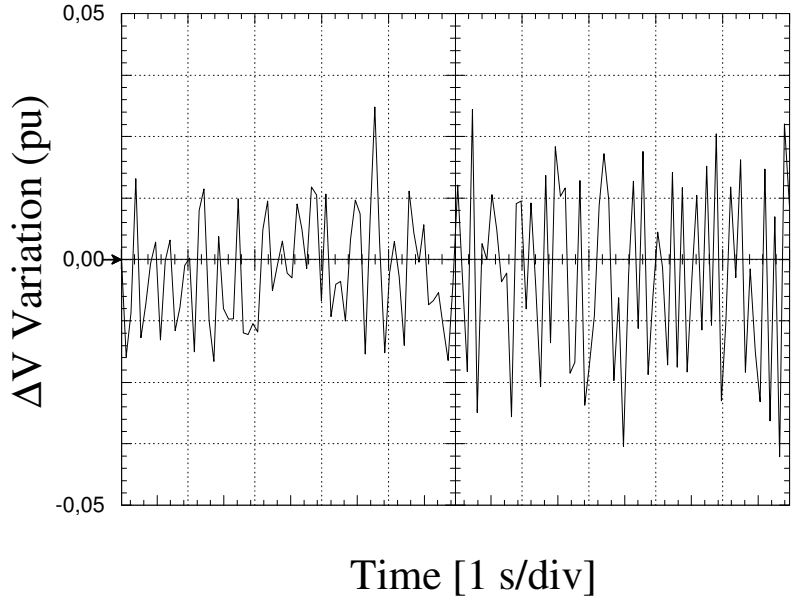

Figure II.25. Experimental Δv variation for 360 r/min.

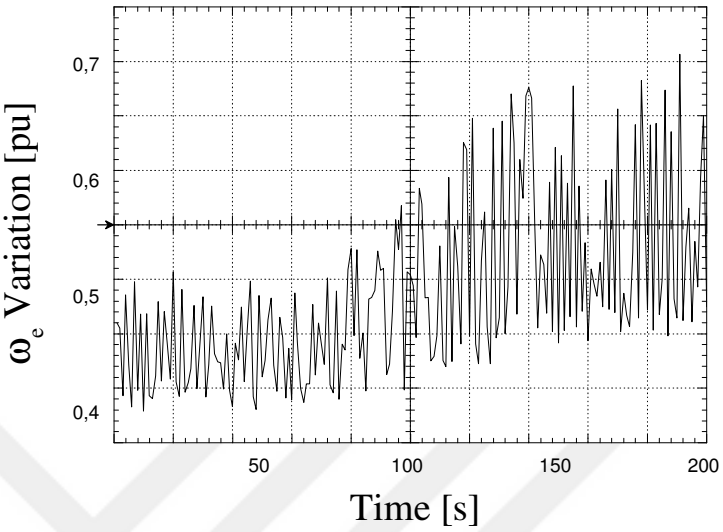

Figure II.26. Experimental ω_e variation for 360 r/min.

In Figure II.28 and Figure II.29, the phase–a and –b currents obtained with sensorless control based on feedforward voltage estimation suggested without parameter estimation under 2 N·m load constantly.

Figure II.28 is measured for 360 r/min motor speed while Figure II.29 is measured for 270 r/min motor speed.

In Figure II.30, the response of PMSM under rapid load changes for 360 r/min is shown.

The dynamic structure and stable working state of proposed method in medium and low speeds are presented in Figure II.28 to Figure II.30. In Figure II.31, the behavior of PMSM under sudden load changes for 270 r/min speed.

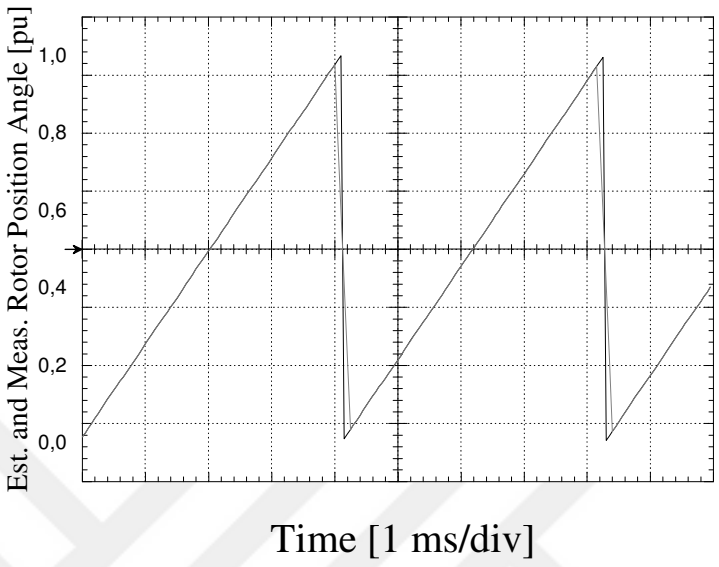

Figure II.27. Experimental estimated and measured rotor angle.

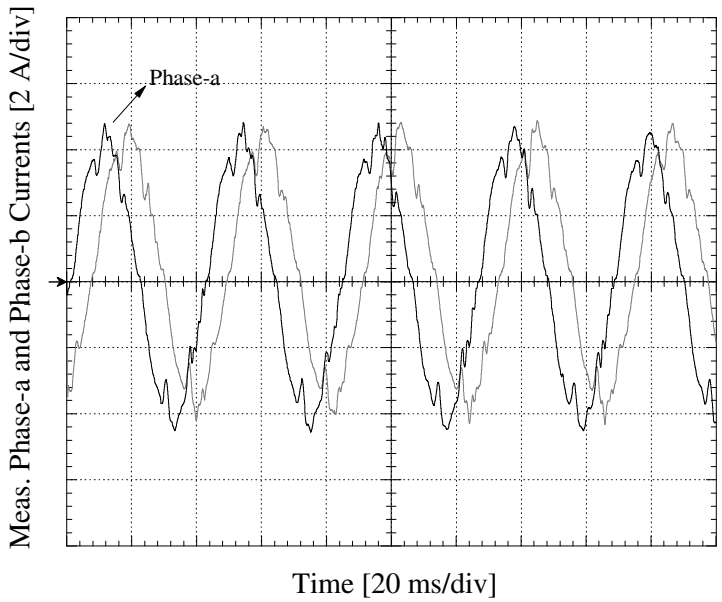

Figure II.28. Experimental steady-state (360 r/min) phase–a and –b current waveforms under full load (2 N·m) without parameter estimation.

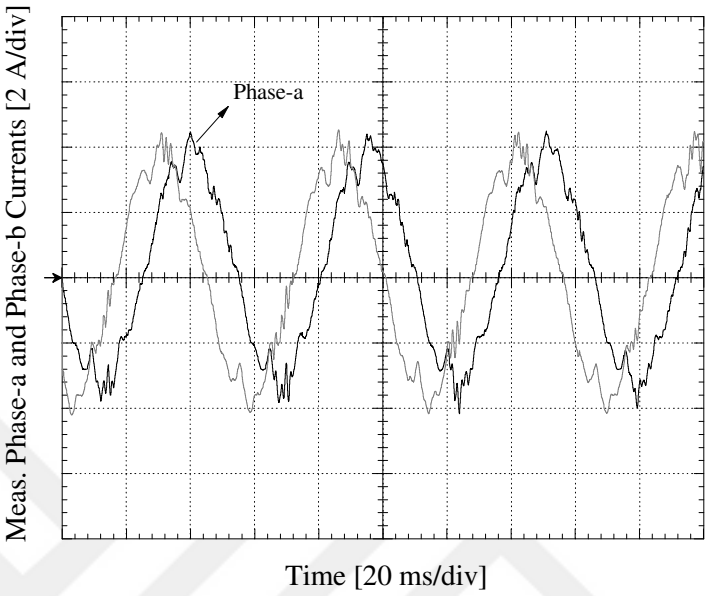

Figure II.29. Experimental steady-state (270 r/min) phase–a and –b current waveforms under full load (2 N·m) without parameter estimation.

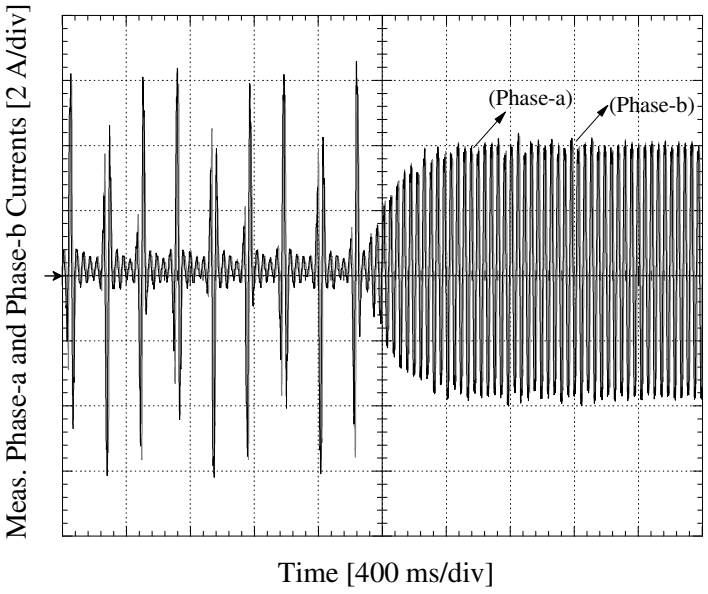

Figure II.30. Experimental phase–a and –b current waveforms for 360 r/min.

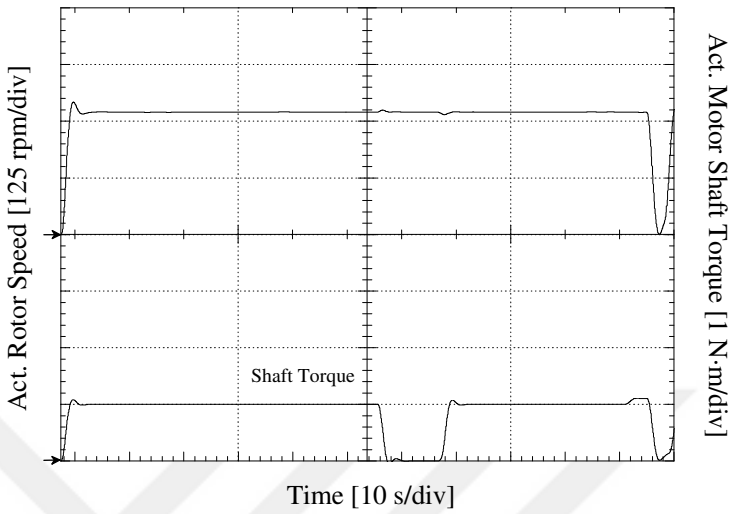

Figure II.31. Experimental speed response when full load rejection (2 N·m) is employed at t = 51 s and full load injection is employed at t = 61 s under 270 r/min steady-state speed without parameter estimation.

In Figure II.32, the waveform of phase–a and –b currents under same working conditions are illustrated. In Figure II.33, initial rotor flux linkage variation is shown. In simulation studies, rotor flux linkage variation is obtained by setting false initial values. But in experimental works, since the rotor flux linkage change occurs slowly, after obtaining true initial values and regulating related controller parameters, update of the rotor flux variable which is found in direct feedforward voltage estimation model is ensured. To prevent saturations, saturation limits are defined and even though being for a short time, not surpassing these limit values is ensured.

Additionally, instead of physically adding an additional resistance to the actual motor terminals, the wrong parameter values are given in the feedforward estimators for simplicity purpose. The differences observed in the transient responses between simulation and experiments are because of the mismatch of moment of inertia, damping and friction of the overall system compared to the one used in simulations. The

proposed robust control algorithm shows a good performance with online parameter estimation. In Figure II.35 shows the case of full load condition by increased stator resistance value adding 30%.

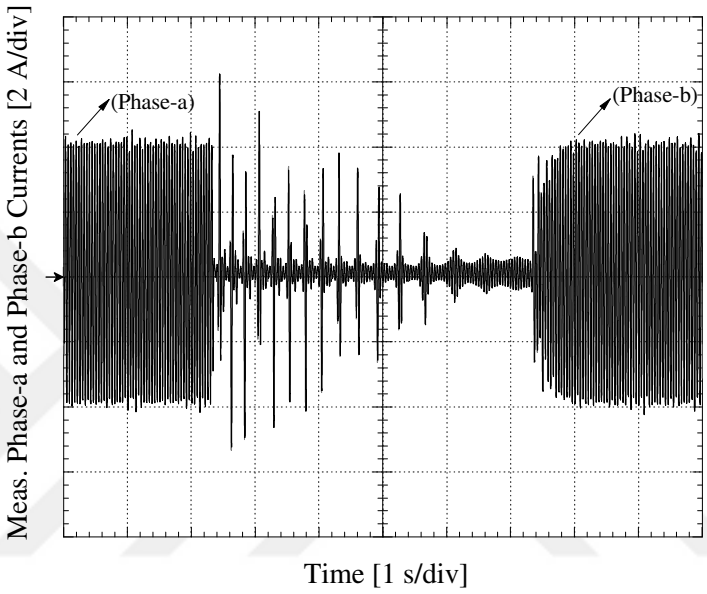

Figure II.32. Experimental phase–a and –b current waveforms for 270 r/min.

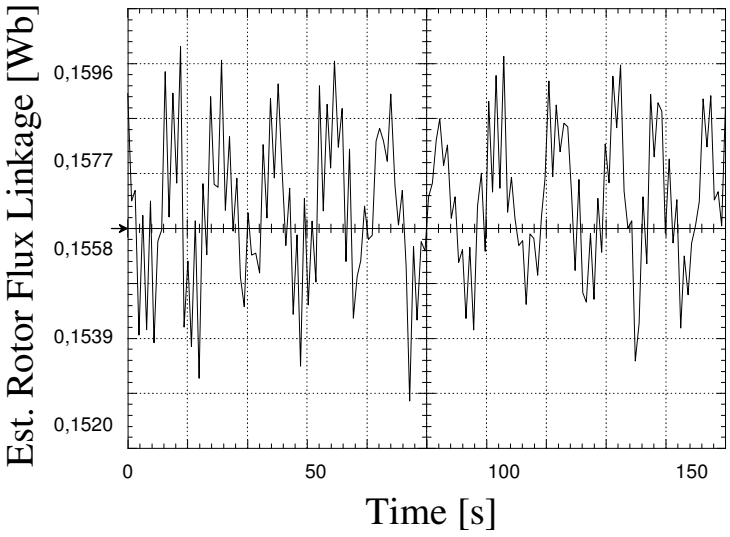

Figure II.33. Experimental initial estimated rotor flux linkage.

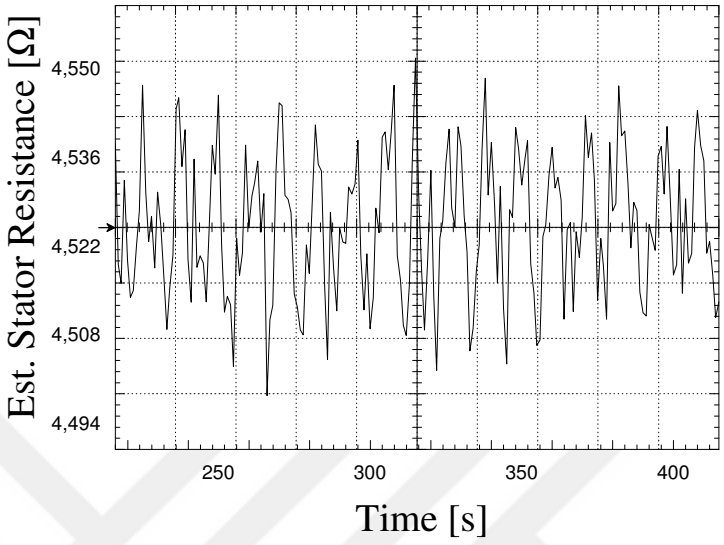

Figure II.34. Experimental estimated stator resistance when by R_s is increased by 30%.

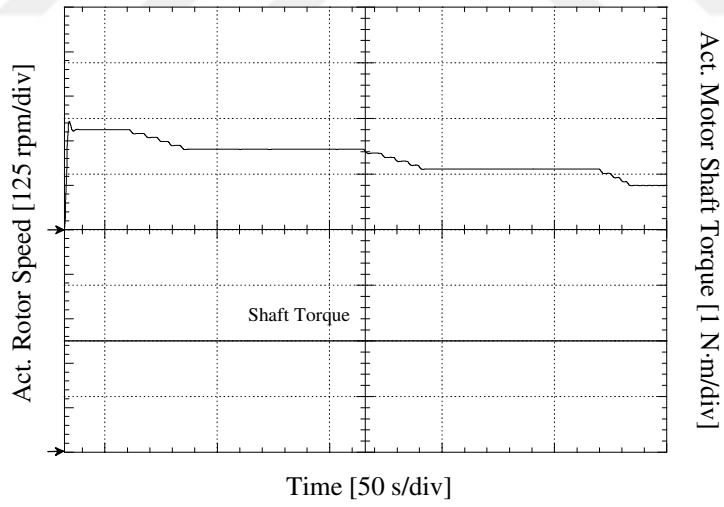

Figure II.35. Experimental rotor speed waveform at steady-state (from 240 r/min to 100 r/min) under full load condition with parameter estimation when R_s is increased by 30%.

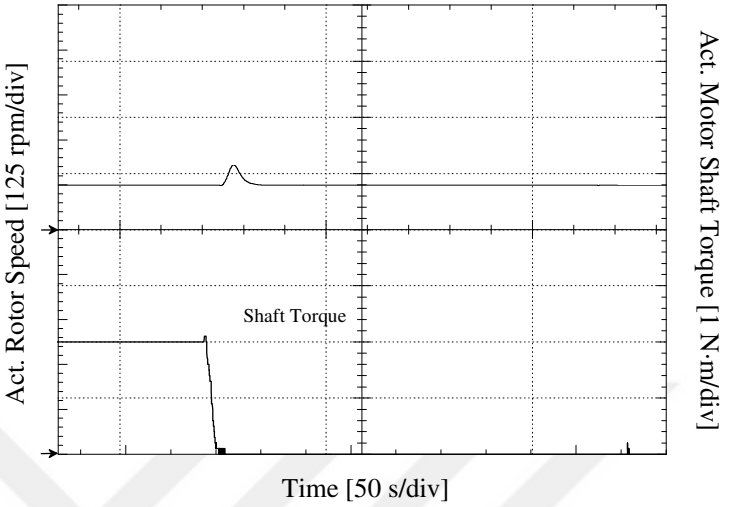

Figure II.36. Experimental rotor speed waveform at steady-state (100 r/min) under full load condition with parameter estimation when R_s is increased by 30%.

Proposed sensorless control method is observed to fail and lose the stability under 240 r/min. The most important reason of this is using PMSM model and this PMSM model taking the initial parameters as reference and developing sensorless control ability. In contrast, the proposed system uses the estimated values of the stator resistance and rotor flux linkage, and so, the estimation position depends on parameter variations. As shown in Figure II.35 and Figure II.36, the parameter variation can be estimated under the low speed region and a stable operation can be achieved in 100 r/min. In Figure II.36 shows the speed estimation response of the proposed control system under full load condition, load rejection and load injection conditions. In contrast to Figure II.36, using combined sensorless method and MRAS, low speed dynamic response is implemented. It is confirmed that the proposed sensorless drive system can operate 100 r/min.

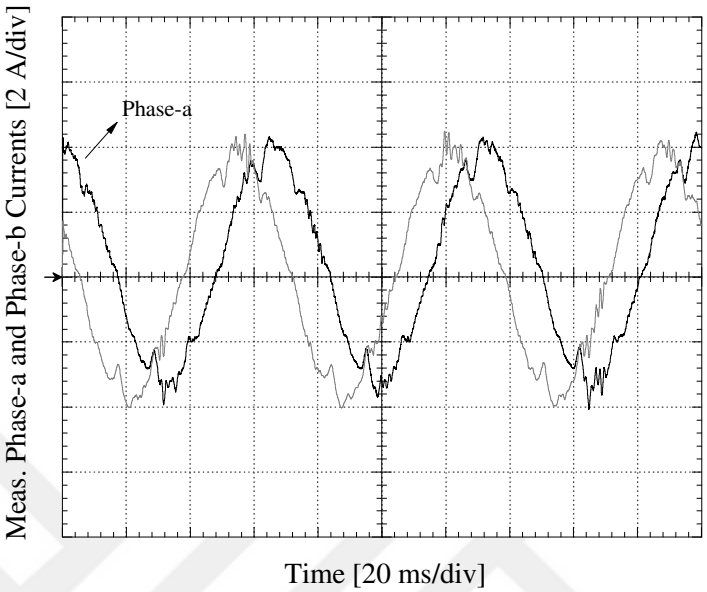

Figure II.37. Experimental steady-state (225 r/min) phase–a and –b current waveforms under full load (2 N·m) with parameter estimation.

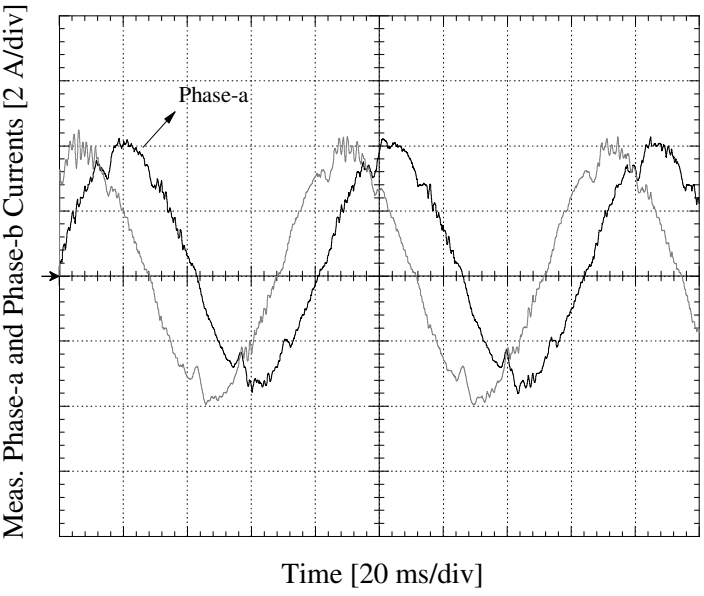

Figure II.38. Experimental steady-state (180 r/min) phase–a and –b current waveforms under full load (2 N·m) with parameter estimation.

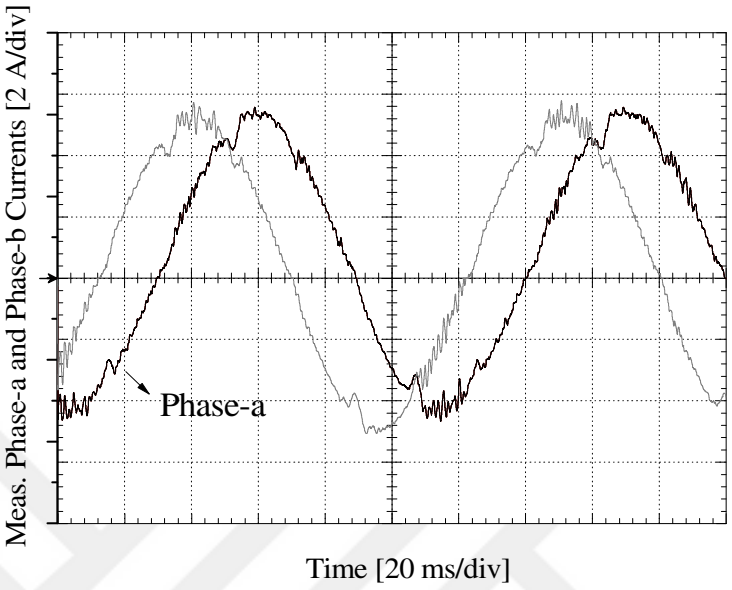

Figure II.39. Experimental steady-state (135 r/min) phase–a and –b current waveforms under full load (2 N·m) with parameter estimation.

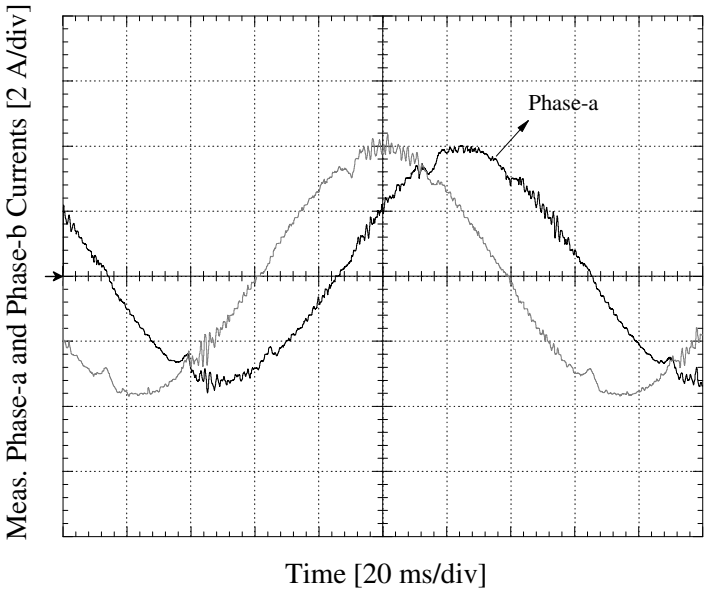

Figure II.40. Experimental steady-state (100 r/min) phase–a and –b current waveforms under full load (2 N·m) with parameter estimation.

The results of experiments are claiming that there is no chance of going below 240 r/min without parameter estimation, but it is possible to approach 100 r/min speed levels with parameter estimation. Here, parameter estimations are being done with MRAS and the rotor flux linkage estimated parameter seen in Figure II.3 and located in FFVE block, and stator resistance estimated parameter is constantly being updated.

Firstly, the estimation algorithm is ensured to work as open loop. By verifying parameter estimation, MRAS outputs are updating FFVE block in loops. With proposed control method, the aimed speed level of 100 r/min is approached with full load and stability is ensured. In Figure II.37, waveforms for phase–a and –b currents at 225 r/min are seen. Except peak declining in current wave form, sinusoidal wave forms are obtained.

In Figure II.41 and Figure II.42, a resistance of approximately 1 Ω is connected between a three-phase resistance PMSM and an inverter. Rotor flux linkage value is setted 40% lower than the original value. Performance of the proposed method in 180 r/min and 100 r/min are shown in Figure II.41 and Figure II.42. The current waveforms between Figure II.38 and Figure II.40 are recorded for 180 r/min, 135 r/min and 100 r/min, respectively.

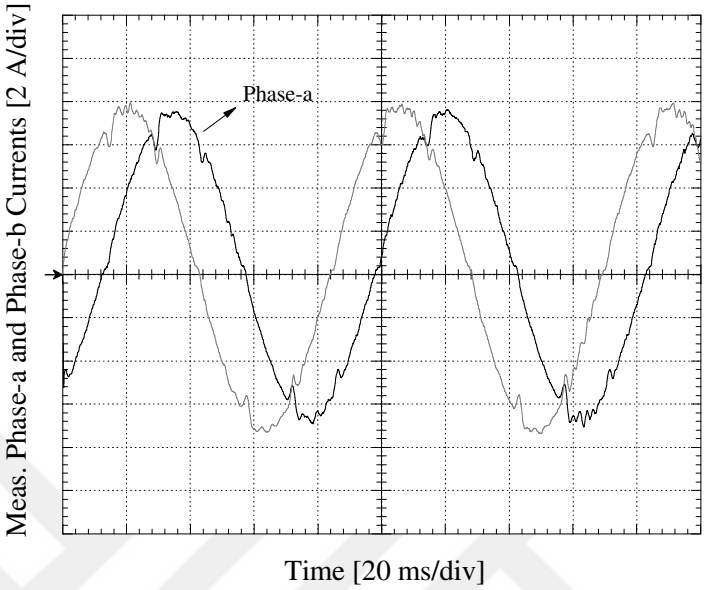

Figure II.41. Experimental steady-state (180 r/min) phase–a and –b current waveforms under full load (2 N·m) with parameter estimation when R_s is increased by 30%.

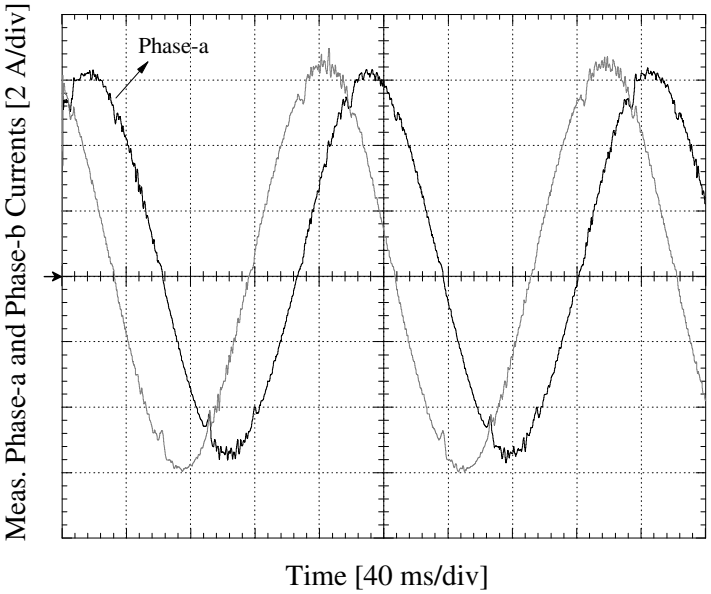

Figure II.42. Experimental steady-state (100 r/min) phase–a and –b current waveforms under full load (2 N·m) with parameter estimation when R_s is increased by 30%.

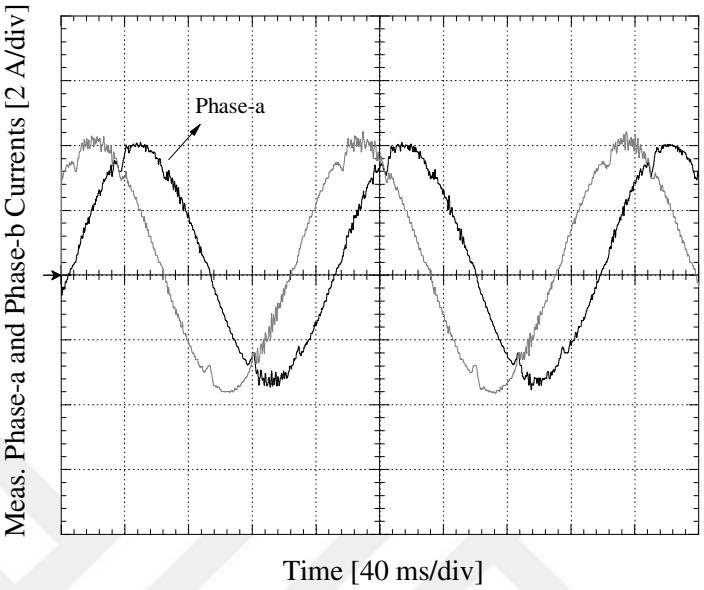

Figure II.43. Experimental steady-state (100 r/min) phase–a and –b current waveforms under full load (2 N·m) with parameter estimation when R_s is increased by 10%.

2.5. Conclusion

This chapter presents a simple and dynamic position sensorless PMSM control method based on feedforward voltage estimation improve with multi-parameter estimation method. With proposed method, compared to other sensorless methods, more dynamical and easily industrializable structure is being suggested. Since the method is based on back-EMF estimation method, the possible disrupting effects due to parameter changes are prevented with MRAS. Due to the reason the MRAS is easier to develop compared to other parameter estimation methods and not exhausting the microprocessor much, it is used in conjunction with feedforward voltage estimation. Depending on the rise in temperature, rotor flux linkage decreases while stator resistance increases. Effects of resistance change directly affects q–axis current. Due to this interaction, speed-torque characteristics of PMSM is changing. Rotor flux linkage

is affecting back-EMF and torque constant. Therefore, in simulation and experimental works, stator resistance's increase and rotor flux linkage's decrease is ensured. In experimental works performed, it is observed that proposed FFVE sensorless method maintains the stability at medium and high speeds, and it also maintains the stability at low speeds when used with MRAS. The whole control system is implemented by TMS320F28335 for a PMSM and the effectiveness is verified through the comparative simulations and experiments.

III. LOW-COST FIELD ORIENTED SPEED CONTROL OF PMSM DRIVE USING REDUCED SWITCH INVERTER

Low-cost inverter topology with reduced number of switching devices was firstly presented for an induction machine drive system in [74] as a four-switch three-phase (FSTP) inverter in which one of the three-phase windings is connected to the center-tap of the two DC-link capacitors and a comparable performance is achieved to the conventional six-switch three-phase (SSTP) inverter. With this modification, the FSTP voltage source inverter (VSI) topology generates only four non-zero active space vectors without any non-zero vectors in the $\alpha\beta$ plane, as oppose to six active and two zero voltage space vectors in the SSTP VSI counterpart and it is acknowledged as the standard reduced switch inverter topology for three-phase AC drives in the literature.

There are several advantages of FSTP inverter compared to traditional SSTP inverter which are summarized as follows: Although each switch rating in FSTP inverter is higher compared to the one in SSTP inverter, the price of each switch in FSTP inverter is 3/2 times less than the one in SSTP inverter, therefore the cost and space are minimized due to the reduction of the number of the semiconductor switches and free-wheeling diodes; driving circuits are only two, therefore complexity of drive and control circuitry are reduced which lowers the overall cost of the drive; due to the elimination of the semiconductor switches, with no change in the amplitude of DC-link voltage conduction and switching losses are reduced by 1/3rd; dependent to a less number of semiconductor switches increases the reliability of the converter; maximum common mode voltage is only 2/3 of SSTP inverter. Due to the above mentioned

benefits, FSTP inverter topology has been implemented in many low to medium power industrial applications ranging from servo to traction. However, the FSTP inverter topology has some drawbacks which are listed as: Since one of the motor phase windings has to be connected to the center-tap of the DC-link capacitors as shown in Figure III.3, current flowing from this leg charges one of the capacitors and discharges the other one, therefore it exposes to low frequency harmonic contents. This will cause significantly large fluctuations in the DC-link voltage and creates considerably large unbalance three-phase currents at the output. These unbalanced currents with harmonic components get bigger when the DC-link voltage is lower. Improved controller design is required to balance the capacitor voltages. Moreover, to eliminate the third-order harmonics, a larger value of switching frequency should be selected [75]–[80].

FSTP inverter control topologies have also been adapted to both sensored and sensorless PMSM and BLDC drives in [81]–[117]. FSTP inverter based BLDC drive is firstly introduced in [81]. The improvement in speed control performance of [81] is achieved in [82]. In [83], one of the first attempts of PMSM speed control using FSTP inverter is performed and compared with SSTP inverter. In [84], BLDC motor with three hall-effect position sensors driven by an FSTP inverter based on a novel current controlled PWM strategy with six commutation modes is proposed. To achieve low-cost sensorless BLDC position control, utilizing crossing detection of the two active phase voltage waveforms with an asymmetric voltage PWM method based on [84] is presented in [85]. In [86]–[89], sensorless control methods for BLDC drive using FSTP inverter are reported. The position sensorless controls of PMSM driven by an FSTP inverter are introduced in [90]–[92]. In [22], a DTC-based BLDC motor driven by an FSTP inverter that employed novel optimum switching table which enables the

independent simultaneous control of the electromagnetic torques developed by the phases connected to the inverter legs without requiring explicit stator flux control is achieved.

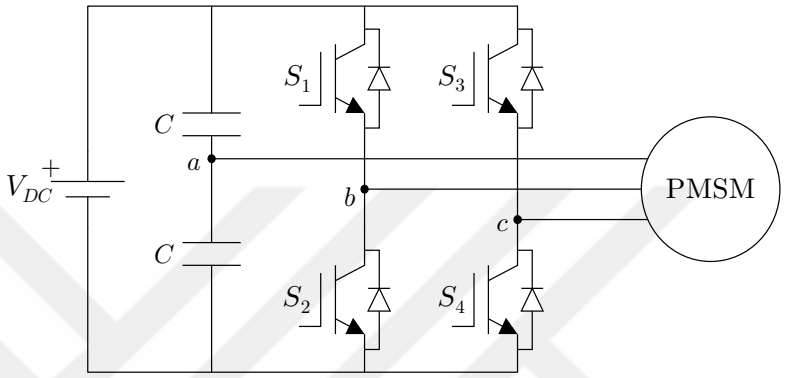

Figure III.1. Four-switch three-phase (FSTP) voltage source inverter (VSI) (phase–a is connected to the center tap of the split capacitors).

The operation of FSTP inverter resembles the faulty one-leg of a traditional SSTP inverter. Therefore, several research topics on reliability and fault tolerance of an SSTP inverter under faulty one-leg have been performed to maintain the stable operation of the overall drive scheme. In [93], the proper operation of an induction motor driven by an SSTP inverter under a short-circuit fault in one leg is accomplished without significant disturbance using a proposed fault isolation topology in which the inverter is reconfigured from six switches to having only four switches. Faulty condition of an SSTP inverter resembling the operation of an FSTP inverter are investigated for PMSM drives using FOC and DTC schemes in [94]–[101].

Minimization of torque and current ripples incorporating space vector pulse width modulation (SVPWM) are investigated for FSTP inverter. In FSTP inverter, one phase is always attached to the uncontrolled center tap of the two DC-link capacitors, therefore current waveforms are distorted and unbalanced. Compensation strategies for

PMSM and BLDC drives are employed to overcome the current and torque distortion and unbalancing issues of FSTP inverter in [102]–[108].

Moreover, efforts on reducing the current sensors from two to one in FSTP inverter driven PMSM and BLDC drives are also attempted in [89], [109] and [110]. The intelligent control methods such as fuzzy-logic and ANN type controller strategies are proposed for FSTP driven PMSM and BLDC drives in [111]–[115]. BLDC drives using FSTP inverter with power factor correction (PFC) are presented in [116] and [117].

This chapter is organized as follows. The principle of the proposed simple sector determination and switching sequence is presented in Section 3.1. In Section 3.2, the mathematical background and structure of the proposed FSTP method is presented. Moreover, the proposed control methods are designed and described in detail. In Section 3.3, electrical simulation model in MATLAB/Simulink is designed and developed. The simulation results are given and analyzed in detail. In Section 3.4, the proposed space vector algorithm scheme has been implemented with 1 kW PMSM drive controlled by a TMS320F28335. The hardware implementation and experimental results of the proposed FSTP inverter drive method including steady-state load disturbance are presented and discussed. Simulation and experimental results demonstrate the feasibility and effectiveness of the proposed method estimation for permanent magnet synchronous motors under full-load condition.

3.1. Proposed Simple Sector Determination and Switching Sequence

Without any additional modifications, there are only four active non-zero voltage space vectors and no zero voltage vectors in a conventional FSTP inverter topology. The switches S_1, S_3 and S_2, S_4 are complementary switches and have either 0 or 1

representation for their state. The following equations defines the state of the switches, Therefore, a binary "1" indicates a closed switch, while "0" indicates the open state. Also, it is assumed that a stiff voltage is available across the two DC-link capacitors, and $\mathcal{V}_{C1} = \mathcal{V}_{C2} = \frac{\mathcal{V}_{dc}}{2}$ where $\mathcal{V}_{dc}$ corresponds to a stiff DC-link voltage. The indice, Z, represents the center point of the split capacitors,

$$S_1 + S_2 = 1 \tag{III.1}$$

$$S_3 + S_4 = 1. \tag{III.2}$$

The phase voltages to its pole voltage in the FSTP inverter bridge are given as

$$\mathcal{V}_{AZ} = \frac{\mathcal{V}_{dc}}{2} \tag{III.3}$$

$$\mathcal{V}_{BZ} = S_1 \mathcal{V}_{dc} \tag{III.4}$$

$$\mathcal{V}_{CZ} = S_3 \mathcal{V}_{DC} \tag{III.5}$$

$$\mathcal{V}_{NZ} = \frac{\mathcal{V}_{AZ} + \mathcal{V}_{BZ} + \mathcal{V}_{CZ}}{3}. \tag{III.6}$$

where $\mathcal{V}_{dc}$ is the DC-link voltage and S_1 and S_2 represent the binary state of the upper switches in the leg. Phase voltages for the $Y-$ connected load can be calculated using (III.7) – (III.12). The third phase is taken from the center tap of the capacitor bank and its pole voltage (Z) is always fixed as $\mathcal{V}_{dc}/2$. The phase voltages are constructed through a control on the other two inverter legs. Phase voltages calculated from the pole voltages are shown in (III.7) – (III.9).

$$\mathcal{V}_{AN} = \mathcal{V}_{AZ} - \mathcal{V}_{NZ} \tag{III.7}$$

$$\mathcal{V}_{BN} = \mathcal{V}_{BZ} - \mathcal{V}_{NZ} \tag{III.8}$$

$$\mathcal{V}_{CN} = \mathcal{V}_{CZ} - \mathcal{V}_{NZ} \tag{III.9}$$

Using (III.10) – (III.12), the phase voltages of the FSTPI can be expressed in terms of switching states as

$$\mathcal{V}_{AN} = \frac{1}{3}(2\mathcal{V}_{AZ} - \mathcal{V}_{BZ} - \mathcal{V}_{CZ}) = \frac{\mathcal{V}_{DC}}{3}(1 - S_1 - S_3) \tag{III.10}$$

$$\mathcal{V}_{BN} = \frac{\mathcal{V}_{DC}}{3}(2S_1 - \frac{1}{2} - S_3) \tag{III.11}$$

$$\mathcal{V}_{CN} = \frac{\mathcal{V}_{DC}}{3}\left(2S_3 - \frac{1}{2} - S_1\right). \tag{III.12}$$

Keeping the same Clarke, Park, and Inverse Park transformations with the direction of the motor chosen as $a \to b \to c \to a$, there are only three possible voltage space vector combinations in the $\alpha\beta$ plane for FSTP inverter, as shown in Figure III.2, Figure III.3(a) and Figure III.3(b). Figure III.2, Figure III.3(a) and Figure III.3(b) illustrate the four voltage space vectors in $\alpha\beta$– axes when phase–a, phase–b, and phase–c are connected to the center-tap of the DC-link capacitors, respectively. The quadrature quantities in the $\alpha\beta$ frame corresponding to these three phase voltages are given by the general Clarke transform equation as

$$\begin{bmatrix}\mathcal{V}_\alpha \\ \mathcal{V}_\beta\end{bmatrix} = \frac{2}{3}\begin{bmatrix}1 & -\frac{1}{2} & -\frac{1}{2} \\ 0 & \frac{\sqrt{3}}{2} & -\frac{\sqrt{3}}{2}\end{bmatrix}\begin{bmatrix}\mathcal{V}_{AN} \\ \mathcal{V}_{BN} \\ \mathcal{V}_{CN}\end{bmatrix} = \frac{2}{3}\begin{bmatrix}\frac{-\mathcal{V}_{DC}}{2}(S_1 + S_3 - 1) \\ \frac{\sqrt{3}\mathcal{V}_{DC}}{2}(S_1 - S_3)\end{bmatrix}. \tag{III.13}$$

Due to the fact that only four combinations are possible for the power switches, $\mathcal{V}_\alpha$ and $\mathcal{V}_\beta$ can also take only a finite number of values in the $\alpha\beta$ frame according to the status of the IGBT gate signals $(\mathrm{a}, \mathrm{b}, \mathrm{c})$. Stationary reference frame voltages which

depend on binary variables S_1 and S_2 and the DC-link voltage are given in (III.14) through (III.17).

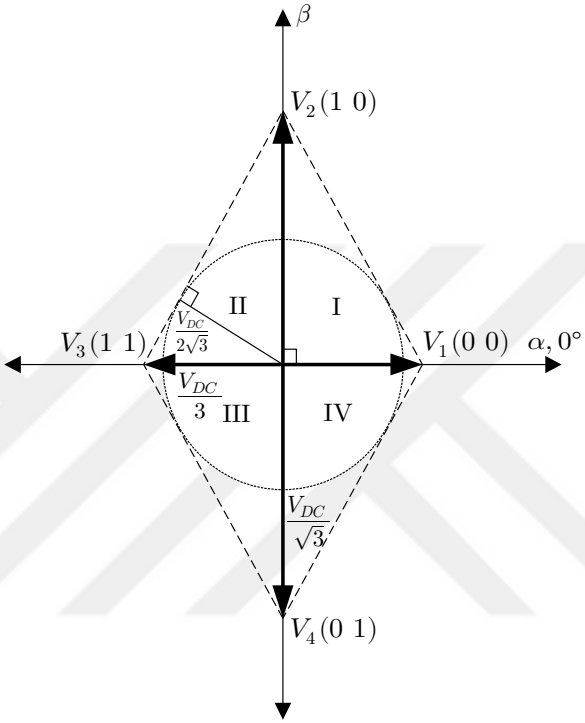

Figure III.2. Space vector representations for FSTP VSI in $\alpha\beta$ plane when phase–a is connected to the center tap.

In the four switch configuration, there are four switching status as expressed in (III.14) – (III.17). These values of $\mathcal{V}_\alpha$ and $\mathcal{V}_\beta$ for the corresponding instantaneous values of the phase voltages $\mathcal{V}_{AN}, \mathcal{V}_{BN}, \mathcal{V}_{CN}$ depend on space vector combinations given by

$$\begin{matrix} \mathcal{V}_\alpha = \dfrac{\mathcal{V}_{DC}}{3} \\ \mathcal{V}_\beta = 0 \end{matrix} \quad \begin{cases} S_1 = 0 \\ S_3 = 0 \end{cases} \tag{III.14}$$

$$\begin{matrix} \mathcal{V}_\alpha = 0 \\ \mathcal{V}_\beta = \dfrac{-\mathcal{V}_{DC}}{\sqrt{3}} \end{matrix} \quad \begin{cases} S_1 = 0 \\ S_3 = 1 \end{cases} \tag{III.15}$$

$$\begin{matrix} \mathcal{V}_{\alpha} = 0 \\ \mathcal{V}_{\beta} = \dfrac{\mathcal{V}_{DC}}{\sqrt{3}} \end{matrix} \quad \begin{cases} S_1 = 1 \\ S_3 = 0 \end{cases} \tag{III.16}$$

$$\begin{matrix} \mathcal{V}_{\alpha} = \dfrac{-\mathcal{V}_{DC}}{3} \\ \mathcal{V}_{\beta} = 0 \end{matrix} \quad \begin{cases} S_1 = 1 \\ S_3 = 1. \end{cases} \tag{III.17}$$

As it can be seen in Figure III.3(a), each corresponding voltage vector has 120º CCW rotations from the previous phase connection that is given in Figure III.2. The similar case is applied for the vectors in Figure III.3(b) such that they are rotated 120º CCW from the ones shown in Figure III.3(a).

If all the transformations are kept as in the classical SSTP inverter, there is only one phase connection (phase–a) shown in Figure III.1 to the center-tap that makes all the four non-zero voltage space vectors align with the α– and β– axes in either positive or negative directions for FSTP inverter which are illustrated in Figure III.2. $\mathcal{V}_{\alpha}$ and $\mathcal{V}_{\beta}$ listed in table are called the (α, β) components of the basic space vectors corresponding to the appropriate IGBT command signal (a, b, c).

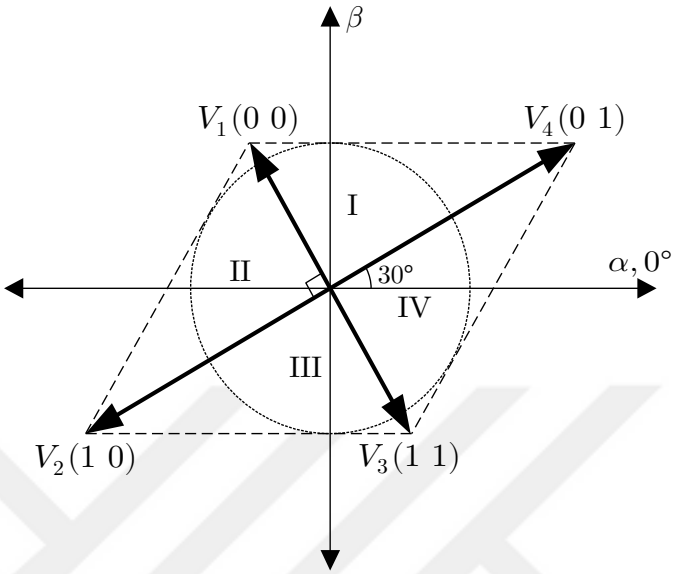

(a)

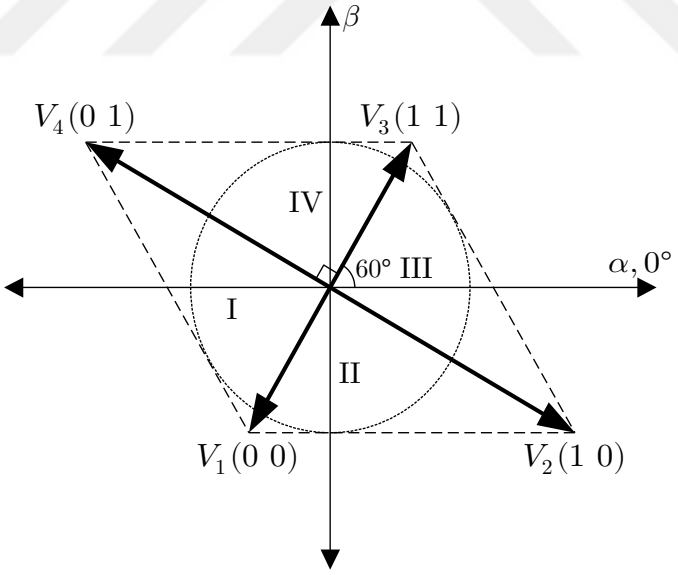

(b)

Figure III.3. Space vector representations for FSTP VSI in $\alpha\beta$ plane when (a) phase–b and (b) phase–c is connected to the center tap.

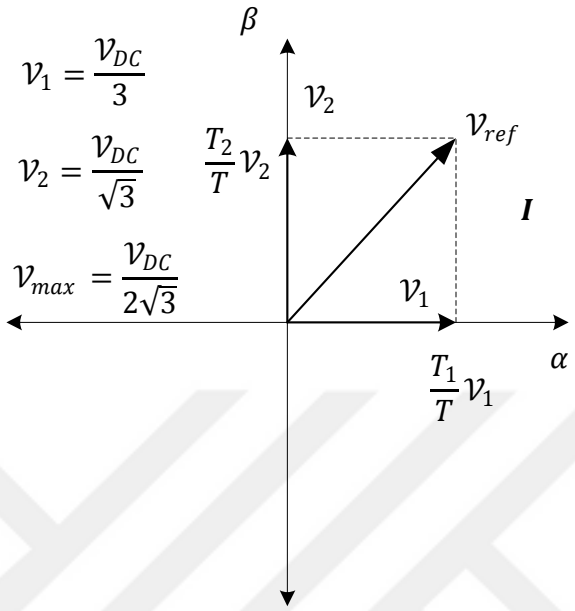

Figure III.4. Sector-I timing calculation diagram.

3.2. The Structure of the Proposed Switching Method

Having all the vectors aligned with the α– and β– axes in either positive or negative directions, there is a simple and very effective way to determine the four sectors by following the already available α– and β– axes stationary voltage references in digital controller without needing estimated position information if the control is achieved without a position sensor. If an actual rotor position is used to determine the sectors, all of the three possible phase connections to the center-tap will be sufficient to obtain the correct sectors.

The objective of space vector PWM technique is to approximate a given stator reference voltage $\mathcal{V}_{ref}$ by combination of the switching pattern corresponding to the basic space vectors. The reference vector $\mathcal{V}_{ref}$ given in (III.18) is represented by its

(α, β) components, $\mathcal{V}_\alpha$ and $\mathcal{V}_\beta$. Figure III.4 shows the reference voltage vector, its (α, β) components and two of the basic space vectors $\mathcal{V}_0$ and $\mathcal{V}_{90}$.

$$\mathcal{V}_{ref} = \frac{T_1}{T}\mathcal{V}_1 + \frac{T_2}{T}\mathcal{V}_2 \tag{III.18}$$

Figure III.4 also indicates the resultant α and β components for the space vectors $\mathcal{V}_0$ and $\mathcal{V}_{90}$. $\mathcal{V}_\alpha$ and $\mathcal{V}_\beta$ given in (III.19) and (III.21), respectively are represented by $\mathcal{V}_0$, $\mathcal{V}_{90}$ and (α, β) components of the other vectors. Since all the vectors are aligned to an axis, vector representations are simple. T_1 and T_2 given in (III.20) and (III.22), respectively are the respective durations in time for which $\mathcal{V}_0$ and $\mathcal{V}_{90}$ are applied within period T.

$$\mathcal{V}_\alpha = \frac{T_1}{T}\mathcal{V}_1 \cos 0 = \frac{T_1}{T}\mathcal{V}_1 \tag{III.19}$$

$$T_1 = \frac{T}{\mathcal{V}_1}\mathcal{V}_\alpha = \frac{\sqrt{3}}{2}T\mathcal{V}_\alpha \tag{III.20}$$

$$\mathcal{V}_\beta = \frac{T_2}{T}\mathcal{V}_2 \sin 90 = \frac{T_2}{T}\mathcal{V}_2 \tag{III.21}$$

$$T_2 = \frac{T}{2}\mathcal{V}_\beta \tag{III.22}$$

When the normalization is applied using the maximum phase voltage (line to neutral), $\mathcal{V}_{dc}/2\sqrt{3}$, the amplitudes of the space vector become $\mathcal{V}_1 = \mathcal{V}_{dc}/3$, $\mathcal{V}_2 = \mathcal{V}_{dc}/\sqrt{3}$. $\mathcal{V}_\alpha$ and $\mathcal{V}_\beta$ are represented by the normalized (α, β) components of $\mathcal{V}_{out}$ with respect to the maximum phase voltage $\mathcal{V}_{dc}/2\sqrt{3}$. The two variables X and Y used in Table III.1 are defined as

$$X = \frac{\sqrt{3}}{2}\mathcal{V}_\alpha \tag{III.23}$$

$$Y = \frac{\mathcal{V}_\beta}{2}. \tag{III.24}$$

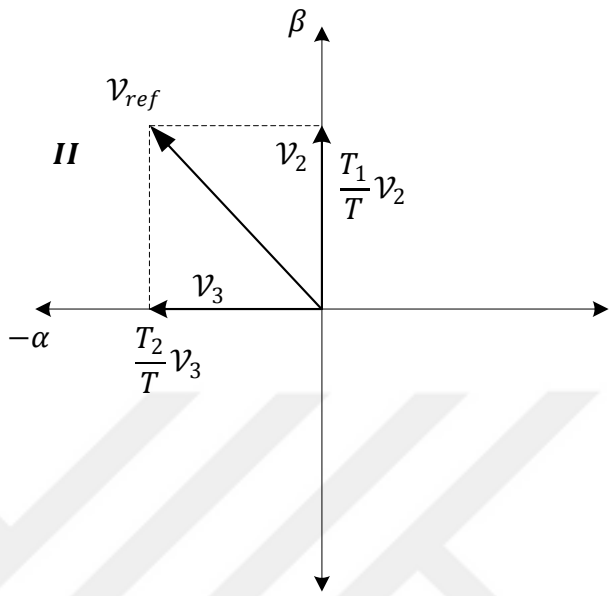

Figure III.5. Sector-II timing calculation diagram.

The rest of the period is spent by the zero vector in T_0. T_0 is the time duration in which the null vector is applied. The time durations for phase–b, phase–c, and zero vectors are calculated as follows

$$T_b = T - T_1 - \frac{T_0}{2} \tag{III.25}$$

$$T_c = T_b - T_2 \tag{III.26}$$

$$T_0 = T - T_1 - T_2. \tag{III.27}$$

The vector and timing calculations performed for sector-I are calculated for sector-II. The general formulations of the proposed sector determination method used in this calculation are shown in (III.28) – (III.34).

$$\mathcal{V}_{ref} = \frac{T_1}{T}\mathcal{V}_2 + \frac{T_2}{T}\mathcal{V}_3 \tag{III.28}$$

$$\mathcal{V}_{\alpha} = \frac{T_2}{T}\mathcal{V}_3\,(\cos 180\,^{\circ}) \tag{III.29}$$

$$T_2 = {-\sqrt{3}}/{2}\, T\mathcal{V}_\alpha = -XT \tag{III.30}$$

$$\mathcal{V}_\beta = \frac{T_1}{T}\mathcal{V}_2(\sin 90°) \tag{III.31}$$

$$T_1 = {T_0}/{2}\, \mathcal{V}_\beta = YT \tag{III.32}$$

$$T_b = T - {T_0}/{2} \tag{III.33}$$

$$T_c = T_b - T_1. \tag{III.34}$$

In a similar manner T_1 and T_2 can be calculated for the axes when $\mathcal{V}_{ref}$ is in other sectors (III and IV, respectively) as

$$T_b = T_c - T_1 \tag{III.35}$$

$$T_c = T - {T_0}/{2} \tag{III.36}$$

$$T_c = T - T_1 - {T_0}/{2} \tag{III.37}$$

$$T_b = T_c - T_2. \tag{III.38}$$

In the proposed simple method, on the other hand, the α– and β– axes voltage signals are already developed inside the controller without any expensive sensors like voltage sensors. Figure III.6 illustrates the sector determination using α– and β– axes voltage signals in the stationary reference frame where when $\mathcal{V}_\alpha > 0$ and $\mathcal{V}_\beta < 0$, Sector-I; when $\mathcal{V}_\alpha < 0$ and $\mathcal{V}_\beta > 0$, Sector-II; when $\mathcal{V}_\alpha < 0$ and $\mathcal{V}_\beta > 0$, Sector-III; and finally when $\mathcal{V}_\alpha < 0$ and $\mathcal{V}_\beta < 0$, Sector-IV is the location for the voltage space vector.

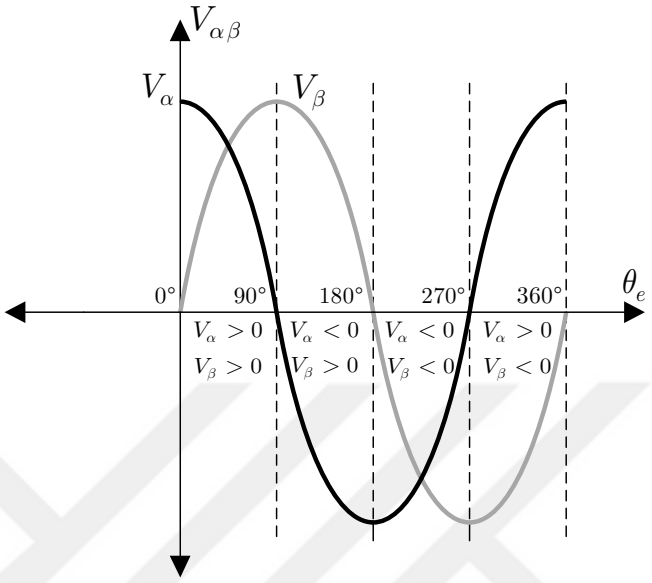

Figure III.6. Sector determination for FSTP inverter (phase–a is connected to the center tap).

The switching sequence is shown in Figure III.7 when phase–a is connected to the center tap, phase–b is connected to the middle leg and phase–c is connected to the remaining leg of the inverter. In that figure, grey sections represent the on states of the corresponding switches and the white colored sections are the off states. As it is seen in Figure III.7 that in each sector, the zero voltage vector effect is formed by using two short vectors $\mathcal{V}_1(0\ 0)$ and $\mathcal{V}_3(1\ 1)$ in equal amount $T_0/2$ because the long vectors create larger voltage drop on inductive loads and generates larger ripples.

Table III.1. Timing values for each sector

	Sector-I	Sector-II	Sector-III	Sector-IV
t_1	X	Y	$-X$	$-Y$
t_2	Y	$-X$	$-Y$	X

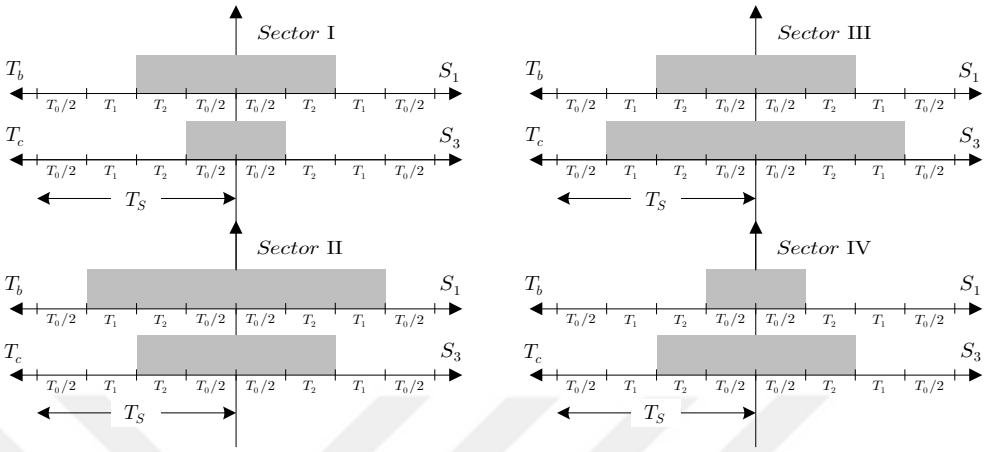

Figure III.7. Switching sequence for (a) Sector-I and -II, (b) Sector-III and -IV.

3.3. Simulation Results

The proposed drive system shown in Figure III.1 has been simulated in MATLAB/Simulink® using an electrical IGBT inverter and electrical PM motor model from the SimPower Systems toolbox in order to demonstrate the validity of the proposed speed sensored PM motor drive scheme.

To set the gating signals of the power switches from the output of the SVPWM module easily and represent the real conditions in simulation as close as possible, the proposed drive scheme including the electrical model of the actual PM motor and the inverter with power semiconductor switches considering the snubber circuit and the parameters of the switches are designed in MATLAB/Simulink® using the SimPower Systems block sets. The dead-time of the inverter and non-ideal effects of the PM synchronous machine are neglected in the simulation models. The DC-link voltage V_{dc} is set to 400 V.

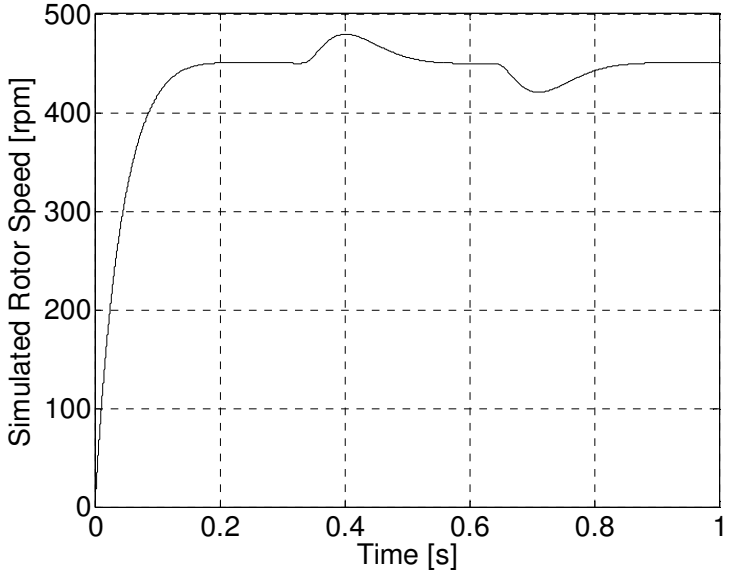

Figure III.8. Simulated speed response when full load rejection (2 N·m) is employed at t = 0.38 s under 450 r/min steady-state speed and full load injection (2 N·m) is employed at t = 0.63 s under 450 r/min steady-state speed.

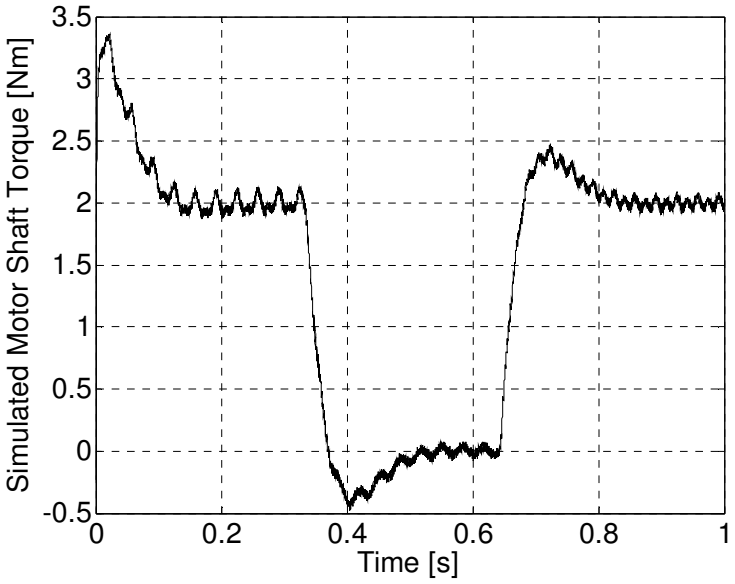

Figure III.9. Simulated torque response when full load rejection (2 N·m) is employed at t = 0.38 s under 450 r/min steady-state speed and full load injection (2 N·m) is employed at t = 0.63 s under 450 r/min steady-state speed.

The step speed reference of 0.5 p.u. (450 rpm) is applied to the PM motor under full load condition. A rated step load torque (2 N·m) is applied at t = 0.7 s, and at t = 0.35 s, the full load rejection is employed. The resultant estimated speed is provided in Figure III.8. The satisfactory transient speed start-up response is achieved with a reasonable overshoot and a settling time. The actual motor speed ramp time and amount of overshoot and its length can be changed by selecting the proper time constant in the speed PI regulator. The motor shaft torque when load rejection and load injection are applied is shown in Figure III.9. Phase–a, –b and –c are depicted in Figure III.10, Figure III.11, and Figure III.12, respectively.

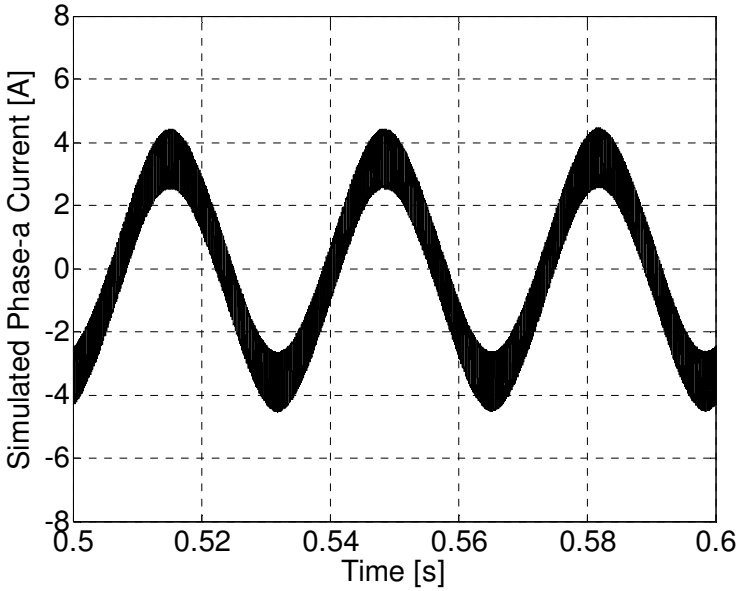

Figure III.10. Simulated steady-state (450 r/min) phase–a current waveform under full load (2 N·m).

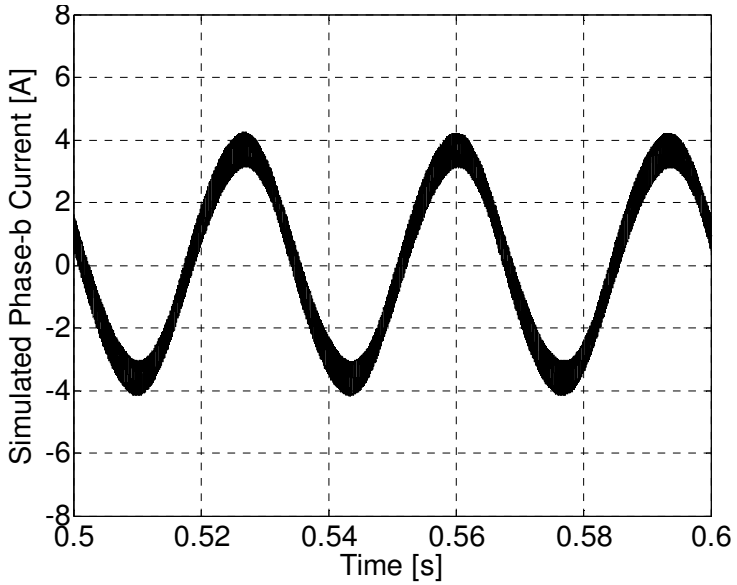

Figure III.11. Simulated steady-state (450 r/min) phase–b current waveform under full load (2 N·m).

In Figure III.10, the phase–a was connected to the center tap of two capacities. Current peak value of phase–a is higher when compared to phase–b and phase–c currents in Figure III.11 and Figure III.12. As expected, a harmonics current wave forms was obtained. The phase–a has a more harmonics than phase–b and phase–c. In Figure III.13, The current wave form of SSTP under the constant torque load was given. When Figure III.10 to Figure III.12 are compared, current peak value, THD analysis are observed.

The steady-state current peak value is 15% higher than the current waveform in Figure III.13 where SSTP PMSM drive circuit is used. These results in more losses than normal operation; however it can be seen from the simulation results given in Figure III.11 and Figure III.13 that the proposed FSTP method is able to drive the PM motor even under full load condition without any stability problem.

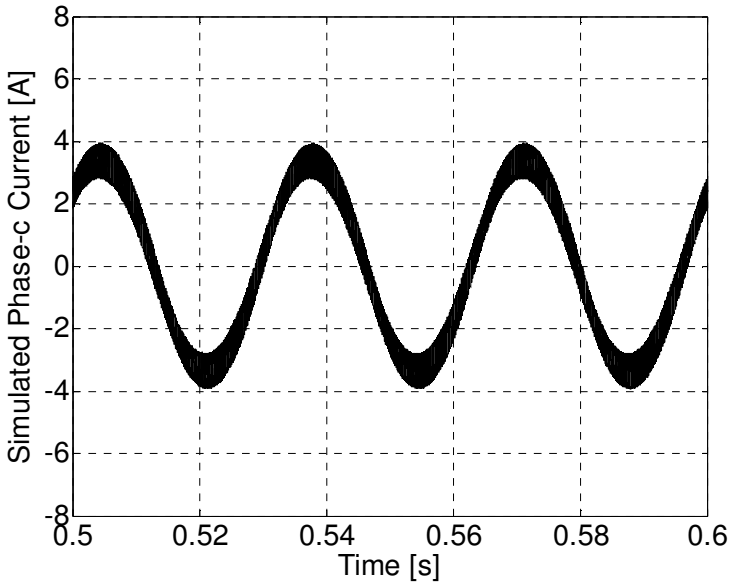

Figure III.12. Simulated steady-state (450 r/min) phase–*c* current waveform under full load (2 N·m).

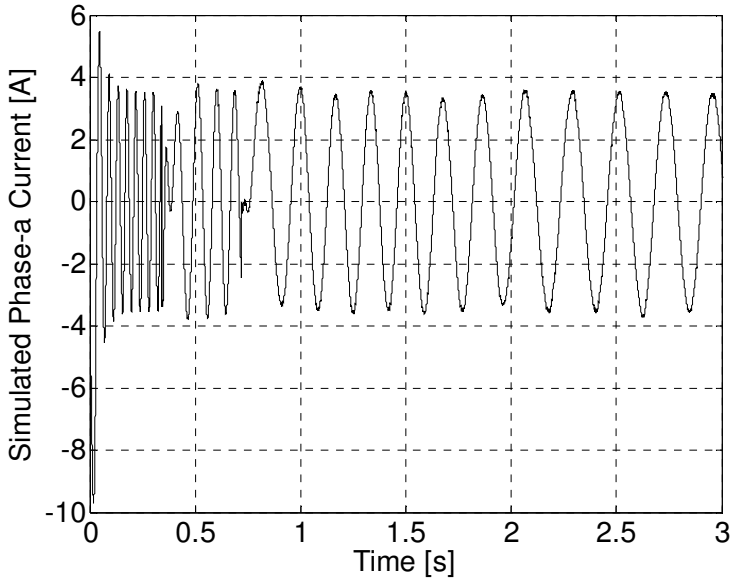

Figure III.13. Simulated steady-state (450 r/min) phase–*a* current waveform under full load (2 N·m) for SSTP inverter.

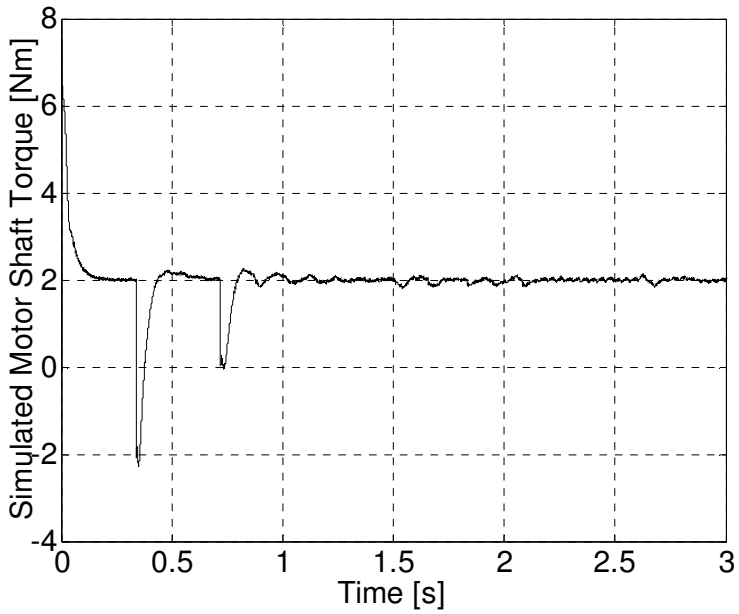

Figure III.14. Simulated torque response of the PMSM under 450 r/min steady-state speed for SSTP inverter.

3.4. Experimental Results

To evaluate the efficiency and to investigate the performance of the proposed method, some experiments are carried out following the sector determination method. Spectrum Digital eZdsp Evaluation Board was used to carry out the real-time algorithm. The parameters of the PMSM are presented in Appendix A. A three-phase IGBT inverter, supplied by a DC-link voltage of 400 V, fed the PMSM. The switching frequency is set to 10 kHz. The Magtrol dynamometer set contains 6 N·m hysteresis brake, a DSP6001 model programmable DSP torque controller, and a Magtrol™ TMS306 model torque transducer to monitor the load torque and shaft speed which is installed between hysteresis brake and the motor shown in Figure III.15.

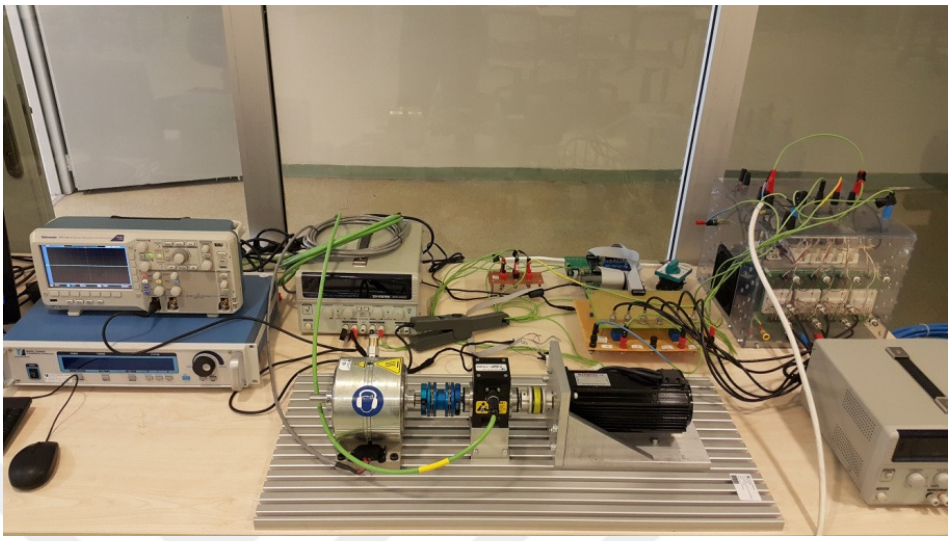

Figure III.15. Experimental test-bed. Dynamometer controller, inverter, DSP control unit, and interface and signal conditioning cards, PM synchronous motor with integrated incremental position encoder (2500 pulse/rev.) coupled to hysterisis brake through torque/speed transducer.

Figure III.16 shows experimental results obtained under similar conditions as in simulation which is provided in Figure III.8. In that figure, the speed response under full load start-up condition (2 N·m) is given with a step speed reference of 0.5 p.u. PMSM is controlled at 450 r/min with full load applied. As it can be seen in Figure III.16 that the proposed speed sensored method is able to drive the PM motor without any instability under full load start-up condition.

Figure III.17 shows experimental result for conventional SSTP PMSM drive under full load. Figure III.18 demonstrates the phase–a and phase–c current waveforms under rated full load at start-up.

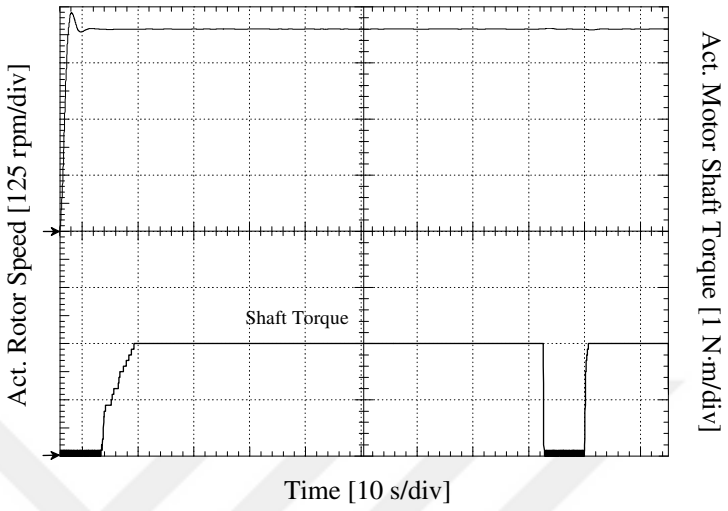

Figure III.16. Experimental speed and torque response when full load rejection and injection (2 N·m) is employed at t = 80 s and t = 88 s under 450 r/min steady-state speed.

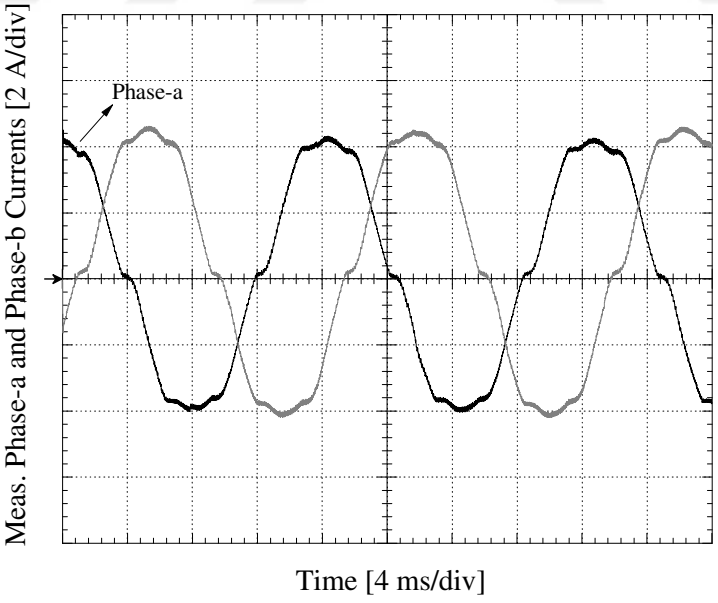

Figure III.17. Experimental steady-state (450 r/min) phase–a and –b current waveforms under full load (2 N·m) with SSTP.

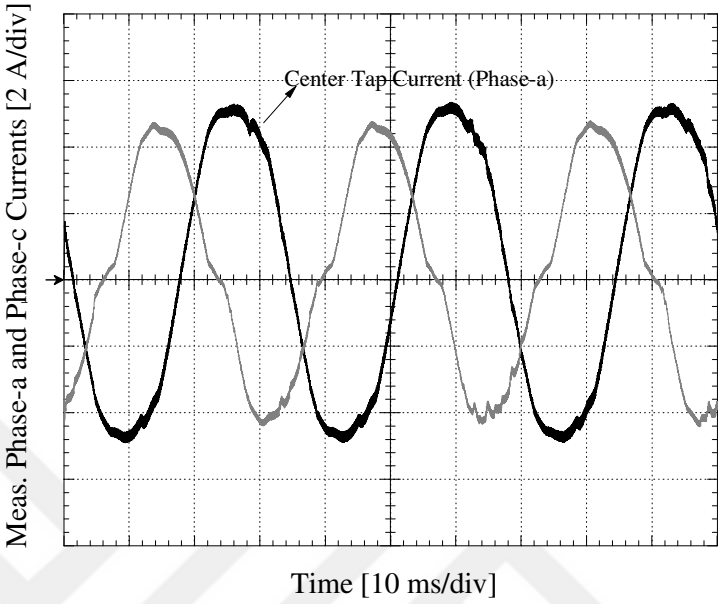

Figure III.18. Experimental steady-state (450 r/min) phase–a (center tap current) and –c current waveforms under full load (2 N·m) with FSTP.

To test the feasibility of the proposed topology based on FSTP, experiments are carried out with different torque and speed conditions. Phase current waveform of FSTP and SSTP obtained in the same conditions are showed in Figure III.17 and Figure III.18. Due to decreasing of voltage gain that is the most important disadvantages of FSTP, the current value increases to ensure the same power value. In Figure III.18, center tap of phase–a is the phase current linked to the center tap and its current value is higher than phase–c. It can be seen that it has a noisier waveform. Figure III.19 shows current waveform of phase–b and phase–c linked to switching components other than the phase linked to the center tap. Contrary to phase–a, stability was observed between phase–b and phase–c.

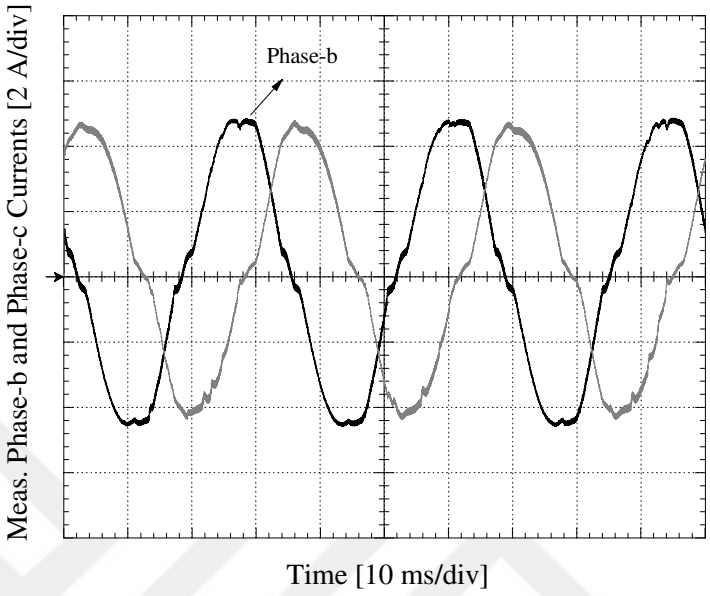

Figure III.19. Experimental steady-state (450 r/min) phase–b and –c current waveforms under full load (2 N·m) with FSTP.

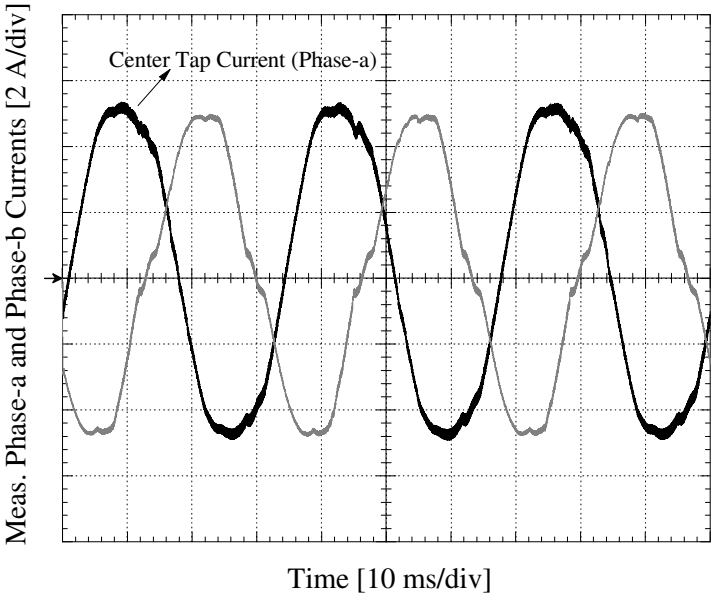

Figure III.20. Experimental steady-state (450 r/min) phase–a (center tap current) and –b current waveforms under full load (2 N·m) with FSTP.

Figure III.20 illustrates phase–b and phase–c current waveforms. Normally, DC voltage in FSTP should be $C_1 = C_2$ at ideal conditions, it becomes $C_1 \neq C_2$ during steady-state operation. Therefore, based on the measurement time, differences are observed between peak values of phase–b and –c currents. In Figure III.21 to Figure III.23, current waveforms of phase–a, phase–b and phase–c, respectively. Similarity is seen between measurements by power analyser results and oscilloscope waveforms. Results of instant measurements are given in Table III.2. Phase–a, phase–b and phase–c and RMS values are given.

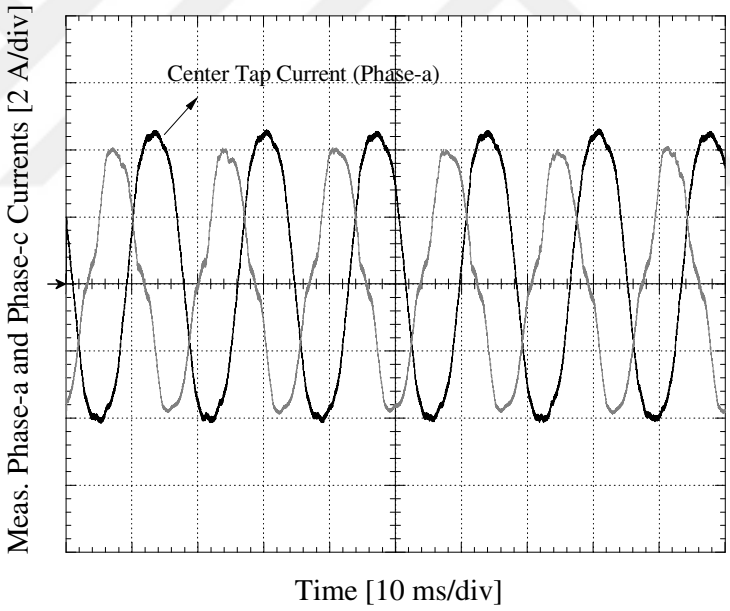

Figure III.21. Experimental steady-state (900 r/min) phase–a (center tap current) and –c current waveforms under full load (2 N·m) with FSTP.

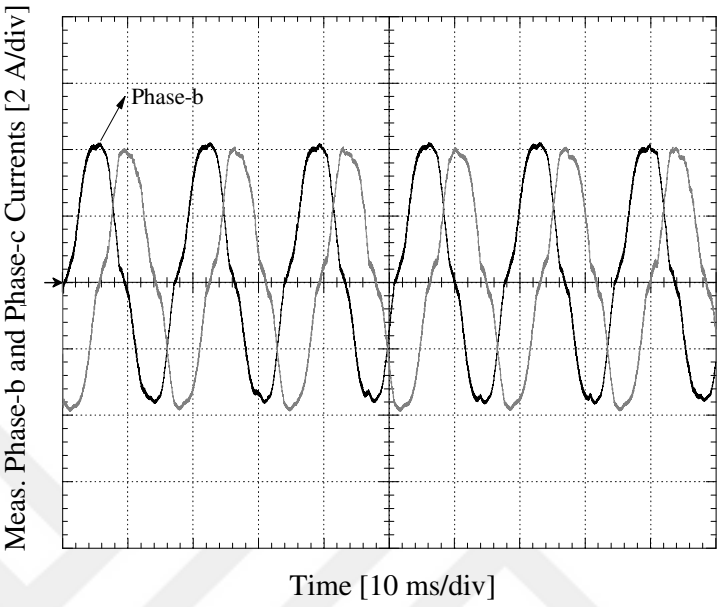

Figure III.22. Experimental steady-state (900 r/min) phase–b and –c current waveforms under full load (2 N·m) with FSTP.

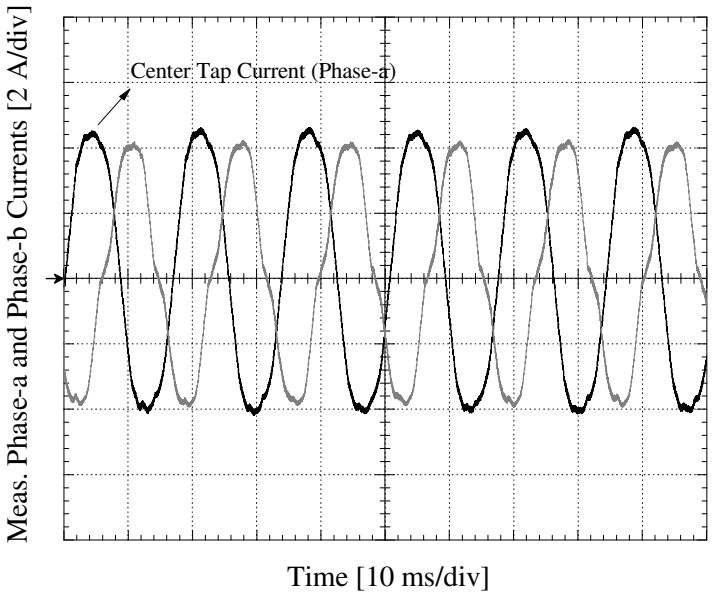

Figure III.23. Experimental steady-state (900 r/min) phase–a (center tap current) and –b current waveforms under full load (2 N·m) with FSTP.

Measurements in Table III.2 are for 450 r/min. Although an unbalanced situation is observed in current levels, any disadvantage was not detected for PMSM control other than decrease in power levels in the tests. In Table III.3, rated speed performance of PMSM was determined for FSTP at full load and 900 r/min speed conditions. Similar results were obtained with Table III.2.

Table III.2. PMSM power analyzer results for 0.5 p.u. speed reference

	Ref. Speed	Ref. Torque	Current	Voltage
Phase–a	0.5 p.u.	2 N·m	5.39 A	172 V
Phase–b	0.5 p.u.	2 N·m	4.97 A	98 V
Phase–c	0.5 p.u.	2 N·m	4.454 A	170 V
Phase–$\sum$	0.5 p.u.	2 N·m	4.9 A	171 V

Table III.3. PMSM power analyzer results for 1.0 p.u. speed reference

	Ref. Speed	Ref. Torque	Current	Voltage
Phase–a	1.0 p.u.	2 N·m	5.47 A	168 V
Phase–b	1.0 p.u.	2 N·m	4.95 A	119 V
Phase–c	1.0 p.u.	2 N·m	4.73 A	166 V
Phase–$\sum$	1.0 p.u.	2 N·m	5.09 A	167 V

3.5. Conclusion

Most important advantages obtained when conventional SSTP and FSTP test results are decrease in switching costs and switching losses, and faster response in control systems based on estimation algorithms. However, disadvantages are increase in current peak value, decrease in rated power and unbalanced phase current and phase

voltage. The most important advantage of the developed FSTP algorithm is easy adaptation to field oriented control and only changing the switching periods. While most of similar methods need rotor position knowledge in sectoral determination, the proposed SVPWM can determine the sector without position knowledge. Especially, FSTP control offered in sensorless control algorithms brings important advantages. In this study a novel sector determination method for FSTP is developed. Using proposed method, the whole system is implemented by TMS320F28335 for a PMSM and the effectiveness is verified through simulation and experimental results. The proposed system can be used in small powerful wind system as well as in structures such as small house appliances operating between similar small power ranges, drive system of white appliances and pump drive systems.

IV. LOW-COST SENSORLESS SPEED CONTROL OF PMSM DRIVE USING REDUCED SWITCH INVERTER BASED ON STATOR FEEDFORWARD VOLTAGE ESTIMATION

Permanent magnet synchronous motors (PMSMs) with sinusoidal shape back-EMF require precise position sensors such as an optical encoder and a resolver for field-oriented control (FOC). However, attaching these position sensors to the rotor is associated with cost, space, additional wiring, mechanical burden, weight, noise interference and reliability. Therefore, there is a motivation to eliminate position sensor from the PMSM drive and operate it as “sensorless” or “encoderless”. Although position sensor is eliminated for sensorless control, the rotor position must be obtained using only measured electrical quantities (such as motor currents, inverter DC-link voltage, voltage at the motor terminals, etc.). Therefore, current and/or voltage sensors are required to achieve a position sensorless PMSM drive scheme. There are different techniques for sensorless operation of permanent magnet synchronous motors and they are divided in two main groups: 1) back-EMF based estimation and 2) high/low frequency signal injection utilizing the magnetic saliency. The back-EMF based sensorless methods present good results in the middle and high-speed regions. Since the amplitude of back-EMF is proportional to the rotor speed, it fails in zero and low-speed regions. Because the latter does not require the back-EMF information, it provides reasonable speed and torque control capability at zero and low stator frequency, even under heavy load condition [118]–[128].

The main contribution of this chapter is to modify the dq–axes stator feedforward voltage estimation (FFVE) algorithms to achieve a simple, effective and low-cost position sensorless speed control scheme for PMSM drive using four-switch three-phase inverter (FSTP). To achieve this goal, the earlier work that have been developed for induction motor (IM), and PM motor which are driven by SSTP inverter in [63] and [72], respectively are extended for FSTP based sensorless PMSM drive. In [72], flux vector (FV) control, one of the pioneering methods to improve the performance of V/Hz drives, which is evolved from the first principles of FOC, is presented for IM as a sensorless speed control strategy with performance lies between V/Hz control and indirect field-oriented control (IFOC) [129]. Analysis of the effects of stator resistance variation on the performance of FV and field-oriented (FO) controllers of IM have been proposed in [129] where a BEMF (back electromagnetic force) detector is developed to reduce the adverse effect of stator resistance on both IFOC, FV and V/Hz control of IM drive with or without position sensors. The performance of the speed sensorless FV control of IM in [73] is attempted to be improved in [33] where stator resistance is adjusted based on the error between the reference d–axis current and its feedback component. It is indicated in [33] that the proposed method is best suited for low frequency operation [73]. In this study, it is demonstrated that the parameter sensitivity is tremendously reduced by properly selecting the highest possible gain of the d–axis current regulator output used in the q–axis stator feedforward voltage estimation equation without effecting the efficiency and proper operation of the speed sensorless FSTP based PMSM drive scheme even at considerable low to medium speed range. Moreover, it is also shown in this study that by proper connection of the PM motor terminals to the FSTP inverter legs, SVPWM for FSTP inverter is successfully achieved

by using a novel and simple sector determination method without requiring any position or voltage sensors. The proposed FSTP VSI based sensorless speed control method is applicable to both surface-mounted as well as interior type PM motors.

The remaining part of this chapter is organized as follows. Analysis of FSTP VSI including a novel and simple sector determination that does not need actual or estimated rotor position information is explained in Section 4.1. The principle of the stator feedforward voltage estimation (FFVE) based position sensorless speed control technique is presented in Section 4.1. In Section 4.2, the proposed drive system is modeled in MATLAB/Simulink by using MATLAB Functions with electrical components. Then, the simulation results are given and analyzed in detail. In Section 4.3, the hardware implementation and experimental results of the proposed FSTP based sensorless PM synchronous motor drive scheme including no-load start-up, steady-state load disturbance and effect of the parameter variations are presented and discussed. Finally, the conclusion is provided in Section 4.4.

4.1. Proposed Sensorless Speed Control of Four Switch Three-Phase PMSM Drive Based on Stator Feedforward Voltage Estimation

dq–axes feedforward stator voltages are normally used in the field-oriented control (FOC) of AC machines at the output stage of the inner dq–axes PI current regulators to enhanced the dynamic performance of the machine. In this work, feedforward voltages are not only used for the dynamic performance improvements, but also are utilized to achieve a simple and effective position sensorless speed control of FSTP based PMSM drive in which starting under no-load is possible without needing an open-loop start-up procedures.

It is visible that stator d– and q–axes currents can be controlled by the d– and q–axes voltages and speed ω_e from (II.1) and (II.2). The control principle is adopted where the current in q–axis is controlled by speed of rotation or frequency of stator voltage applied to q–axis winding. The amplitude of q–axis voltage is obtained by neglecting the derivative term and assuming that real currents closely follow the reference values $i_q = i_q^*$ and $i_d = i_d^*$ (reference values are marked with $*$ in the superscript). Below are the modified stator feedforward voltage equations for the proposed sensorless speed control of PMSM driven by FSTP inverter given in dq reference frame.

$$v_q^* = i_q^* R_s + \left(\omega_e L_d i_d^* + \omega_e \lambda_f\right) + K\Delta v \tag{IV.1}$$

$$v_d^* = i_d^* R_s - \omega_e L_q i_q^* + \Delta v \tag{IV.2}$$

where Δv is the output of the d–axis PI current regulator and ω_e is the output of the q–axis PI current regulator. Δv is multiplied by gain K and added to q–axis voltage equation such that $K\Delta v$ term given in (IV.1) represents the derivative term in the q–axis dynamic voltage equation which is given in (II.1). Similarly, Δv term in (IV.2) also acts as the derivative representation in d–axis voltage equation given in (II.2) for achieving better transient response in the sensorless operation.

The dq frame stator voltages given in (IV.1) and (IV.2) are obtained by modifying the dynamic machine model and used as the basic reference signals to control the PM machine without requiring a position sensor. The signals depend on machine parameters. The components of the dq frame voltage reference signals given in (IV.1) and (IV.2) are derived from (II.3) and (II.4), respectively under the assumption of steady-state conditions where derivative terms are replace with the regulator correction terms and a relevant gain. Overall stability of the proposed sensorless speed control of

PMSM scheme driven by FSTP inverter under multiple simultaneous parameter variations (R_s, L_s, and λ_f) is improved by proper selection of K gain in (IV.1). The selection criteria of K gain under heavy multiple parameter detuning in (IV.2) are investigated through the simulations and experiments in Section 4.2 and 4.3, respectively.

A complete block diagram representation for a field-oriented control of the proposed speed sensorless PMSM drive scheme based-on stator feedforward voltage estimation (FFVE) using four-switch space vector PWM (SVPWM) three-phase voltage-source inverter is illustrated in Figure IV.1. In (IV.1) and (IV.2), the d– and q–axes currents are replaced by their reference values. The resulting stator feedforward voltage estimation signals are represented in Figure IV.1. The voltages applied to the motor are calculated by (II.1) and (II.2). Note that estimation of rotor speed $\hat{\omega}_r$ is obtained by passing ω_e obtained from output of the q–axis PI current regulator through a first order low-pass filter resembling the closed-loop form of PLL, as shown in Figure IV.1. The time constant of the filter depends on the overall system mechanical characteristics and heavily affects the dynamics and stability of the sensorless speed control scheme.

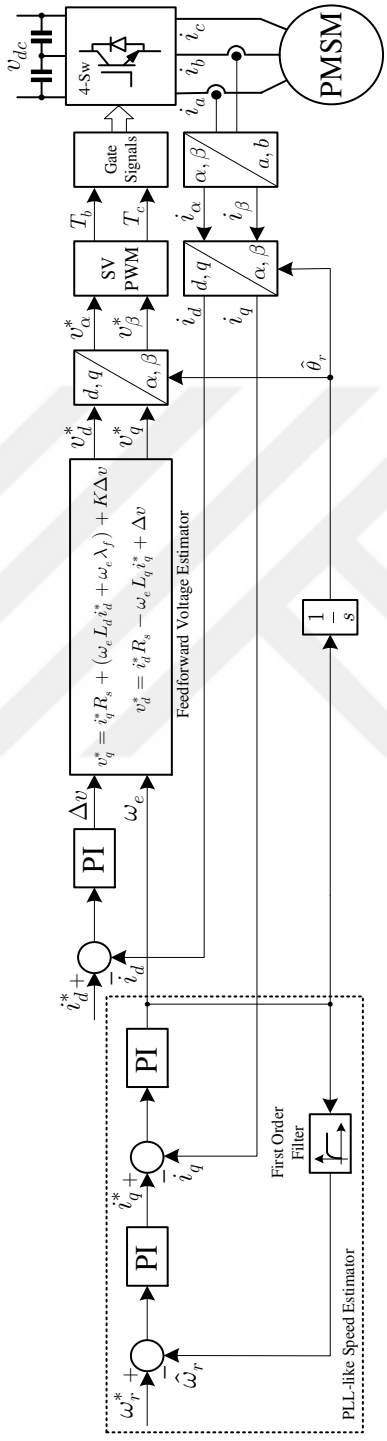

Figure IV.1. Overall block diagram of the proposed speed sensorless PMSM drive scheme using FSTP inverter.

4.2. Simulation Results

The proposed drive system shown in Figure IV.1 is simulated in MATLAB/Simulink® using an electrical two-leg IGBT inverter and electrical surface-mount PM synchronous motor model ($L_d = L_q = L_s$) from the SimPowerSystems™ toolbox in order to demonstrate the validity of the proposed speed sensorless FSTP based PMSM drive scheme.

C programming like codes written in MATLAB Programming language are developed for the simulation of the proposed FOC of PMSM drive in MATLAB/Simulink using MATLAB Function blocks without using expensive toolboxes such as Embedded Coder® [130].

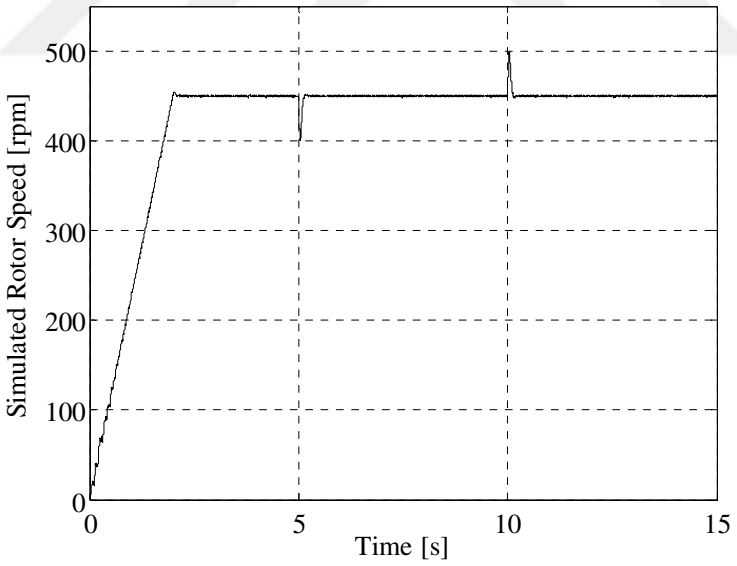

Figure IV.2. Simulated ramp speed response (referenced 0 to 450 r/min in 2 s) without parameter detuning when K = 1 (low) when full step load is applied at t = 5 s and load rejection is performed at t = 10 s (initially no-load).

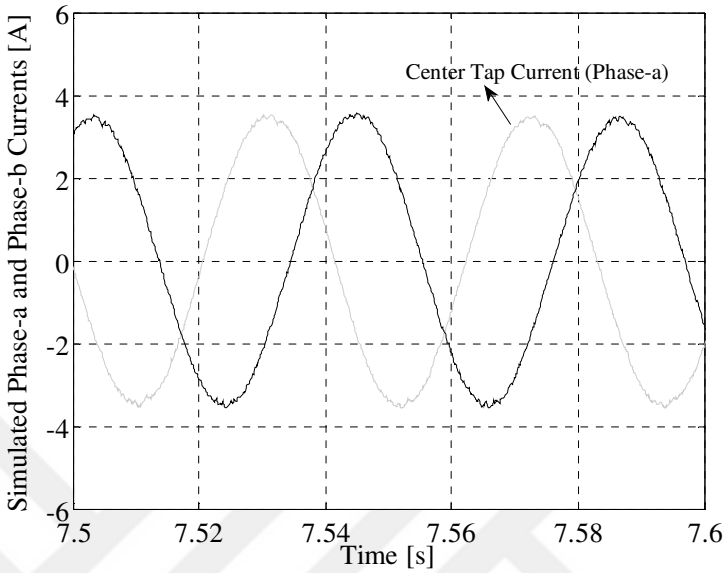

Figure IV.3. Simulated steady-state (360 r/min) phase–a and –b current waveforms under full load (2 N·m) without parameter detuning when K = 1 (low).

To set the gating signals of the power switches from the output of the SVPWM module easily and represent the real conditions in simulation as close as possible, the proposed drive scheme including the electrical model of the actual PM motor and the inverter with power semiconductor switches considering the snubber circuits along with the parameters of the switches are designed in MATLAB/Simulink using the SimPowerSystems blocksets. The dead-time of the inverter and non ideal effects of the PM synchronous machine are neglected in the simulation models. The DC-link voltage V_{dc} is set to 400 V.

Initial rotor position is set to zero. Since the proposed sensorless algorithm relies on the back-EMF based method, the full load starting is not possible. Therefore, the motor is ramped from zero to 450 r/min in 2 second under no-load condition. During the steady-state speed of 450 r/min, a rated step load torque (2 N·m) is applied at t = 5 s under no-load, and at t = 10 s, the full load rejection is employed. The resultant speed

is provided in Figure IV.2. The satisfactory transient and steady-state speed response are achieved with a reasonable low frequency oscillation. The performance of transient speed response at no-load startup and during steady-state load injection and rejection can be improved by selecting the proper K gain and time constants in the speed PI regulator and speed estimator filter. In Figure IV.3, the steady-state phase–a and phase–b current waveforms are presented at 360 r/min under full load without parameter detuning when $K = 1$. As it can be seen in Figure IV.2 and Figure IV.3 that the proposed speed sensorless method is able to drive the PM motor without any instability under full load injection and rejection assuming that there is no parameter variations in the PM motor when low K gain is selected as 1.

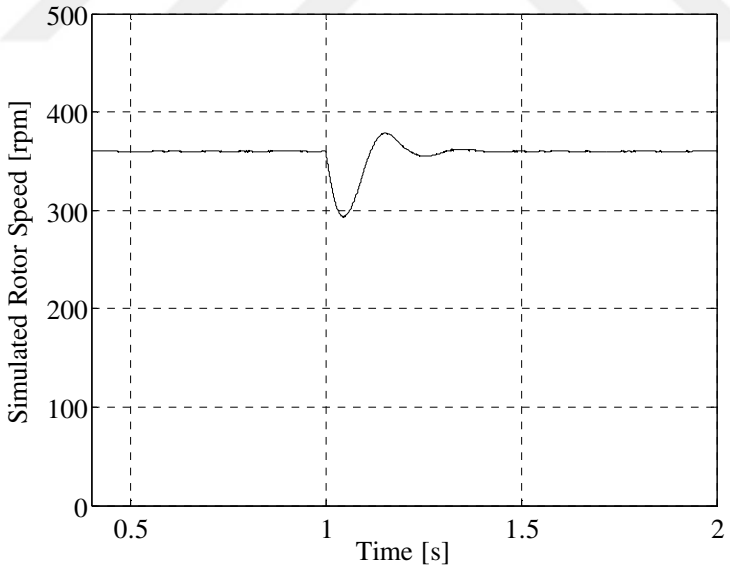

Figure IV.4. Simulated steady-state and transient speed response when full step load (2 N·m) is applied at t = 1 s under 360 r/min speed reference when R_s is increased by %82.35 (extra 2.8 Ω) and K = 5 (high).

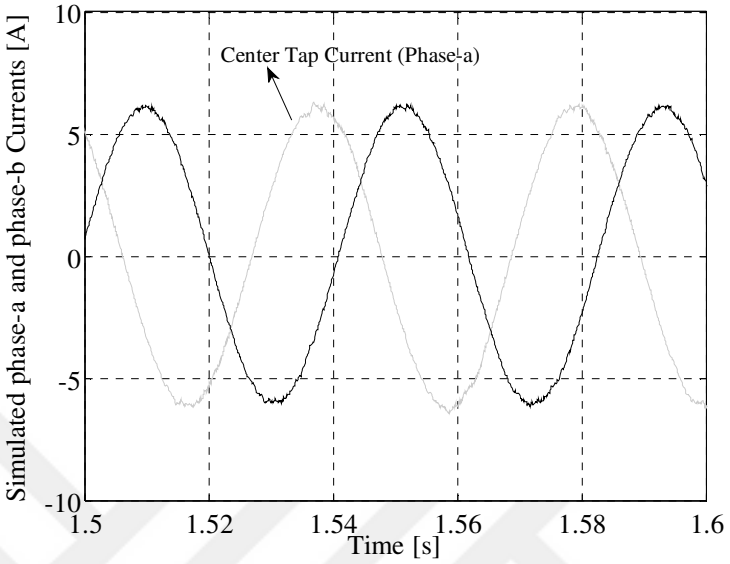

Figure IV.5. Simulated steady-state (360 r/min) phase–a and –b current waveforms under full load (2 N·m) when R_s is increased by 82.35% (extra 2.8 Ω) and λ_f is decreased by 40% with K = 5 (high).

The effects of stator resistance, R_s, and rotor flux linkage, λ_f, variations on the overall performance of the proposed drive are also investigated in simulations. The simulations are performed at 360 r/min without implementing any parameter adaptation method. Additional 2.8 Ω resistors are added to each phase between the frequency converter and the PMSM resulting 82.35% increase in R_s. The resistance is changed stepwise by opening or closing a manually operated three-phase switch connected in parallel with the resistors. The flux linkage λ_f value is decreased by 40% from the original value in the electrical motor model.

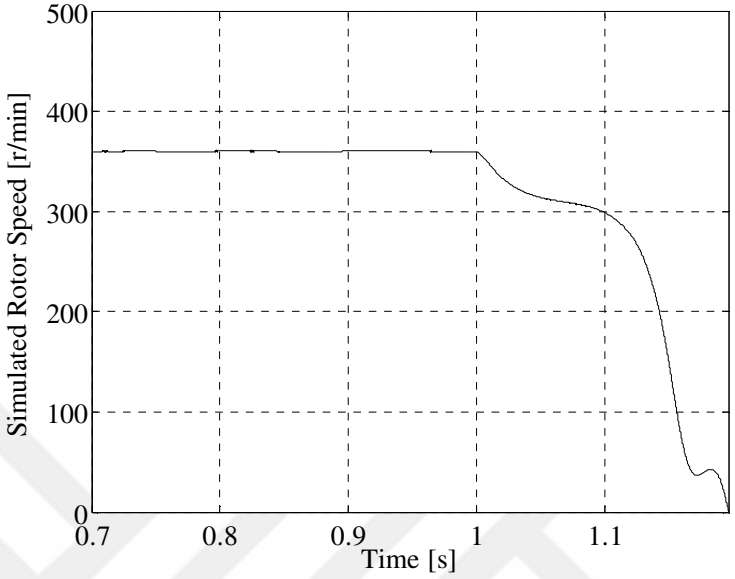

Figure IV.6. Simulated speed response under full load (2 N·m) when R_s is increased by 82.35% (extra 2.8 Ω) stepwise at t = 1 with K = 1 (low) and 360 r/min speed reference.

It is observed from the simulations that selecting a proper high K gain (between 4 to 7) in (IV.1) maintains the sensorless scheme stable even if the parameters of the machine (R_s is 82.35% higher and λ_f is 40% lower) change greatly at the same time under low to medium speed range. First, the step rated load (2 N·m) is applied when the stator resistance R_s value is increased by 82.35% higher than the rated value at t = 1 s using external resistance at the steady-state speed of 360 r/min under full load (2 N·m). Figure IV.4 represents the speed performance of the proposed sensorless method in this condition. Next, in addition to R_s detuning, PM rotor flux linkage $\lambda_f$value is decreased by 40% at 360 r/min steady-state speed. The steady-state phase–a and –b axes current waveforms under this condition are depicted in Figure IV.5 where the peak phase– a current value is 78% higher than the one in Figure IV.3 at which there is no parameter variation exists in the machine. These results in more losses than normal

operation, however it can be seen from the simulation results given in Figure IV.5 that the proposed speed sensorless method is able to drive the PM motor even under multiple simultaneous high parameter variations without any stability problem.

If the PM rotor flux linkage λ_f is estimated using observer like methods without estimating the remaining parameters (R_s and L_s) almost simultaneously, the correct PM rotor flux linkage λ_f value cannot be obtained when these remaining parameters vary greatly. It is shown in the previous work that L_s is not affected by the variation of PM rotor flux linkage [65], [131]. However, it is also previously reported in [65] and [131] that R_s is highly sensitive to PM rotor flux linkage λ_f variations and vice versa. It is observed in the simulations that when a classical full-order observer is used to estimate the PM rotor flux linkage λ_f when R_s is changed 82.35% higher than its rated value, then the PM rotor flux linkage is estimated 68% higher than the actual value in the proposed sensorless speed control scheme. Even though the correct PM rotor flux linkage estimation can be achieved in the drive scheme when R_s is increased 82.35% higher than its actual value and λ_f is decreased 40% lower than its original value at the same time, the peak motor phase current increases 90% more than the expected full loaded value under multiple parameter variations. Although observing the changed values correctly allows stable sensorless speed control, it does not help obtaining a high efficient machine. Because the machine inherently draws more current when the parameters are highly detuned. Figure IV.6 shows that when stator resistance R_s is increased stepwise 82.35% more than its actual value at t = 1 with low K gain as 1, then the speed control becomes unstable.

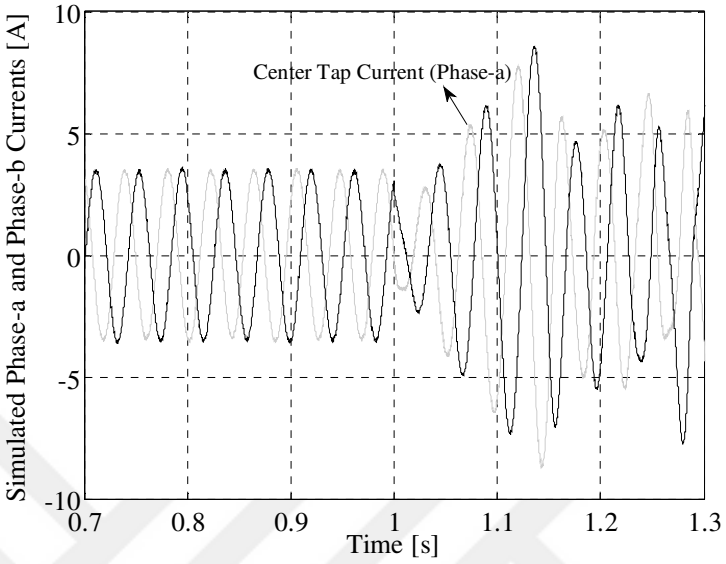

Figure IV.7. Simulated phase–a and –b current waveforms under full load (2 N·m) when R_s is increased by 82.35% (extra 2.8 Ω) stepwise at t = 1 with K = 1 (low) and 360 r/min speed reference.

The rotor speed suddenly decreases when R_s change is taken place and large fluctuations in phase–a and –b axes current waveforms are observed, as illustrated in Figure IV.7.

The importance of K gain in (IV.1) is observed at low and medium speed range. When K is selected low such as between 1 to 3, the low to medium speed sensorless method fails under heavy parameter detuning, however if it is high enough such as between 3 to 7, stability of the sensorless speed control scheme is maintained even under heavy multiple simultaneous parameter detuned condition at low to medium speed range. The value of K under parameter variation depends on the size of the PM motor, speed, DC-link value, amount of the parameter variations, nonlinearities of the overall system, and etc.

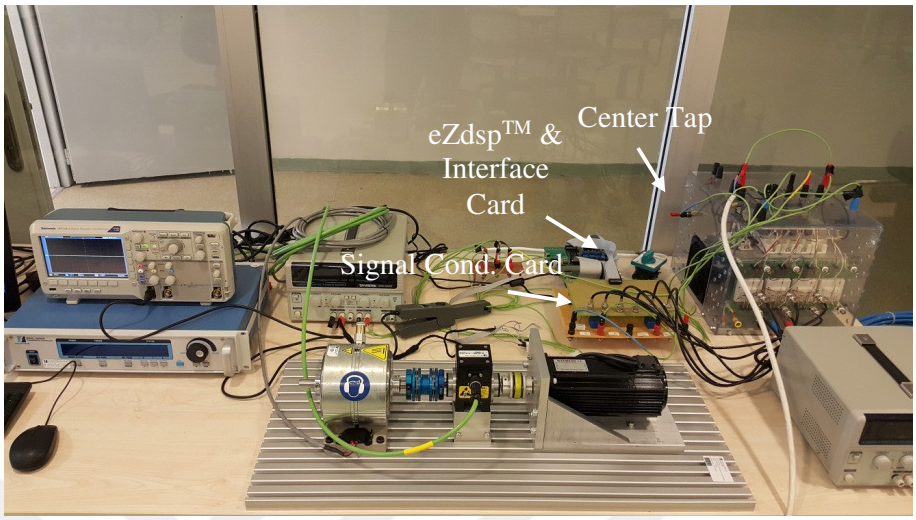

Figure IV.8. Experimental test-bed. (top) Dynamometer controller, inverter, DSP control unit, and interface and signal-conditioning cards, (bottom) PM synchronous motor with integrated incremental position encoder (2500 pulse/rev.) coupled to hysteresis brake through torque/speed transducer.

4.3. Experimental Verification

The feasibility and practical features of the proposed position sensorless speed control scheme of a four-switch three-phase (FSTP) PMSM drive with sinusoidal back-EMF have been evaluated using an experimental test-bed, shown in Figure IV.8. The same conditions are applied as in simulation. The proposed control algorithm is digitally implemented using the eZdsp™ board from Spectrum Digital, Inc. based on a floating-point TMS320F28335 DSP, as shown in Figure IV.8 (top).

4.3.1. Experimental setup

The experimental set-up consists of a Magtrol AHB-6 model hysteresis dynamometer set, a SEMIKRON Semiteach inverter, a PM Synhronous motor, a eZdsp™ board with TMS320F28335 DSP chip, and an interface and a signal conditioning cards.

The Magtrol dynamometer set contains 6 N·m hysteresis brake, a DSP6001 model programmable DSP torque controller, and a Magtrol TMS306 model torque transducer to monitor the load torque and shaft speed which is installed between hysteresis brake and the motor.

The signal conditioning card which comprises two LEM LA25NP model current sensors which read two motor phase currents and convert the analog current values into equivalent low-voltage values.

Interface card that is connected to the signal conditioning card scales the voltage values into proper positive representations for the DSP to sensitize.

The SEMIKRON Semiteach PWM VSI which comprises SKM 50 GB 123D model IGBT modules, SKHI 22 model gate drivers with 4.3 μs dead-time, and two 2200 μF caps. The inverter has a maximum DC-link voltage of 750 V and RMS current of 30 A.

In addition, an optical incremental encoder integrated to the PM servo motor with 2500 ppr resolution is used to detect the actual position/speed for evaluating the estimator.

The proposed sensorless control scheme is verified using an off the shelf 2 N·m surface-mounted PMSM drive which is coupled to the overall system, as shown in Figure IV.8 (bottom). The parameters and specifications of the PMSM are provided in Appendix A.

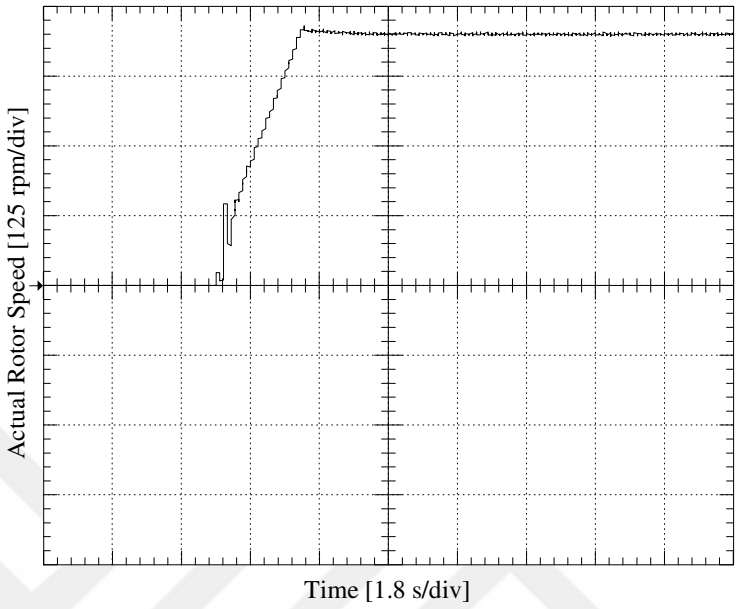

Figure IV.9. Experimental no-load ramp speed response (referenced 0 to 450 r/min in 2 s) without parameter detuning when K = 1 (low).

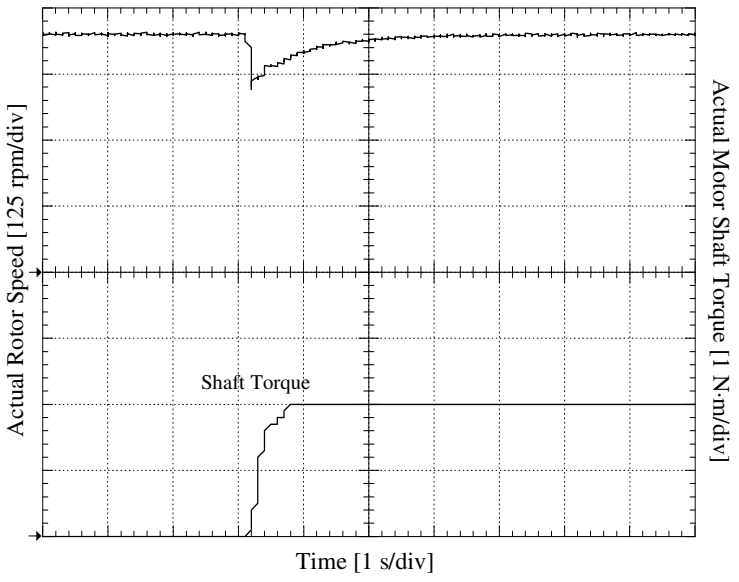

Figure IV.10. Experimental speed response when full load (2 N·m) is applied at t = 3 s under 450 r/min steady-state speed when K = 1 (low).

4.3.2. Experimental results

Similar to the simulations, in the experiments, digital proportional-integral (PI) controllers are used in the speed and current loops. The coefficients of the PI speed and current controllers are obtained using symmetrical and technical optimum methods.

The experimental result given in Figure IV.9 corresponds to the one in simulation shown in Figure IV.2 in which the motor is ramped from 0 to 450 r/min in 2 s. Due to mechanical possible slippage in the motor coupling; the rotor speed has oscillatory behavior during transient stage, as seen in Figure IV.9. The rotor speed data are obtained by M-TEST 5.0 Motor Testing Software of Magtrol dynamometer at 0.1 s sample rate. High frequency ripples observed in the measured speed data is due to this low sampling rate of the dynamometer data logging system. However, there is no instability is observed in the experimental no-load start-up using the proposed sensorless scheme, as shown in Figure IV.9.

During the steady-state speed of 450 r/min, a rated step load torque (2 N·m) is applied at t = 3 s. The resultant speed and shaft torque are provided in Figure IV.10. Figure IV.11 shows the speed result and shaft torque when full step load rejection is employed at t = 1 s. The satisfactory transient speed response is achieved under full load injection and rejection with a reasonable low frequency oscillation with low K gain of 1. In Figure IV.12, the experimental steady-state phase–a and –b current waveforms are presented under full load without parameter detuning. In the oscilloscope data, 6 kHz noise filter is used to reduce the high frequency ripples in the currents. The results are comparable with simulation given in Figure IV.3.

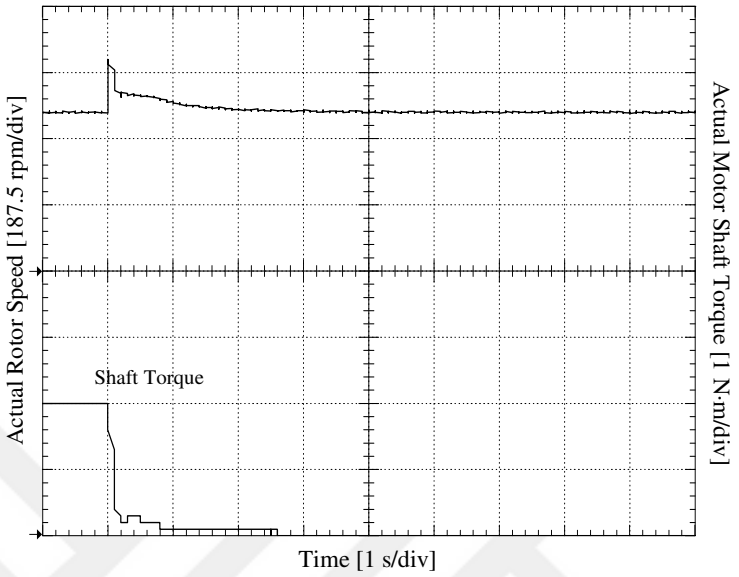

Figure IV.11. Experimental speed response when full load rejection (2 N·m) is employed at t = 1 s under 450 r/min steady-state speed when K = 1 (low).

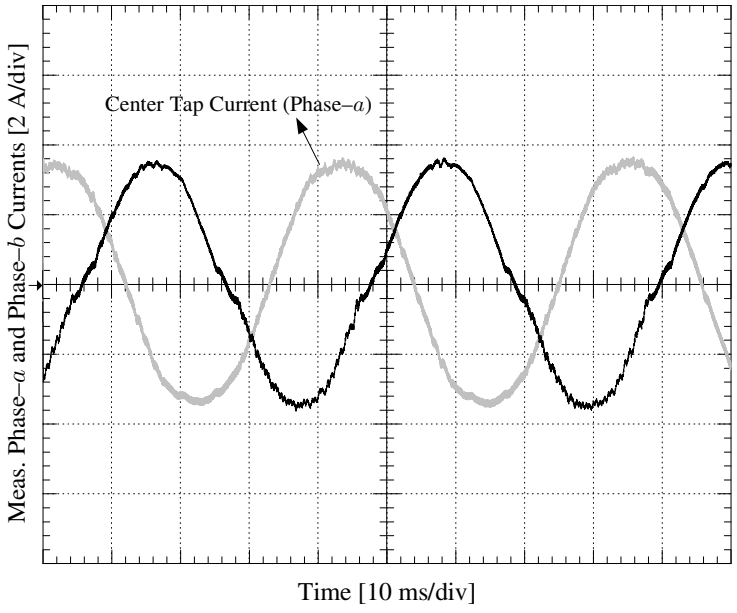

Figure IV.12. Experimental steady-state (360 r/min) phase–a and –b current waveforms under full load (2 N·m) without parameter detuning when K = 1 (low).

In experiment, the switching update is performed at 10 kHz rate as in simulation. However, the microcontroller runs the algorithms in 150 MHz clock frequency and the PWM update is executed at every 10 kHz independent of the algorithm sampling as oppose to the simulation. These results in high frequency ripples in the actual current waveforms in experiments compared to the ones obtained in simulations.

Also, because of slight misalignment and concentrated windings of the motor, phase currents show some harmonic signatures, as seen in Figure IV.12. Moreover, because the dead-time effect is not compensated, the phase current waveform exhibits some additional distortion especially at zero crossings and at around positive and negative peaks.

Figure IV.11 shows the speed response when sudden rated load injection is applied at t = 3.5 s under steady-state speed of 360 r/min with high K gain of 5. In this condition, the machine has 82.35% higher R_s than its original value. There is no instability in the speed is observed. The machine is run with external resistance under heavy load for certain time until the PM rotor flux-linkage λ_f amplitude decreases 40% less than its actual value. Because changing λ_f directly in the actual machine is a difficult task, therefore the motor is heated up with external resistance under heavy load first to achieve 82.35% higher R_s and 40% less λ_f, then the back-EMF constant and the final R_s are measured afterwards. The resultant phase–a and –b axes current waveforms when both R_s and PM rotor flux linkage λ_f values are detuned provided in Figure IV.14. Although 90% higher currents are drawn by the motor, the speed is stable.

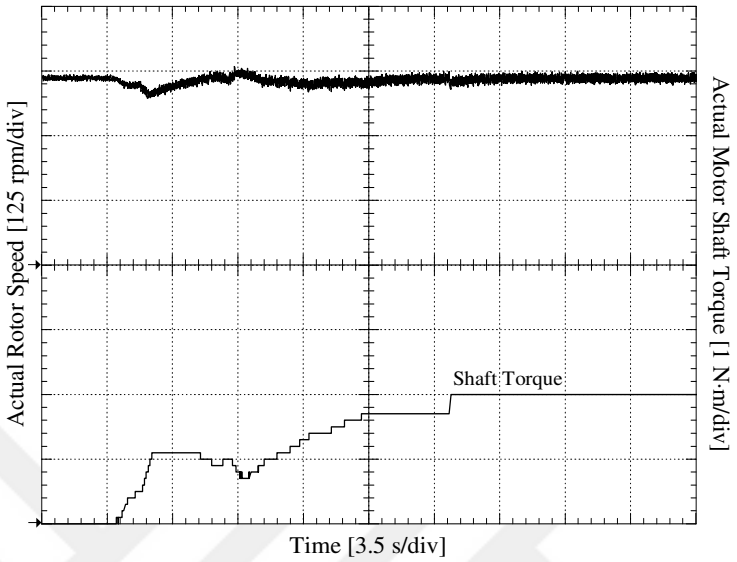

Figure IV.13. Experimental speed response when full step load (2 N·m) is applied at t = 3.5 s under 360 r/min speed reference when R_s is increased by 82.35% (extra 2.8 Ω) and K = 5 (high) (3.5 s/div).

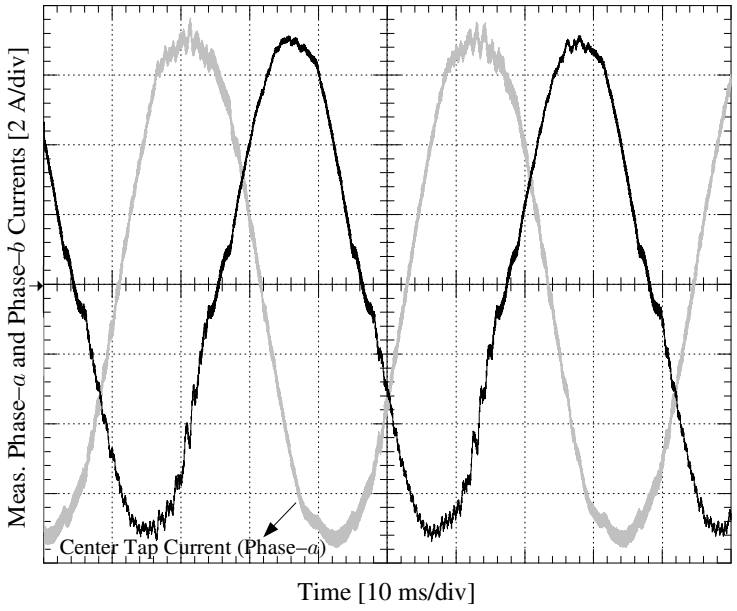

Figure IV.14. Experimental steady-state (360 r/min) phase–a and –b current waveforms under full load (2 N·m) with R_s increased by 82.35% and λ_f is decreased by 40% with K = 5 (high).

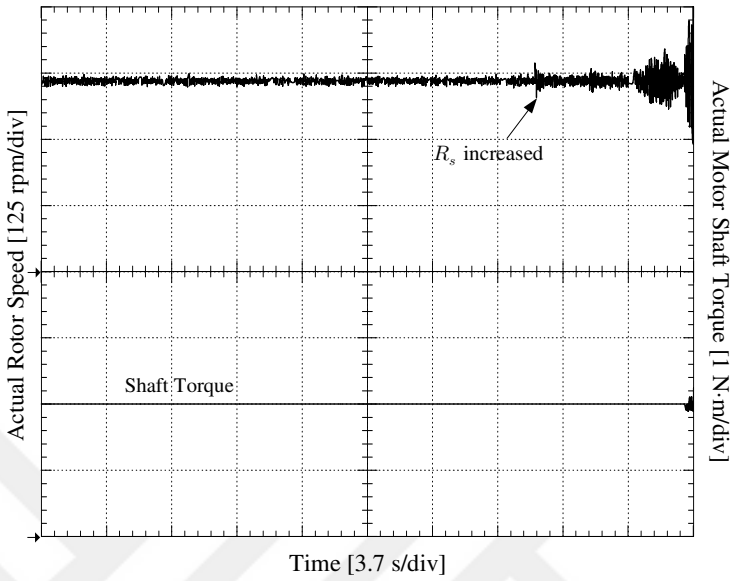

Figure IV.15. Experimental speed response under full load (2 N·m) with the steady-state 360 r/min speed reference when R_s is increased by 82.35% (extra 2.8 Ω) at t = 28 s with K = 1 (low).

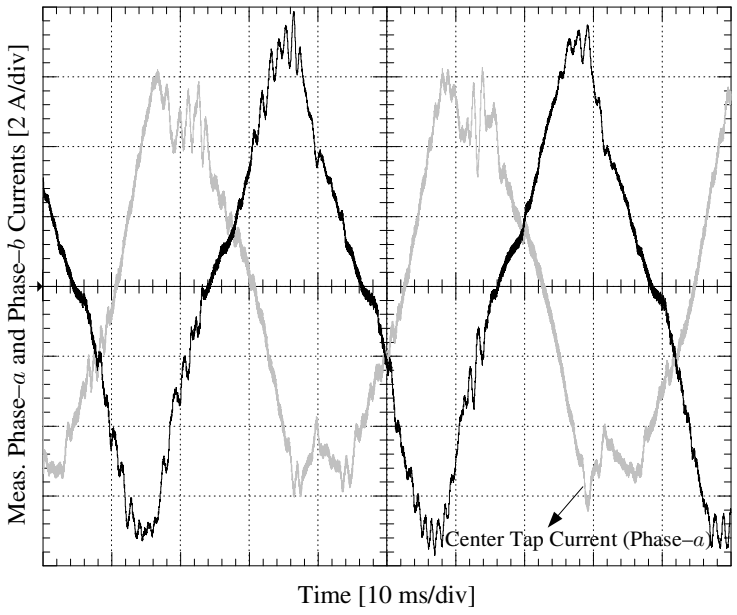

Figure IV.16. Experimental steady-state (360 r/min) phase–a and –b current waveforms under full load (2 N·m) with R_s is detuned by 82.35% (extra 2.8 Ω) with K = 1 (low).

Figure IV.15 illustrates the effect of sudden R_s increase under low K gain of 1 at t = 28 s. It is seen that when increase in step R_s is applied under full load, instability in speed is observed which is shown in Figure IV.15. The corresponding phase–a and –b axes currents after the switch is made are provided in Figure IV.16. It is shown in Figure IV.16 that the phase currents are distorted.

The differences observed in the transient responses between simulations and experiments are because of the nonlinearities of the actual machine and inverter along with mismatch of moment of inertia, damping and friction of the overall system compared to the one used in simulations.

4.4. Conclusion

In this chapter, a position sensorless speed control method based on stator feedforward dq–axes voltage estimation (FFVE) has been proposed for low-cost FSTP PMSM drive. Comparing to the traditional sensorless methods, the proposed method is simpler, effective, and leads to a lower implementation processing time. Moreover, with the proposed method the FSTP driven PMSM can start-up from zero speed under no-load without requiring any additional open-loop start-up procedures.

It is shown in the simulations and experiments that selecting a possible high *K* gain in the stator FFVE algorithm enhances the stability of the overall drive even under heavy multiple simultaneous parameter variations, making the overall sensorless speed control scheme quite insensitive to multiple parameter variations. It is also demonstrated in this study that a simple sector determination without the need of any sensors is possible using internally already available digital signals for SVPWM of FSTP inverter.

V. STATOR FEEDFORWARD VOLTAGE ESTIMATION BASED SENSORLESS PERMANENT MAGNET SYNCHRONOUS GENERATOR DRIVE USING MULTI-PARAMETER ESTIMATION BASED ON MRAS

The difference between fossil energy sources and demanded energy needs is rapidly increasing. This increase leads to alternative search and solutions in energy production. With the integration of smart grid to energy production at the macro level, individual energy production is supported by companies and governments [132]. Utilization of the wind turbines in small energy production is increasing rapidly. In US, the small wind turbine market shares in 2014 reached $60 million. In England, energy capacity of wind turbines ranging between 0 and 1.5 kW is recorded as 1.84 MW in 2013. In small wind turbines, Permanent Magnet Synchronous Generator (PMSG) is preferred for high performance, high power density, reliability, and high efficiency. The outer rotor and the inner rotor PMS generators that have axial flow direction are used in various industries with wide power ranges as direct-drive [133]. In small PMSG systems that generate less than or equal 10 kW power, there is no need for gearbox and the connection can be made directly to the turbine [133]–[141]. This is an important factor lowering the cost in small wind turbine systems [139]–[141]. PMSG is suitable for wind power generation allowing maximum power generation in a wide speed range and at different wind speeds [142]. Efficient wind turbine system can be constructed by adjusting the speed of the generator shaft optimally for variable wind speeds at maximum power operating point [143]. In variable-speed PMSG control, it is required

to know the rotor position information and wind speed [144]. Because the working conditions of the turbine changes so often, speed and torque change reduce the control performance. Moreover, in order to ensure power generation at wide speed range, sensitive and high resolution position control is performed by encoder, resolver or hall sensors. On the other hand, sensorless PMSG control can be accomplished without using position sensors [141]. In the control of PMSGs, with the elimination of the position sensor, cost, maintenance and robustness problems of the overall system are reduced [139]–[141]. Because no initial position problem and operating at flux-weakening region exist, sensorless control is a significant cost reductive solution for the control of PMSG drives. Determining the wind speed and rotor position can be accomplished with the methods which are Direct Torque Control (DTC), Model Reference Adaptive System (MRAS), and Sliding Mode Observer (SMO) depending on back-EMF prediction [67], [139], [145]–[148]. Because these methods are often affected by parameter variation and cause loss of stability at low speeds, they have severe disadvantages in sensorless PMSG control [26], [48], [149]. Moreover, because of complex calculation and the difficulty of adjusting control parameters, the methods like EKF, FL and ANN are not preferred in industrial applications [46], [53], [140], [150]–[152], [175]. Since the amplitude of the back-EMF is poor and fluctuates at low generator operating speeds in sensorless control algorithms that are based on back-EMF estimation, it is difficult to predict the rotor position [153]. Thus, stability of the entire system can be increased and efficient and stable power generation can be achieved at lower speeds. In order to provide parameter adaptation in sensorless control methods, rotor flux linkage estimation and stator resistance adaptation are performed with MRAS, observer based methods, and genetic algorithms [153]–[157].

In this study, in order to obtain the position and speed information of the driven PMSG directly, feedforward voltage estimation method is suggested. With the proposed method even in the situations where the wind speed is low, it is ensured that a superior PMSG control performance compared to other sensorless control methods based on back-EMF prediction is achieved. Because the rotor flux and the stator resistance undergo a change due to the effects of the loss of magnetic properties of magnets and temperature rise, a highly efficient control is ensured by estimating the rotor flux linkage and stator resistance using MRAS observer [23], [155], [158]. In this study, in order to get the maximum efficiency from PMSG, MPPT curve of the wind turbine is obtained in the real system. Active power reference that is required for power control is obtained from this curve after predicting the generator speed. Compared to other position sensorless control algorithms in which the majority of the methods require rotor position estimation first and then the speed is obtained by derivation of the position, in the proposed method primarily the speed is estimated, the position is then estimated with the help of a simple integration and first degree low pass filter without using any derivative term.

This chapter is organized as follows. The principle of PMSG modelling and MPPT studies are presented Section 5.1. In Section 5.1, the dynamic and steady-state models of surface mounted permanent magnet synchronous generator (SMPMSG) are explained in detail. In Section 5.1.1, wind turbine characteristics and MPPT algorithm based on indirect speed control are explained. In Section 5.1, the proposed stator feedforward voltage control using MRAS parameter estimation sensorless speed control strategy. Moreover the proposed control methods are designed and described in detail. In Section 5.1, electrical simulation model in MATLAB/Simulink is designed

and developed. The simulation results are given and analyzed in detail. In Section 5.2, the proposed speed sensorless control scheme based on MRAS has been implemented with 1 kW PMSG drive controlled by a TMS320F28335. The hardware implementation and experimental results of the proposed sensorless PM synchronous generator drive including steady-state load disturbance are presented and discussed. Simulation and experimental results demonstrate the feasibility and effectiveness of the proposed stator feedforward voltage estimation (FFVE) based position sensorless control scheme improved by MRAS multi-parameter estimation for permanent magnet synchronous generator under various load condition.

5.1. PMSG Modeling and MPPT Studies

The dq model in the rotating synchronous reference frame is used to analyze the PMSG for the proposed speed and position estimations, as shown in Figure V.1 in which the direction of the dq–axes currents are depicted out of the circuit as opposite to PMSG. The stator voltage equations of the PMSG in the rotating dq reference frame are given by (II.1) and (II.2), omitting the influences of magnetic field saturation and magnetic hysteresis as

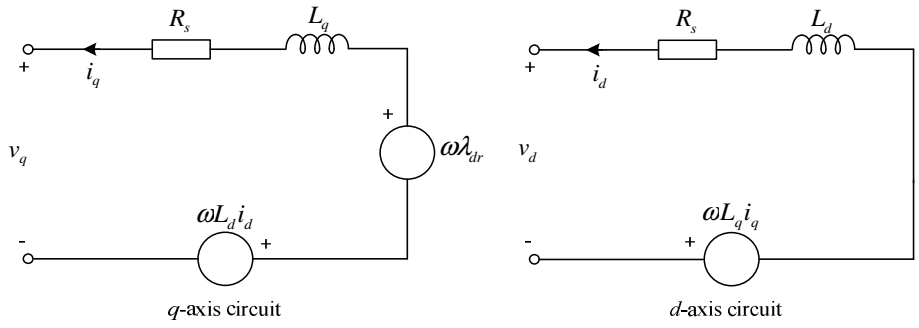

Figure V.1. Equivalent electrical circuit diagrams of quadrate q– and d–axes synchronous reference frame of PMSG.

5.1.1. Wind turbine characteristics and MPPT algorithm based on indirect speed control

The energy produced in wind turbine systems is not only based on the turbine characteristics, but also based on the control method. Output mechanical power of wind turbine is shown as

$$P_{tur} = P_{wind} C_p = \frac{1}{2} \rho \pi r^2 v_w^3 C_p(\lambda, \beta). \tag{V.1}$$

where ρ is the air density, r is the radius of wind turbine rotor plane, πr^2 is the area swept by the blades, v_w is the wind speed, C_p is the turbine power coefficient, λ is the tip-speed ratio, and β is the pitch angle. In small wind turbines, fixed pitch angle is used because of cost and restrictions. Thus, in (V.1), β = 0 is assumed. The aerodynamic model of a wind turbine can be characterized by the well-known $C_p(\lambda, \beta)$ curves. λ is defined by

$$\lambda = \frac{Tip\ Speed}{Wind\ Speed} = \frac{\omega_e r}{v_w}. \tag{V.2}$$

Considering the relationship between λ and C_p as the speed changes for a given wind velocity, there is a unique turbine speed which gives the maximum output power. The peak power for each wind speeds occurs at the point where C_p is maximum. In order to maximize the generated power, it is desirable for the generator to have a power characteristic that follow the maximum C_p curve [67]. C_p is the sixth order polynomial of the tip-speed ratio. C_p curve is modeled based on the sixth order polynomial expression [160].

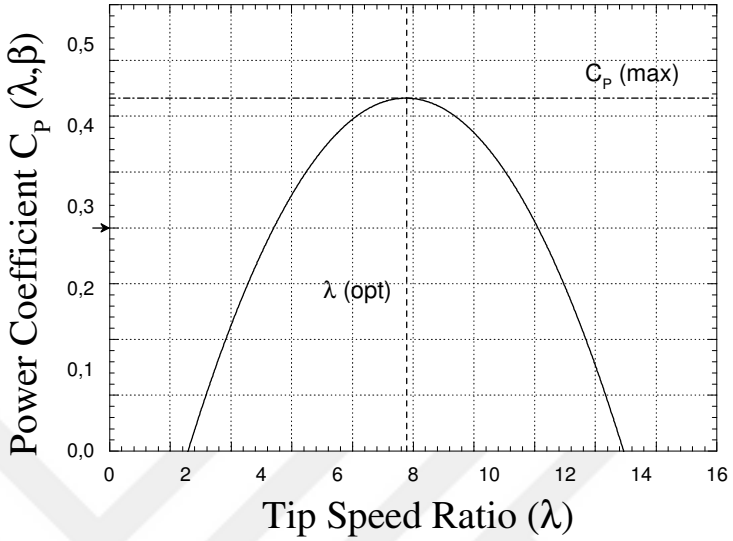

Figure V.2. Power coefficient and tip speed ratio curve.

In this section, the mathematical representation of the C_p curves used in Figure V.2, wind turbine characteristics is obtained by curve fitting using (V.4) in which the coefficients c_i are given in Table V.1.

Table V.1. Coefficients of wind turbine model

c_i	Value
c_1	0.5176
c_2	116
c_3	0.4
c_4	5
c_5	21
c_6	0.0068

Curve fitting is a good approximation for wide wind speed values between 2 m/s and 15 m/s. The results of the C_p vs. tip speed ratio simulation is shown in Figure V.2.

$$C_p(\lambda) = \lambda(c_0 + \sum_{i=1}^{i=6} c_i \lambda_i) \tag{V.3}$$

$$C_p(\lambda) = c_1 \left(\frac{c_2}{\lambda_i} - c_3\beta - c_4\right) e^{\frac{-c_5}{\lambda_i}} + c_6\lambda_i. \tag{V.4}$$

The $C_p(\lambda)$ curves expressed in (V.3) and (V.4) depend on the blade design and are given by the wind turbine characteristic [144].

The purpose of the proposed sensorless MPPT algorithms is to control the shaft speed of the PMSG to maintain the optimal tip-speed ratio without the knowledge of the PMSG rotor speed and wind speed. In literature, researchers recommended various methods for sensorless control of PMSG with MPPT control. Optimal torque control, perturbation and observation control, fuzzy logic control and some genetic algorithms are certain methods.

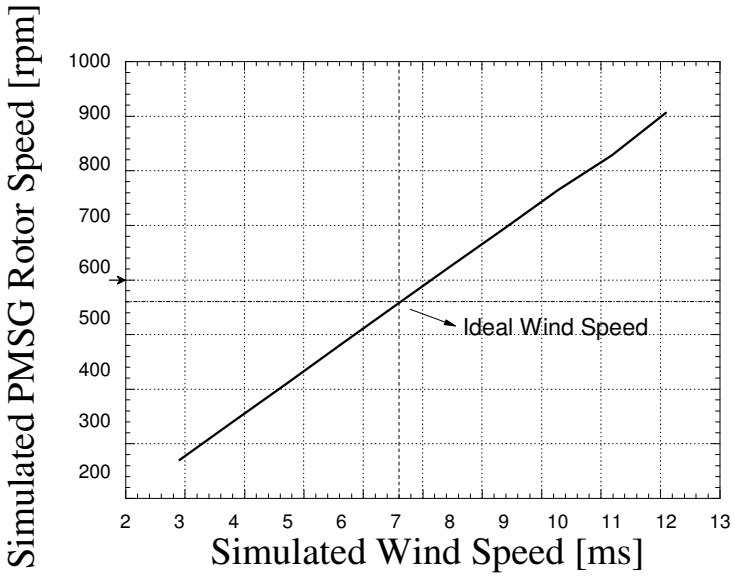

Figure V.3. Simulated rotor speed vs. simulated wind speed curve for the proposed turbine characteristics.

In this study, torque reference is provided by reference speed command called indirect speed control with MPPT [160]. In this way, when the rotor speed higher than the optimum, the generator torque is higher than that of the turbine, the system is decelerated. Inversely, when the rotor speed is lower than the optimum, the generator torque is lower than the turbine, the system is accelerated.

For experimental studies, a simplified speed ratio curve is provided by the manufacturer. MPPT algorithm is obtained based on this curve. However, the selected PMSG is not suitable for direct drive wind system. Thus, MPPT algorithm is not applied in experiments. However, simulation results proved that the constraints about the selected PMSG parameters are not appropriate. In Figure V.3, relation of the simulated wind speed and PMSG rotor speed is demonstrated. The value of ideal wind speed is selected 7 m/s and 560 W power is generated from the turbine at this wind speed. In the rest of simulation studies, optimal values are obtained based on this critical point.

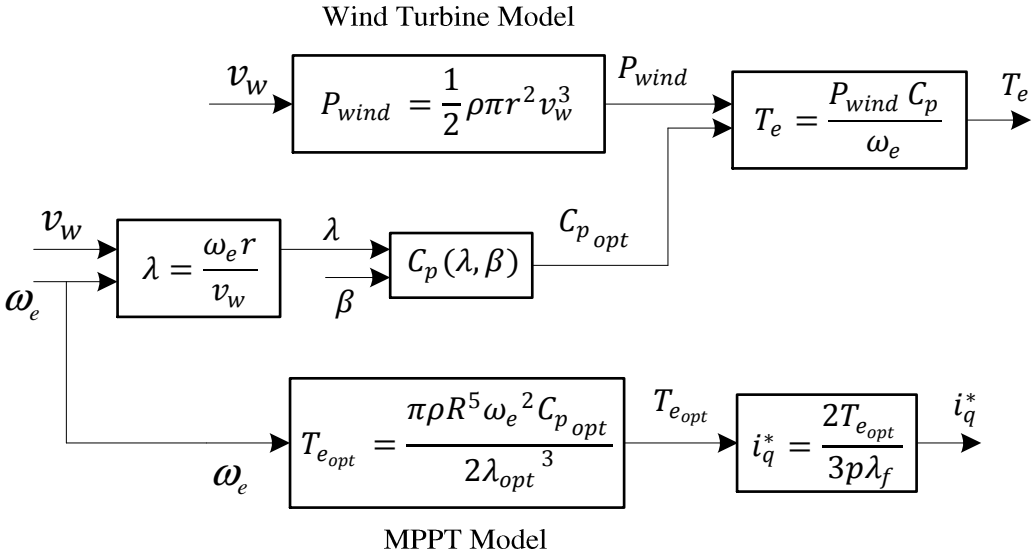

Figure V.4. Block diagram of MPPT control algorithm.

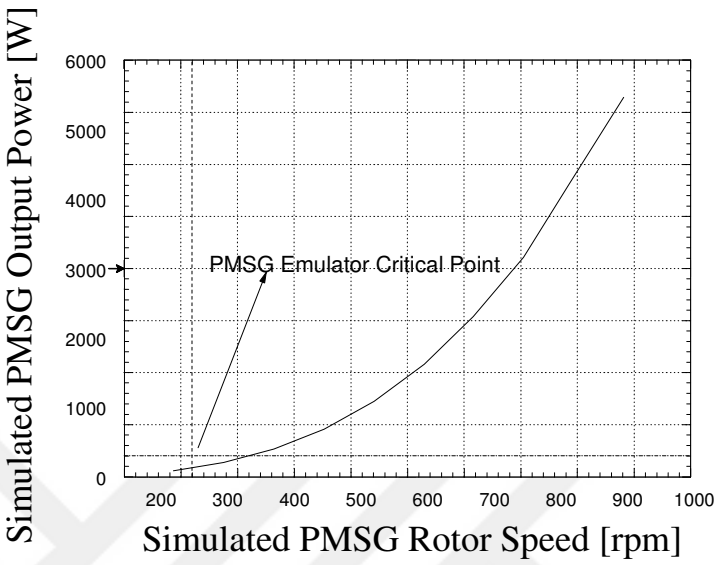

Figure V.5. Simulated PMSG output power vs. simulated PMSG rotor speed curve.

The prediction of wind speed and rotor speed are important parameters for maximum power output. To obtain maximum active power for variable wind speed, λ_{opt} can be calculated from the roots of the derivative of the polynomial in (V.4). Then, based on the reference wind speed, v_w, the corresponding optimal generator speed is obtained.

Figure V.4 shows that the proposed MPPT algorithm is based on the reference wind turbine model which is given in Table V.1. Thus, Figure V.5 demonstrates the output power supplied by the wind turbine model using reference wind speed, as shown in Figure V.3. The equation (V.5) shows torque calculation based on P_{wind} and C_p.

$$T_e = \frac{3p}{2}\lambda_f i_q = \frac{P_{wind}C_p}{\omega_e} \tag{V.5}$$

Reference current is generated from the outer voltage loop via regulating the DC-link voltage based on control error. In both voltage control loops, the PI feedback controllers are enhanced simple by robust control scheme, as shown in Figure V.4 to

yield good dynamic performance. Reference current is generated based on the specific wind speed with MPPT mechanism. In order to produce maximum DC-power in DC-link at variable speeds, a sensorless control method that is capable of doing precise position estimation at different wind speeds is suggested in Section 5.1.1.

$$T_{e_{opt}} = \frac{\pi \rho R^5 {\omega_e}^2 C_{p_{opt}}}{2 {\lambda_{opt}}^3} \tag{V.6}$$

$$i_q^* = \frac{2T_{e_{opt}}}{3p\lambda_f} = \frac{\pi C_{p_{opt}} R^5 {\omega_e}^2}{3p\lambda_f {\lambda_{opt}}^3}. \tag{V.7}$$

The equations (V.6) and (V.7) show optimal torque and optimal q–axis current command that are given as reference variable wind speed. And also, Figure V.6 shows the MPPT algorithm optimal torque curve and optimal q–axis current reference curve corresponding to simulated PMSG rotor speed.

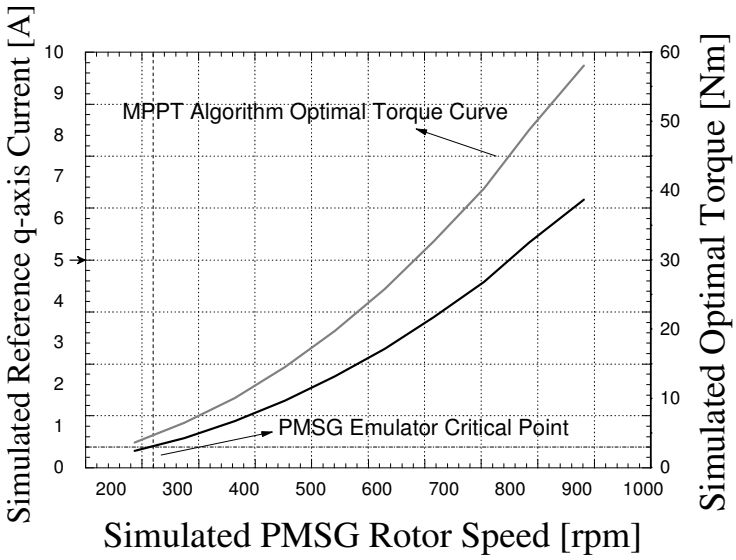

Figure V.6. Simulated reference q–axis current vs. simulated PMSG rotor speed.

dq–axes stator feedforward voltages are normally used in the FOC of AC machines at the output of the inner dq–axes PI current regulators to enhanced the dynamic performance of the machine [58]. In this method, feedforward voltages are not only used for the dynamic performance improvements, but also used to achieve a simple but effective position sensorless speed control of PMSG drive.

It is visible that stator d– and q–axes currents can be controlled by the d– and q–axes voltages and speed ω using (V.8) and (V.9). The control principle is adopted where the current in q–axis is controlled by speed of rotation or frequency of stator voltage applied to q–axis winding [26]. The amplitude of q–axis voltage is obtained by neglecting the derivative term and assuming that real currents closely follow reference values $i_q = i_q^*$ and $i_d = i_d^*$ (reference values are marked with $*$ in the superscript and heat $\wedge$ above is the symbol indicates estimates) [58]. Below are the modified stator feedforward voltage equations for the proposed speed sensorless scheme given in dq reference frame,

$$v_q^* = i_q^* R_s + (\omega_e L_d i_d^* + \omega_e \lambda_f) + K\Delta v \tag{V.8}$$

$$v_d^* = i_d^* R_s - \omega_e L_q i_q^* + \Delta v \tag{V.9}$$

where Δv is the output of the d–axis PI current regulator and ω_e is the output of the q–axis PI current regulator. Δv is multiplied by gain K and added to q–axis voltage equation v_q^* representing the part of the derivative term in the dynamic voltage equation given in (II.1). Similarly, Δv term in (V.8) also acts as the derivative representation given in (II.2) for achieving a better transient response in the sensorless operation.

The dq frame stator voltages given in (V.8) and (V.9) are obtained by modifying the dynamic machine model and used as the basic reference signals to control the PM

machine without requiring a position sensor. The signals depend on machine parameters. At any operating point, the machine itself determines the required voltages at its terminal by letting the inverter duplicate the voltages. This process is so called as self-control.

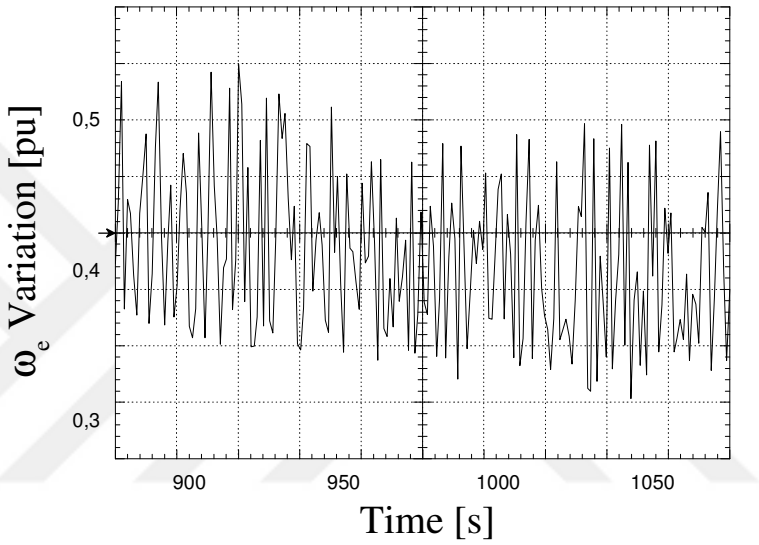

Figure V.7. Experimental ω_e variation.

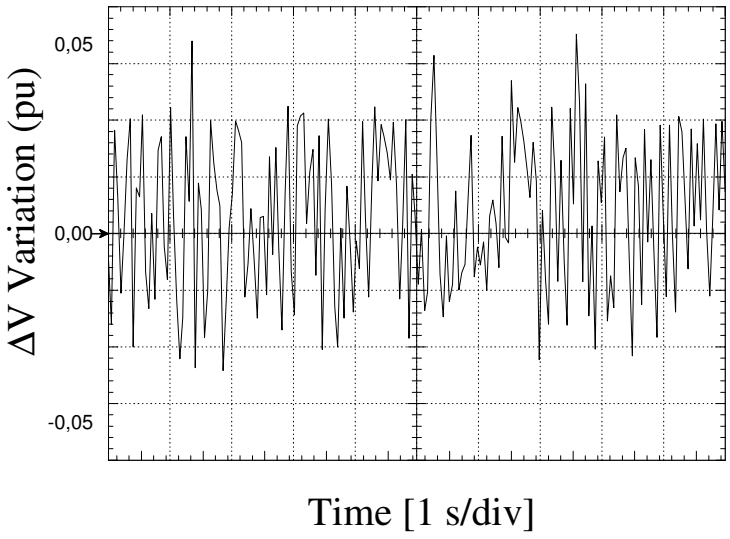

Figure V.8. Experimental Δv variation.

In Figure V.7, time based change in ω_e having q–axis output obtained through experimental studies is represented. In Figure V.8, change in Δv i.e. d–axis output is shown. The components of the dq frame voltage reference signals given in (V.8) and (V.9) are derived from (II.1) and (II.2), respectively under the assumption of steady-state conditions where derivative terms are replace with the regulator correction terms and a relevant gain.

In stator voltage estimation, stator resistance is arranged depending on the error between reference d–axis current and feedback d–axis current component. Since the stator resistance variation has minimal effect on the control, the method provides high dynamic control capability. Moreover, q–axis current flow is controlled by speed feedback. The method proposed by Okuyama et al. [129] has been applied for IM. The variation of the rotor flux linkage is estimated by observer and updated online. According to the method based on stator voltage estimation, the voltage signal is added to v_q as a feedforward signal. In this study, a high performance sensorless operation is performed in a wide speed range without using high-frequency signal injection. In speed estimation, Δv is taken as the reference which varies proportional to speed. In the proposed method, while the stator resistance change effects are not taken into consideration continuously, the rotor flux linkage variation determines the performance of the proposed control method [23], [161]. The rotor flux linkage is controlled by an additional feedforward voltage signal. According to the speed reference and flux change is determined. K value is a gain which is set manually based on the variable speed region. Start-up performance of the generator relies on K value that should be fixed properly as an important parameter in the proposed sensorless control.

The complete block diagram representation for a field-oriented control of the proposed speed sensorless PMSG scheme based-on stator feedforward voltage estimation using a SVPWM VSI is illustrated in Figure V.14. In (V.8) and (V.9), the *d*– and *q*–axes currents are replaced by their reference values. The resulting feedforward voltage estimation signals are represented in Figure V.14. The voltages applied to the motor are calculated by (V.8) and (V.9). Note that estimation of rotor speed $\hat{\omega}_r$ is obtained by passing ω_e obtained from output of the PI current regulator in q–axis through a first order filter, as shown in Figure II.4. The time constant of the filter depends on the overall system mechanical characteristics and heavily affects the dynamics and stability of the sensorless control scheme. The estimated speed and the estimated position are obtained as shown in Figure II.4 through the PI compensator and the integrator. In Figure V.9, simulation results of estimated and actual rotor angle change are represented.

Obtaining the generator parameters such as stator resistance and rotor flux linkage with MRAS method increases system stability and low speed performance. In simulation studies, MRAS multiple parameter estimator and PMSG model are run as an open-loop to verify the MRAS and sensorless algorithm, as shown in Figure V.14. To be able to obtain an open-loop operation of PMSG, the steady-state operation is desired for proper estimation of parameters. To achieve a steady-state operation, constant synchronous reference frame voltage values are applied to the machine terminal and the initial speed is selected in the speed integrator in the PMSG model as 450 r/min.

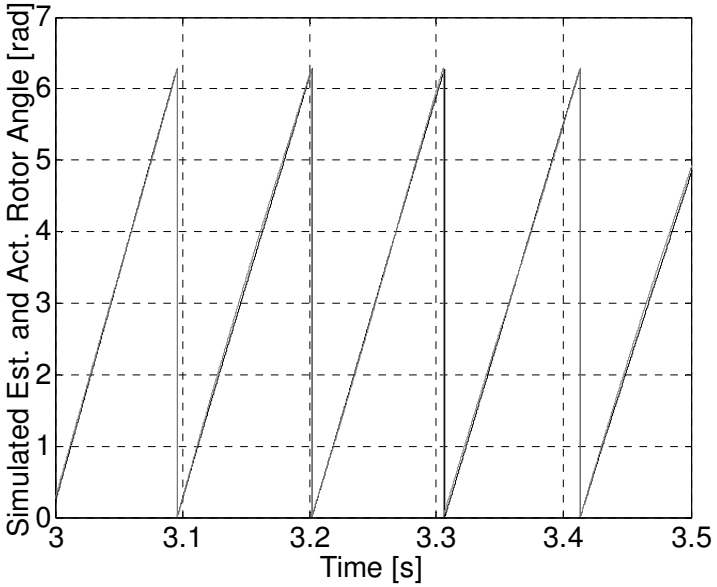

Figure V.9. Simulation of the estimated and actual rotor angles.

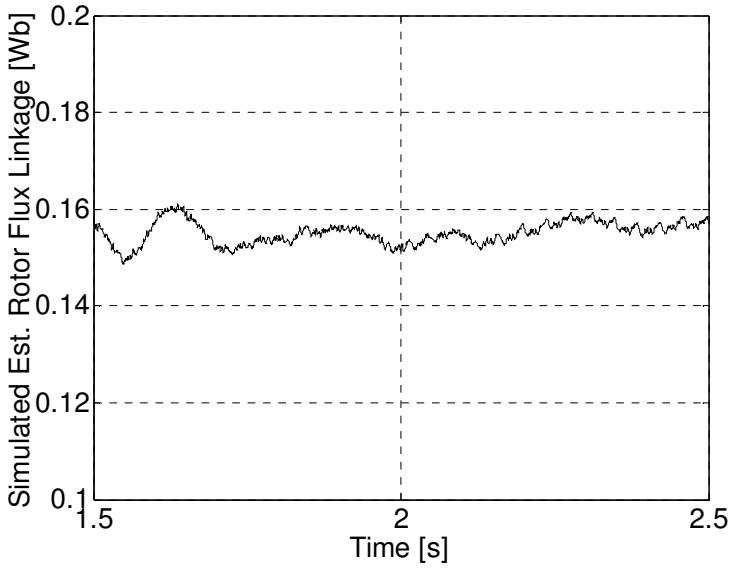

Figure V.10. Simulated initial value of the rotor flux linkage.

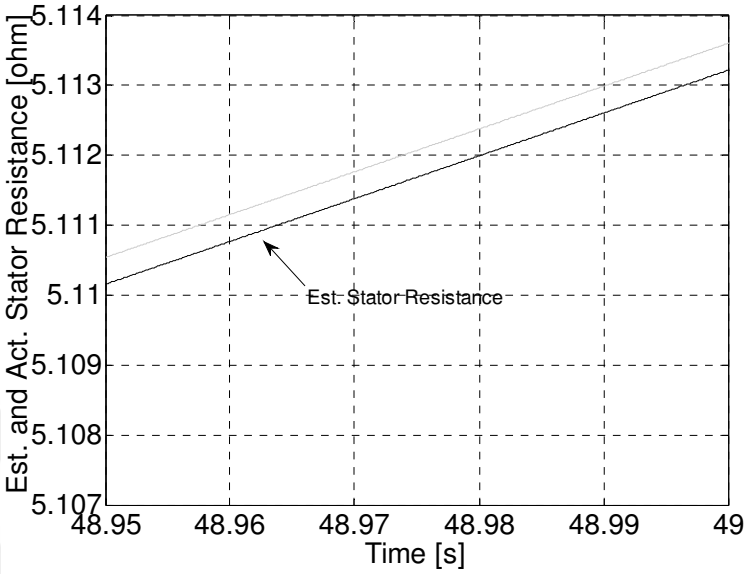

Figure V.11. Simulation of the estimated and actual stator resistance variation when λ_f is decreased by 20% and R_s is increased by 50%.

For the investigation of the behavior of the MRAS parameter estimation algorithm, initial stator resistance value is increased linearly from the original value starting from 45 seconds to 50% higher than the original value in ten seconds, as shown in Figure V.11. The error between actual and observed stator resistance is around 1% during the steady-state between 48 s to 50 s.

Also, the observed error for rotor flux linkage variation from the actual value started from 2.6 seconds to 20% lower than the original value in three seconds is given in Figure V.12. This error is considerably small which is around 0.5%. Figure V.12 shows the change in rotor flux which has been reduced by 20%. Rotor flux linkage value has been estimated by MRAS in less than 0.2 s. Since rotor flux linkage fluctuates according to the temperature which is a slow-changing parameter. Therefore, estimation length of 0.2 s is required and adequate.

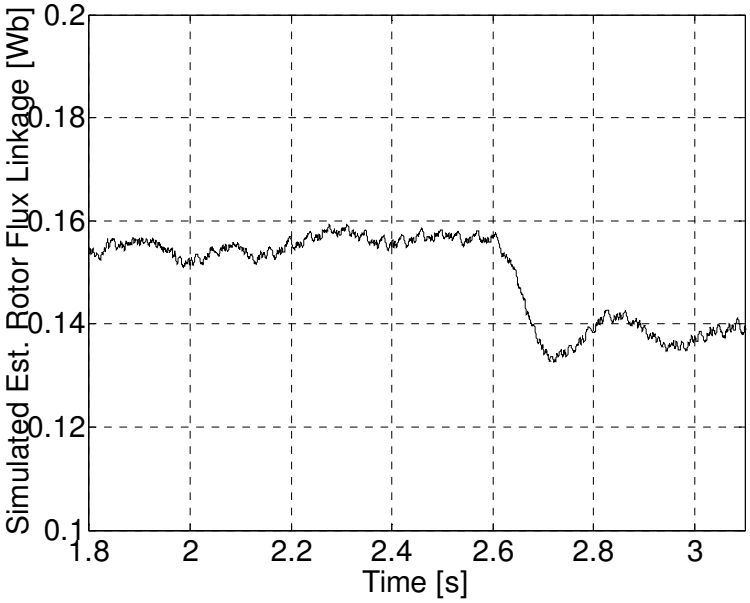

Figure V.12. Simulation of the estimated rotor flux linkage variation when λ_f is decreased by 20% and R_s is increased by 50%.

5.2. Experimental Results

To show validity of the proposed control scheme, the experimental studies are carried out for the systems shown in Figure V.18 to Figure V.28 under various operation conditions. A sensorless drive system for a PMSG, in which stator resistance and rotor flux linkage variation are estimated, is proposed in this section.

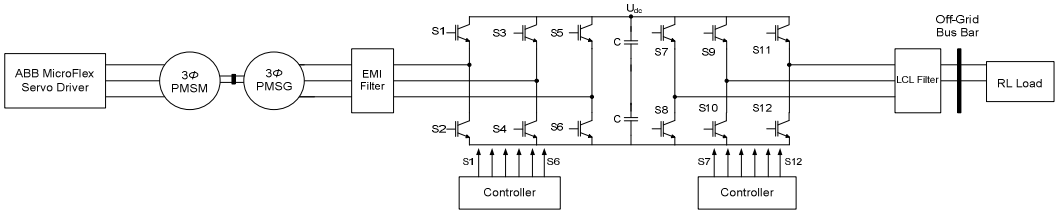

Figure V.13. PMSG emulator system block diagram.

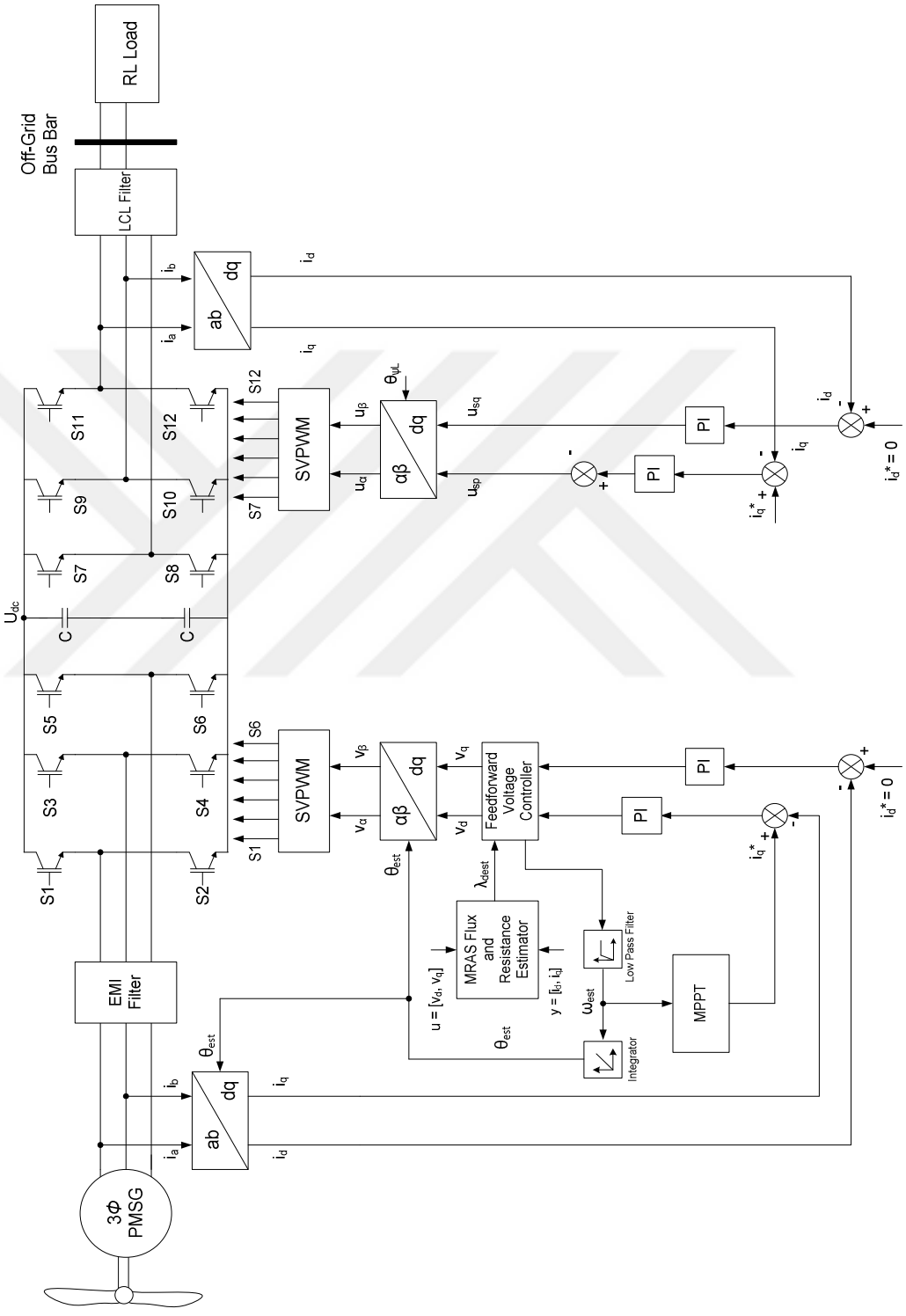

Figure V.14. Overall block diagram of proposed sensorless PMSG drive model based on MRAS parameter estimation.

In this study, the value of stator resistance and rotor flux linkage are estimated using MRAS. However, inductance variation is neglected because the influence of the q–axis inductance is independent from the speed and position estimation, but variation of stator resistance and rotor flux linkage increases errors in low speed region. A simplified block diagram of PMSG emulator is shown in Figure V.13. Figure V.14 shows the schematic diagram of the proposed overall control system.

The complete system is experimented for various conditions. The control algorithm is implemented on TMS320F28335 DSP and the proposed method is validated through experimental results.

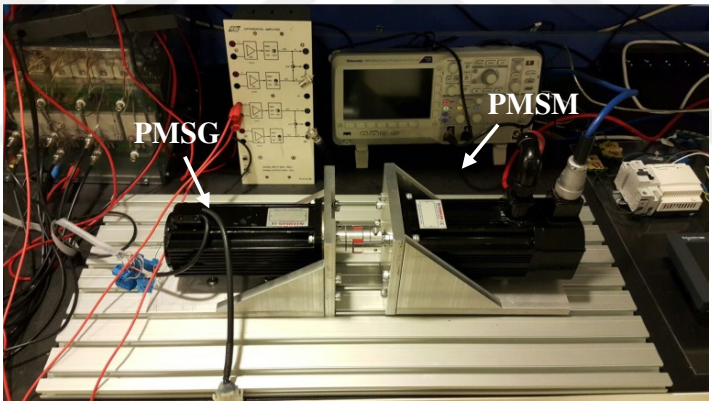

Figure V.15. Installation of PMSM and PMSG.

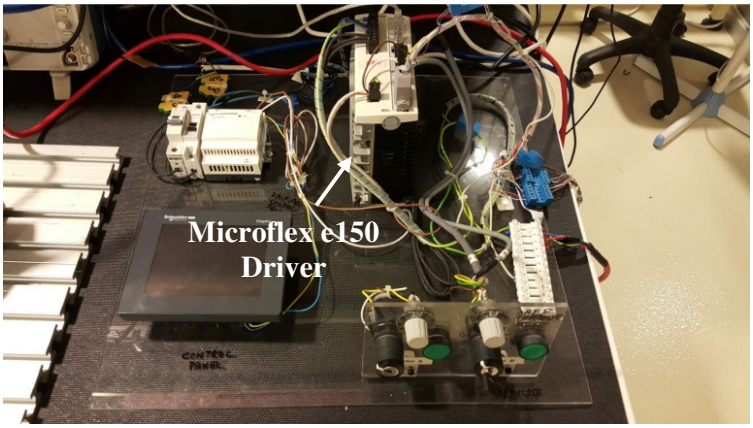

Figure V.16. Emulator system including Microflex e150 driver.

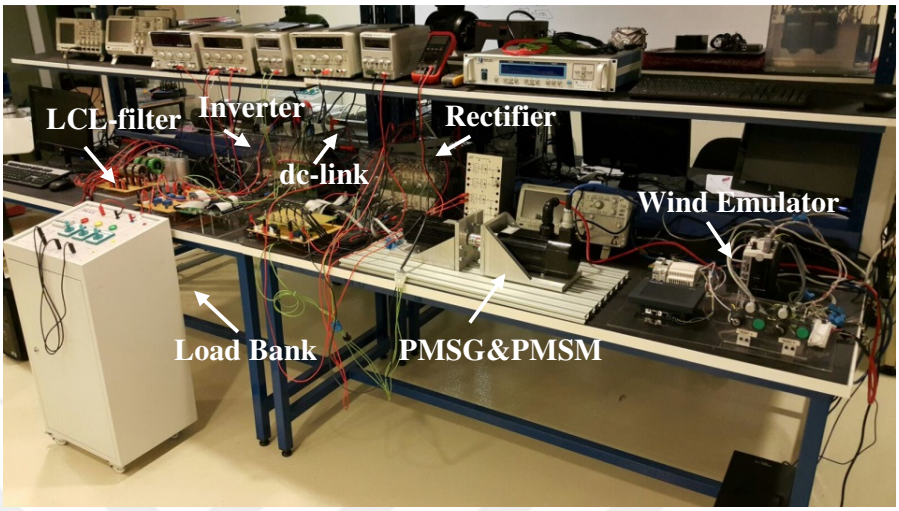

Figure V.17. Experimental test-bed.

In PMSG sensorless drive system, stator resistance and flux linkage variation depend on temperature rise and affect the sensorless control. These parameters are estimated using MRAS in order to improve the accuracy of position estimation. The parameter estimation of the stator resistance and rotor flux linkage is important because of their effects in the reference PMSM equations shown in (II.1) and (II.2). The experimental results verify the validity of the parameter estimation and the effectiveness of the proposed sensorless control system.

Figure V.14 shows a block diagram of the sensorless PMSG drive system combined with online parameter estimation. Figure V.18 and Figure V.19 shows the estimated change in stator resistance and rotor flux linkage during the experiment. While stator resistance was measured as about 3.4 Ω, it has been observed that it reached to 3.77 Ω depending on thermal change during the experiment. This corresponds to the pre-estimated temperature values.

In case of demands of high current in wind turbines, stator resistance changes depend on the temperature. Therefore, the stator winding temperature estimation can be modeled as

$$T_{est} = \frac{\hat{R}_s - R_0}{R_0 \alpha} + T_0. \tag{V.10}$$

where, R_0 is the initial resistance value at temperature T_0, $\widehat{R}_s$ is the estimated stator winding resistance at temperature T_{est} using MRAS and $\propto$ is the temperature coefficient of copper (3.93×10^{-3} per °C). Point temperature measurements has revealed to be 44° on the surface temperature. When the estimated stator resistance value is placed in (V.10), it is seen that the estimated temperature has been calculated to be 47 °C. Considering that the temperature of stator winding is high, estimated stator resistance value is proved to be correct.

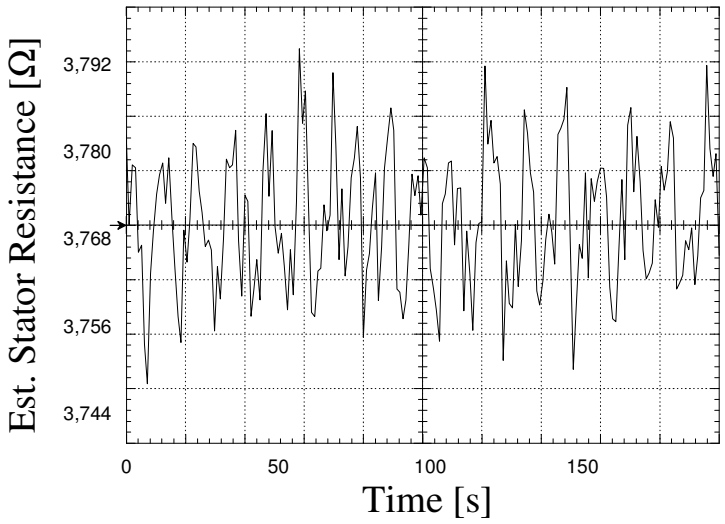

Figure V.18. Estimated initial stator resistance.

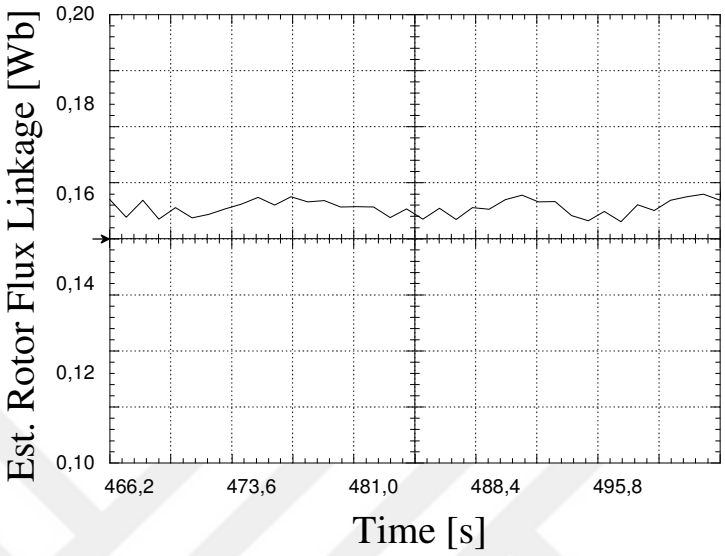

Figure V.19. Estimated initial rotor flux linkage.

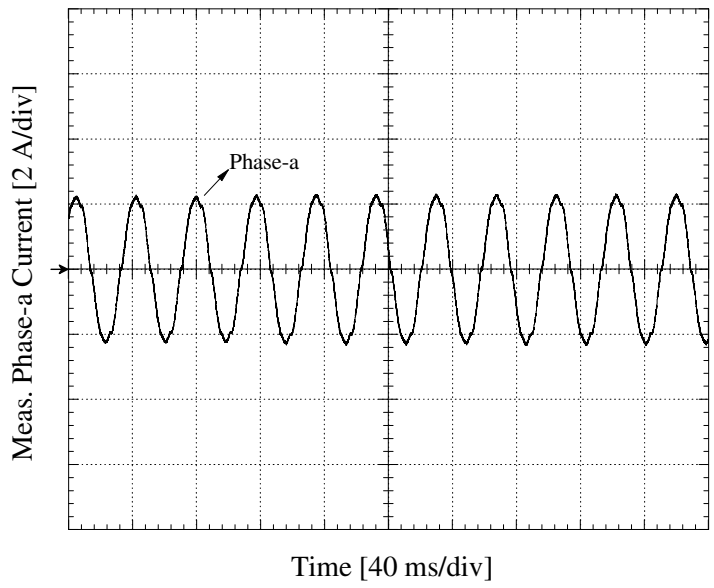

Figure V.20. Experimental PMSG phase–a current, (U_{DC} = 50 V) and (R_{Load} = 22 Ω).

The estimation error of the position and speed appears at the transient state. However, at steady-state speed and position error decrease and stable sensorless PMSG control is achieved. In Figure V.20, phase–a current waveform of PMSG at 50 V at DC-link. In Figure V.20, phase-*a* current for PMSG driven by 400 r/min is represented. U_{DC} is the DC-link voltage of PMSG forming at the power stage output. Measurements have been done by connected loads (R_{Load} = 22 Ω) to the DC-link that PMSG is connected to, and current with 2.28 A peak value has been obtained. Figure V.21 shows phase–a current for PMSG driven by 1050 r/min. Measurements have been done by connected load (R_{Load} = 43 Ω) to the DC-link that PMSG is connected to, and current with 2.12 A peak value has been obtained.

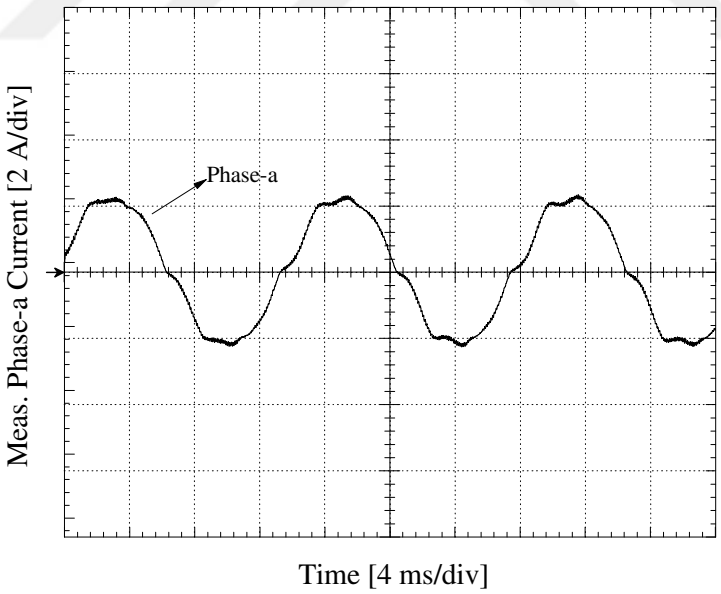

Figure V.21. Experimental PMSG phase–a current (U_{DC} = 100 V) and (R_{Load} = 43 Ω).

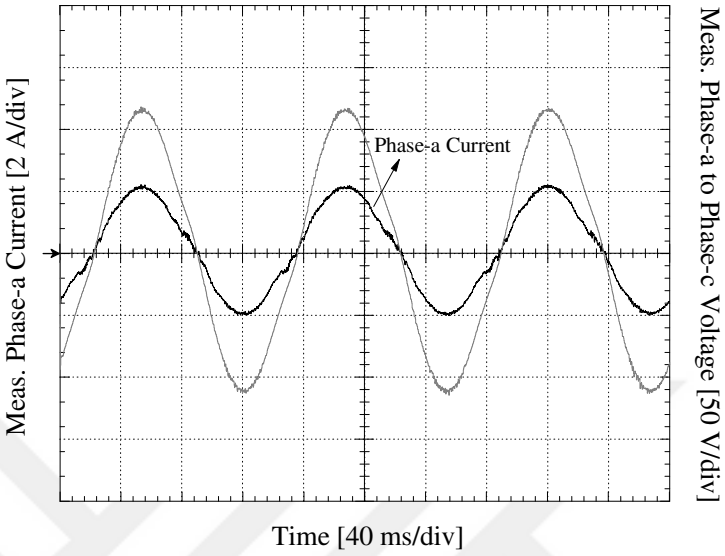

Figure V.22. Experimental off-grid side phase–a current and phase–a to phase–c voltage for m = 0.6, (U_{DC} = 225 V) and (R_{Load} = 43 Ω).

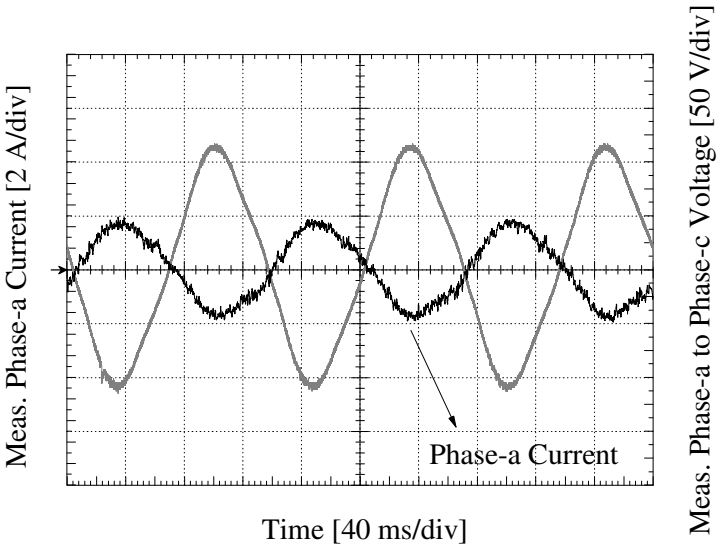

Figure V.23. Experimental off-grid side phase–a current and phase–a to phase–c voltage for m = 0.6, (U_{DC} = 225 V) and (R_{Load} = 43 Ω and L_{Load} = 50 mH).

In Figure V.22, off-grid generator measurements is seen. m represents modulation index and peak phase–a to phase–c voltage has been measured as 117 V. Phase–a current has been measured to be 2.8 A. DC-link voltage can be controlled by calculating the voltage of the peak value to the DC-link via the equation seen in (V.11). RMS value of 117 V phase voltage is ($V_{LL(rms)}$) 82.73 V, and of DC-link voltage is (m = 0.6) is 225 V. In Figure V.22, R_{Load} = 43 Ω connected as a star has been used at the LCL filter output.

$$U_{DC} = 2\sqrt{2}V_{LL(rms)}/(\sqrt{3}m) \tag{V.11}$$

In Figure V.23, phase–a current for the off-grid part of PMSG driven by 1000 r/min, and the voltage waveform phase–a to phase–b is illustrated. While peak voltage value phase to phase is 117 V, DC-link voltage has been measured as 225 V. Resistive and inductive loads have been connected to the LCL filter output.

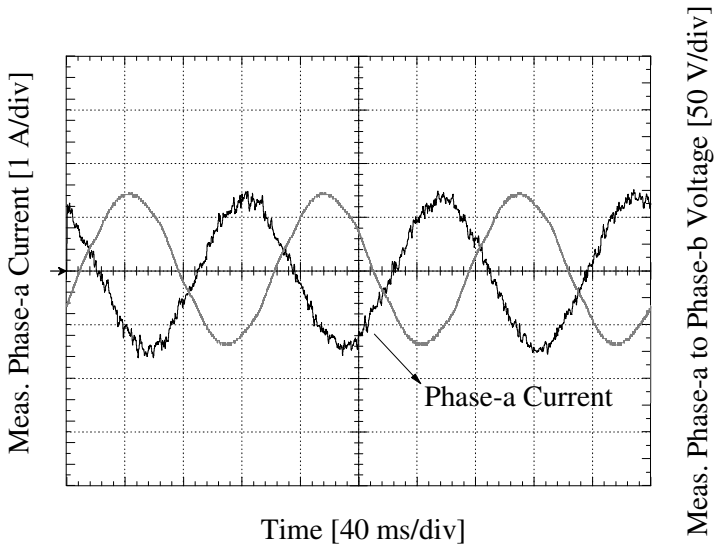

Figure V.24. Experimental off-grid side phase–a current and phase–a to phase–b voltage for m = 0.4, (U_{DC} = 210 V) and (R_{Load} = 43 Ω and L_{Load} = 50 mH).

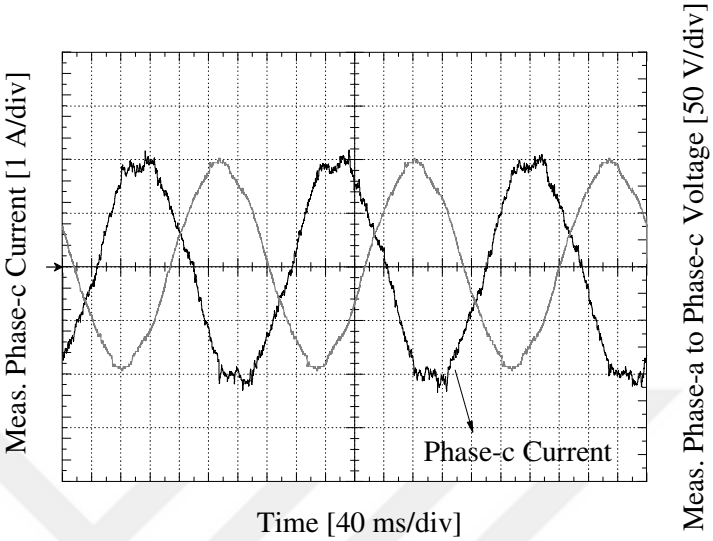

Figure V.25. Experimental off-grid side phase–c current and phase–a to phase–c voltage for m = 1.0, (U_{DC} = 210 V) and (R_{Load} = 43 Ω and L_{Load} = 50 mH).

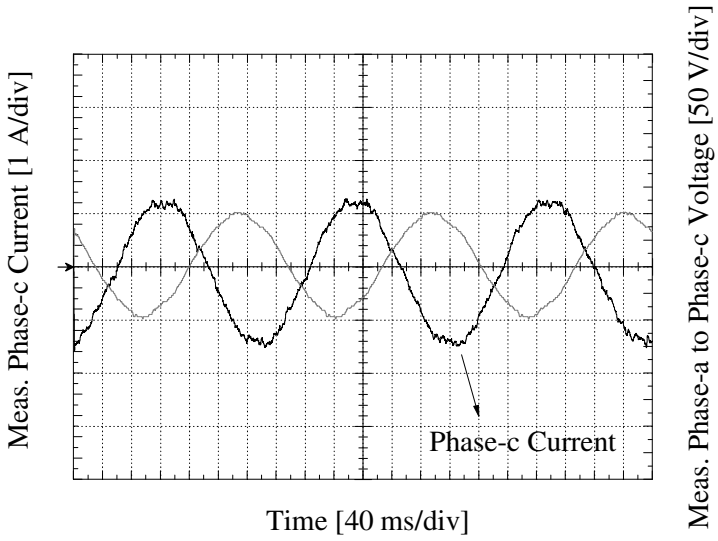

Figure V.26. Experimental off-grid side phase–c current and phase–a to phase–c voltage for m = 1.0, (U_{DC} = 59 V) and (R_{Load} = 43 Ω and L_{Load} = 50 mH).

In Figure V.24, phase–a current for the off-grid side of PMSG driven by 500 r/min, and the voltage waveform phase–a to phase–b is shown. Peak voltage value phase to phase is 73 V, DC-link voltage has been measured as 210 V.

In Figure V.25 phase–c current and voltage modulation index phase–a to phase–c has been adjusted to be 1.0 for the same conditions. Under this working condition, peak value of voltage phase to phase is 101 V, and current peak value is 2.1 A.

In Figure V.26, phase–c current for the off-grid side of PMSG driven by 300 r/min and voltage waveform for phase–a and phase–c is given. Peak voltage value phase to phase has been measured as 51 V while DC-link voltage is 59 V and phase–c current is 1.28 A.

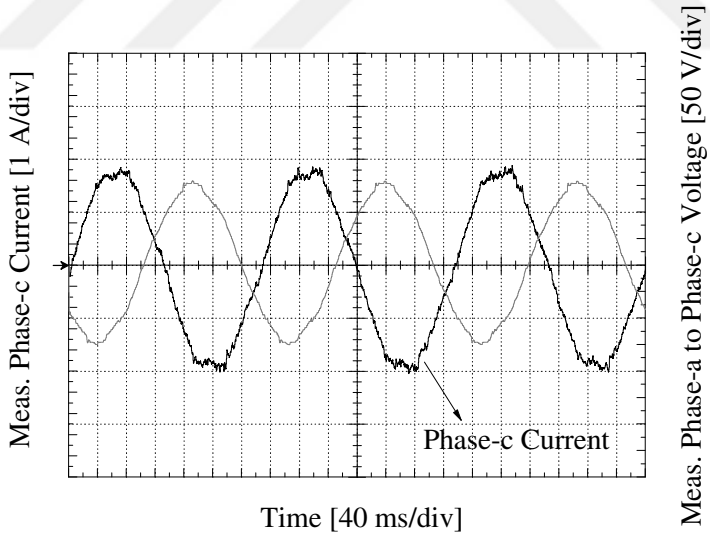

Figure V.27. Experimental off-grid side phase–c current and phase–a to phase–c voltage for m = 1.0, (U_{DC} = 59 V) and (R_{Load} = 43 Ω and L_{Load} = 50 mH).

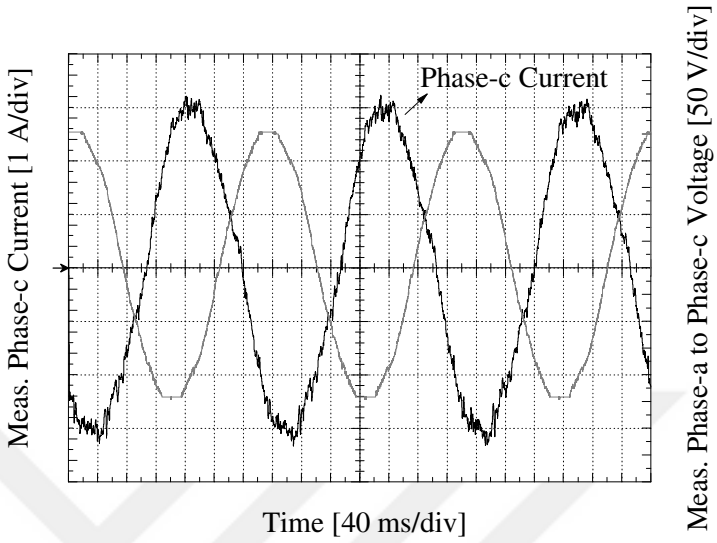

Figure V.28. Experimental off-grid side phase–c current and phase–a to phase–c voltage for m = 1.0, (U_{DC} = 127 V) and (R_{Load} = 43 Ω and L_{Load} = 50 mH).

In Figure V.27, phase–c current for the off-grid side of PMSG driven by 400 r/min and voltage waveform for phase–a and phase–c is illustrated. Peak voltage value phase to phase has been measured as 79 V while DC-link voltage is 91 V and phase–c current is 1.88 A.

In Figure V.28, phase–c current of the off-grid side of PMSG driven by 750 r/min and voltage waveform for phase–a and phase–c is given. Peak voltage value between phases has been measured as 127 V while DC-link voltage is 147 V and phase–c current is 3.24 A.

Measurements reflect that THD of the voltage between phase–a to phase–b at the LCL-filter input in the off-grid side of SSTP (assuming there is no LCL filter) is 51.15 % and it is too high. The THD of the voltage phase–a to phase–b at the LCL filter output in the off-grid side of SSTP is around 4%.

5.3. Conclusion

The rotor flux linkage that changes due to aging, vibration, humidity and temperature reduces the drive control performance. So, the effects of aging are tried to be eliminated and the control performance is increased with life estimation algorithms in the literature using online-learning methods and parameter estimation methods. In this study, in order to obtain the position and speed information of the driven PMSG directly, feedforward voltage estimation method is suggested. With the proposed method even in the situations where the wind speed is low, it is ensured that a superior PMSG control performance compared to other sensorless control methods based on back-EMF prediction is achieved. Because the rotor flux and the stator resistance undergo a change due to the effects of the loss of magnetic properties of magnets and temperature rise, a highly efficient control is ensured by estimating the rotor flux linkage and stator resistance using MRAS observer. With the proposed method, maximum power generation is achieved compared to other back-EMF estimation methods even at low wind speeds.

VI. IMPROVED SENSORLESS FOUR-SWITCH THREE PHASE (FSTP) PMSG DRIVE BASED ON STATOR FEEDFORWARD VOLTAGE ESTIMATION USING MRAS MULTIPLE PARAMETER ESTIMATION

The difference between fossil energy sources and demanded energy needs is rapidly increasing. This leads to alternative search and solutions in energy production. These solutions encourage utilizing the existing sources most efficiently. While the macro-scale systems meet existing needs in industrial and high power level practices, participating of individual users in energy production is possible with micro-scale systems [162]–[165]. Especially in rural areas, base stations, highways where the electricity cannot be delivered and individual usages are considered as micro-scale energy production application areas [132]. With the integration of smart grid, it is predicted that there may be a rapid increase in small energy production. In renewable energy production, the largest production share except hydroelectric power plants is provided from the wind turbines. With the standard three-blade wind turbine structure, both micro and macro levels of energy are produced. Small wind market share is $ 60 million in the USA in 2014. In the “Small Wind Turbines” report prepared in 2010, unit, market and power capacity are analyzed. According to the report, it is stated that the number of unit decreased 20%, the total power capacity increased 26% and market share increased 53% when compared to the previous year [162], [163]. It is stated that in England electricity generation reached to 1.84 MW capacity in 2013 based on wind energy in which the power range is between 0 and 1.5 kW [165]. To get the maximum

use of wind energy, variable speed generators that can operate at wide speed range are widely used in industry. With variable speed power generation, it is possible to obtain the maximum power at variable wind speeds [166]. By adjusting the generator speed at different working points according to speed-power characteristics of wind turbines, the maximum power point is obtained. In the variable speed wind turbines systems PMSG, asynchronous machine and squirrel cage asynchronous machine are used [134]–[138]. PMSG is used in small turbine systems due to its high power density, high efficiency and reliable design. The turbine connection of PMSG can be performed with or without gear-box [67], [139]. However, because of cost, reliability and maintenance needs, gear-box is not used in small powered systems. In variable-speed PMSGs, rotor rotational speed and wind speed are known with the position sensors and anemometer, respectively. However, in order to increase the robust and reliability of the system, sensorless control methods are applied in PMSG [159]. Thus, maintenance need and complex connection and assembly resulting from the usage of sensors are eliminated. In the proposed system, sensorless control method based on the principle of feedforward stator voltage estimation is suggested for maximum power output of direct drive PMSG. The rotor flux linkage and stator resistance available at generator steady-state equations are predicted on-line with MRAS observer in order to prevent the loss of positioning accuracy caused from parameter changes and then the updates are performed in the feedforward voltage estimation (FFVE) equations [67], [72]. Field-oriented control and DTC technique need the accurate electrical parameters of the PMSM [139]. Least-square method slows down the processor too much because it has a repetitive process structure. Sliding-Mode Control (SMO) is used as an adaptive control method superior for uncertain parameters and parameters showing gradual

change [32], [167]. Similarly, an on-line parameter identification method uses EEMF method for more accurate position estimation [168]. In PMSG, rotor flux linkage undergoes a change during the operation depending on the magnetic properties of the magnets and temperature rise [23]. The proposed method suggested by Okuyama et al. [72] is called the Flux-Vector control in which a PI controller is employed on the flux component of the current for IM. Additionally, the special advantage of this method is the elimination of voltage feedback. In the proposed feedforward voltage estimation method, flux change affects the control system and stability [59]. In the proposed method, when compared to other position sensorless control algorithms, because primarily the speed is predicted, the position is predicted with the help of a simple integration and first degree low pass filter without derivative term [53], [72], [169]. In the proposed small wind turbine control system, PMSG control is developed by using an inverter/rectifier structure in a back-to-back, bi-directional and reduced switching structure for variable speed wind turbines. In this topology, four of the switched are used composing two-leg in the generator side and the other four are used as two-leg in the grid (off-grid) side [170]–[174]. Third phase leg of both of the circuits are connected in the center tap of capacities that were divided into two by DC bus. Although in PMSG control systems a structure containing twelve switches is often used, because the proposed method is for low power and for individual use, the elements increasing the cost are reduced [170]–[174]. With the MPPT method, power generation with optimum tip-speed ratio is obtained. In this study, two four-switch converter structures are established with two DC-link capacitors between them [170]–[174]. By keeping the d–axis current as zero with a PI regulator that is in generator side of the rectifier, maximum electrical torque production is achieved. The MPPT method is used in order to obtain

the maximum output power depending on optimum rotor speed under variable wind speeds.

The principle of PMSG modelling and MPPT studies are presented Section 5.1. In Section 5.1, the dynamic and steady-state models of surface mounted permanent magnet synchronous generator (SMPMSG) are explained in detail. In Section 5.1.1, wind turbine characteristics and MPPT algorithm based on indirect speed control are explained. In Chapter III, the proposed FSTP inverter drive structure is described in detail. In Chapter IV, the proposed stator feedforward voltage control using MRAS parameter estimation sensorless speed control strategy. In Section 6.2, electrical simulation model in MATLAB/Simulink is designed and developed. The simulation results are given and analyzed in detail. In Section 6.3, LCL output harmonic filter is designed and developed. The simulation results are given and analyzed in detail. In Section 6.4, the proposed speed sensorless control scheme based on MRAS has been implemented with 1 kW PMSG drive controlled by a TMS320F28335. The hardware implementation and experimental results of the proposed sensorless PM synchronous generator drive including steady-state load disturbance are presented and discussed.

6.1. Rotor Flux Linkage and Stator Resistance Estimator Based on MRAS

PMSG parameters vary depending on temperature, frequency, load conditions, and operation region. In order to eliminate the effects of parameter changes, an MRAS estimator structure that works with the proposed sensorless control method is suggested. While the rotor position error is caused by stator resistance change at low and variable speeds, with multi-parameter estimation operation in unstable region is eliminated [54]. Also, the effects of the rotor flux linkage variation in permanent magnet due to the temperature change are eliminated [34]. A high performance PI

regulator is used for PMSG sensorless speed control; moreover for low speeds and transients an adaptive MRAS observer is developed. In addition to rotor flux linkage and stator resistance changes, feedforward voltage estimation method is used together with MRAS in order to eliminate the disturbance effects in position estimation. Recursive Least Square Estimation (RLSE) is used for determination of the parameters [39], [42]. However, the sensitivity of RLSE is not sufficient [66]. Moreover, the methods such as fuzzy logic, artificial neural network (ANN), and genetic algorithms limit the dynamic behavior of the system due to their complex calculations [46]. The complex estimation methods not only extend the processing time, but also reduce the reliability of the processor. Parameter estimation obtained with Sliding Mode Observer (SMO) is not preferred in critical applications due to incompatibility in response at different frequencies. Moreover, Extended Kalman Filter (EKF) is not recommended for PMSG systems, because it is not suitable for multiple simultaneous estimations and contains complex mathematical functions [152]. Simplicity and rapid response capability of the proposed Model Reference Adaptive System (MRAS) for PMSG is the most prominent parameter estimation method compared to other techniques [48], [56]. Predictability of stator resistance and rotor flux independently is important for PMSG systems which require updating of generator variables individually with minimum error.

6.2. Simulation Results

The proposed drive system shown in Figure VI.7 is simulated in MATLAB/Simulink® using an electrical two-leg IGBT inverter and electrical surface-mount PM synchronous generator model from the SimPowerSystems™ toolbox in order to demonstrate the validity of the proposed multiple parameter estimation FSTP based PMSG drive scheme.

C programming like codes written in MATLAB Programming language are developed for the simulation of the proposed sensorless control of PMSG drive in MATLAB/Simulink using MATLAB Function blocks without using expensive toolboxes such as Embedded Coder®.

In simulation results, initial rotor flux linkage, estimated stator resistance, estimated rotor flux linkage estimation using MRAS under various working conditions is shown Figure VI.1, Figure VI.2 and Figure VI.3, respectively.

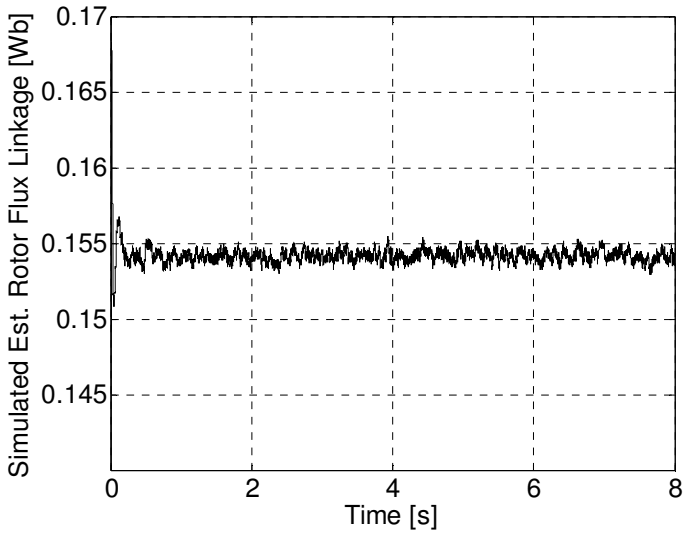

Figure VI.1. Simulation of the estimated initial rotor flux linkage (λ_f = 0.15 Wb).

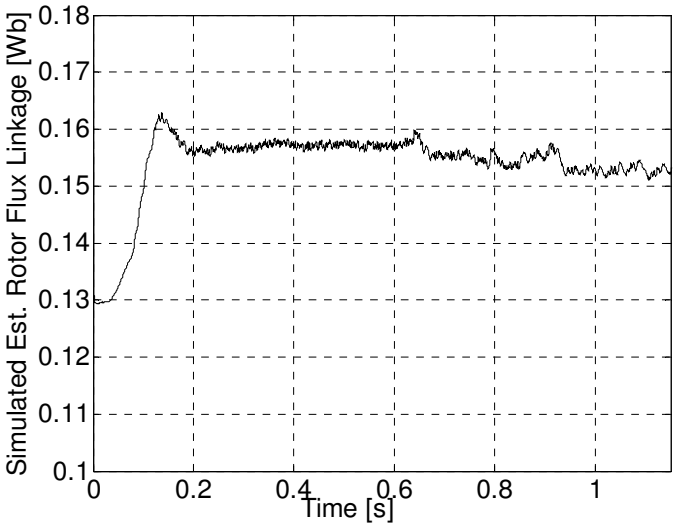

Figure VI.2. Simulation of the estimated stator resistance when λ_f is decreased by 20% and R_s is increased by 50%.

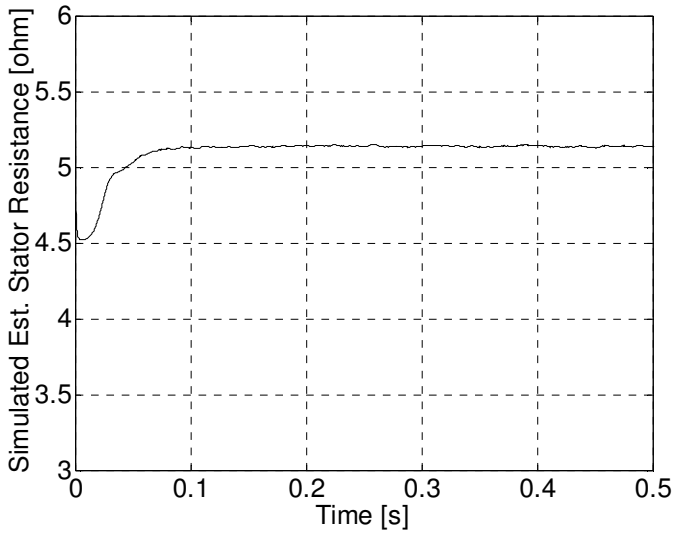

Figure VI.3. Simulation of the estimated rotor flux linkage when λ_f is decreased by 20% and R_s is increased by 50%.

Figure VI.2 shows the estimation results of MRAS method for initial rotor flux linkage. Figure VI.2 and Figure VI.3 show the combined effects of parameter estimation method. Figure VI.2, using "Matlab/Simulink-SimPowerSystem" PMSG model, rotor flux linkage is decreased by 20%. In Figure VI.3, stator resistance initial value is increased by 50%. To eliminate oscillation effects of the transient region, a low pass filter is designed in this simulation. Figure VI.3 shows the stator resistance estimation curve after LPF.

In Figure VI.3, initial errors are applied to the stator resistance ($R_s = 1.5R_s$) rotor flux linkage ($\lambda_f = 0.8\lambda_f$). As it can be seen in Figure VI.3 that the transient state is smooth and less than 0.5 s convergence is obtained to the expected values such that at any update of the stator resistance and rotor flux linkage set during that period may not affect the overall control performance.

6.3. LCL Harmonic Filter Design

The inverter located on the load/grid side transmits the current/voltage that contains too much harmonic to load/grid with high frequency DGM (PWM) signals [176]. With a harmonic filter that can be located between inverter and load/network, the harmonics that would be transmitted to load/grid are greatly reduced and voltage and current waveforms in low THD (Total Harmonic Distortion) values close to pure sine are obtained [177]. Harmonic filter can also prevent the possible short circuit that can arise in direct connection stage between two sources (inverter and load/grid) as well as decreasing high frequency harmonics. These harmonics diminishing techniques can be classified under the main approach of magnetic flux compensation, multilevel inverter, active and passive filtering. In order to diminish the current harmonics around

the switching frequency and to conform to standards like *IEEE 519-1992, IEEE 1547-2008, IEEE 929-2000, IEC 61000-3* and *IEC 61727*, in industry and literature, in the studies of renewable energy sources connected to an independent (off-grid, standalone etc.) the grid, low pass passive filter is used between inverter output and grid/load [178]. Ideally, a filter that has high damping attenuation in lower cut-off frequency and high switching frequency can diminish the fluctuation occurring in the switching frequency, significantly. In passive filter design, the issues such as switching loss, efficiency, voltage drop and stability (the system's entering into resonance) must be considered. For example, in the inverter systems operating synchronized to grid, IEEE standards states that each current harmonic above 35^{th} harmonic must be less than 0.3% of rated current in the fundamental frequency. In industry and literature; L, LC and LCL type and their various derivatives are used in the inverter output with low pass passive harmonic filtered grid/load [179]. Third degree low pass LCL-filter better weakens the harmonics in the switching frequency of the inverter than the other two filters mentioned above. LCL-filter provides better coupling impedance between grid/load and the filter [180]. Because the high harmonics will be absorbed by shunt capacity, it will receive much less ripple current on the L_2 inductance in the side of grid/load and that's why it will enable this inductance to be selected smaller than L_1 inductance in the inverter side input. LCL-filter provides a good harmonic weakening even with small L and C_f values. However, it is necessary to address to the problems of resonance effect, current ripple that may occur in inductances, total filter impedance, attenuation of current harmonics that may occur in switching frequency and around it and the amount of reactive power that is absorbed by capacity in LCL-filter design [181].

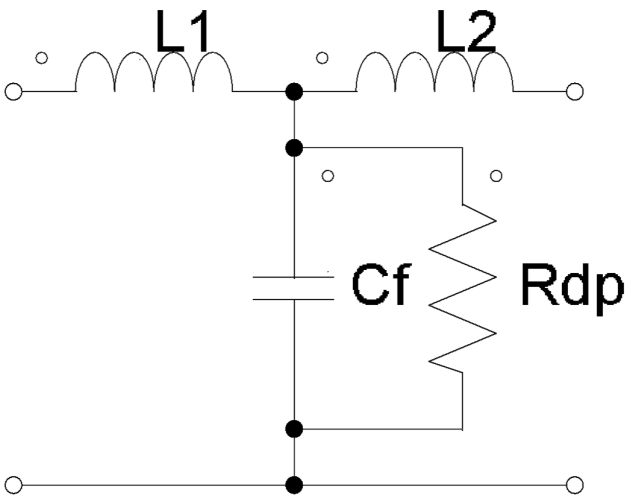

Figure VI.4. LCL-filter circuit scheme.

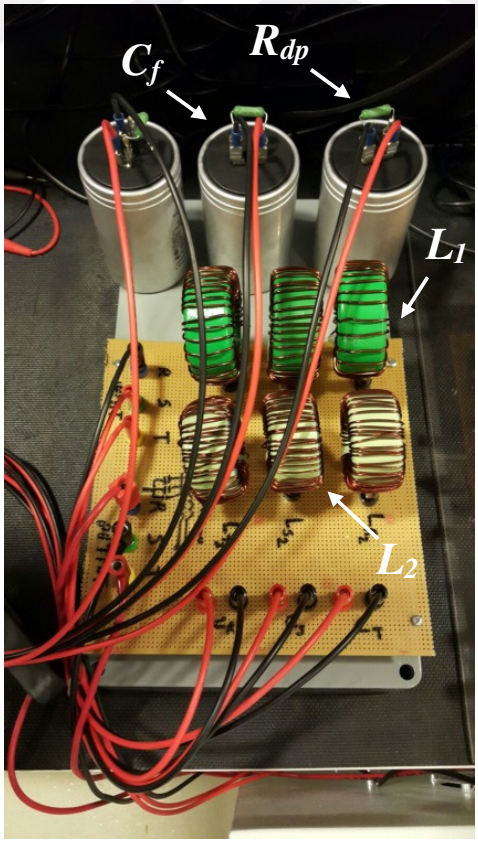

Figure VI.5. LCL-filter circuit.

A parallel suppressor resistor has been inserted to the shunt capacitor used in LCL-filter. The reason of this process is the harmonic declination in characteristic resonance frequency. Figure VI.4 demonstrates the LCL-filter design. According to the circuit diagram in Figure VI.4, 50 μF EPCOS™ capacitor has been used. L_1 has been designed to be 5.2 mH and L_2 to be 1 mH. A 2.5 kW 46 μF capacitor that was found on the market has been used although C_f 3.3 μF was found via calculations. The filter resonance frequency is 810 Hz in order not to allow any overlapping problem between the system cycle and the switching frequency.

6.4. Experimental Results

To show validity of the proposed control scheme, the experimental studies are carried out for the systems shown in Figure VI.10 to Figure VI.24 under various loading conditions. A sensorless drive system for a PMSG in which stator resistance and rotor flux linkage variation are estimated is proposed in this chapter. The estimated position is compensated by a proportional and integral compensator so that the position error converges to zero. In this study, the values of stator resistance and rotor flux linkage are estimated using MRAS. However, inductance variation is neglected because the influence of the q–axis inductance is independent from the speed and position estimation, however variation of stator resistance and rotor flux linkage increase errors in low speed region. A simplified block diagram of PMSG emulator is shown in Figure VI.6. Figure VI.7 shows the schematic diagram of the proposed system. The complete system is experimented for various working conditions. The control algorithm is implemented on TMS320F28335 DSP and the proposed method is validated through experimental results. Figure VI.6 shows the block diagram of the established emulator

system. 3 N·m PMSM has been used via ABB® Microflex™ e150 driver to drive PMSG. Experiments have been carried out and prospected results have been obtained for the speed levels that correspond to different wind velocity levels through real-time torque control. In the system, two Semikron Semiteach module have been modified in compliance with four-switched FSTP topology and back-to-back converter structure has been created. ALCON™ RC is used as the snubber loop. The control signals obtained through MRAS and FFVE algorithm are transmitted to the inverter/rectifier module via a signal processing card seen in Figure VI.8. DC-link formed with 2200x2 μF capacitors are connected to the rectifier and inverter inputs and outputs. For the off-grid system model, LCL output filter, seen in Figure VI.5, has been designed and developed. Reaction of the system to the RL loads have been investigated by using five-level resistive and inductive load bank. A phase-a center tap has been created for the FSTP via a connection from the center tap of the two 2200x2 μF capacitors to the outside in Experimental-bed, in Figure VI.8. Output voltage of the off-grid side has been controlled through modulation index (m). System capabilities have been tested to obtain different values of m.

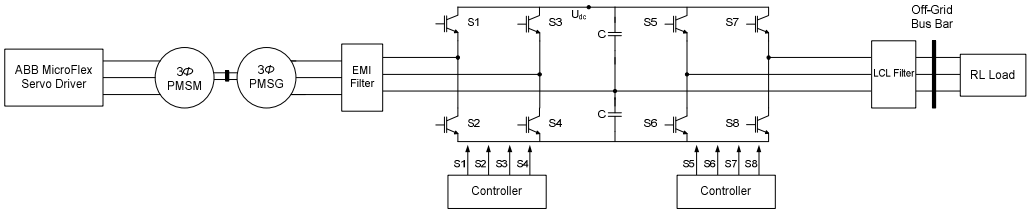

Figure VI.6. PMSG emulator system block diagram.

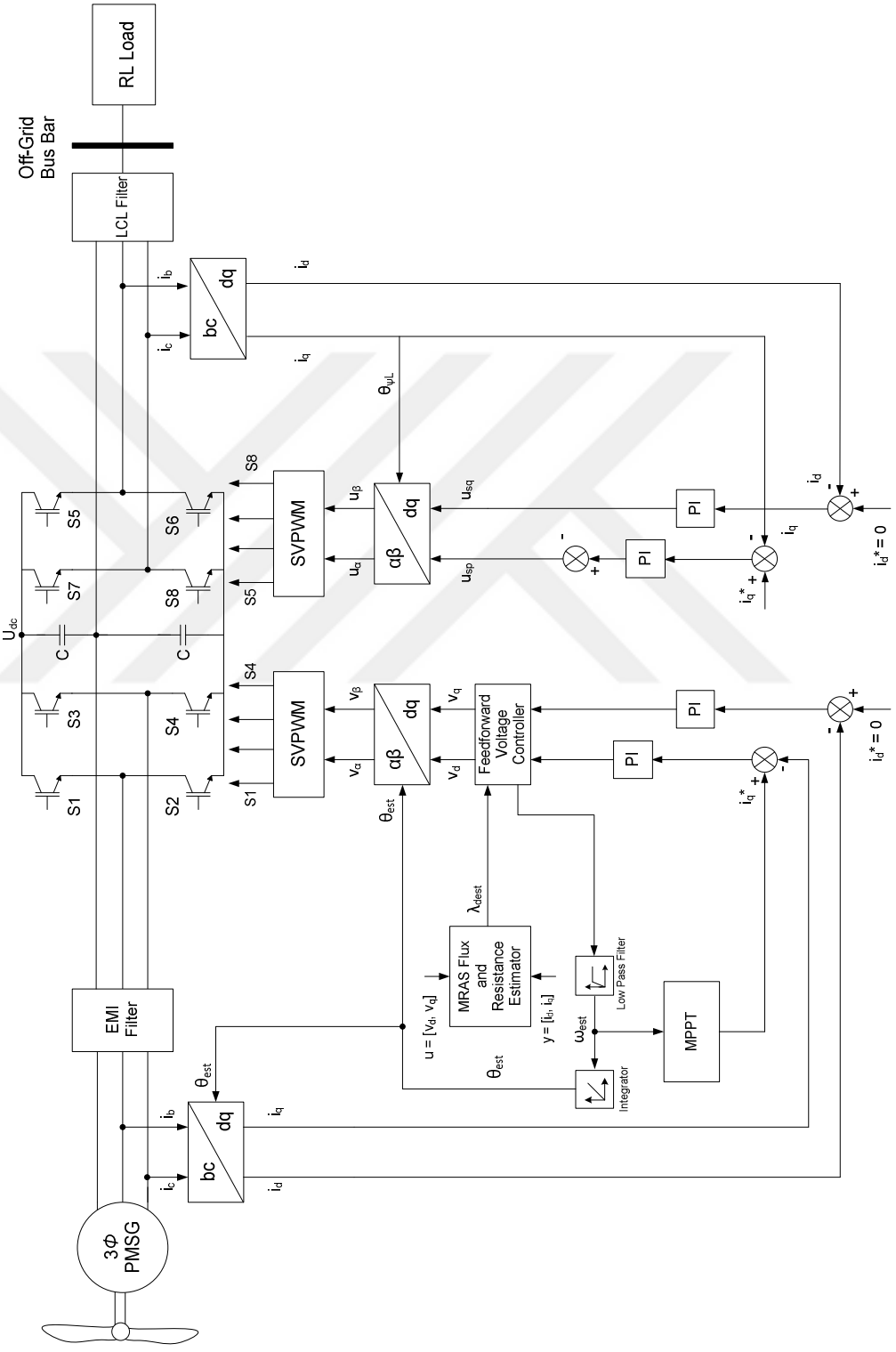

Figure VI.7. Overall block diagram of proposed sensorless PMSG drive model based on MRAS parameter estimation.

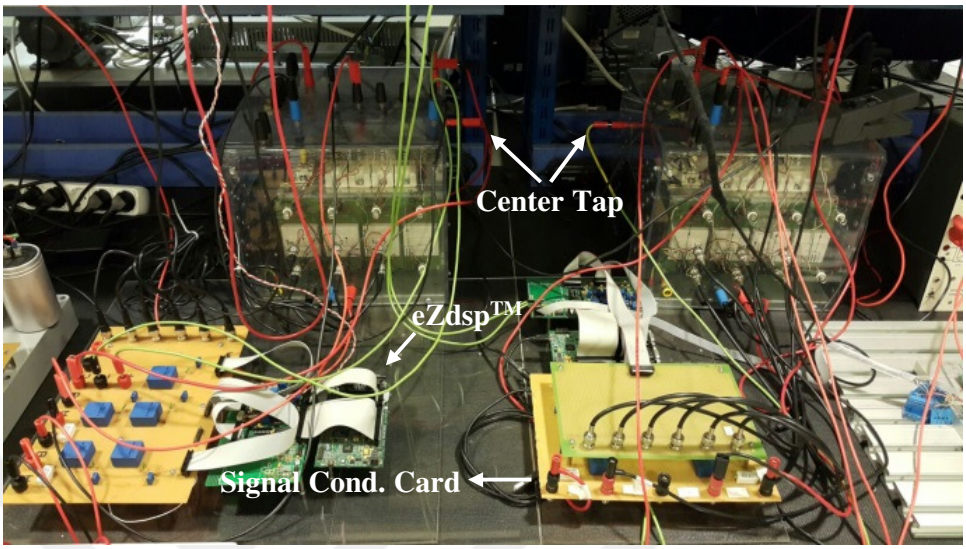

Figure VI.8. FSTP inverter structure (phase–a connected center tap of capacitors).

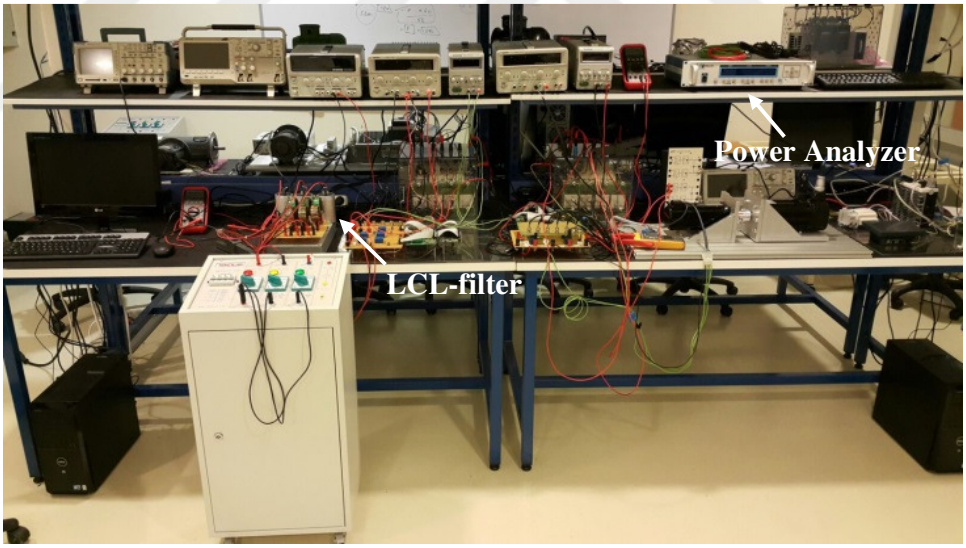

Figure VI.9. Experimental test-bed.

MRAS is simulated to examine the effects of stator resistance and rotor flux linkage variation for the proposed sensorless control of PMSG. Figure VI.10 and Figure VI.24 show the experimental results of MRAS that is applied to the proposed sensorless method. In this system, PMSG parameters are estimated at various operating

conditions. The proposed sensorless PMSG control algorithm and MRAS parameter estimator are combined in experimental studies.

PMSG position estimation performance is improved by using online parameter estimation that is adapted to the proposed sensorless control algorithm. While open-loop parameter estimations were conducted during the experiments and simulations, closed-loop parameters were estimated after the estimations reached the required level and the parameters in the FFVE block have been updated. In experimental studies, stator resistance estimation spontaneously, initial rotor flux linkage, estimated stator resistance when R_s is increased by 50% estimation using MRAS under various working conditions is shown Figure VI.10, Figure VI.11 and Figure VI.12, respectively.

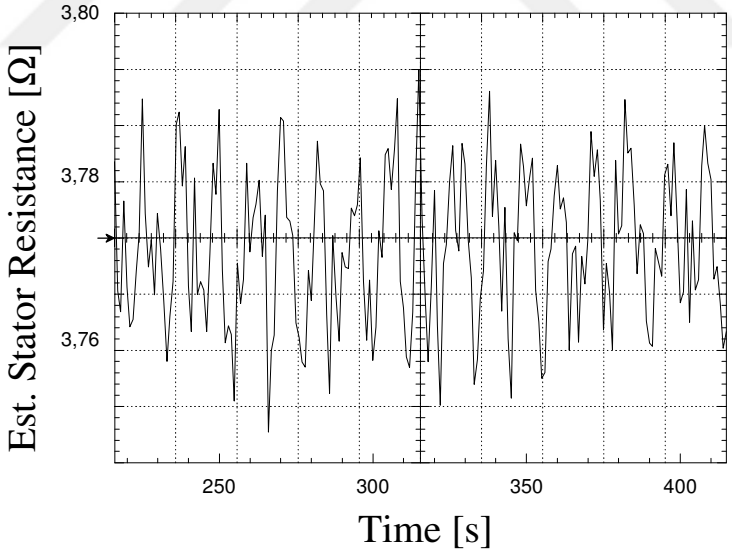

Figure VI.10. Estimated initial stator resistance.

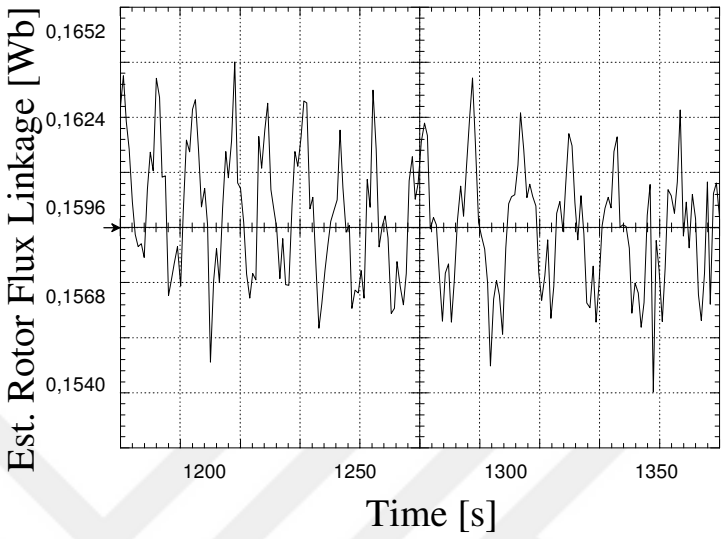

Figure VI.11. Estimated initial rotor flux linkage.

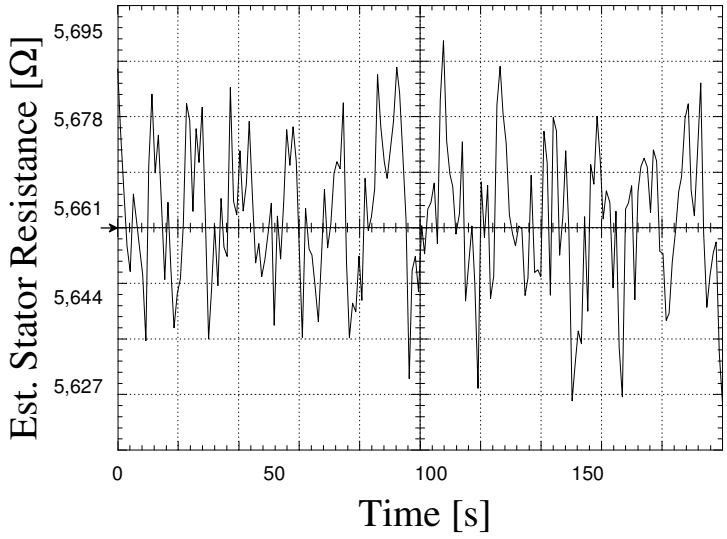

Figure VI.12. Estimated stator resistance when R_s is increased by 50%.

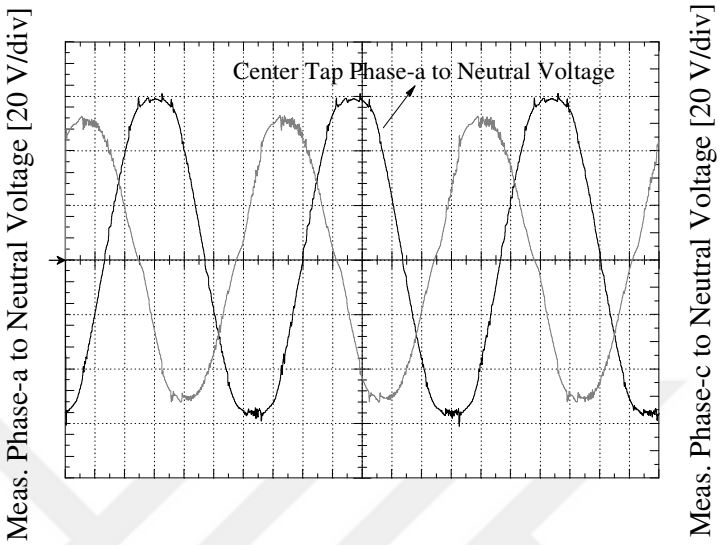

Figure VI.13. Phase–a to neutral and phase–c to neutral voltages.

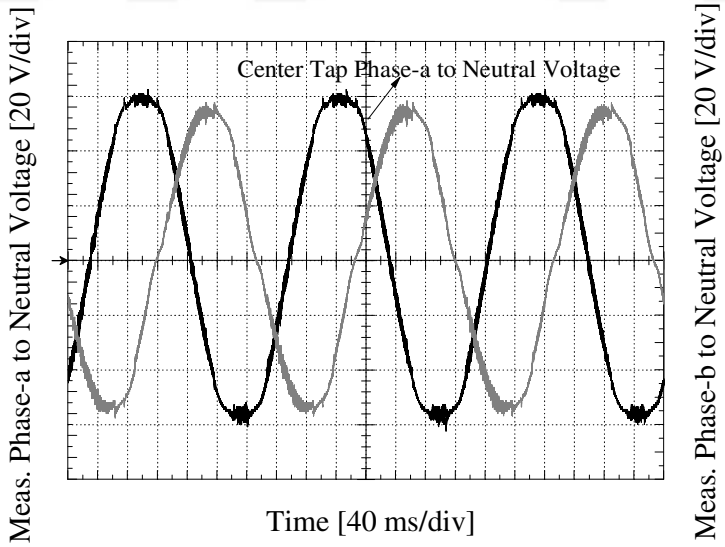

Figure VI.14. Phase–a to neutral and phase–b to neutral voltages.

In Figure VI.13, phase–a to neutral voltage and phase–c to neutral voltage are represented. Phase–a to neutral voltage is 61 V and phase–c to neutral voltage is 53 V. Phase–a is the center tap point and its voltage value is more than phase–c at about the rate of 15%. In Figure VI.14, phase–a to neutral voltage and phase–b to neutral voltage are shown. Phase–a to neutral voltage is 61 V and phase–b to neutral voltage is 53 V. Following the measurements, while balance at phase–b and phase–c voltages is observed, voltage is high at the phase connected to the center tap as it is expected. In Figure VI.15 and Figure VI.16, controlling the stability of the recommended method for sudden load changes by stabilizing load L being at the output of the off-grid part and connecting five different resistive resistor levels (22 Ω - 220 Ω) is illustrated.

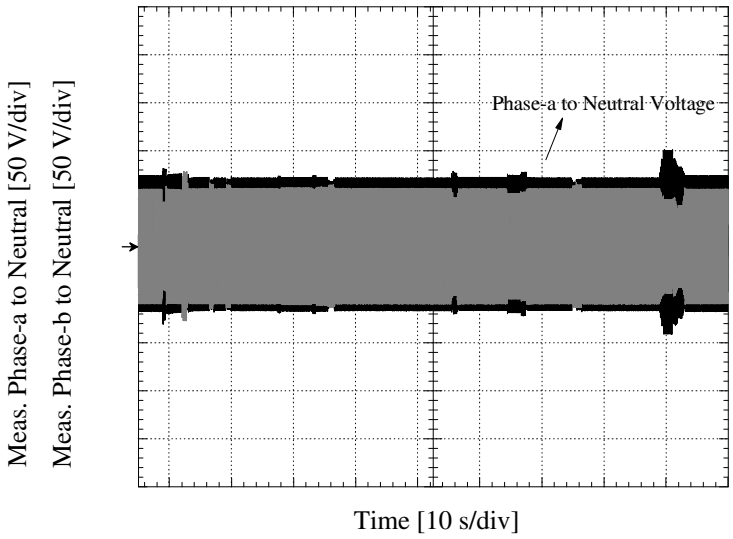

Figure VI.15. Meas. phase–a to neutral and phase–b to neutral voltages (R_{Load} has been changed five levels).

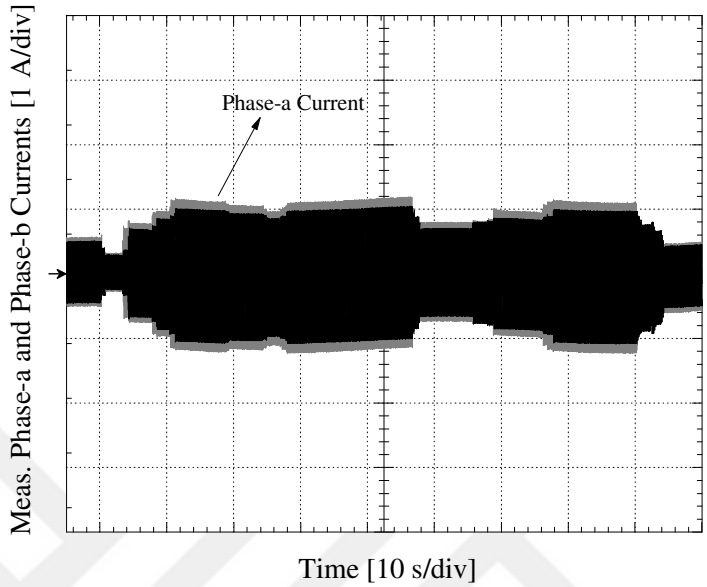

Figure VI.16. Meas. phase–a and phase–b currents (R_{Load} has been changed five levels).

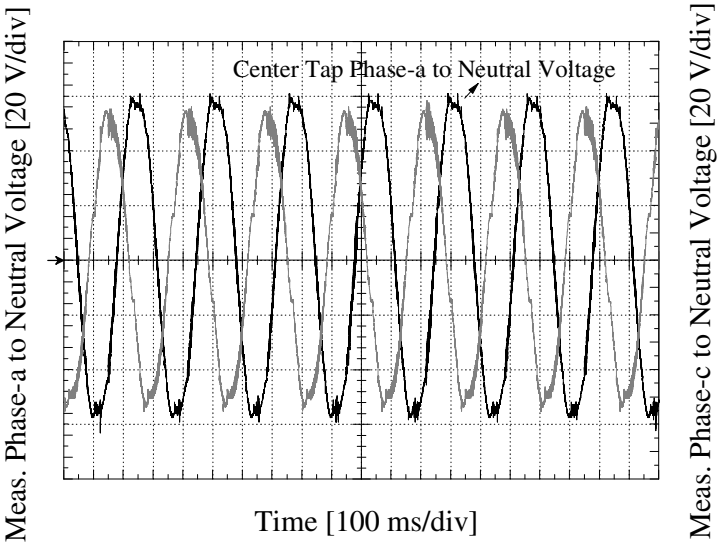

Figure VI.17. Meas. phase–a to neutral and phase–c to neutral voltages for m = 1.0, (U_{DC} = 100 V) and (R_{Load} = 43 Ω and L_{Load} = 50 mH).

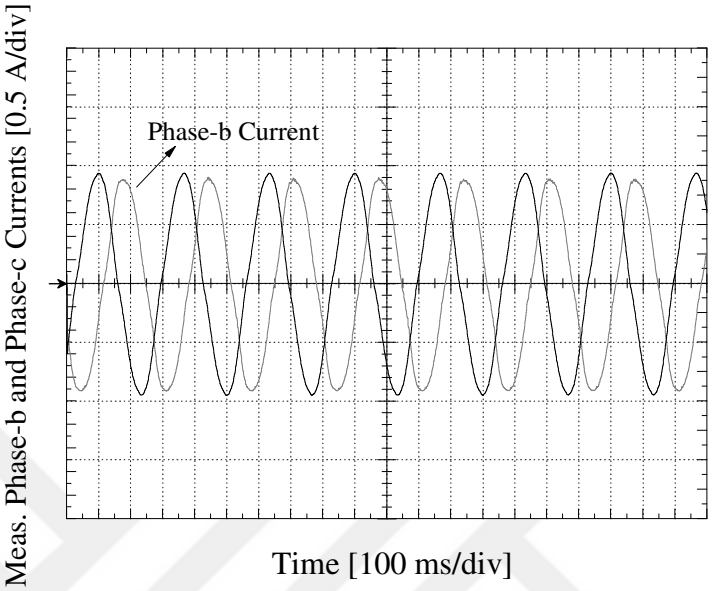

Figure VI.18. Meas. phase–a and phase–b current for m = 1.0, (U_{DC} = 100 V) and (R_{Load} = 43 Ω and L_{Load} = 50 mH).

In Figure VI.17, neutral voltage of phase–a is 59.2 V. PMSG has been driven to be 100 V to the DC-link (The emulator control mode is setted in control mode). Phase–a to neutral voltage has been recorded to be 54.4 V. The ratio of the voltage forming between the center tap and the second leg has been recorded to be 10%.

Measurements under the same conditions regarding phase–a and phase–b currents are represented in Figure VI.18. Peak values for phase–a current is 1.24 A and for phase–b is 1.3 A. Imbalance between phase–b and –c is at the rate of 5%. Figure VI.19 shows phase–a and phase–b currents of the PMSG driven with 750 r/min. Peak values for phase–a current is 2.84 A and for phase–b current is 2.36 A. In Figure VI.20, phase–c current under the same conditions have been measured. Peak value of phase–c current has been measured to be 2.36 A. Unbalance state between the phases in FSTP controlled PMSG has been measured to be 15% at voltage levels and 20% at current changes.

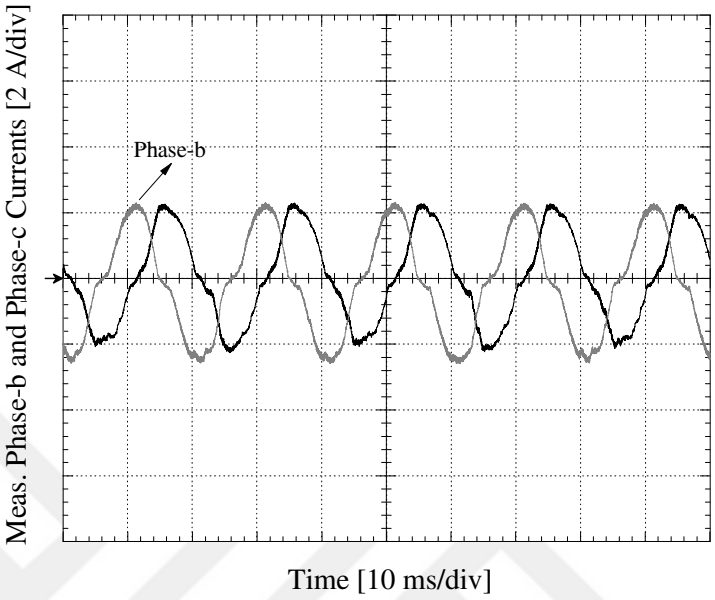

Figure VI.19. Meas. phase–a and phase–b current for m = 0.4, (U_{DC} = 100 V) and (R_{Load} = 43 Ω and L_{Load} = 50 mH).

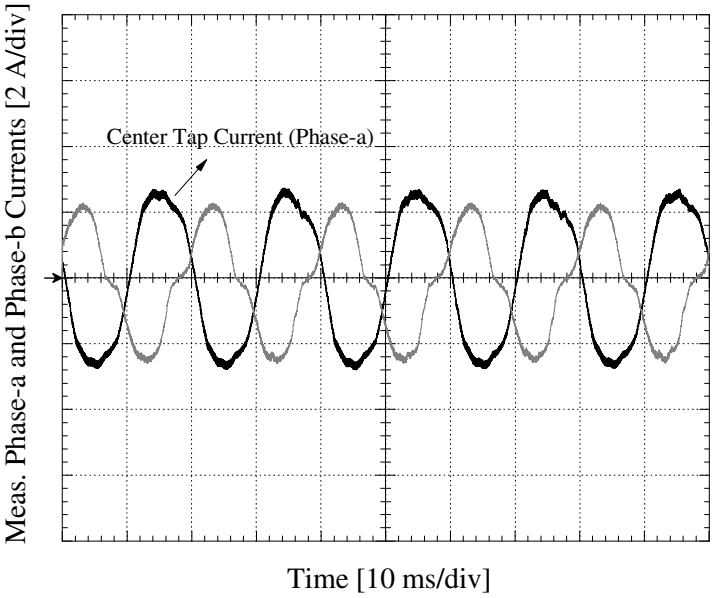

Figure VI.20. Meas. phase–a and phase–b current for m = 1.0, (U_{DC} = 100 V) and (R_{Load} = 43 Ω and L_{Load} = 50 mH).

Figure VI.21 illustrates phase–a and phase–b currents of the PMSG driven with 500 r/min. Peak values for phase–a current is 2.68 A and for phase–b current is 2.36 A. In VI.22, phase–c current under the same conditions have been measured. Peak value of phase–c current has been measured to be 2.12 A. According to the measurements, imbalance state between the phases in FSTP controlled PMSG is 15% for phase–a and phase–b, 10% for the phase–b and phase–c, and 25% for the phase–a and phase–c at voltage changes. Figure VI.23 illustrates phase–a and phase–b currents of the PMSG driven with 300 r/min. Peak values for phase–a current is 2.6 A and for phase–b current is 2.52 A. In Figure VI.24, phase–a and phase–b currents of the PMSG driven with 200 r/min is shown. Peak values has been measured to be 3.64 A for phase–a current and 2.52 A for phase–b current. According to the measurements, unbalance condition between the phases in FSTP controlled PMSG is at the rate of 45% at voltage changes for phase–a and phase–b.

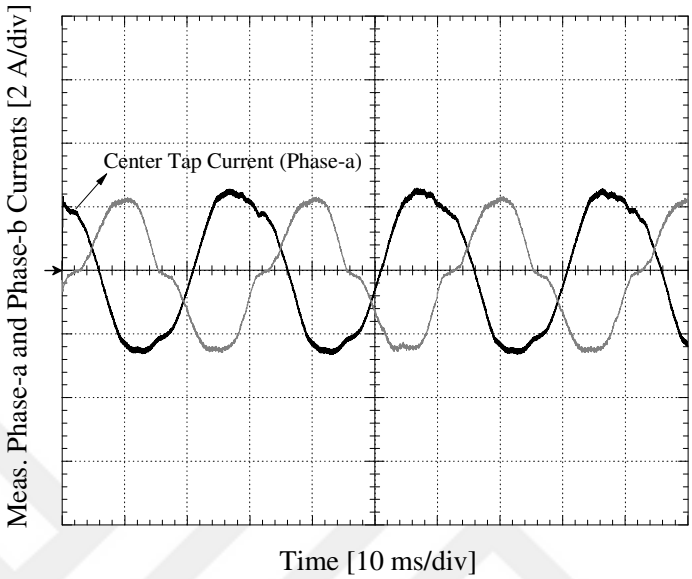

Figure VI.21. Meas. phase–a and phase–b current for m = 0.5, (U_{DC} = 100 V) and (R_{Load} = 43 Ω and L_{Load} = 50 mH).

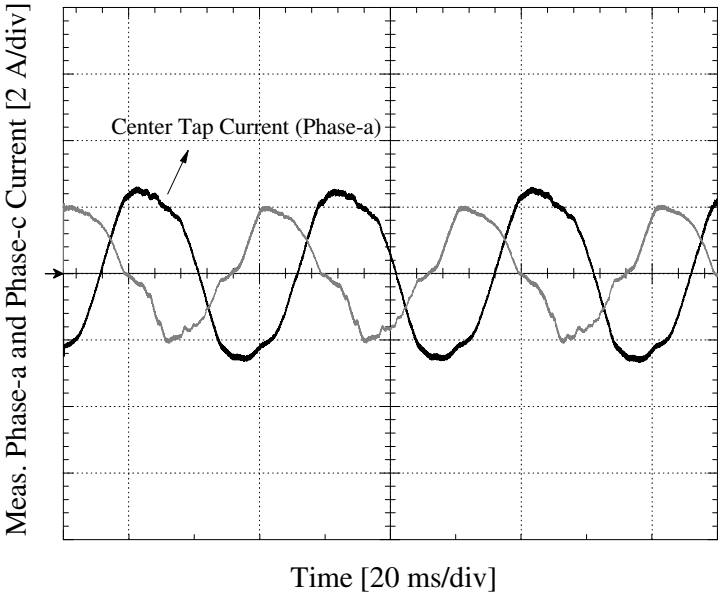

Figure VI.22. Meas. phase–a and phase–c current for m = 0.5, (U_{DC} = 100 V) and (R_{Load} = 43 Ω and L_{Load} = 50 mH).

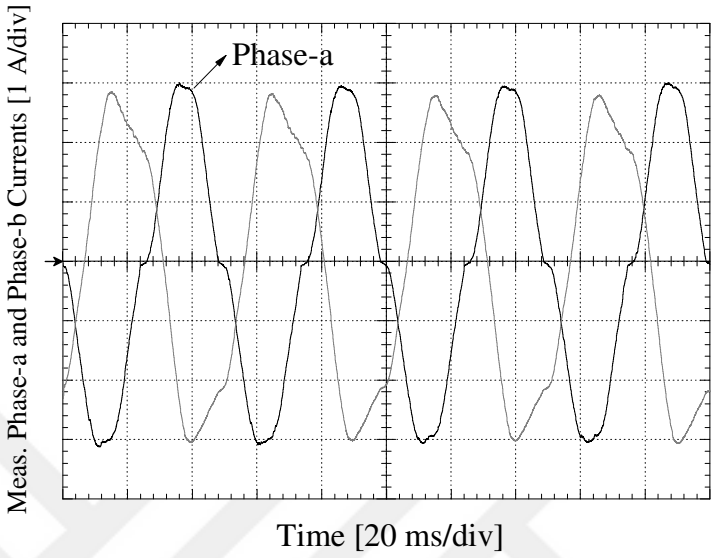

Figure VI.23. Meas. phase–a and phase–b current f for m = 0.5, (U_{DC} = 100 V) and (R_{Load} = 43 Ω and L_{Load} = 50 mH).

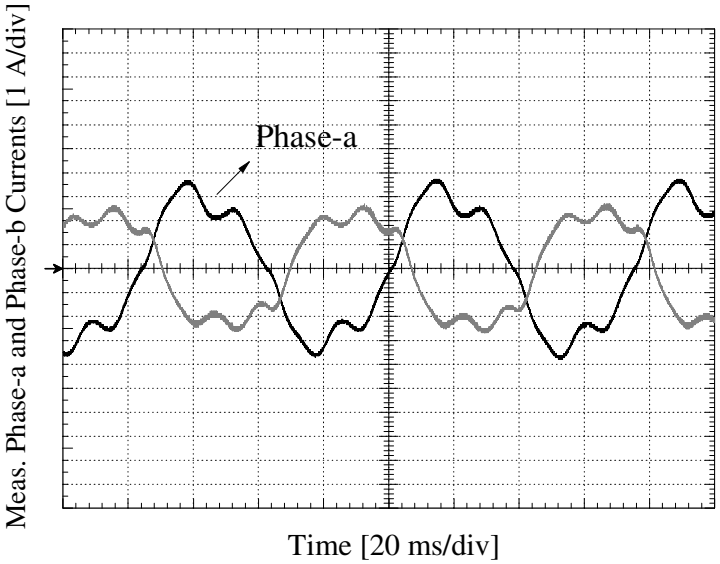

Figure VI.24. Meas. phase–a and phase–b current for m = 0.5, (U_{DC} = 100 V) and (R_{Load} = 43 Ω and L_{Load} = 50 mH).

It can be observed that the lower the speed level under PMSG control gets, the more unbalance condition between the phases increases. 200 r/min speed level has been

achieved which using proposed method which is performance enhancement based on parameter estimation. Experimental results show that the corrupting effects of stator resistance and rotor flux linkage dominate at low speed position estimation. This value corresponds to 0.06 p.u. at the PMSG having 3000 r/min rated speed.

The THD of the voltage between phase–a to phase–b at the LCL-filter output of four-switched off-grid side output is 6.6% and it is acceptable.

6.5. Conclusions

While macro-scale wind turbines are solving problems at industrial and high power levels, participation of individual users into energy production is possible with micro-scale wind turbines. Especially, rural zones without electric energy, base stations, highways and individual uses are said to be application areas for micro-scale energy production. It can be easily predicted that the small powerful energy production can be rapidly increased with integration of smart grid.

It is proved with this study that the inclusion of a simple, effective and low-cost position sensorless control in the generator side show that renewable wind energy system can be a viable distributed green energy solution for rural areas.

VII. SUMMARY AND CONCLUSIONS

Because the proposed method depends on back-EMF estimation, it is affected by the parameter variation. Elimination of the position errors caused from parameter change is estimated with online rotor flux linkage and stator resistance estimators using MRAS and the updates are provided in the feedforward voltage estimation model. With the MRAS parameter estimation, performance and stability of the sensorless drive scheme in steady state and in low speed are improved. Similar hybrid algorithms, in addition to a position estimation method, an observer algorithm and on-line parameter estimation method are required as superiors. In order to improve the position estimation especially in low speed region, EKF and MRAS are used together and a hybrid position control algorithm is suggested. In that method, while rotor flux variation is estimated by EKF, position estimation is done by MRAS. In the other study, while MRAS is used in the estimation of slowly changing parameters, the SMO is used for the position estimation. In controlling of the sensorless PMSM drive that is developed by using V/Hz and FOC, Luenberger observer is developed for rotor flux estimation and the effects caused from rotor flux change are minimized. The most important reason of using these hybrid approaches is that parameters affect each other and one prediction algorithm does not deliver the desired result. However, when compared to other methods, because MRAS is simple and applicable, it provides fast stability in parameter estimation. Therefore, it presents an advantage in the proposed sensorless control method.

A low-power and low-cost wind generator control algorithm is developed for areas where energy transfer is difficult and impossible. While macro-scale wind turbines

solve energy problems at industrial and high power levels, participation of individual users in energy production is possible with micro-scale wind turbines. Especially, rural zones without electric energy, base stations, highways and individual usages are considered to be application areas for micro-scale energy production. It can be easily predicted that the low power energy production can be rapidly increased with integration of smart grid.

One of the most important disadvantages of wind turbines are the low productivity and failure in producing energy under 7 m/s that plays a more vital role in low-power wind turbines. Also, energy must be produced between 2-7 m/s in order to enable energy production at maximum productivity for individual uses. A sensor-fitted PMSG must be used in order to enable more productive energy production at these speed levels. However, the cost of encoder in PMSG turbine structures in low power levels makes the system expensive. Therefore, uncontrolled and sensorless PMSGs are generally used in the industry. In the study, without gearbox, a sensorless control algorithm that enables true position estimation at low speeds is developed. Additionally, with the aim of reducing the total cost of semiconductors, the control of both generator and grid/load sides are ensured by developing a four switch inverter topology. The results show that compared to a six switch and sensored structure, 15% power loss is experienced and less than 5% harmonics are observed. The high values of total harmonics deterioration observed in some phase values can be minimized with compensation algorithm that is added to the control system in four switch inverter.

The proposed system can be used in small (low power) wind turbine systems as well as in household appliances operating in similar power ranges and pump drive systems. Thus, a small-sized low-cost inverter use is ensured. The cost of frequency

converters for electric machines can be reduced at the rate of 15% by 2020. Approximately 75% of electric machines used in Turkey are driven as line start or without frequency converter, therefore the quality of energy and machine operating efficiency are reduced. In order to obtain IE4 energy efficiency class aimed in 2020, these motors must be either replaced with high-efficient permanent-magnet motors (LSPMSM) or driven with the help of a frequency converter. The cost of frequency converter will have been decreased and the energy efficiency will have been increased with the proposed structure.

7.1. The Comments and Findings

- The sensorless control method based on the feedforward voltage estimation model has a simple and easily applicable structure. The method which previously applied to induction motors is presented in the study as an important option also for PMSM and IPMs. This can create a bridge for an important gap in literature and market, because it reacts fast effected from parameter changes less, and easily-applicable when compared to sensorless control methods commonly used in the industry.

- Feedforward voltage estimation model provides an efficient solution in low speed levels. In the studies, the rotor speed is reduced to 0.1 p.u. level. The proposed method can also be used in very low speeds with selecting the compounds of the system and regulation of non-linear variables more compatible.

- The issue that should be focused in sensorless motor control methods based on back-EMF estimation is the control of low-changing and fast-changing parameters with separate methods. While fast variables such as speed, position, inertia are controlled with fast, simple and dynamic algorithm; stator resistance, rotor flux linkage and stator inductance change slowly due to temperature, environmental conditions and aging.

These values should be observed with an observer or parameter estimation methods and should update PMSM steady-state model variables at each cycle.

- The proposed SVPWM algorithm does not need the rotor position angle.
- With the feedforward stator voltage estimation model, PMSM can be started from zero speed under no load. In literature, there is no method exist based on back-EMF estimation that can start from zero speed for PMSM. The proposed method in the studies done in literature resembles to V/Hz method. Moreover, torque control can also be efficiently performed with the proposed method.
- Stator resistance and rotor flux linkage are estimated separately with MRAS method. The sensorless PMSM control performance is improved by enabling the parameter estimation to update the PMSM steady-state model.
- Oscillations generated by MRAS method in zero crossing points can be considerably decreased with the help of a LPF that is designed at the output of the MRAS block.
- It is planned to use the developed model with High Frequency Signal Injection method with the aim of improving working performance in very low speed region (<5 rpm) later on. HF Signal frequency method will only be engaged in low speeds and the dynamic and simple structure of proposed FFVE method shall be used in middle and high speeds.
- It is observed that FFVE method is less affected from parameter changes compared to other methods. It is also observed that PMSM kept its stability even when stator resistance value is increased up to 85% of the initial value.

• MRAS method takes more work out of the controller when compared to other observer and parameter estimation methods. Therefore, it offers advantages for parameter estimation among other hybrid sensorless methods.

• The most important advantages obtained when traditional SSTP and FSTP test results are compared are reduction in switch cost, reduction in switching losses, faster reaction in control systems based on estimation algorithms. However, disadvantages are increase in current peak value, decrease in rated power and unbalanced phase currents and phase voltages. The most important advantage of the developed FSTP algorithm is easy adaptation to field oriented control by just changing the switching periods. While most of similar methods need rotor position knowledge in sectoral determination, the proposed SVPWM can determine the sector without position information. Especially, FSTP control offered in sensorless control algorithms brings important advantages:

• The direct-drive is a productive factor in small wind turbines.

• The K constant in feedforward algorithm is the leading coefficient among other basic variables affecting the stability of the system. It is stipulated that an efficient sensorless control can be ensured in very low speed fields by providing adaptive K value structure.

• With this study, the position knowledge in low speed ranges is obtained with much better sensibility compared to many other sensorless algorithms and the opportunity to work in a wide speed range in motor and generator studies is provided.

• An algorithm at the same stability without intervening field-oriented control algorithm is designed with the method developed for the four switch space vector

algorithm. With the help of a macro code that can be added to the environmental library, all desired vector control algorithms can be driven with four switch inverter.

- Speed range of the four switch space vector algorithm appears similar to the six switch version. However, this can fulfill the 2 N·m loading conditions at the ratio of 85%.
- Except the peak decline of sinusoidal form produced in four-switch space vector, sinus current waveform with purity close to six-switched space vector is obtained.
- The total harmonics distortion, drop to below 3% in the six switch system, is observed below 5% in the four switch system.
- While capacitor voltages of the center tap point that is connected to the third phase in the four switch structure are needed to be equal ideally, it is observed in measurements that two capacitors are not equalized due to non-linear variables.
- The most important advantage of FSTP is to decrease the cost of switching components. Some applications (washing machine, micro-scale wind turbines etc.) that high position sensibility is not required, gearbox, encoder and two switching components are eliminated.
- One-leg fault situations that will appear in SSTP inverters can be prevented with the proposed FSTP structure.
- An innovative approach in simulation studies is developed by using C like Matlab Function and a ready-to-test system is obtained.
- When the obtained results in experimental studies are compared with the developed simulation model, changes in switching signals and other non-linear effects

of variables have similarities with each other. The proposed method enables to obtain data close to experimental results and simulations for DSPs of C2000 family.

REFERENCES

[1] H. Le-huy, "Modeling and simulation of electrical drives using MATLAB/Simulink and power system blockset," *in Proc. IEEE IECON*, Denver, CO, Nov. 29-Dec 2., vol. 3, pp. 1603–1611, 2001.

[2] S. B. Ozturk et al., "Low-cost direct torque control of permanent magnet synchronous motor using hall-effect sensors," *in Proc. IEEE APEC*, Dallas, TX, Mar. 19-23, pp. 667–673, 2006.

[3] Z. L. Z. Lu et al., "The modeling and simulation of a permanent magnet synchronous motor with direct torque control based on Matlab/Simulink," *in Proc. IEEE IEMDC San Antonio*, TX, May 15–18, pp. 1150–1156, 2005.

[4] T. T. Liu et al., "Simulation of PMSM vector control system based on matlab/simulink," *2009 International Conference on Measuring Technology and Mechatronics Automation, ICMTMA 2009*, vol. 2, pp. 343–346, 2009.

[5] X. Wang, N. Liu, and R. Na, "Simulation of PMSM field-oriented control based on SVPWM," *5th IEEE Vehicle Power and Propulsion Conference, VPPC '09*, no. 4, pp. 1465–1469, 2009.

[6] J. Zhang, Z. Shu, "Matlab based permanent magnet synchronous motor vector control simulation," *in Proc. IEEE ICCSIT*, Amsterdam, Netherlands, Dec. 10-11, pp. 539–542, 2010.

[7] A. Kamalaselvan and S. L. Prakash, "Modeling simulation and analysis of closed loop speed control of PMSM drive system," *2014 International Conference on Circuits, Power and Computing Technologies [ICCPCT-2014]*, pp. 692–697, 2014.

[8] G. Yan, “Simulation for the vector control algorithm of permanent magnet synchronous motor,” *2015 7th International Conference on Intelligent Human-Machine Systems and Cybernetics*, vol. 1, pp. 456–459, 2015.

[9] H. Qi, Y. Zhang, and N. Gao, “Research and implement of PMSM regenerative braking strategy based on controllable rectification,” *in Proc. IEEE PEDS*, Jun. 9–12, pp. 289–294, 2015.

[10] A. Adriana, L. Zaharia, and M. V. Zaharia, “Modeling and simulation of a brushless DC wind energy conversion system,” *in Proc. IEEE EVER*, Mar. 31–Apr. 2, pp. 1–7, 2015.

[11] M. S. Mahammadsoaib and M. P. Sajid, “Vector controlled PMSM drive using SVPWM technique-A MATLAB/simulink implementation,” *International Conference on Electrical, Electronics, Signals, Communication and Optimization, EESCO 2015*, pp. 1–5, 2015.

[12] D. J. Vaghela and H. N. Chaudhari, “Investigation of design , analysis and performance of hysteresis current control PMSM drive,” *International Conference on Electrical, Electronics, Signals, Communication and Optimization (EESCO)*, pp. 1–6, 2015.

[13] R. Duma et al., “Rapid prototyping of control systems using embedded target for TI C2000 DSP,” *2007 Mediterranean Conference on Control and Automation, MED*, pp. 1–5, 2007.

[14] C. Rusu, I. Birou, and M. M. Radulescu, “Developing embedded control system platform for testing PMSM drives,” *in Proc. IEEE EPE, Iasi, Romania*, Oct. 16–18, pp. 677–682, 2014.

[15] C. Rusu et al., "Embedded motor drive prototype platform for testing control algorithms," *2014 International Conference on Applied and Theoretical Electricity, ICATE 2014 - Proceedings*, pp. 1–6, 2014.

[16] B. K. Bose, *Power Electronics and Variable Frequency Drives – Technology and Applications*. Piscataway, NJ: IEEE Press, 1997.

[17] R. Krishnan, *Permanent Magnet Synchronous and Brushless DC Motor Drives.* Boca Raton, FL: CRC Press, 2009.

[18] P. Pillay and R. Krishnan, "Modeling, simulation and analysis of permanent-magnet motor drives, Part. I: The permanent-magnet synchronous motor drive," *IEEE Trans. Ind. App.*, vol. 25, no. 2, pp. 265–273, 1989.

[19] S. B. Ozturk, "Modelling, simulation and analysis of low-cost direct torque control of PMSM using hall-effect sensors," M.S. thesis, Texas A&M University, College Station, TX, USA, 2005.

[20] M. Bhardwaj, "Sensored Field Oriented Control of 3-Phase Permanent Magnet Synchronous Motors," Texas Instruments, Dallas, TX, USA, Appl. Rep. SPRABQ2, Jul. 2013.

[21] S. B. Ozturk and H. A. Toliyat, "Direct torque and indirect flux control of brushless DC motor," *IEEE/ASME Trans. on Mechatronics*, vol. 16, no. 2, pp. 351–360, 2011.

[22] S. B. Ozturk, W. C. Alexander, and H. A. Toliyat, "Direct torque control of four-switch brushless DC motor with non-sinusoidal back-EMF," *IEEE Trans. Power Electron.*, vol. 25, no. 2, pp. 263–271, 2008.

[23] X. Xiao, C. Chen, and M. Zhang, "Dynamic permanent magnet flux estimation of permanent magnet synchronous machines," *IEEE Trans. Applied*

Superconductivity, vol. 20, no. 3, pp. 1085–1088, 2010.

[24] Y. Inoue et al., "Performance improvement of sensorless IPMSM drives in a low-speed region using online parameter identification," *IEEE Trans. Ind. App.*, vol. 47, no. 2, pp. 798–804, 2011.

[25] P. D. C. Perera et al., "A sensorless, stable V/f control method for permanent-magnet synchronous motor drives," *IEEE Trans. Ind. App.*, vol. 39, no. 3, pp. 783–791, 2003.

[26] K. Akatsu and A. Kawamura, "Sensorless very low-speed and zero-speed estimations with online rotor resistance estimation of induction motor without signal injection," *IEEE Trans. Ind. App.*, vol. 36, no. 3, pp. 764–771, 2000.

[27] A. Piippo, M. Hinkkanen, and J. Luomi, "Adaptation of motor parameters in sensorless PMSM drives," *IEEE Trans. Ind. App.*, vol. 45, no. 1, pp. 203–212, 2009.

[28] S. Mouna and B. Lassaad, "Speed sensorless indirect stator field oriented control of induction motor based on luenberger observer," *IEEE International Symposium on Ind. Electronics*, vol. 3, pp. 2473–2478, 2006.

[29] A. Piippo, M. Hinkkanen, and J. Luomi, "Analysis of an adaptive observer for sensorless control of interior permanent magnet synchronous motors," *IEEE Trans. Ind. Electron.*, vol. 55, no. 2, pp. 570–576, 2008.

[30] A. Consoli, G. Scarcella, and A. Testa, "Industry application of zero-speed sensorless control techniques for PM synchronous motors," *IEEE Trans. Ind. App.*, vol. 37, no. 2, pp. 513–521, 2001.

[31] U. Schaible and B. Szabados, "Dynamic motor parameter identification for high speed flux weakening operation of brushless permanent magnet synchronous

machines," *IEEE Trans. Energy Conversion*, vol. 14, no. 3, pp. 486–492, 1999.

[32] J. K. Seok, J. K. Lee, and D. C. Lee, "Sensorless speed control of nonsalient permanent-magnet synchronous motor using rotor-position-tracking PI controller," *IEEE Trans. Ind. Electron.*, vol. 53, no. 2, pp. 399–405, 2006.

[33] R. J. Kerkman et al., "A new flux and stator resistance identifier for AC drive systems," *IEEE Trans. Ind. App.*, vol. 32, no. 3, pp. 585–593, 1996.

[34] B. Stumberger et al., "Evaluation of saturation and cross-magnetization effects in interior permanent-magnet synchronous motor," *IEEE Trans. Ind. App.*, vol. 39, no. 5, pp. 1264–1271, 2003.

[35] T. S. Low, T. H. Lee, and K. T. Chang, "A nonlinear speed observer for permanent-magnet synchronous motors," *IEEE Trans. on Ind. Electron.*, vol. 40, no. 3, pp. 307–316, 1993.

[36] S. Morimoto, M. Sanada, and Y. Takeda, "Mechanical sensorless drives of IPMSM with online parameter identification," *IEEE Trans. Ind. App.*, vol. 42, no. 5, pp. 1241–1248, 2006.

[37] K. W. Lee, D. H. Jung, and I. J. Ha, "An online identification method for both stator resistance and back-EMF coefficient of PMSMs without rotational transducers," *IEEE Trans. Ind. Electron.*, vol. 51, no. 2, pp. 507–510, 2004.

[38] S. Bolognani, M. Zigliotto, and M. Zordan, "Extended-range PMSM sensorless speed drive based on stochastic filtering," *IEEE Trans. Power Electron.*, vol. 16, no. 1, pp. 110–117, 2001.

[39] R. Ramakrishnan et al., "Real time estimation of parameters for controlling and monitoring permanent magnet synchronous motors," *in Proc. IEEE IEMDC*, no. 2, pp. 1194–1199, 2009.

[40] O. Hernandez et al., “Parameter identification of PMSMs ssing experimental measurements and a PSO algorithm,” *IEEE Trans. Ins. and Meas.*, vol. 64, no. 8, pp. 2146–2154, 2015.

[41] K. Liu and Z. Q. Zhu, “Position offset-based parameter estimation for permanent magnet synchronous machines under variable speed control,” *IEEE Trans. Power Electron.*, vol. 30, no. 6, pp. 3438–3446, 2015.

[42] S. J. Underwood and I. Husain, “Online parameter estimation and adaptive control of permanent-magnet synchronous machines,” *IEEE Trans. Ind. Electron.*, vol. 57, no. 7, pp. 2435–2443, 2010.

[43] S. Bolognani, L. Peretti, and M. Zigliotto, “Parameter sensitivity analysis of an Improved open-loop speed estimate for induction motor drives,” *IEEE Trans. on Power Electron.*, vol. 23, no. 4, pp. 2127–2135, 2008.

[44] D. P. Marcetic and S. N. Vukosavic, “Speed-sensorless AC drives with the rotor time constant parameter update,” *IEEE Trans. Ind. Electron.*, vol. 54, no. 5, pp. 2618–2625, 2007.

[45] Y. Shi et al., “Online identification of permanent magnet flux based on extended Kalman filter for IPMSM drive with position sensorless control,” *IEEE Trans. Ind. Electron.*, vol. 59, no. 11, pp. 4169–4178, 2012.

[46] K. Liu, Z. Q. Zhu, and D. A. Stone, “Parameter estimation for condition monitoring of PMSM stator winding and rotor permanent magnets,” *IEEE Trans. Ind. Electron.*, vol. 60, no. 12, pp. 5902–5913, 2013.

[47] T. Boileau, B. Nahid-Mobarakeh, and F. Meibody-Tabar, “On-line identification of PMSM parameters: Model-reference vs EKF,” *in Proceedings- IAS Annual Meeting (IEEE Industry Applications Society)*, pp. 1–8, 2008.

[48] M. Eskola and H. Tuusa, "Comparison of MRAS and novel simple method for position estimation in PMSM drives," *in Proceedings IEEE 34th Annual Conference on Power Electronics Specialist, 2003. PESC '03*, vol. 2, pp. 550–555, 2003.

[49] M. Hilairet et al., "Industrial applications of the kalman filter: A review," *IEEE Trans. Ind. Electron.*, vol. 60, no. 12, pp. 5458–5471, 2011.

[50] Z. Wang, Q. Teng, and C. Zhang, "Speed identification about PMSM with MRAS," *in Proceedings IEEE 6th International Power Electronics and Motion Control Conference, IPEMC '09*, vol. 3, pp. 1880–1884, 2009.

[51] P. Castaldi and A. Tilli, "Parameter estimation of induction motor at standstill with magnetic flux monitoring," *IEEE Trans. Control Systems Tech.*, vol. 13, no. 3, pp. 386–400, 2005.

[52] M. A. Hamida et al., "An adaptive interconnected observer for sensorless control of PM synchronous motors with online parameter identification," *IEEE Trans. Ind. Electron.*, vol. 60, no. 2, pp. 739–748, 2013.

[53] T. F. Chan et al., "Sensorless permanent-magnet synchronous motor drive using a reduced-order rotor flux observer," *IET Electric Power App.*, vol. 2, no. 2, pp. 88–98, 2008.

[54] B. Nahid-Mobarakeh, F. Meibody-Tabar, and F. M. Sargos, "Mechanical sensorless control of PMSM with online estimation of stator resistance," *IEEE Trans. Ind. App.*, vol. 40, no. 2, pp. 457–471, 2004.

[55] M. Rashed et al., "Sensorless indirect-rotor-field-orientation speed control of a permanent-magnet synchronous motor with stator-resistance estimation," *IEEE Trans. Ind. Electron.*, vol. 54, no. 3, pp. 1664–1675, 2007.

[56] I. Baik, K. H. Kim, and M. J. Young, "Robust nonlinear speed control of PM synchronous motor using boundary layer integral sliding mode control technique," *IEEE Trans. Control Systems Tech.*, vol. 8, no. 1, pp. 47–54, 2002.

[57] D. A. Liu, L. Cartes, "Synchronisation based adaptive parameter identification for permanent magnet synchronous motors," *IET Control Theory & App.*, vol. 1, no. 4, pp. 1015–1022, 2007.

[58] J. Holtz, "Sensorless speed and position control of induction motor drives," *in Proceedings 27th Annu Conf IEEE Industrial Electronics*, pp. 1200–1205, 2003.

[59] R. J. Kerkman, G. L. Skibinski, and D. W. Schlegel, "A.C. drives; Year 2000 and beyond," *in Proceedings APEC '99, Fourteenth Annual Applied Power Electronics Conference and Exposition*, vol. 1, pp. 28–39, 1999.

[60] A. F. Rashed, M. Stronach, "A stable back-EMF MRAS-based sensorless low-speed induction motor drive insensitive to stator resistance variation," *IEE Proceedings-Electric Power Applications*, vol. 151, no. 6, pp. 685–693, 2003.

[61] W. Yan et al., "A MRAS based speed identification scheme for a PM synchronous motor drive using the sliding mode technique," *IEEE International Conference on Mechatronics and Automation, ICMA 2009*, pp. 3656–3661, 2009.

[62] Y. Zhao, W. Qiao, and L. Wu, "Improved rotor position and speed estimators for sensorless control of interior permanent-magnet synchronous machines," *IEEE Journal of Emerging and Selected Topics in Power Electron.*, vol. 2, no. 3, pp. 627–639, 2014.

[63] V. Blasko, L. Arnedo, and D. Jiang, “An integral method combining V / Hz and vector control of permanent magnet motor,” *in Proceedings IEEE Energy Conversion Congress and Exposition (ECCE)*, pp. 4472–4477, 2014.

[64] B. Hafez et al., “Single sensor based three-phase permanent-magnet synchronous motor drive system with luenberger observers for motor line current reconstruction,” *IEEE Trans. Ind. App.*, vol. 50, no. 4, pp. 2602–2613, 2014.

[65] K. Liu et al., “Online multiparameter estimation of nonsalient-pole PM synchronous machines with temperature variation tracking,” *IEEE Trans. Ind. Electron.*, vol. 58, no. 5, pp. 1776–1788, 2011.

[66] K. H. Kim, “DSP-based sequential parameter estimation of PWM inverter-fed IPM synchronous machine for auto-tuning applications,” *Int. Journal of Control and Automation*, vol. 6, no. 2, 2013.

[67] Y. Feng et al., “Improved sliding mode model reference adaptive system speed observer for fuzzy control of direct-drive permanent magnet synchronous generator wind power generation system,” *IET Renewable Power Generation*, vol. 7, no. 1, pp. 28–35, 2013.

[68] J. Holtz, “Sensorless control of induction machines - with or without signal injection?,” *IEEE Trans. Ind. Electron.*, vol. 53, no. 1, pp. 7–30, 2006.

[69] K. Nagata et al., “A simple robust voltage control of high power sensorless induction motor drives with high start torque demand,” *IEEE Trans. Ind. App.*, vol. 44, no. 2, pp. 604–611, 2008.

[70] S. N. Vukosavic and A. M. Stankovic, “Sensorless induction motor drive with a single DC-link current sensor and instantaneous active and reactive power feedback,” *IEEE Trans. Ind. Electron.*, vol. 48, no. 1, pp. 195–204, 2001.

[71] S.S. Perng, Y.S. Lai, and C.H. Liu, "Sensorless control for induction motor drives based on new speed identification scheme," *in Proceedings of the Power Conversion Conference*, pp. 553–558, 1997.

[72] Y. Okuyama, T. Fujimoto, N. Matsui, T. Kubota, "A high performance speed control scheme of induction motor without speed and voltage sensors," *in Proceedings IEEE IAS*, pp. 106–111, 1986.

[73] Z. F. Wang et al., "Real-time PMSM temperature rising in electric vehicles with MRAS," *in Proceedings of the 2009 WRI Global Congress on Intelligent Systems, GCIS 2009*, vol. 3, pp. 66–70, 2009.

[74] H. W. V. Broeck and J. D. V. Wyk, "A comparative investigation of a three-phase induction machine drive with a component minimized voltage-fed inverter under diferent control options," *IEEE Trans. Ind. App.*, vol. 20, no. 2, pp. 309–320, 1984.

[75] S. Kazemlou and M. R. Zolghadri, "Direct torque control of four-switch three phase inverter fed induction motor using a modified SVM to compensate DC-link voltage imbalance," *in Proceedings International Conference on Electric Power and Energy Conversion Systems, EPECS'09*, pp. 1–6, 2009.

[76] T. D. Nguyen, H. M. Nguyen, and H. H. Lee, "An adaptive carrier-based PWM method for four-switch three-phase inverter," *in Proceedings IEEE International Symposium on Industrial Electronics*, pp. 1552–1557, 2009.

[77] P. Q. Dzung et al., "A new FPGA implementation of four- switch three-phase inverter," *in Proceedings of the International Conference on Power Electronics and Drive Systems*, pp. 882–887, 2009.

[78] H. H. Lee et al., “The adaptive space vector PWM for four switch three phase inverter fed induction motor with DC - Link voltage imbalance,” *in Proceedings IEEE Region 10 Annual International Conference*, pp. 1–6, 2008.

[79] T. C. Dzung, P. Q. Phuong, L. M. Ving, P. Q. Hoang, N. M. Binh, “New space vector control approach for four switch three phase inverter (FSTPI),” *in Proceedings 7th International Conference on Power Electronics and Drive Systems*, pp. 1002–1008, 2007.

[80] Y. Bhadauria et al., “Simulation & analysis of three phase voltage source Inverter using four semiconductor switches,” *in Proceedings Nirma University International Conference on Engineering (NUiCONE)*, pp. 1–14, 2012.

[81] J. Lee, S. Ahn, and D. Hyun, “A BLDCM drive with trapezoidal back EMF using four-switch three phase inverter,” *in Proceedings IEEE Industry Applications Conference*, vol. 3, pp. 1705–1709, 2000.

[82] J. Lee, T. Kim, and D. Hyun, “A study for improved of speed response characteristic in four-switch BLDC motor,” *in Proc. IEEE IECON*, vol. 2, pp. 1339–1343, 2004.

[83] M. N. Uddin et al., “Performance analysis of a 4-Switch, 3-Phase inverter based cost effective IPM motor drives,” *in Proc. IEEE CCECE*, vol. 1, pp. 85–88, 2004.

[84] B. K. Lee, T. H. Kim, and M. Ehsani, “On the feasibility of four-switch three-phase BLDC motor drives for low cost commercial applications: topology and control,” *IEEE Trans. Power Electron.*, vol. 18, no. 1 I, pp. 164–172, 2003.

[85] C.T. Lin, C.W. Hung, and C.W. Liu, “Position sensorless control for four-Switch three-phase brushless DC motor drives,” *IEEE Trans. Power Electron.*, vol. 23,

no. 1, pp. 438–444, 2008.

[86] A. Halvaei Niasar, A. Vahedi, and H. Moghbelli, “A novel position sensorless control of a four-switch, brushless DC motor drive without 30° phase shifter,” *IEEE Trans. Power Electron.*, vol. 23, no. 6, pp. 3079–3087, 2008.

[87] C. W. Hung et al., “Fuzzy gain scheduling PI controller for a sensorless four switch three phase BLDC motor,” *Conference Proceedings - IEEE Applied Power Electronics Conference and Exposition - APEC*, pp. 420–424, 2010.

[88] A. H. Niasar, H. Moghbeli, and A. Vahedi, “A novel sensorless control method for four-switch , brushless DC motor Drive without using any phase shifter,” *in Proc. IEEE ICEMS*, pp. 408–413, 2007.

[89] M. Ebadpour, M. B. B. Sharifian, and M. R. Feyzi, “A simple position sensorless control strategy for four-switch three-phase brushless DC motor drives using single current sensor,” *2011 2nd Power Electronics, Drive Systems and Technologies Conference*, vol. 2, no. 5, pp. 235–240, 2011.

[90] C. Lin et al., “A sensorless position control for four-switch three-phase inverter-fed interior permanent magnet synchronous motor drive systems,” *IEEE/ASME International Conference on Advanced Intelligent Mechatronics*, pp. 1036–1041, 2012.

[91] J. Jang et al., “Sensorless control of four-switch three-phase PMSM drive using extended kalman filter,” *in Proc. IEEE IECON*, pp. 1368–1372, 2008.

[92] E. M. Fernandes et al., “Speed sensorless PMSM motor drive system based on four-switch three-phase converter,” *Proceedings, IECON 2014 - 40th Annual Conference of the IEEE Industrial Electronics Society*, pp. 902–906, 2014.

[93] J. R. Fu and T. A. Lipo, “A strategy to isolate the switching device fault of a current regulated motor drive,” *Conference Record of the 1993 IEEE Industry Applications Conference Twenty-Eighth IAS Annual Meeting*, pp. 1015–1020, 1993.

[94] D. Sun et al., “Four-switch inverter fed PMSM DTC with SVM approach for fault tolerant operation,” *Proceedings of IEEE International Electric Machines and Drives Conference, IEMDC 2007*, vol. 1, pp. 295–299, 2007.

[95] Ł. Dominik and K. Siembab, “Comparison of fault tolerant control algorithm using space vector modulation of PMSM drive,” *in Proc. IEEE ICEMS*, pp. 24–31, 2014.

[96] D. Sun and J. Meng, “Research on fault tolerant inverter based permanent magnet synchronous motor direct torque control drives,” *in Proceedings Industrial Electronics and Applications, 2006 1ST IEEE Conference on*, pp. 1–5, 2006.

[97] D. Sun and Y. He, “A modified direct torque control for PMSM under inverter fault,” *Electrical Machines and Systems, 2005. ICEMS 2005. Proceedings of the Eighth International Conference on*, vol. 3, p. 2473, 2005.

[98] B. Wang, Y. He, and Y. B. Ivonne, “Four switch three phase inverter fed PMSM DTC system with nonlinear perpendicular flux observer and sliding mode control,” *International Conference on Electrical Machines and Systems, ICEMS 2008*, pp. 3206–3211, 2008.

[99] J. D. Lee et al., “A simple fault detection of the open-switch damage in BLDC motor drive systems,” *in Proc. IEEE PESC*, pp. 733–737, 2007.

[100] B. G. Park et al., “Fault tolerant system under open phase fault for BLDC motor drives,” *in Proc. IEEE PESC*, pp. 18–22, 2006.

[101] B. G. Park et al., “Fault tolerant strategies for BLDC motor drives under switch faults,” *in Proc. IEEE IAS*, vol. 4, pp. 1637–1641, 2006.

[102] K. D. Hoang, Z. Q. Zhu, and M. P. Foster, “Influence and compensation of inverter voltage drop in direct torque-controlled four-switch three-phase PM brushless AC drives,” *IEEE Trans. Power Electron.*, vol. 26, no. 8, pp. 2343–2357, 2011.

[103] M. Masmoudi, B. El Badsi, and A. Masmoudi, “DTC of B4-inverter-fed BLDC motor drives with reduced torque ripple during sector-to-sector commutations,” *IEEE Trans. Power Electron.*, vol. 29, no. 9, pp. 4855–4865, 2014.

[104] S. Park et al., “A simple current control algorithm for torque ripple reduction of brushless DC motor using four-switch three-phase inverter,” *in Proc. IEEE PESC*, vol. 2, pp. 574–579, 2003.

[105] H. Niasar, A. Vahedi and H. Moghbelli, “Analysis and control of commutation torque ripple in four-switch three-phase brushless DC motor drive,” *in Proc. IEEE ICIT*, pp. 239–246, 2006.

[106] A. Halvaei Niasar, H. Moghbelli, and A. Vahedi, “Commutation torque ripple of four-switch, brushless DC motor drives, part I: Analysis,” *International Workshop on Advanced Motion Control, AMC*, pp. 541–546, 2006.

[107] A. Halvaei Niasar, H. Moghbelli, and A. Vahedi, “Commutation torque ripple of four-switch, brushless DC motor drives, part II: controllability and minimization,” *International Workshop on Advanced Motion Control, AMC*, pp. 547–552, 2006.

[108] T. Shi et al., “Three effective vectors-based current control scheme for four-switch three-phase trapezoidal brushless DC motor,” *IET Electric Power Applications*, vol. 7, no. 7, pp. 566–574, 2013.

[109] Q. Fu, H. Lin, and H. T. Zhang, “Single-current-sensor sliding mode driving strategy for four-switch three-phase brushless DC motor,” *Proceedings of the IEEE International Conference on Industrial Technology*, pp. 2396–2401, 2006.

[110] X. Changliang, Z. Li, and T. Shi, “A control strategy for four-switch three-phase brushless DC motor using single current sensor,” *IEEE Trans. Ind. Electron.*, vol. 26, no. 6, pp. 2058–2066, 2009.

[111] X. Changliang et al., “Current threshold on-line identification control theme based on intelligent controller for four-switch threephase brushless DC motor,” *Proceedings of 2008 IEEE International Conference on Mechatronics and Automation, ICMA 2008*, pp. 954–958, 2008.

[112] M. N. Uddin, T. S. Radwan, and M. A. Rahman, “Fuzzy-logic-controller-based cost-effective four-switch three-phase inverter-fed IPM synchronous motor drive system,” *IEEE Trans. Ind. App.*, vol. 42, no. 1, pp. 21–30, 2006.

[113] A. H. Niasar, H. Moghbelli, and A. Vahedi, “Adaptive neuro-fuzzy control with fuzzy supervisory learning algorithm for speed regulation of 4-switch inverter brushless DC machines,” *in Proceedings - IPEMC 2006: CES/IEEE 5th International Power Electronics and Motion Control Conference*, pp. 1–5, 2006.

[114] H. Niasar, A. Halvaei and A. Vahedi and H. Moghbelli, “ANFIS-based controller with fuzzy supervisory learning for speed control of 4-switch inverter brushless DC motor drive,” *in Proc. IEEE PESC*, pp. 1–5, 2006.

[115] X. Changliang, Z. Li, and Y. Wang, "A current control algorithm based on variable current threshold for four-switch three-phase BLDCM using intelligent controller," *in Proc. IEEE ICIT*, pp. 1–5, 2008.

[116] S. M. Madani, L. Hao, and H. A. Toliyat, "A low-cost four-switch BLDC motor drive with active power factor correction," *IECON Proceedings (Industrial Electronics Conference)*, vol. 1, pp. 579–584, 2002.

[117] V. Krishnaveni, K. Kiruthika, and S. S. Kumar, "Design and implementation of low cost four switch inverter for BLDC motor drive with active power factor correction," *in Proc. IEEE ICGCCEE*, pp. 1–7, 2014.

[118] S. Kim, S. Sul, and a F. Principle, "Sensorless control of AC motor - where are we now ?," *in Proc. IEEE ICEMS*, pp. 1–6, 2011.

[119] A. V. Krishna and S. Kumar, "Position-sensorless operation of brushless permanent-magnet machines - a review," *in Proc. IEEE ICGCEE*, pp. 1–10, 2014.

[120] R. Bojoi et al., "Sensorless control of PM motor drives - A technology status review," *2013 IEEE Workshop on Electrical Machines Design, Control and Diagnosis (WEMDCD)*, pp. 168–182, 2013.

[121] O. Benjak and D. Gerling, "Review of position estimation methods for IPMSM drives without a position sensor part I: Nonadaptive methods," *19th International Conference on Electrical Machines, ICEM 2010*, pp. 1–6, 2010.

[122] O. Benjak and D. Gerling, "Review of position estimation methods for IPMSM drives without a position sensor part II: Adaptive methods," *19th International Conference on Electrical Machines, ICEM 2010*, pp. 1–6, 2010.

[123] O. Benjak and D. Gerling, “Review of position estimation methods for PMSM drives without a position sensor, part III: Methods based on saliency and signal injection,” *Electrical Machines and Systems (ICEMS), 2010 International Conference on*, 2010.

[124] A. S. Ravikumar, S. Wekhande, and K. Chatterjee, “Comparison of high frequency signal injection techniques for rotor position estimation atlow speed to standstill of PMSM,” *in Proc. IEEE IICPE*, pp. 1–6, 2012.

[125] E. D. M. Fernandes et al., “Comparison of HF signal injection methods for sensorless control of PM synchronous motors,” *Conference Proceedings - IEEE Applied Power Electronics Conference and Exposition - APEC*, pp. 1984–1989, 2010.

[126] O. Bel, H. Brahim, and H. S. Attia, “Continuous HFSI techniques applied to rotor position estimation of IPMSM at standstill and low speed - a survey,” *in Proc. IEEE SSD*, pp. 1–10, 2011.

[127] D. Montesinos, S. Galceran, and F. Blaabjerg, “Low cost sensorless control of permanent magnet motors - an overview and evaluation,” *in Proc. IEEE IEMDC*, pp. 1681–1688, 2005.

[128] D. Montesinos and S. Galceran, “Sensorless control of PM synchronous motors and brushless DC motors - an overview and evaluation.,” *in Proc. IEEE EPE*, pp. 1–10, 2005.

[129] H. . Okuyama, T. Fujimoto, N. Fujii, “A simplified vector control system without speed and voltage sensors-effect of setting errors of control parameters and their compensation,” *Electrical Engineering Japan*, vol. 110, no. 4, pp. 129–139, 1990.

[130] O. C. Kivanc and S. B. Ozturk, "MATLAB function based approach to FOC of PMSM drive," *in Proc. IEEE EMS*, 2015.

[131] T. Boileau et al., "Online identification of PMSM parameters: Parameter identifiability and estimator comparative study," *IEEE Trans. Ind. App.*, vol. 47, no. 4, pp. 1944–1957, 2011.

[132] S. Dasgupta et al., "Application of four-switch-based three-phase grid-connected inverter to connect renewable energy source to a generalized unbalanced microgrid system," *IEEE Trans. Ind. Electron.*, vol. 60, no. 3, pp. 1204–1215, 2013.

[133] F. Iov and F. Blaabjerg, "Power electronics and control for wind power systems," *in Proc. IEEE PEMWA*, pp. 1–16, 2009.

[134] A. Parviainen, J. Pyrhonen, and P. Kontkanen, "Axial flux permanent magnet generator with concentrated winding for small wind power applications," *IEEE International Conference on Electric Machines and Drives*, pp. 1187–1191, 2005.

[135] J. R. Bumby et al., "A permanent magnet generator for small scale wind and water turbines," *in Proceedings of the 2008 International Conference on Electrical Machines, ICEM'08*, pp. 1–6, 2008.

[136] M. Andriollo et al., "Permanent magnet axial flux disc generator for small wind turbines," *Proceedings of the 2008 International Conference on Electrical Machines, ICEM'08*, pp. 1–6, 2008.

[137] A. Olano et al., "Design and construction of an outer-rotor PM synchronous generator for small wind turbines; comparing real results with those of FE model," *Proceedings of the 2008 International Conference on Electrical*

Machines, ICEM'08, no. 1, pp. 1–6, 2008.

[138] H. Haraguchi, S. Morimoto, and M. Sanada, "Suitable design of a PMSG for a small-scale wind power generator," *Proceedings - The 12th International Conference on Electrical Machines and Systems, ICEMS 2009*, pp. 1–6, 2008.

[139] Z. Zhang et al., "A space-vector-modulated sensorless direct-torque control for direct-drive PMSG wind turbines," *IEEE Trans. Ind. App.*, vol. 50, no. 4, pp. 2331–2341, 2014.

[140] M. Benadja and A. Chandra, "Sensorless control for wind energy conversion system (WECS) with power quality improvement," *IEEE PES General Meeting Conference and Exposition*, pp. 1–5, 2014.

[141] C.-M. Liaw and K.-W. Hu, "Position sensorless surface-mounted permanent-magnet synchronous generator and its application to power DC microgrid," *IET Power Electronics*, vol. 8, no. 9, pp. 1636–1650, 2015.

[142] J. A. Baroudi, V. Dinavahi, and a M. Knight, "A review of power converter topologies for wind generators," *IEEE International Conference on Electric Machines and Drives*, pp. 458–465, 2005.

[143] S. Müller, M. Deicke, and D. W. Doncker, "Doubly fed induction generator systems for wind turbines," *Ind. App. Magazine, IEEE Trans.*, vol. 8, no. 3, pp. 26–33, 2002.

[144] W. Qiao et al., "Wind speed estimation based sensorless output maximization control for a wind turbine driving a DFIG," *IEEE Trans. Power Electron.*, vol. 23, no. 3, pp. 1156–1169, 2008.

[145] L. Guo et al., "Super-twisting sliding mode observer based speed sensorless torque control for PMSG used in wind turbines," *9th International Conference*

on Power Electronics - ECCE Asia: "Green World with Power Electronics", ICPE 2015-ECCE Asia, pp. 2457–2462, 2015.

[146] Z. Ding, G. Wei, and X. Ding, "PMSM control system based on sliding mode technology and MRAS method," *International Conference on Mechatronics and Control (ICMC)*, pp. 1276–1281, 2014.

[147] G. Koch et al., "Sensorless technique applied to PMSG of WECs using sliding mode observer," *IEEE 13th Brazilian Power Electronics Conference and 1st Southern Power Electronics Conference (COBEP/SPEC)*, pp. 1–6, 2015.

[148] Y. S. Han, J. S. Choi, and Y. S. Kim, "Sensorless PMSM drive with a sliding mode control based adaptive speed and stator resistance estimator," *IEEE Trans. Magnetics*, vol. 36, no. 5 I, pp. 3588–3591, 2000.

[149] M. Burth, Michael, Verghese and G. C. Velez-Reyes, "Subset selection for improved parameter estimation in on-line identification of a synchronous Generator," *IEEE Trans. Power Sys.*, vol. 14, no. 1, pp. 218–225, 1999.

[150] G. Rigatos, P. Siano, and N. Zervos, "Sensorless control of distributed power generators with the derivative-free nonlinear kalman filter," *IEEE Trans. Ind. Electron.*, vol. 61, no. 11, pp. 6369–6382, 2014.

[151] M. Shasadeghi, "Sensorless control of PMSG-based wind turbine with parallel distributedcompensator with fuzzy observer," *The 6th International Power Electronics Drive Systems and Technologies Conference*, pp. 3–4, 2015.

[152] M. Benadja and A. Chandra, "Adaptive sensorless control of PMSGs-based offshore wind farm and VSC-HVDC stations," *IEEE Journal of Emerging and Selected Topics in Power Electron.*, vol. 3, no. 4, pp. 918–931, 2015.

[153] Y. Inoue et al., "Accuracy improvement of IPMSM sensorless drives with on-line parameter identification," *Fourth Power Conversion Conference-NAGOYA, PCC-NAGOYA 2007 - Conference Proceedings*, pp. 860–866, 2007.

[154] I. Colovic, M. Kutija, and D. Sumina, "Rotor flux estimation for speed sensorless induction generator used in wind power application," *IEEE International Energy Conference*, pp. 23–27, 2014.

[155] K. Liu and Z. Q. Zhu, "Online estimation of the rotor flux linkage and voltage-source inverter nonlinearity in permanent magnet synchronous machine drives," *IEEE Trans. Power Electron.*, vol. 29, no. 1, pp. 418–427, 2014.

[156] T. Lei et al., "Using improved power electronics modeling and turbine control to improve wind turbine reliability," *IEEE Trans. Energy Conv.*, vol. 3, no. 2, pp. 1043–1051, 2015.

[157] S. M. Jung et al., "An MRAS-based diagnosis of open-circuit fault in PWM voltage-source inverters for PM synchronous motor drive systems," *IEEE Trans. Power Electron.*, vol. 28, no. 5, pp. 2514–2526, 2013.

[158] B. Dumnic et al., "An improved MRAS based sensorless vector control method for wind power generator," *Journal of Applied Research and Technology*, vol. 10, no. 5, pp. 687–697, 2012.

[159] K. Tan and S. Islam, "Optimum control strategies in energy conversion of PMSG wind turbine system without mechanical sensors," *IEEE Trans. Energy Conv.*, vol. 19, no. 2, pp. 392–399, 2004.

[160] S. A. Diaz et al., "Indirect sensorless speed control of a PMSG for wind application," *2009 IEEE International Electric Machines and Drives Conference, IEMDC '09*, pp. 1844–1850, 2009.

[161] K. Akatsu and A. Kawamura, "Online rotor resistance estimation using the transient state under the speed sensorless control of induction motor," *IEEE Trans. Power Electron.*, vol. 15, no. 3, pp. 553–560, 2000.

[162] American Wind Energy Turbine Market Report, "AWEA Small Wind Turbine Global Market Study," 2010.

[163] U. S. Department of Energy, "*2014 Distributed Wind Market Report,*" 2014.

[164] J. Smith et al., "*Wind Turbine Generator System Power Performance Test Report for The EW50 Wind Turbine Simulation Model of Wind Turbine,*" 2011.

[165] RenewableUK, "Small and Medium Wind UK Market Report," 2013.

[166] Y. Zhao et al., "A review on position/speed sensorless control for permanent-magnet synchronous machine-based wind energy conversion systems," *IEEE Journal of Emerging and Selected Topics in Power Electron.*, vol. 1, no. 4, pp. 203–216, 2013.

[167] S. Yang et al., "A parameter-robust sliding mode observer for speed sensorless torque control of PMSG in wind power generation system," *Proceeding of the IEEE 28th Canadian Conference on Electrical and Computer Engineering*, pp. 1083–1087, 2015.

[168] S. Ichikawa et al., "Sensorless control of permanent-magnet synchronous motors using online parameter identification based on system identification theory," *IEEE Trans. Ind. Electron.*, vol. 53, no. 2, pp. 363–372, 2006.

[169] A. Cacciato, M. Scarcella, G. Scelba, G. Bille, S. M. Costanzo, D. Cucuccio, "Comparison of low-cost-implementation sensorless schemes in vector controlled adjustable speed drives," *in Proc. SPEEDAM*, pp. 1082–1087, 2008.

[170] Z. Chen et al., "A review of the state of the art of power electronics for wind turbines," *IEEE Trans. Power Electron.*, vol. 24, no. 8, pp. 1859–1875, 2009.

[171] C. B. Jacobina et al., "Induction generator static systems with a reduced number of components," *Industry Applications Conference, 1996. Thirty-First IAS Annual Meeting, IAS '96., Conference Record of the 1996 IEEE*, vol. 1, pp. 432–439, 1996.

[172] A. B. Raju, K. Chatterjee, and B. G. Fernandes, "A simple maximum power point tracker for grid connected variable speed wind energy conversion system with reduced switch count power converters," *Power Electronics Specialist Conference, 2003. PESC '03. 2003 IEEE 34th Annual*, vol. 2, pp. 748–753, 2003.

[173] E. C. dos Santos et al., "Single-phase to three-phase four-leg converter applied to distributed generation system," *IET Power Electron.*, vol. 3, no. 6, p. 892, 2010.

[174] A. Baktash, A. Jalilian, and A. Vahedi, "Direct power control of reduced switch active filters," *in Proc. ICHQP*, pp. 1–5, 2010.

[175] H. Li, K. L. Shi, and P. G. McLaren, "Neural-network-based sensorless maximum wind energy capture with compensated power coefficient," *IEEE Trans. Ind. App.*, vol. 41, no. 6, pp. 1548–1556, 2005.

[176] A. Reznik et al., "LCL filter design and performance analysis for small wind turbine system," *IEEE Trans. Ind. App.*, pp. 1–7, 2012.

[177] R. Beres et al., "A review of passive power filters for three-phase grid Connected voltage-source converters," *IEEE Journal of Emerging and Selected Topics in Power Electron.*, vol. 4, no. 1, pp. 54–69, 2015.

[178] S. V. Araújo et al., "LCL filter design for grid-connected NPC inverters in offshore wind turbines," *7th Internatonal Conference on Power Electronics, ICPE'07*, pp. 1133–1138, 2007.

[179] K. H. Ahmed, S. J. Finney, and B. W. Williams, "Passive filter design for three-phase inverter interfacing in distributed generation," *in Proceeding Compatibility in Power Electronics Conf.,* pp. 1–9, 2007.

[180] A. Reznik et al., "LCL Filter design and performance analysis for grid-interconnected systems," *IEEE Trans. Ind. App.*, vol. 50, no. 2, pp. 1225–1232, 2014.

[181] M. Zabaleta et al., "LCL grid filter design of a multimegawatt medium-voltage converter for offshore wind turbine using SHEPWM modulation," *IEEE Trans. Power Electron.*, vol. 31, no. 3, pp. 1993–2001, 2016.

APPENDIX A

PARAMETERS AND SPECIFICATIONS OF THE PMSM

Number of poles	8
Line-to-neutral RMS voltage (V)	230
Rated speed (r/min)	3000
Rated RMS current (A)	4
Rated torque (N·m)	2
Stator inductance (mH)	0.0033
Stator resistance (Ω)	3.4
Rotor magnetic flux linkage (Wb)	0.15
Moment of inertia ($kg.m^2$)	0.0075

APPENDIX B

```
function [Ta,Tb,Tc] = svgen_dq(Ualpha,Ubeta)
    tmp1 = Ubeta;
    tmp2 = Ubeta/2 + sqrt(3)/2 * Ualpha;
    tmp3 = tmp2 - tmp1;
    VecSector = 3;
    if (tmp2 > 0)
        VecSector = VecSector - 1;
    end
    if (tmp3 > 0)
        VecSector = VecSector - 1;
    end
    if (tmp1 < 0)
        VecSector = 7 - VecSector;
    end
    if(VecSector == 1 || VecSector == 4)
        Ta = tmp2;
        Tb = tmp1 - tmp3;
        Tc = -tmp2;
    elseif(VecSector == 2 || VecSector == 5)
        Ta = tmp3 + tmp2;
        Tb = tmp1;
        Tc = -tmp1;
    else
        Ta = tmp3;
        Tb = -tmp3;
        Tc = -(tmp1 + tmp2);
    end
end
```

APPENDIX C

```
v.tmp1= v.Ubeta;
v.tmp2= _IQdiv2(v.Ubeta) +(_IQmpy(_IQ(0.866),v.Ualpha));
v.tmp3= v.tmp2 - v.tmp1;
v.VecSector=3;
v.VecSector=(v.tmp2> 0)?( v.VecSector-1):v.VecSector;
v.VecSector=(v.tmp3> 0)?( v.VecSector-1):v.VecSector;
v.VecSector=(v.tmp1< 0)?(7-v.VecSector) :v.VecSector;
    if(v.VecSector==1 || v.VecSector==4)
      { v.Ta= v.tmp2;
        v.Tb= v.tmp1-v.tmp3;
        v.Tc=-v.tmp2;
      }
    else if(v.VecSector==2 || v.VecSector==5)
      { v.Ta= v.tmp3+v.tmp2;
        v.Tb= v.tmp1;
        v.Tc=-v.tmp1;
      }
    else
      { v.Ta= v.tmp3;
        v.Tb=-v.tmp3;
        v.Tc=-(v.tmp1+v.tmp2);
      }
```

APPENDIX D

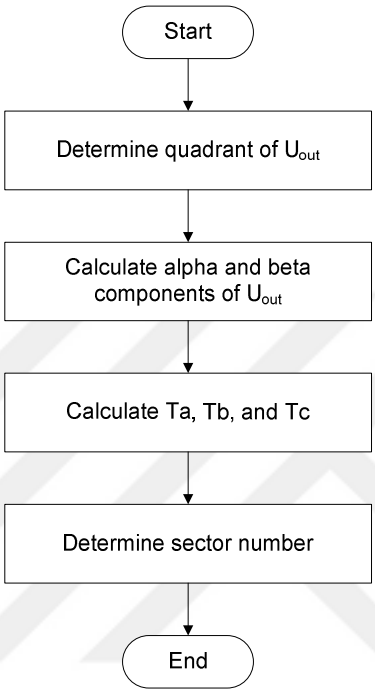
Start
Determine quadrant of U_{out}
Calculate alpha and beta components of U_{out}
Calculate Ta, Tb, and Tc
Determine sector number
End

VITA

Omer Cihan Kivanc received the B.S. degree in electrical engineering from Istanbul Technical University, Istanbul, Turkey, in August, 2011. In September 2011, he joined the Power Electronics and Electromechanical Energy Conversion Laboratory research group at Okan University, Istanbul, Turkey, where he received the Ph.D. degree in mechatronics engineering in June 2016. Asst. Prof. S. Baris Ozturk was his advisor.

Since September 2011, Kivanc has been graduate researcher and teaching assistant in the Department of Electrical and Electronics Engineering at Okan University, and he has also worked as electrical engineering and researcher at Mekatro Research and Development Company since 2011.

His current research interests include ac motor drives, in particular sensorless control of permanent magnet synchronous and brushless dc motors, power electronics, control systems, electric and hybrid vehicle applications, renewable&clean energy systems, intelligent and connected vehicle applications, internet of things applications and autonomous robots.

Omer Cihan Kivanc is a student member of the IEEE.

Transaction Papers

- **O. C. Kivanc** and S. B. Ozturk, "Low-cost sensorless speed control of PMSM drive using reduced switch inverter based on stator feedforward voltage estimation," *IEEE Trans. Power Electron.*, 2016. (re-submitted)

- O. Ustun, **O. C. Kivanc**, S. Senol, G. Tosun, B. Fincan and R. N. Tuncay, “On field weakening performance of a BLDC motor with higher winding inductance: why does design matter?” *IEEE Trans. Ind. Electron.*, 2016. (re-submitted)

Internationally Indexed Journals

- **O. C. Kivanc** and S. B. Ozturk, “MATLAB function based approach to FOC of PMSM drive”, *International Journal of Simulation Systems, Science & Technology (IJSSST)*, vol. 17, no. 3, 2016.

Conference Papers

- O. Ustun, S. B. Ozturk, **O. C. Kivanc**, P. G. Ali Zade and R. N. Tuncay, "Exciting system selection for brushless synchronous machine," *in Proc. 8th Mediterranean Conference on Transmission, Distribution and Energy Conversion (MEDPOWER 2012),* pp. 1–6, 2012.
- P. G. Ali-Zade, R. N. Tuncay, S. B. Ozturk, **O. C. Kivanc**, “Quasi-smart construction synchronous machine working with extensive cycling load”, *in Proc. International Conference on Application of Information and Communication Technology and Statistics in Economy and Education (ICAICTSEE – 2012),* pp. 93–101, UNWE, Sofia, Bulgaria, Oct. 5–6, 2012
- O. Ustun, M. Cakan, R. N. Tuncay, M. S. Mokukcu, **O. C. Kivanc**, Y. Mutlu and G. Tosun, “Design and manufacture of electric vehicle powertrain and its cooling system for ITU EV project,” *in Proc. 2014 International Conference on Electrical Machines (ICEM),* pp. 730–735, 2014.
- O. Ustun, R. N. Tuncay, M. S. Mokukcu, **O. C. Kivanc** and G. Tosun, “Istanbul technical university full electric battery vehicle project–ITU EV”, *in Proc. 7th Automotive Technologies Congress (OTEKON’14)*, Bursa, 2014.

- O. Ustun, R. N. Tuncay, **O. C. Kivanc**, B. Fincan and G. Tosun, “Development and implementation of field weakening algorithm for brushless DC motors”, *ELECO 2014*, Bursa, 2014.
- G. Tosun, O. Ustun, **O. C. Kivanc**, E. Oguz, O. Ustun; R. N.Tuncay, "Development of high efficiency multi-output flyback converter for industrial applications," *9th International Conference on Electrical and Electronics Engineering (ELECO)*, pp. 1102–1108, 2015.
- **O. C. Kivanc** and S. B. Ozturk, “MATLAB function based approach to FOC of PMSM drive,” *in Proc. IEEE European Modeling Symposium (EMS)*, pp. 96–102, Madrid, Spain, 2015.
- B. Atila, T. E. Mungan and **O. C. Kivanc**, "Different filter approaches and performance analysis of fundamental sensors in autonomous ground vehicles," *in Proceedings 24th Signal Processing and Communication Application Conf. (SIU)*, pp. 1605–1608, 2016.
- G. Tosun, **O. C. Kivanc**, O. Ustun, E. Oguz, Y. Mutlu, "Design of a position controlled electric actuator used in fluid control valves," *IEEE International Conf. on Power Electronics and Motion Control*, 2016, Varna, Bulgaria.
- O. Ustun, G. Tanc, **O. C. Kivanc**, G. Tosun, "In pursuit of proper BLDC motor design for electric bicycles," *IEEE International Conference on Electrical Machines*, 2016, Lausanne, Switzerland.
- **O. C. Kivanc**, O. Ustun, G. Tosun, R.N. Tuncay, "On regenerative braking capability of BLDC motor," *Annual Conference of IEEE Industrial Electronics Society*, 2016, Florence, Italy.

- **O. C. Kivanc**, S. B. Ozturk, R. N. Tuncay, E. Kesici and C. Yazi, "Electro-hydraulic power steering system modelling for parameter fault detection based on model reference adaptive frame," *Annual Conference of IEEE Industrial Electronics Society*, 2016, Florence, Italy.

Patents

- P. G. Ali-Zada, **O. C. Kivanc**, S. B. Ozturk, R. N. Tuncay, "Cok Kanatli Yelken Tipi Dairesel Bir Ruzgar Turbini," Turkish Patent Institute (TPE) Pub. No: 2013–G–456408, July 21, 2015.

Projects

- ***TUBITAK-3501****-Implementation of Position Sensorless Direct-Drive Permanent Magnet Generator-based Small-Scale Wind Power Generating System for Wide Speed Ranges* ***(Researcher)***

  Beginning: 01/04/2013 Ending: 01/01/2016
- ***TUBITAK-1002****-Very Low Speed Control of Three Phase AC Motor Using Least Mean Square Method With Low Resolution Encoder*

  Beginning: 01/11/2015 Ending: 31/10/2016 ***(Researcher)***
- ***TUBITAK-1002****-Design and Implementation of High Maneuverability Autonomous Robot Platform for Industrial and Military Purposes*

  Beginning: 01/07/2016 Ending: 01/07/2017 ***(Principle Investigator)***
- *Innovative and Sustainable Electric and Hybrid Electric Vehicle Technology Development and Clustering Center* ***(ISTKA)****-TR10/14/YEN/0088* ***(Researcher)***

  Beginning: 01/09/2013 Ending: 01/09/2015

- *Intelligent and Connected Vehicle Technologies Development and Clustering Center* ***(ISTKA)****-TR10/15/YNK/0022* ***(Researcher)***

  Beginning: 01/09/2015 Ending: 01/09/2016
- ***KOSGEB****-Design and Implementation of E-Bike Power Train* ***(Researcher-MEKATRO R&D Comp.)***
- ***KOSGEB****-Design and Implementation of Electric Machine Driver* ***(Researcher-MEKATRO R&D Comp.)***
- *Linear BLDC Motor and Driver Design for a Ramp System Project* ***(Researcher-MEKATRO R&D Comp.)***
- *Design and Development of Electric Power Train for Solar Car Project* ***(Researcher-MEKATRO R&D Comp.)***
- *Development of Electric Power Train for Hub-Motor Electric Vehicle Project* ***(Researcher-MEKATRO R&D Comp.)***
- *High Efficiency (IE4) LSIPMSM Design Project* ***(Researcher-MEKATRO R&D Comp.)***
- *Design of a Position Controlled Electric Actuator Used in Fluid Control Valves Project* ***(Researcher-MEKATRO R&D Comp.)***
- *Smart Pump Selection Algorithm Development Based on WEB Project* ***(Researcher-MEKATRO R&D Comp.)***
- *Three-Level UPS Control Software Development Project* ***(Researcher-MEKATRO R&D Comp.)***